MULTISCALE IONOSPHERIC ELECTRODYNAMICS AND THEIR IMPACTS ON THE IONOSPHERE-THERMOSPHERE SYSTEM

by

QINGYU ZHU

DISSERTATION

Submitted in partial fulfillment of the requirements

for the degree of Doctor of Philosophy at

The University of Texas at Arlington

August, 2020

Arlington, Texas

Supervising Committee:

Yue Deng, Supervising professor

Ramon Lopez

Zdzislaw Musielak

Daniel Welling

Mingwu Jin

ABSTRACT

MULTISCALE IONOSPHERIC ELECTRODYNAMICS AND THEIR IMPACTS ON THE IONOSPHERE-THERMOSPHERE SYSTEM

Qingyu Zhu, Ph.D.

The University of Texas at Arlington, 2020

Supervising Professor: Yue Deng

In this dissertation, multiscale ionospheric electrodynamics at different latitudinal regions and their impacts on the ionosphere and thermosphere (I-T) system have been studied in three aspects. Firstly, impacts of the vertical neutral dynamics on the dayside low- and mid-latitude thermosphere have been evaluated using a non-hydrostatic model, Global Ionosphere Thermosphere Model (GITM), for the first time. It is found that the upward neutral wind increases the F-region neutral density, which plays an important role in balancing for the neutral density reduction associated with the divergent meridional wind in the equatorial region. The divergent meridional wind contributes to the formation of the equatorial thermosphere anomaly. Meanwhile, acoustic waves triggered by the vertical ion-neutral coupling processes are generated in the simulation. Secondly, this dissertation greatly advances the statistical knowledge of small-scale and mesoscale structures in high-latitude electrodynamical forcings, which is still lacking to date. Better understanding on small-scale and mesoscale structures in high-latitude electrodynamical forcings can

improve the estimation of Joule heating, which is a critical pathway for the electromagnetic energy from the magnetosphere to deposit into the I-T system. On the one hand, the correlation between the electric field and the electron precipitation has been systematically quantified unprecedentedly. The overall anti-correlation results in a significant depression of Joule heating on the dusk side. On the other hand, the relationship between the field-aligned currents (FACs) and electric fields has been studied. It is found that strong FACs do not necessary correspond to strong electric field on small scale and mesoscale. Nevertheless, mesoscale FACs have a non-negligible contribution to Joule heating. Thirdly, efforts have also been made to improve high-latitude electrodynamical forcing specifications and estimations of Joule heating. First, a new empirical model, ASHLEY, has been established based on measurements from the Defense Meteorological Satellite Program satellites. As compared with most existing empirical models, new features of ASHLEY include improvements in specifications of soft electron precipitations and electric field variabilities. Moreover, by coupling the electron precipitation component of ASHLEY (ASHLEY-A) into GITM, a real event study illustrates that advanced soft electron precipitation specifications can remarkably improve the data-model comparison of the F-region neutral density during geomagnetic storms. Finally, potential applications of the boundary-oriented binning method in the high-latitude empirical modeling have been explored. It is found that the boundary-oriented binning method can address the deficiency of the commonly used static binning method and further improve Joule heating estimations.

ACKNOWLEDGEMENTS

I would like to express my sincere thanks to my graduate research advisor at UT Arlington, Dr. Yue Deng, for her excellent mentorship and continuous encouragements throughout my graduate career. Her enthusiasm of discovery has fostered my passion for pursuing the space physics in different areas. I would also like to acknowledge my undergraduate research advisor, Dr. Jiuhou Lei. His initial guidance of my academic coding and writing was uniquely helpful for my graduate research. Moreover, many thanks to my committee members: Drs. Ramon Lopez, Zdzislaw Musielak, Daniel Welling, Mingwu Jin. Their valuable comments and suggestions have greatly improved this dissertation.

I am also grateful for the mentorships from Drs. Astrid Maute and Arthur Richmond at the High Altitude Observatory (HAO) of the National Center of Atmospheric Research (NCAR). Astrid kindly hosted my summer visits to HAO during last three years and generously shared the data and codes with me which have been used throughout this dissertation. Meanwhile, Art consistently addressed my questions and provided very insightful suggestions on my research projects and paper manuscripts with his extensive knowledge and broad experience, which has greatly advanced my understanding of those projects and significantly improved my writing skills. I would like to thank my other collaborators in other institutes: Ryan McGranaghan, Yun-ju Chen, Marc Hairston, Delores Knipp, Liam Kilcommons, Robert Redmon, Elizbeth Mitchell, Phil Anderson and Aaron Bukowski. The dissertation could not have been completed without their sustained contributions.

Thank you to all my colleagues in or ever in our research group during my stay at UT Arlington. In particular, I would like to acknowledge Drs. Cheng Sheng and Cissi Lin who patiently taught me how to run simulations and process data on the supercomputer which I had never touched before joining UT Arlington.

Thank you to all faculties and staffs in the Department of Physics at UT Arlington and all my class lecturers in other departments. Meanwhile, thank you for all NCAR scientists I have met during my summer visits and NCAR staffs who helped me process traveling stuffs. Studying at UT Arlington and visiting NCAR are definitely impactful and rewarding experiences of my life.

Thank you to all my old friends and all new friends I have met during past five years who are really inspiring and supportive. In particular, I would like to thank those who sent their warm regards to me and those who were willing to spend their time communicating with me remotely during this challenging time. A list of their names is too long to include here.

Last but not least, I would like to express my deep thanks to my family who have provided consistent supports to me. In particular, my parents Yuzhu and Yan, who were my constant rocks throughout my life. I could not have made it without their supports.

This dissertation is supported by NASA through grants NNX13AD64G as well as NNX14AD46G, and AFOSR through award FA9550-16-1-0059 and FA9559-16-1-0364. I also acknowledge high-performance computing support from the Texas Advanced Computing Center at the University of Texas at Austin, and from Cheyenne provided by NCAR's Computational and Information Systems Laboratory, sponsored by the National Science Foundation.

July 28, 2020

Arlington, TX

TABLE OF CONTENTS

LIST OF FIGURES

LIST OF TABLES

CHAPTER 1

Introduction

In this Chapter, a brief introduction of the background of this dissertation is presented at first. Next, several open questions concerning the multiscale ionospheric electrodynamics that are addressed in this dissertation are highlighted. Finally, the objectives of this dissertation are outlined.

1.1 Background

This section aims to provide an general overview of Earth's ionosphere and thermosphere (I-T) system, dominant ionospheric electrodynamical processes in different latitudinal regions and the geomagnetic storm which is one major focus of space weather research. More comprehensive reviews can be found in *Rishbeth and Garriott* (1969), *Schunk and Nagy* (2000) and *Kelley* (2009).

1.1.1 Ionosphere and thermosphere

The Earth's atmosphere can be distinguished into several stratified layers according to its temperature variation. At about 90 - 600 km above the sea level, the neutral temperature of Earth's atmosphere increases with the altitude due to the absorption of solar extreme ultraviolet (EUV) radiations, and this layer is referred to as the thermosphere (Figure 1.1). The neutral temperature increases dramatically at altitudes between 90 and 200 km and be-

comes roughly constant above 200 km due to the high thermal conductance. The lower part (<120 km) of the thermosphere is well-mixed as the atmosphere below the thermosphere while different species are separated at higher altitudes due to the prevailing molecular diffusion (*Schunk and Nagy*, 2000). Although the number density for all species decrease with the altitude, the heavier species decrease faster. Meanwhile, the atomic Oxygen (O) associated with the photodissociation of O_2 becomes more important at higher altitudes than N_2 and O_2 molecules which are dominant species at the lower part of the atmosphere.

At above 60 km above the see level, the atmosphere becomes weakly ionized, and the ionized part of the atmosphere is called ionosphere (Figure 1.1). The primary ionization sources are solar EUV radiations, energetic particle precipitations as well as soft X-ray radiations, and their relative significance may differ in different regions and altitudes. The ionosphere can also be divided into several stratified layers according to the vertical electron density profile. Typically, the ionosphere can be divided into D (60-90 km), E (100-150 km) and F (150-600 km) regions with D and E regions dominated by chemical processes and F region dominated by plasma transport processes. The major ion species in the D and E regions are molecular ions (e.g., NO^+, O_2^++ and N_2^+) while O^+ dominates in the F region. For a typical dayside electron density profile, two peaks can be found with one in the E region and the other in the F region which is roughly an order larger than the E-region peak. The ionosphere and thermosphere are closely coupled through the ion-neutral coupling process, which is one major focus of this dissertation.

Both the neutral/electron/ion densities and temperatures can be significantly affected by the solar activity, of which the intensity exhibits an 11-year cycle. The neutral density and temperature are typically higher when the Sun is more active (solar maximum) than those when the Sun is less active (solar minimum). However, the electron temperature decreases as the Sun become more active due to the increased electron-ion coupling (e.g., *Roble*, 1976), although the electron density increases from the solar minimum to the solar

maximum. Apart from the solar cycle dependence, the ionosphere and thermosphere also exhibits variations on different time scales (e.g., *Forbes et al.*, 2000).

1.1.2 Ionospheric electrodynamics

Observations have proved that there are electric currents flowing in the ionosphere (maximize at ∼90-200 km) and the existence of currents can significantly affect the dynamics of ions and neutrals in the I-T system. The electrical phenomena and their interacting dynamical effects are referred to as the electrodynamics (*Richmond*, 2016). This subsection provides an overview on the current generation theorem in different latitudinal regions. Above 90 km, it is adequate to consider all ion species together as a single fluid of which the number density is equal to the electron number density, N, since the major ion species are single charged (*Richmond*, 2016). The ionospheric current density $\mathbf{J}$ is equal to N multiplied by the ion and electron velocity difference $\mathbf{V_i} - \mathbf{V_e}$:

$$\mathbf{J} = Ne(\mathbf{V_i} - \mathbf{V_e}) \tag{1.1}$$

The ion and electron velocities can be solved from the momentum equation, and the current density $\mathbf{J}$ in the the frame of reference of the neutral wind (velocity is $\mathbf{U_n}$) is (see details in *Richmond*, 2016):

$$\mathbf{J} = \sigma_P \mathbf{E}_\perp^{'} + \sigma_H \mathbf{b} \times \mathbf{E}_\perp^{'} + \sigma_\parallel (E_\parallel - E_a)\mathbf{b} + \mathbf{J}_{pg} \tag{1.2}$$

Where $\mathbf{E}_\perp + \mathbf{U}_\mathrm{n} \times \mathbf{B}_0$ is the perpendicular component of $\mathbf{E}_\perp$ in the frame of reference of the neutral wind, and the $\mathbf{U_n} \times \mathbf{B_0}$ component is often called the dynamo electric field. $\mathbf{B}_0$ is the geomagnetic main field of which the unit vector is $\mathbf{b}$, $\mathrm{E}_\parallel$ is the parallel electric field, $\mathrm{E_a}$ is the parallel electric field is the ambipolar electric field and $\mathbf{J}_\mathrm{pg}$ is the current related to the pressure gradient and gravity which is typically insignificant. In addition,

σ_{P}, σ_{H} and $\sigma_{\parallel}$ are Pedersen, Hall and parallel conductivities, respectively, which can be expressed as (*Richmond*, 2016):

$$\sigma_P = \frac{Ne}{B}\left(\frac{\nu_{in}\Omega_i}{\nu_{in}^2+\Omega_i^2}+\frac{\nu_{en\perp}\Omega_e}{\nu_{en\perp}^2+\Omega_e^2}\right) \tag{1.3}$$

$$\sigma_H = \frac{Ne}{B_0}\left(\frac{\Omega_i^2}{\nu_{in}^2+\Omega_i^2}+\frac{\Omega_e^2}{\nu_{en\perp}^2+\Omega_e^2}\right) \tag{1.4}$$

$$\sigma_{\parallel} = \frac{Ne^2}{m_e(\nu_{en\parallel}+\nu_{ei\parallel})} \tag{1.5}$$

Where ν_{in} is the ion-neutral collision frequency, $\nu_{\mathrm{en}\parallel}$ and $\nu_{\mathrm{en}\perp}$ are electron-neutral collision frequencies along **b** and perpendicular to **b**, respectively, and $\nu_{\mathrm{ei}\parallel}$ is the electron-ion collision frequency along **b**. In addition, Ω_{e} and Ω_{i} are electron and ion gyro-frequencies, respectively.

The ion-neutral and electron-neutral collision frequencies decrease with the altitude and are much smaller than the gyro-frequencies in the F-region (See Figure 2 of *Richmond* (2016)). The very large gyro-frequencies in the F region allow the ions and electron move approximately in the same velocity ($\frac{\mathbf{E}\times\mathbf{B}_0}{\mathrm{B}_0^2}$), namely the $\mathbf{E}\times\mathbf{B}$ drift (*Heelis*, 2004). Figure 1.2 exhibits typical conductivities profiles at a mid-latitude location. It is clear that the parallel conductivity ($\sigma_{\parallel}$) increases with the altitude and is much larger than σ_{P} and σ_{H} regardless of the local time. The very large parallel conductivity prohibits the existence of the electric field (i.e., electric potential drop) along **b**, so that the magnetic field lines are essentially equipotential (*Richmond*, 2016). As for σ_{P} and σ_{H}, both of them decrease with the altitude and peak at the E region. On the dayside, Pedersen and Hall conductivities are much larger in the E-region than F-region. Moreover, σ_{H} is much larger than σ_{P} at lower part of the E region ($<$110 km) while σ_{P} is more important than σ_{H} at higher altitudes. On the nightside, E-region Pedersen and Hall conductivities decrease significantly, and F-region Pedersen and Hall conductivities become dominant.

1.1.2.1 Low- and mid-latitude ionospheric electrodynamics

At low and middle latitudes, the neutral winds in the thermosphere are important for the ionospheric current generation, and the corresponding physical process is called the wind dynamo process. During the daytime, E-region conductivities dominate, so that E-region neutral winds are primarily responsible for generating the ionospheric electric currents (*Heelis*, 2004). At the altitudes where Hall conductivity dominates ($<$110 km), a circular current system can be created on the dayside, namely the Sq (S: solar; q: quiet) current system. In addition, there is also a strong electrojet near the magnetic equator, namely the equatorial electrojet (EEJ), which is associated with the large ratio between Hall and Pedersen conductivities (*Rishbeth and Garriott*, 1969). Both the Sq current and EEJ have been detected by magnetometers from ground and space.

At the upper part of E region ($>$110 km), the dayside poleward neutral winds generate a westward Pedersen current, so that positive (negative) charges accumulate on the dawn (dusk) side, which induces an eastward (westward) electric field on the day (night) side. The electric field is mapped to higher altitudes along the field line, generating an upward (also slightly westward) and downward (also slightly eastward) ion drift on dayside and nightside in the equatorial region, respectively (Figure 1.3). There is also a sharp enhancement in the vertical ion drift on the dusk side, namely the pre-reversal enhancement (PRE), of which the governing physical mechanism is not well established. Discussions related to the formation of the PRE can be found in *Kelley* (2009). The dayside vertical ion drift can predominantly alter the topography of the low- and mid-latitude ionosphere. For example, it was found that the vertical ion drift can lead to the formation of the equatorial ionization anomaly (EIA) where two peaks in the ionospheric electron density forms instead of one peak near the subsolar point (*Appleton*, 1946). The corresponding process is called fountain effect (*Hanson and Moffett*, 1966).

On the night side, F-region neutral winds play a more important role in generating ionospheric currents than E-region winds owing to higher F-region conductivities (*Heelis*, 2004). The typical eastward nightside F-region neutral winds (e.g., *Wharton et al.*, 1984) generate an upward Pedersen current at the F region, so that a downward polarization electric field is induced at the F-region, generating an additional eastward ion drift on top of that related to the dayside dynamo processes. Therefore, the magnitude of the nightside zonal drift is larger than the dayside zonal drift (See Figure 2 of *Fejer* (2011)).

1.1.2.2 High-latitude ionospheric electrodynamics

The Earth's atmosphere is surrounded by the magnetosphere (Figure 1.4), which forms due to the existence of the intrinsic terrestrial magnetic field. The magnetosphere prevents the direct interaction between the magnetized plasma ejected from the Sun (i.e., solar wind) and terrestrial atmosphere, which has played a crucial role in the Earth's habitability. The dayside magnetosphere is compressed by the solar wind with its outer boundary (magnetopause) located at around 6-10 Earth Radii (R_e), while the nightside magnetosphere can be stretched by the solar wind to possibly $>$100 R_e. The solar wind-magnetosphere (SW-M) coupling plays an important role in the high-latitude electrodynamics.

Figure 1.5 provides an overview of the SW-M coupling processes when the magnetic field in the solar wind (i.e., the interplanetary magnetic field - IMF) is southward. First, a reconnection occurs at the dayside magnetopause, so that the IMF connects with the previously closed geomagnetic field lines, forming open field lines, and the region where the open field lines are located is referred to as the polar cap. Then the open field lines are dragged toward the magnetotail, leading to another reconnection. New closed field lines form and convect sunward. This process is known as the Dungey cycle (*Dungey*, 1961).

Ionospheric ion convection: The electric fields generated during the SW-M interaction are mapped down to ionosphere along the equipotential magnetic field lines, driving

the ionospheric plasma convection. In the F-region, the ionospheric plasma moves at the $\mathbf{E} \times \mathbf{B}$ velocity due to the low ion-neutral collision frequency. The F-region convection exhibits a two-cell pattern when the IMF has a southward component, with the plasma drifting anti-sunward across the polar cap and sunward at lower latitudes. In addition, the dawn-dusk component of the IMF can significantly impact the convection pattern (e.g., *Reiff and Burch*, 1985; *Burch et al.*, 1985). Moreover, a multicell pattern may appear when the IMF has a strong northward component. Although the ion convection at high latitudes is highly variable, their large-scale statistical pattern is well captured by several empirical models by using different measurements (e.g., *Foster et al.*, 1986; *Heppner and Maynard*, 1987; *Holt et al.*, 1987; *Ruohoniemi and Greenwald*, 1996; *Papitashvili and Rich*, 2002; *Ruohoniemi and Greenwald*, 2005; *Weimer*, 2005; *Haaland et al.*, 2007; *Cousins and Shepherd*, 2010; *Thomas and Shepherd*, 2018). When a two-cell pattern appears, the location separating sunward and anti-sunward ion drifts is referred to as the convection reversal boundary (CRB), which is well-aligned with the polar cap boundary (also known as the open-closed field line boundary, OCB) especially when the IMF B_z is southward (e.g., *Sotirelis et al.*, 2005; *Drake et al.*, 2009). Variations of the CRB under different conditions have been extensively investigated in previous studies (e.g., *Hairston and Heelis*, 1990; *de la Beaujardiere et al.*, 1991; *Bristow and Spaleta*, 2013; *Chen et al.*, 2015; *Koustov and Fiori*, 2016; *Chen and Heelis*, 2018)

Auroral particle precipitation: The SW-M coupling also leads to the precipitation of energetic particles, including both ions and electrons, which are important ionization sources of the upper atmosphere at high latitudes. In general, precipitating electrons play a more important role in affecting the upper atmosphere than precipitating ions, so this dissertation mainly focuses on the electron precipitations. Most energetic electrons tend to precipitate in a region called the auroral oval, which can be identified from both in-situ particle observations (e.g., *Newell et al.*, 1996; *Redmon et al.*, 2010; *Kilcommons et al.*,

2017) and auroral emission observations (e.g., *Holzworth and Meng*, 1975; *Baker et al.*, 2000; *Ding et al.*, 2017). The total electron energy flux and average electron energy vary with the locations, and their variations with the geomagnetic activity level are well captured in several empirical models (e.g., *McDiarmid et al.*, 1975; *Spiro et al.*, 1982; *Fuller-Rowell and Evans*, 1987; *Hardy et al.*, 1985, 1987; *Zhang and Paxton*, 2008; *Newell et al.*, 2009; *Mitchell et al.*, 2013; *Newell et al.*, 2014). Furthermore, precipitating electrons penetrate at different altitudes depending on their average energies. In general, electrons with higher energy penetrate to lower altitudes so that the E-region ionization is mainly associated with $>$1 keV incident electrons while the F-region ionization is typically related to $<$1 keV precipitating electrons (also known as soft electron precipitations).

Field-aligned currents: The ionospheric currents exist due to the existences of the ionospheric electric fields and conductivities. The ionospheric currents are not divergence-free and are closed by the currents following along geomagnetic field lines, i.e., field-aligned currents (FACs). The current continuity equation is:

$$\nabla_\perp \cdot \mathbf{J}_\perp = \nabla_\perp \cdot (\Sigma \cdot \mathbf{E}_\perp) = -J_\parallel \tag{1.6}$$

Where $\mathbf{J}_\perp = \Sigma \cdot \mathbf{E}_\perp$ is the ionospheric current density and $J_\parallel$ is the FAC density. In addition, Σ is the ionospheric conductance (height-integrated conductivity) tensor and $\mathbf{E}_\perp$ is the ionospheric electric field.

The morphological features of large-scale FACs have been established since 1970s (e.g., *Iijima and Potemra*, 1976a,b, 1978). Basically, large-scale FACs can be categorized into Region 1 (R1) and Region 2 (R2) currents, where R1 currents are located at higher latitudes and R2 currents are located at lower latitudes with smaller current densities than R1 currents. In addition, R1 currents flow into the ionosphere on the dawn side and flow out from the ionosphere on the dusk side and the opposite is true for the R2 currents. A schematic diagram of the large-scale FAC is shown in Figure 1.6. Further, it has been found

that the distribution of the large-scale FACs greatly depends on the geophysical conditions (e.g., *Wang et al.*, 2005; *Ohtani et al.*, 2005; *Juusola et al.*, 2009; *He et al.*, 2012; *Coxon et al.*, 2014; *Korth et al.*, 2014; *Milan et al.*, 2015; *Carter et al.*, 2016).

1.1.2.3 Joule heating

Joule heating is an important electrodynamical process at high latitudes (*Cole*, 1962). Since different species (ion, electron, neutral) have different bulk velocities, collisions between different species result in momentum change and heating (e.g., *Thayer and Semeter*, 2004), and the total frictional heating rate (Q) is (*Richmond*, 2020):

$$Q = Nm_i\nu_{in}(\mathbf{V}_i - \mathbf{U}_n)^2 + Nm_e\nu_{en}(\mathbf{V}_e - \mathbf{U}_n)^2 + Nm_e\nu_{ei}(\mathbf{V}_e - \mathbf{V}_i)^2 \tag{1.7}$$

All parameters in the above equation are the same as those defined earlier in this Section. Because $\mathrm{m_i}\nu_{\mathrm{in}}$ is much larger than $\mathrm{m_e}\nu_{\mathrm{en}}$ and $\mathrm{m_e}\nu_{\mathrm{ei}}$, so that ion-neutral collisional heating rate usually dominates. The ion-neutral collision can significantly increase the ion temperature due to the large difference between $\mathbf{V}_{\mathrm{i}}$ and $\mathbf{U}_{\mathrm{n}}$ (typically on the order of 100 m/s), which then remarkably increases the neutral temperature. Hence, the ion-neutral collisional heating is an important energy source for the upper atmosphere.

The total collisional heating rate Q is found to be approximated to the total Joule heating deposition rate, $\mathbf{J}\cdot\mathbf{E}'_{\perp}$ (e.g., *Thayer and Semeter*, 2004). If neglecting $\mathbf{J}_{\mathrm{pg}}$ in Eq. 1.2 and the electric field along the field line, the total Joule heating deposition rate can be written as:

$$Q = \mathbf{J}\cdot\mathbf{E}'_{\perp} = \sigma_P(\mathbf{E}_{\perp} + \mathbf{U}_n \times \mathbf{B}_0)^2 \tag{1.8}$$

Which is part of the total electromagnetic energy transfer rate $\mathbf{J}\cdot\mathbf{E}$ to the medium:

$$\mathbf{J}\cdot\mathbf{E} = Q + \mathbf{U}_n\cdot\mathbf{J}\times\mathbf{B}_0 \tag{1.9}$$

The second terms on the right-hand side (RHS) of Eq. 1.9 is called the *kinetic energy rate*. Unlike the Joule heating deposition rate, which is always positive, the kinetic energy

rate, which represent the rate of work done on the medium by the Ampere force, can be either positive or negative (*Richmond*, 2020). In general, the total electromagnetic energy deposited in the upper atmosphere is mainly converted into Joule heating although kinetic energy can be important at certain locations and under certain conditions (e.g., *Thayer and Vickrey*, 1992; *Thayer et al.*, 1995). In addition to affecting the kinetic energy, neutral winds also substantially affect the Joule heating (e.g., *Lu et al.*, 1995; *Billett et al.*, 2018).

1.1.3 Geomagnetic storms

The geomagnetic storm refers to a temporary disturbance of the magnetosphere, which is more likely occur when the IMF has a strong and steady southward component. During geomagnetic storms, the I-T system can also be significantly disturbed. The communication, navigation, satellite operation, ground power grid can be severely affected during geomagnetic storms, so that the geomagnetic storm is a central topic of the space weather research.

During the main phase of a geomagnetic storm, the intensity of high-latitude ionospheric currents increases significantly due to the increased ionospheric electric field intensity and electron precipitation, so that substantial Joule heating is deposited into the high-latitude I-T system. The enhanced Joule heating causes neutral temperature and density variations. In addition, the heating can effectively change the global circulation within several hours, which remarkably alters the thermospheric compositions at different latitudes and can further change the ionospheric electron density. Moreover, gravity waves can be launched due to rapid variations of heating and gravity waves can propagate to lower latitudes, generating large-scale traveling atmospheric disturbances (TADs) and traveling ionospheric disturbances (TIDs) (e.g., *Fuller-Rowell et al.*, 1997a).

The low- and mid-latitude electrodynamics can also be significantly changed during geomagnetic storms. Strong eastward electric fields can penetrate to the equatorial region

at the early stage of the storm on the dayside, increasing equatorial upward vertical drifts (e.g., *Spiro et al.*, 1988). The enhanced vertical drifts result in more pronounced EIA structures and enhancements of the electron density at low and middle latitudes (e.g., *Mannucci et al.*, 2005). The storm-time equatorward neutral winds in response to the high-latitude heating inputs can also modify the low- and mid-latitude electrodynamics (e.g., *Blanc and Richmond*, 1980), which tends to generate polarized electric fields that depress the dayside upward ion drifts in the equatorial region (e.g., *Fejer and Scherliess*, 1997). The relative importance of two mechanisms to the low-latitude electrodynamics differs at different stages of a storm (e.g., *Maruyama et al.*, 2005). In addition, it was found that the storm-time equatorward neutral winds also tend to increase the mid-latitude electron density through the transport process, leading the formation of the storm-enhanced densities (SEDs) (e.g., *Lu et al.*, 2008).

However, the big picture discussed in the above two paragraphs probably only represents an over-simplified case, the response of the I-T system to a geomagnetic storm can be very complicated in reality. For example, the response strongly depend on the longitudes, latitudes and universal time. Moreover, the response of the I-T system to different storms can be very different. Therefore, understanding the impacts of a geomagnetic storm on the I-T system is an very important and challenging topic in the space weather research.

1.2 Open questions

Although great efforts have been made in studying Earth's ionospheric electrodynamics and their impacts on the I-T system, many questions still remain unsolved (*Heelis and Maute*, 2020). In this dissertation, we mainly focus on three questions that are described in detail in this section.

1.2.1 Impacts of neutral winds on the thermosphere at low and middle latitudes

At low and middle latitudes, one challenge is to understand the connections between neutral winds and neutral density. For example, although the equatorial thermosphere anomaly (ETA), which is a phenomenon similar to the EIA that has been discussed in Section 1.1.2.1, has been studied for several decades (*Hedin and Mayr*, 1973; *Mayr et al.*, 1974; *Raghavarao et al.*, 1991, 1993, 1998; *Pant and Sridharan*, 2001; *Liu et al.*, 2005, 2007; *Lei et al.*, 2010), it is still unclear whether and how the neutral winds can contribute to the formation of the ETA.

Hedin and Mayr (1973) suggested that the latitudinal variations in the zonal ion-drag results in the production of the ETA, which means that less energy will flow from the dayside to the nightside of the Earth in the latitudes of high electron density, leading to the enhanced neutral temperature and density. The observations from the Dynamic Explorer 2 (DE2) satellite seem to support this mechanism (e.g., *Raghavarao et al.*, 1991, 1993, 1998), since two minima in the zonal wind and corresponding maxima in the neutral temperature have been found to be nearly co-located with the EIA crests. However, as revealed by *Lei et al.* (2010), the observations from CHAMP suggested that the formation of the ETA is not necessarily related to the zonal wind. Furthermore, as mentioned in *Fuller-Rowell et al.* (1997b) and *Lei et al.* (2010), the zonal ion-drag mechanism generates a temperature bulge in the equator, which is not consistent with the satellite observations of *Mayr et al.* (1974) and *Liu et al.* (2007).

Great efforts have also been made to explore the formation mechanism of the ETA through simulations of coupled thermosphere-ionosphere models (e.g., *Fuller-Rowell et al.*, 1997b; *Maruyama et al.*, 2003; *Miyoshi et al.*, 2011; *Lei et al.*, 2012a,b, 2014a,b; *Hsu et al.*, 2014). *Fuller-Rowell et al.* (1997b) suggested that the ETA is likely to be related to the chemical heating due to the charge transfer from O^+ to N_2 (or O_2). However, this

mechanism is unable to explain the separation of the latitude locations of the EIA and ETA crests as well as the different variations between the EIA and the ETA (e.g., *Liu et al.*, 2007; *Lei et al.*, 2010). *Miyoshi et al.* (2011) showed that the in-situ diurnal tide and the upward propagating terdiurnal tide may contribute to the formation of the ETA structure in the neutral mass density, however no ETA structure appeared in the neutral temperature in their simulations. A few recent studies pointed out that the vertical neutral wind can have a significant contribution to the formation of the ETA structure, especially the ETA trough (e.g., *Maruyama et al.*, 2003; *Lei et al.*, 2012a; *Hsu et al.*, 2014). The field-aligned ion-drag force associated with the formation of the EIA leads to a divergence in meridional winds near the magnetic equator, which further induces large upward vertical winds. Consequently, stronger adiabatic cooling takes place near the magnetic equator, resulting in the reduction in the neutral temperature and neutral density. Furthermore, *Lei et al.* (2012b) proposed that the plasma-neutral collisional heating is likely to be the main contributor to the formation of the ETA crests.

While the previous studies show that the vertical dynamics did impact the thermosphere (e.g., *Lei et al.*, 2012a; *Hsu et al.*, 2014), the calculations of the vertical dynamics in their models were based on the incompressibility assumption (i.e., $\nabla \cdot \mathbf{u} = 0$) instead of the vertical momentum equation due to the hydrostatic assumption (the pressure gradient force and gravity force are balanced in the vertical direction) carried by those models. However, the vertical ion drift near the geomagnetic equator is generally around 20 m/s during daytime (e.g., *Fejer et al.*, 1991) and can reach more than 100 m/s during the main phase of strong geomagnetic storms storms (e.g., *Lei et al.*, 2014c). The corresponding vertical ion-drag force can be significant and may not be simply neglected in the vertical momentum equation, implying that the hydrostatic assumption may not be valid anymore near the geomagnetic equator and non-hydrostatic effects may need to be taken into account. Nevertheless, it is challenging for most GCMs to simulate such effects due to the embedded

hydrostatic assumptions. Therefore, it is necessary to revisit impacts of the vertical neutral dynamics on the thermosphere at low and middle latitudes by using a non-hydrostatic GCM.

1.2.2 Small-scale and mesoscale structures in the high-latitude electrodynamical forcings

The high-latitude electrodynamics is the major focus of this dissertation, and one outstanding issue regarding the high-latitude electrodynamics is our statistical knowledge of the small-scale and mesoscale (<500 km) structures in the high-latitude electrodynamical forcings (i.e., electric fields, electron precipitations and FACs) is still insufficient, so that their impacts on the I-T system cannot be well evaluated in GCMs.

The small-scale and mesoscale structures in the high-latitude electrodynamical forcings can be treated as the variabilities that deviate from their large-scale patterns in a statistical sense. The small-scale and mesoscale variabilities in the high-latitude electric field has been extensively explored and their distributions under different geophysical conditions has been established (e.g., *Codrescu et al.*, 1995; *Matsuo and Richmond*, 2008; *Cosgrove et al.*, 2011; *Cousins and Shepherd*, 2012a,b). Moreover, the impact of small-scale and mesoscale electric field variabilities on Joule heating has also been investigated in GCMs (e.g., *Matsuo and Richmond*, 2008; *Fedrizzi et al.*, 2012), where it was found that the contribution of small-scale and mesoscale variabilities to Joule heating is not negligible.

However, in previous GCM studies, the small-scale and mesoscale electric field variabilities are considered to be independent with the electron precipitation variability on those scales, which are associated with the very intense and dynamic auroral structures (e.g., aurora arcs) that can typically found in observations (e.g., *Zhang and Paxton*, 2008). Previous observational studies suggested that the electric field might be anti-correlated with the electron precipitation on small scale and mesoscale (e.g., *Evans et al.*, 1977; *Clayton et al.*, 2019), leading to substantial reduction in Joule heating (e.g., *Evans et al.*, 1977;

Baker et al., 2004). If such correlation is ubiquitous but not taken into account, the Joule heating might be overestimated after including small-scale and mesoscale electric field variabilities. Nevertheless, since our knowledge related to the distribution of small-scale and mesoscale electron precipitation variability and the correlation between small-scale and mesoscale electric field and electron precipitation variabilities is still lacking, it is still unclear how can the correlation between the small-scale and mesoscale electric fields and electron precipitations can affect the Joule heating.

The small-scale and mesoscale FACs have been found to be much stronger than the FAC on large scale (e.g., *Lühr et al.*, 1994, 2004), and the distributions of small-scale and mesoscale FAC variabilities have been established (e.g., *Neubert and Christiansen*, 2003; *Hasunuma et al.*, 2008). Moreover, it has been found that the significant neutral density enhancements near the dayside cusp region are associated with the large-amplitude small-scale and mesoscale FACs (e.g., *Lühr et al.*, 2004; *Liu et al.*, 2005; *Rentz and Lühr*, 2008; *Liu et al.*, 2010), implying the potentially important impacts of the small-scale and mesoscale FACs on the I-T system. However, in order to better understand how the multiscale FACs would impact the I-T system, it is important to understand the difference and relationship between the FACs and ionospheric electrodynamics on different scales. One question still needs to be addressed is: do the FACs and ionospheric electric fields tend to have similar scale dependence?

1.2.3 High-latitude electrodynamical forcing specifications in GCMs

Another well-known issue in high-latitude studies is the specification of high-latitude electrodynamical forcing specifications in GCMs. Typically, the high-latitude electric field and electron precipitation in GCMs are specified by empirical models, which may have following deficiencies:

(1) Missing variabilities

Empirical models are usually good at representing the average large-scale electric field and electron precipitation for specific geophysical conditions. However, they typically do not provide the electric field and electron variabilities about the average. Therefore, there could be very large errors in GCM simulation results when only large-scale electric field and electron precipitation models are used.

For example, as discussed in Section 1.1.2 Joule heating is roughly proportional to the squared electric field $\mathbf{E}^2$. The average of $\mathbf{E}^2$ is the sum of the squared mean electric field $\overline{\mathbf{E}}^2$ and squared electric field variability σ^2. It was found that the contribution of the electric field variability to Joule heating is comparable with that of the mean electric field (*Codrescu et al.*, 1995; *Rodger et al.*, 2001; *Codrescu et al.*, 2008; *Matsuo and Richmond*, 2008; *Deng et al.*, 2009; *Fedrizzi et al.*, 2012). Although great efforts have been made to investigate more detailed characteristics of the electric field variability by utilizing a variety of observations (e.g., *Codrescu et al.*, 2000; *Golovchanskaya et al.*, 2002; *Matsuo et al.*, 2003; *Johnson and Heelis*, 2005; *Cosgrove and Thayer*, 2006; *Matsuo and Richmond*, 2008; *Cosgrove et al.*, 2011; *Cousins and Shepherd*, 2012a,b; *Hurd and Larsen*, 2016), empirical models that can provide consistent electric field variability together with large-scale mean electric field are still lacking.

(2) Underestimation of soft electron precipitations

To date, most existing auroral electron precipitation models assume the energy spectrum of incident electrons have a certain shape and a Maxwellian spectrum assumption is commonly used (e.g., *Fuller-Rowell and Evans*, 1987; *Hardy et al.*, 1987; *Zhang and Paxton*, 2008). However, it was found that a Maxwellian spectrum can significantly underestimate soft electron precipitations when comparing with the observed energy spec-

trum, sometimes by orders of magnitude (e.g., *McIntosh and Anderson*, 2014; *Wing et al.*, 2019). Despite more types of electron precipitations with energy spectra different from a Maxwellian spectrum have been included in recently developed electron precipitation models to improve soft electron precipitation specifications (e.g., *Newell et al.*, 2009, 2014; *Zhang et al.*, 2015a), the soft electron precipitation may still be underrated owing to deficient precipitation spectral identification techniques and incomplete inclusion of soft electron precipitations from different sources (*Wing et al.*, 2019). Soft electron precipitations are important ionization sources of F-region as discussed in Section 1.1.2, and the underestimation of soft electron precipitations can result in substantial underestimation of F-region Joule heating. It has been found that the neutral density and temperature at F region altitudes are more sensitive to the Joule heating deposited in the F-region than that deposited in the E region (*Deng et al.*, 2011; *Huang et al.*, 2012) especially on a short time scale ($<$1 day). However, to date, an empirical electron precipitation model that is able to provide the statistical energy spectrum of incident electrons without any assumption at different locations and under different geophysical conditions are still unavailable. Further, it is not well established to what extent the I-T system can be by soft electron precipitation globally during geomagnetic storms.

(3) Non-optimal developing methodology

Besides missing physics, the methodology used to develop an empirical model may also result in inaccurate specifications of the high-latitude electrodynamic forcing. Typically, to develop an empirical model, the data from different times and under similar conditions are binned according to their magnetic local times (MLTs) and magnetic latitudes (MLATs), i.e., in fixed geomagnetic coordinates. Hereafter, such method is referred to as the static binning method. However, it is likely that data from different source regions are combined in the same bin. For instance, the same geomagnetic location with fixed MLT

and MLAT can be either inside and outside of the auroral oval due to the dynamic nature of the auroral zone. Therefore, it is possible that particle precipitation measurements inside and outside the auroral oval are combined into the same bin when using the static binning method. Likewise, the electric field poleward or equatorward of the CRB can be mixed in the same bin. Therefore, the climatological patterns obtained through the static binning method can be smoothed and smeared (e.g., *Sotirelis and Newell*, 2000; *Chisham*, 2017).

To resolve the aforementioned issue caused by the static binning method, some studies have explored alternative binning approaches to process the ion convection and particle precipitation data (e.g., *Rich and Hairston*, 1994; *Sotirelis and Newell*, 2000; *Weimer*, 2005; *Chisham*, 2017). In those studies, the data are organized and binned according to certain boundaries instead of their MLATs and MLTs. In other words, the data are binned through a boundary-oriented binning method. For instance, *Sotirelis and Newell* (2000) binned particle precipitation data from the Defense Meteorological Satellite Program (DMSP) dataset according to a sophisticated auroral boundary system, and they asserted some improvements in comparison with static patterns, although quantitative comparisons were lacking. As for the ion convection pattern, *Heppner and Maynard* (1987) presented average convection/potential patterns, based on manual alignment of DE-2 crossings. In their maps, the gradients near the CRB are much larger than in many modern models based on the static binning method. Later, *Rich and Hairston* (1994) organized the DMSP electric potential data according to the equatorward auroral boundary and *Weimer* (2005) organized the electric potential data from the Dynamic Explorer 2 (DE-2) satellite according to a low-latitude boundary. In those two studies, the location of the boundary is given by an empirical formula, which is a function of geomagnetic activity. Again, improvements have been claimed, but it is still unclear how significant the improvements are in terms of the distribution and magnitude of the electric potential. Recently, *Chisham* (2017) binned ionospheric vorticity data deduced from Super Dual Auroral Radar Network (SuperDARN)

radars measurements according to the OCB determined from IMAGE FUV data. Furthermore, *Chisham* (2017) compared patterns organized according to the OCB with the static patterns, and found significant differences in the intensity and distribution.

While considerable efforts have been made to improve the accuracy of the specification of high-latitude electrodynamic forcing, it is uncertain to what extent high-latitude ion convection and particle precipitation patterns differ between the static and boundary-oriented binning approaches. Meanwhile, it is not well-established to what extent the Joule heating can be different if high-latitude ion convection and particle precipitation patterns obtained through different binning methods are utilized to drive a GCM.

1.3 Dissertation objectives and outline

The overarching goal of this dissertation is to address the questions discussed in Section 1.2 through a combination of data analysis, numerical simulation and model development. More specifically, there are three major objectives in this dissertation:

- Objective 1: Investigate impacts of quiet-time dayside neutral winds on the thermosphere at low and middle latitudes:
  (a) Study impacts of the neutral dynamics on the thermosphere and key ion-neutral coupling processes that affect the neutral dynamics (in both horizontal and vertical directions) at low and middle latitudes;
  (b) Explore the phenomena associated with the non-hydrostatic process at low and middle latitudes.
- Objective 2: Investigate small-scale and mesoscale structures in high-latitude electrodynamical forcings and their impacts on Joule heating:
  (a) Study small-scale and mesoscale electric fields and electron precipitations and quantify their impacts on Joule heating;

(b) Examine the relationship between the electric field and FAC on different scales and estimate impacts of multiscale FACs on Joule heating.

- Objective 3: Establish a new high-latitude empirical model and explore potential improvements in high-latitude empirical model developments:
  (a) Develop a new empirical model that can better specify high-latitude electron precipitations and electric fields;
  (b) Evaluate the impacts of soft electron precipitations on the storm-time F-region neutral density estimation in GCMs;
  (c) Explore impacts of binning method on high-latitude empirical model developments.

The remaining part of this dissertation is organized as follows: Chapter 2 provides an overview of the data and models utilized in this dissertation; Chapters 3-5 present results related to the objectives 1-3 described above, respectively; Chapter 6 summarizes the work presented herein and outlines some of the remaining questions concerning multiscale ionospheric electrodynamics.

1.4 Figures and tables

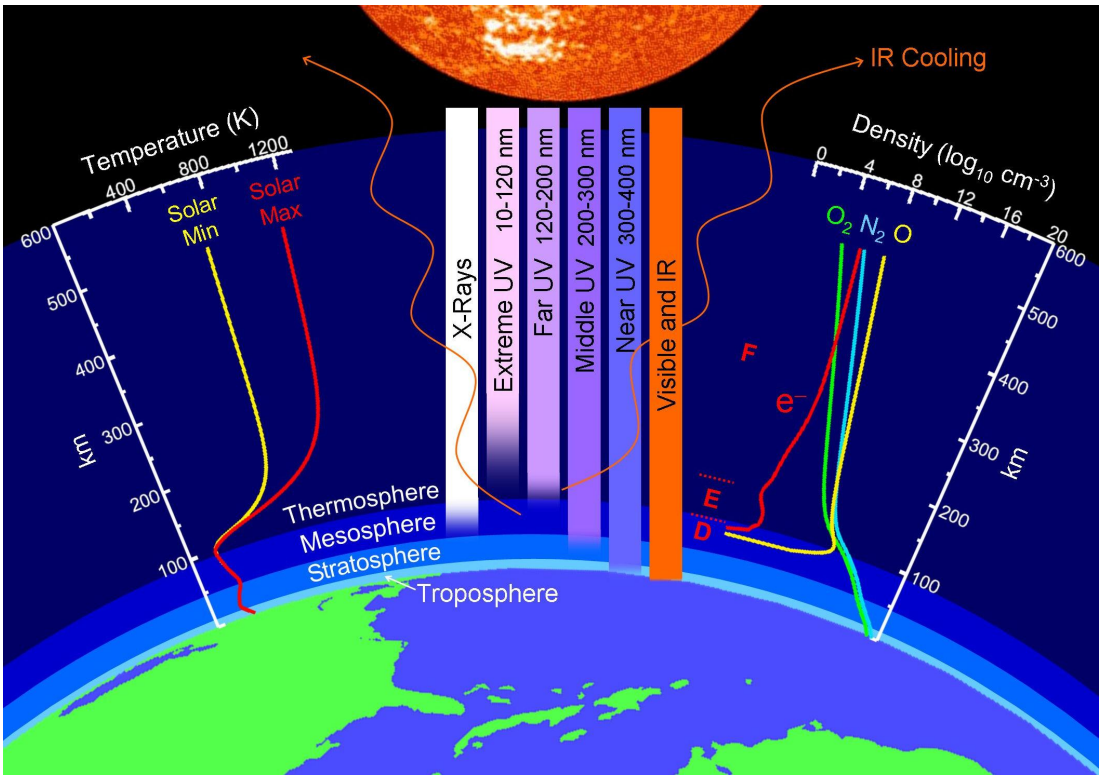

Figure 1.1: Earth's upper atmosphere (Credit: John Emmert/Naval Research Lab)

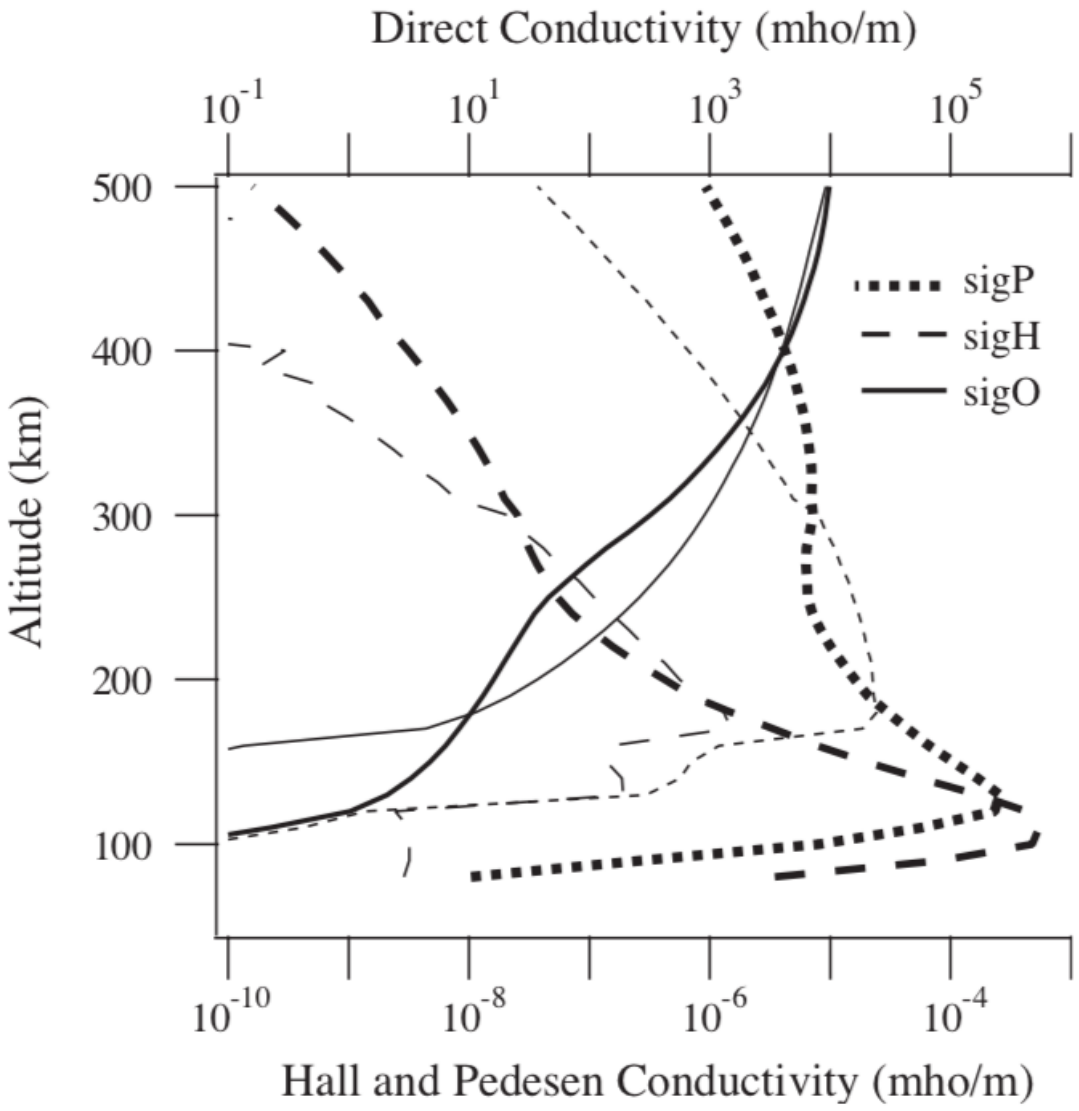

Figure 1.2: Typical mid-latitude height profiles of σ_P (solid), σ_H (long dashed) and $\sigma_\parallel$ (dotted). Heavy lines denote daytime values and light lines indicate nighttime values. Note that the scale on the top is orders larger than the scale on the bottom. Reprinted from Journal of Atmospheric and Solar-Terrestrial Physics, 66(10), R.A. Heelis, Electrodynamics in the low and middle latitude ionosphere, 825-838, 2004, with permission from Elsevier.

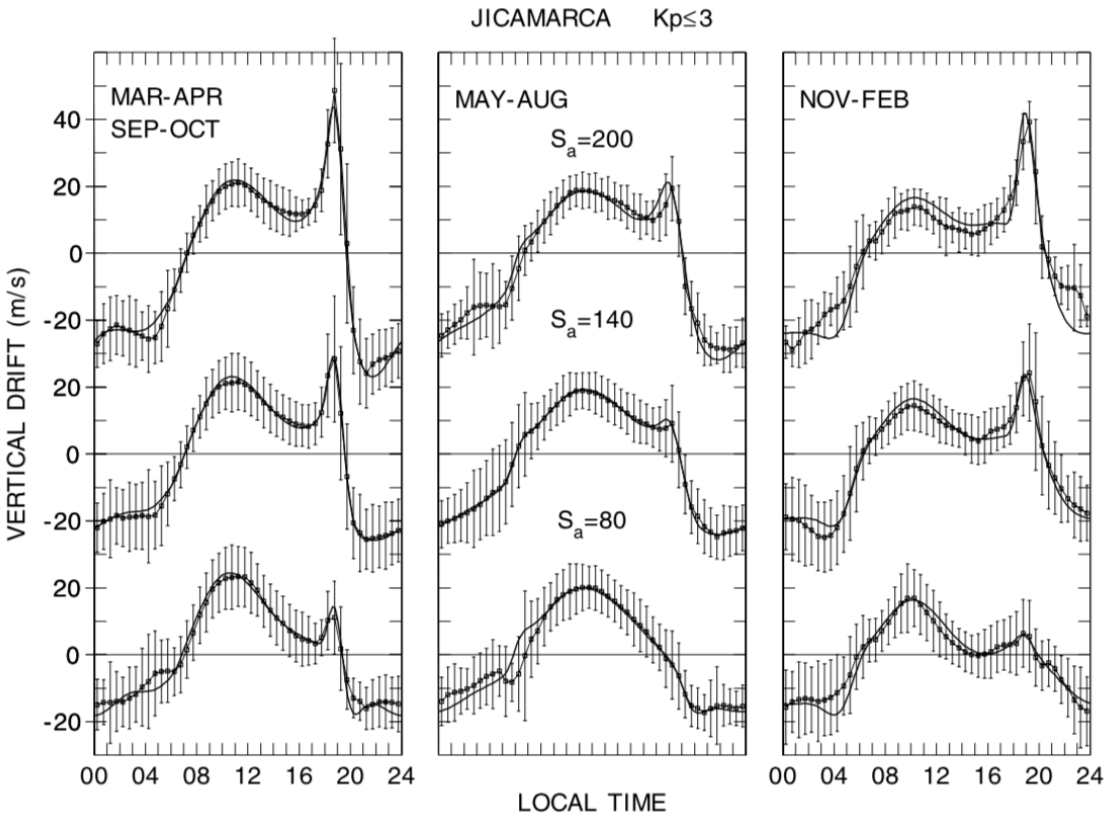

Figure 1.3: Local-time variations of quite-time F region vertical plasma drifts at Jicamarca (77° W, 12°S) for different solar fluxes and seasons. Reprinted by permission from the Springer Nature: Springer, Space Science Review, Low Latitude Ionospheric Electrodynamics, Bela G. Fejer, 2011.

.

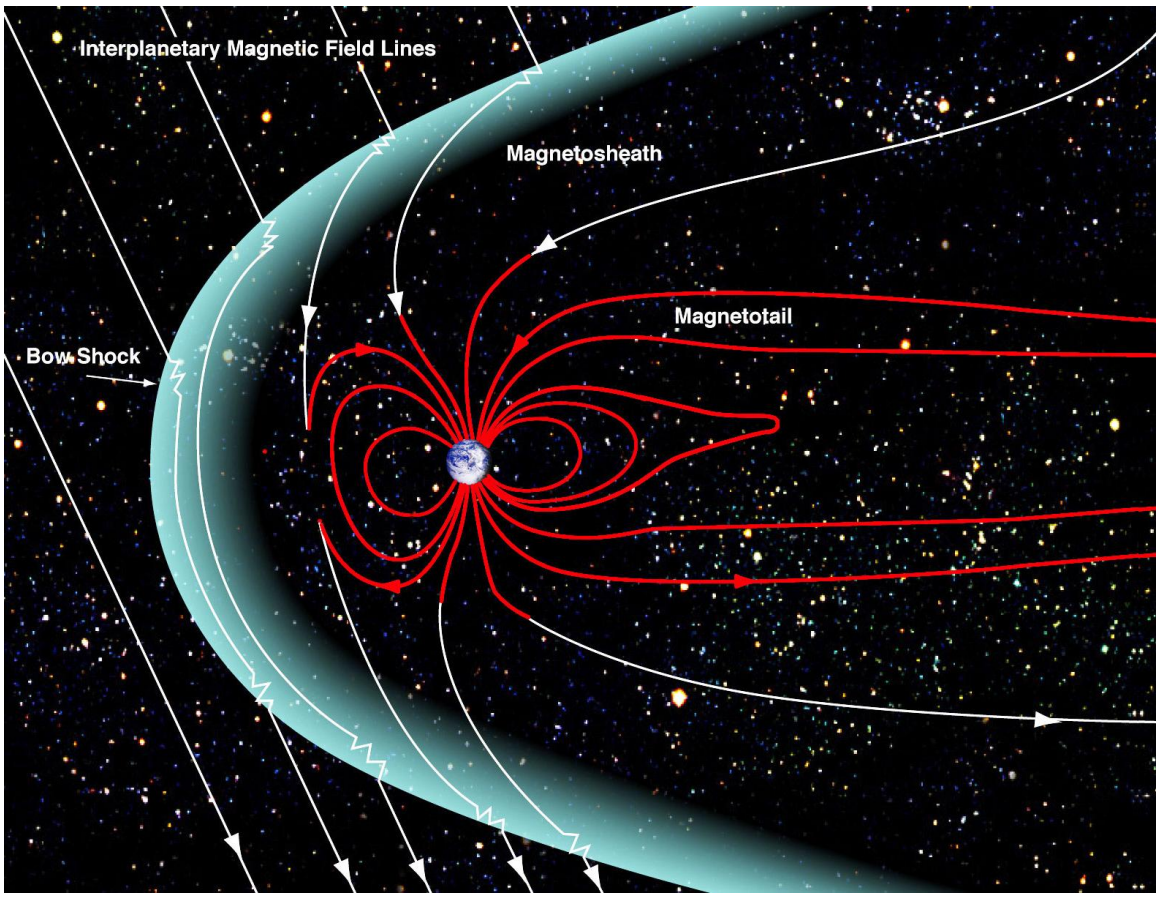

Figure 1.4: Earth's magnetosphere (Credit: NASA/Goddard/Aaron Kaase)

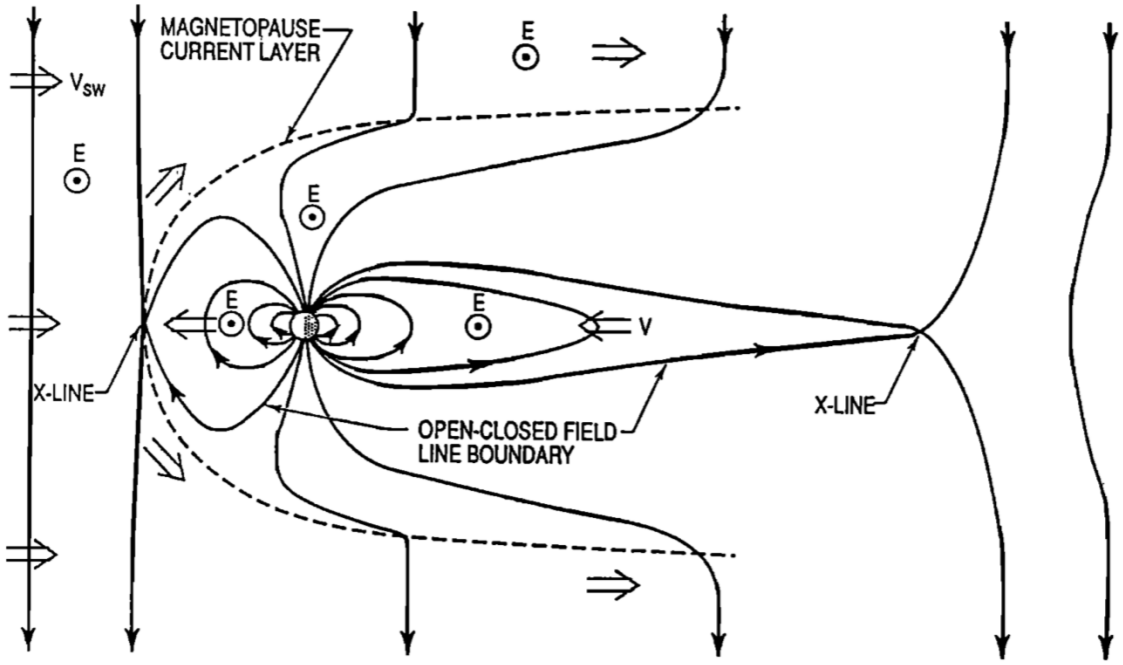

Figure 1.5: Illustration of the solar wind-magnetosphere coupling process. Reprinted from Reviews of Geophysics, 30(2), L. R. Lyons, Formation of auroral arcs via magnetosphere-ionosphere coupling, 1992, with permission from John Wiley and Sons.

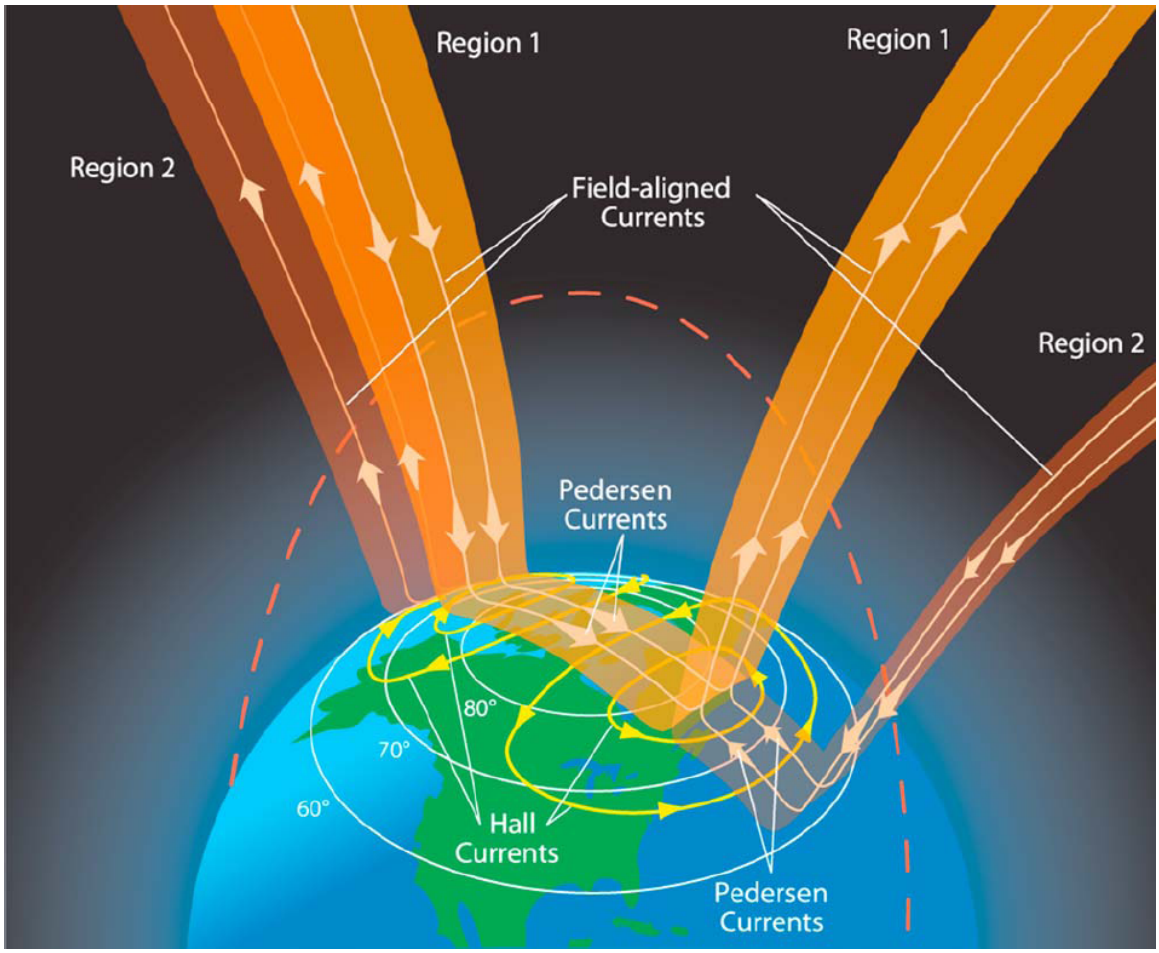

Figure 1.6: Schematic diagram shown the FACs and ionospheric currents. Reprinted from Journal of Geophysical Research: Space Physics, 115(A7), G. Le, J. A. Slavin and, R. J. Strangeway, Space Technology 5 observations of the imbalance of regions 1 and 2 field-aligned currents and its implication to the cross-polar cap Pedersen currents, 2010, with permission from John Wiley and Sons.

CHAPTER 2

Data and models

In this Chapter, first, a brief introduction of the satellites of which the measurements were used in this dissertation is provided, and details about their data process will be shown in Chapters 4 and 5. Moreover, the Global Ionosphere and Thermosphere Model (GITM, *Ridley et al.*, 2006), which is the primary simulation tool for this dissertation, is introduced in details.

2.1 Data

2.1.1 Dynamic Explorer 2 (DE-2) satellite

DE-2 (Figure 2.1(a)) was a polar-orbiting satellite at the altitudes roughly between 300 km and 1000 km with an orbital period of 98 minutes (i.e., the velocity of DE2 is $\sim$8 km/s). It was launched in September 1981 and operated till February 1983. DE-2 precessed through all local time sectors once per year, producing a dataset with relatively good local time coverage but poor separation of local time and seasonal variations. The instruments carried by DE-2 provided measurements for the in-situ ambient plasma and neutral properties, velocities of bulk ion drift and neutral wind, the ionospheric electric field, precipitating electrons and ions together with the geomagnetic field. In addition, DE-2 also measured neutral winds through the remote sensing. In this dissertation, the bulk ion drift and electron precipitation measurements from the DE-2 satellite are used.

2.1.2 Swarm satellites

The European Space Agency (ESA) Swarm mission consists of three identical satellites (Figure 2.1(b)), and all of them were launched in 2013. Two of them (Swarm A and C) fly side by side in circular orbits at an altitude of $\sim$460 km with an inclination of 87.5°. Swarm A and Swarm C are separated by 1.4° in longitude and by $<$75 km along orbit. Another satellite, Swarm B, flies at an altitude of $\sim$510 km with an orbital inclination of 88°. The Swarm satellites also precess through all local time sectors but with a shorter period than the DE-2 satellite, but the velocity of the Swarm satellite is similar to the DE-2 velocity ($\sim$7.5 km/s).The instruments carried by Swarm satellites measures the geomagnetic field, ambient plasma properties and bulk velocity, neutral mass density, neutral winds and topside total electron content (TEC). In this dissertation, we primarily focus on the field-aligned current (FAC) measurements.

2.1.3 Defense Meteorological Satellite Program (DMSP) satellites

DMSP satellites (Figure 2.1(c)) fly in circular Sun-synchronous (i.e., fixed local time) orbits at an altitude of about 840 km with an inclination of about 98.8° (i.e., polar-orbiting), and they typically have an orbital period of about 101 minutes. The important payloads onboard recent DMSP satellites include instruments to measure the in-situ precipitating electrons and ions, geomagnetic field, ambient plasma properties and bulk velocities and to remotely sense the ionosphere and thermosphere. In this dissertation, the bulk ion drift and electron precipitation measurements from DMSP satellites are used.

2.1.4 Gravity Field and Steady-State Ocean Circulation Explorer (GOCE) satellite

The ESA GOCE satellite (Figure 2.1(d)) was launched in March 2009 and operated until November 2013. It flew in a Sun-synchronous dusk-dawn orbit at altitudes between

230 and 280 km with an inclination of 96.7° and an ascending node at 18:00 local time. Although the main focus on the GOCE satellite is to map in unprecedented detail the Earth's gravity field, the thermospheric data (e.g., neutral mass density and neutral winds) can also be derived from the atmospheric drag force measured by the onboard accelerometer (*Doornbos et al.*, 2013). In this dissertation, we primarily focus on the neutral mass density measurements.

2.2 GITM

GITM is a 3-dimensional general circulation model (GCM) that simulate Earth 's ionosphere and thermosphere (I-T) system in a spherical coordinate system. GITM explicitly solves for the density, velocity and temperature of several neutral (O, O_2, N(^{2}D), N(^{2}P), N(^{4}S), N_2, NO, H and He) and ion (O^+(^{4}S), O^+(^{2}D), O^+(^{2}P), O_2^+, N^+, N_2^+, NO^+, H^+, He^+) species by solving their continuity, momentum and energy equations with complex physical and chemical processes taken into account. GITM is a fully parallelized 3D code, which is achieved by using a block-based two-dimensional domain decomposition with latitude and longitude ghost-cells bordering the blocks and the Message Passing Interface (MPI) standard. Therefore, GITM can run efficiently with high-resolution settings (e.g., 1° latitude by 5° longitude by 60 vertical levels). One outstanding difference between GITM and other GCMs for the I-T system used in the community (see Section 2.2.6), GITM uses an altitude grid instead of a pressure grid and relaxes hydrostatic assumptions. Moreover, GITM have a more complex chemistry scheme and more flexible options for the grid setting.

The GITM simulations are typically initialized using MSIS and IRI for a given date and time. In general, the system takes about one day to reach a quasi-steady state (*Ridley et al.*, 2006; *Deng and Ridley*, 2006), so that GITM simulations are typically conducted

after a 24-h pre-run. GITM can restart from the outputs of a previous run at a certain point, which allows long simulations and maximum flexibility in the usefulness of the code. GITM can run in 1D mode as well as 3D mode: when running in 1D mode, the horizontal transport is ignored and only the vertical advection is taken into account. Furthermore, GITM can run both globally and locally: When running locally, the horizontal resolution can be extremely high, making it feasible to investigate small-scale phenomena (small-scale gravity waves, e.g., *Lin et al.*, 2017).

In the following subsections, equations related to the neutral and ion species are discussed at first. Then, the chemistry scheme in GITM is briefly introduced. Next, a new electrodynamo solver that can improve the low- and mid-latitude electrodynamics and that has been recently coupled in GITM is presented. Further, specifications of high-latitude electric field and electron precipitation in GITM are demonstrated. Finally, other commonly used GCMs in the community are briefly introduced and compared with GITM.

2.2.1 Neutral Equations

One major difference between GITM and other GCMs is that GITM does not assume hydrostatic equilibrium and solves the vertical momentum equation. Therefore, the neutral equations in GITM different than most GCMs and are demonstrated in details in this subsection, which is a summary of the Section 2.1 of *Ridley et al.* (2006) with some corrections.

For individual neutral species, the continuity equation for each species is:

$$\frac{\partial \mathscr{N}_s}{\partial t} + \nabla \cdot \mathbf{u_s} + \mathbf{u_s} \cdot \nabla \mathscr{N}_s = \frac{1}{N_s} \mathscr{S}_s \tag{2.1}$$

Where, N_s is the number density of the species s, $\mathscr{N}_s = \ln(N_s)$, t is the time, $\mathbf{u_s}$ is the velocity of the species s and $\mathscr{S}_s$ is the source term of the species s which will be discussed in Eq. 2.5.

Before introducing the momentum equation, a couple of variables are defined here: 1) total mass density ρ, which can be calculated via $\rho = \sum_{\mathrm{s}} \mathrm{M_s N_s}$ and $\mathrm{M_s}$ is the mass of the species s; 2) normalized neutral temperature $\mathscr{T}$, which is the ratio between total neutral pressure and total mass density (it is assumed that all neutrals have the same temperature); 3) un-normalized temperature T, which is defined as $\mathrm{T} = \frac{\overline{\mathrm{m}}_{\mathrm{n}}}{\mathrm{k}} \mathscr{T}$. Here, $\overline{\mathrm{m}}_{\mathrm{n}}$ is the weighted average mass, k is the Boltzmann constant. With those variables, the momentum equation for each species is:

$$\frac{\partial \mathbf{u_s}}{\partial t} + \mathbf{u_s} \cdot \nabla \mathbf{u_s} + \frac{k}{M_s} \nabla T + \frac{k}{M_s} T \nabla \mathscr{N}_s = \mathscr{F}_s \tag{2.2}$$

The term $\mathscr{F}_{\mathrm{s}}$ is the forcing term which will be discussed in Eq. 2.7. As for the energy equation:

$$\frac{\partial \mathscr{T}}{\partial t} + \mathbf{u} \cdot \nabla \mathscr{T} + (\gamma - 1) \mathscr{T} \nabla \cdot \mathbf{u} = \frac{1}{c_v \rho} \mathscr{Q} \tag{2.3}$$

Where γ is the special heat and is set as a constant (5/3), $\mathbf{u}$ is the average velocity calculated via $\mathbf{u} = \frac{1}{\rho} \sum_{\mathrm{s}} \mathrm{M_s N_s} \mathbf{u_s}$ and $\mathrm{c_v}$ is the specific heat at constant volume. The term $\mathscr{Q}$ is the energy source term which will be discussed in Eq. 2.9.

In the spherical coordinate system, the vertical continuity equation becomes:

$$\frac{\partial \mathscr{N}_s}{\partial t} + \frac{\partial u_{r,s}}{\partial r} + \frac{2 u_{r,s}}{r} + u_{r,s} \frac{\partial \mathscr{N}_s}{\partial r} = \frac{1}{N_s} \mathscr{S}_s \tag{2.4}$$

Where r is the radial distance from the center of the Earth, and the subscript r denotes the radial component. The source term $\mathscr{S}_{\mathrm{s}}$ includes the eddy diffusion and chemical sources and losses:

$$\mathscr{S}_s = \frac{\partial}{\partial r} \left[N_s K_e \left(\frac{\partial N_s}{\partial r} - \frac{\partial N}{\partial r} \right) \right] + C_s \tag{2.5}$$

Where $\mathrm{K_e}$ is the eddy diffusion coefficient, N is the total number density and $\mathrm{C_s}$ represent the total of chemical sources and losses.

In a rotating spherical coordinate system, the vertical momentum equation becomes:

$$\begin{aligned}\frac{\partial u_{r,s}}{\partial t}+u_{r,s}\frac{\partial u_{r,s}}{\partial r}+\frac{u_\theta}{r}\frac{\partial u_{r,s}}{\partial \theta}+\frac{u_\phi}{r\cos\theta}\frac{\partial u_{r,s}}{\partial \phi}+\frac{k}{M_s}\frac{\partial T}{\partial r}+T\frac{k}{M_s}\frac{\partial \mathscr{N}_s}{\partial r}\\ =g+\mathscr{F}_s+\frac{u_\theta^2+u_\phi^2}{r}+2\Omega u_\phi\cos\theta\end{aligned} \tag{2.6}$$

Where θ and ϕ represent north latitude and east longitude, respectively; u_θ and u_ϕ are northward and eastward ion velocities (it is assumed that all neutral species move with same horizontal velocities), respectively; Ω is the angular velocity of the Earth, g is the gravity and $\mathscr{F}_s$ is the total of ion-neutral and neutral-neutral frictional forces. The second to the last right-hand-side (RHS) term is due to the spherical geometry, and the last RHS term is associated with the Coriolis force. The term $\mathscr{F}_s$ can be expressed as:

$$\mathscr{F}_s=\frac{\rho_i}{\rho_s}\nu_{in}(v_r-u_{r,s})+\frac{kT}{M_s}\sum_{q\neq s}\frac{N_q}{ND_{qs}}(u_{q,s}-u_{r,s}) \tag{2.7}$$

where v_r is the vertical ion bulk velocity, ρ_i is the ion mass density, ν_{in} is the ion-neutral collision frequency, $u_{r,q}$ indicates the vertical velocity of the species q ($q \neq s$), N_q is the number density of species q and D_{qs} is the diffusion coefficient between the s and q species. In general, the second term of Eq. 2.7 is relatively trivial when comparing with the first term.

The vertical energy equation In the spherical coordinate system becomes

$$\frac{\partial \mathscr{T}}{\partial t}+u_r\frac{\partial \mathscr{T}}{\partial r}+(\gamma-1)\mathscr{T}\left(\frac{\partial u_r}{\partial r}+\frac{2u_r}{r}\right)=\frac{k}{c_v\rho\overline{m}_n}\mathscr{Q} \tag{2.8}$$

Where

$$\begin{aligned}\mathscr{Q}=&Q_{EUV}+Q_{NO}+Q_O+\frac{\partial}{\partial r}\left((\kappa_c+\kappa_{eddy})\frac{\partial T}{\partial r}\right)\\ &+N_e\frac{\overline{m}_i\overline{m}_n}{\overline{m}_i+\overline{m}_n}\nu_{in}(\mathbf{v}-\mathbf{u})^2\end{aligned} \tag{2.9}$$

where κ_c is the heat conductance, κ_{eddy} is the heat conductivity related to the eddy diffusion; Q_{EUV} is the heating due to the solar EUV radiation, Q_{NO} and Q_O are cooling terms,

N_e is the electron number density, $\overline{m}_i$ is the average mass of the ions, $\mathbf{v}$ is the ion bulk velocity. The last term represents the Joule (frictional) heating caused by ion and neutral velocity differences (See Section 1.1.3).

In the horizontal direction, the neutral continuity equation is:

$$\begin{aligned}\frac{\partial N_s}{\partial t}+N_s\left(\frac{1}{r}\frac{\partial u_\theta}{\partial \theta}+\frac{1}{r\cos\theta}\frac{\partial u_\phi}{\partial \phi}-\frac{u_\theta\tan\theta}{r}\right)\\ +\frac{u_\theta}{r}\frac{N_s}{\partial\theta}+\frac{u_\phi}{r\cos\theta}\frac{\partial N_s}{\partial\phi}=0\end{aligned} \tag{2.10}$$

The momentum equation in the eastward direction is:

$$\begin{aligned}\frac{\partial u_\phi}{\partial t}+u_r\frac{\partial u_\phi}{\partial r}+\frac{u_\theta}{r}\frac{\partial u_\phi}{\partial\theta}+\frac{u_\phi}{r\cos\theta}\frac{\partial u_\phi}{\partial\phi}+\frac{1}{r\cos\theta}\frac{\partial\mathscr{T}}{\partial\phi}+\frac{\mathscr{T}}{r\rho\cos\theta}\frac{\partial\rho}{\partial\phi}\\ =\frac{\mathscr{F}_\phi}{\rho}+\frac{u_\phi u_\theta\tan\theta}{r}-\frac{u_r u_\phi}{r}+2\Omega(u_\theta\sin\theta-u_r\cos\theta)\end{aligned} \tag{2.11}$$

And the momentum equation in the northward direction is:

$$\begin{aligned}\frac{\partial u_\theta}{\partial t}+u_r\frac{\partial u_\theta}{\partial r}+\frac{u_\theta}{r}\frac{\partial u_\theta}{\partial\theta}+\frac{u_\phi}{r\cos\theta}\frac{\partial u_\theta}{\partial\phi}+\frac{1}{r}\frac{\partial\mathscr{T}}{\partial\theta}+\frac{\mathscr{T}}{r\rho}\frac{\partial\rho}{\partial\theta}\\ =\frac{\mathscr{F}_\theta}{\rho}-\frac{u_\phi^2\tan\theta}{r}-\frac{u_r u_\theta}{r}-2\Omega u_\phi\sin\theta\end{aligned} \tag{2.12}$$

The source terms $\mathscr{F}_\phi$ and $\mathscr{F}_\theta$ can be expressed as:

$$\begin{aligned}\mathscr{F}_\theta &= \rho_i\nu_{in}(v_\theta-u_\theta)+\frac{\partial}{\partial r}\left(\eta\frac{\partial u_\theta}{\partial r}\right)\\ \mathscr{F}_\phi &= \rho_i\nu_{in}(v_\phi-u_\phi)+\frac{\partial}{\partial r}\left(\eta\frac{\partial u_\phi}{\partial r}\right)\end{aligned} \tag{2.13}$$

Where η is the viscosity coefficient, and the second term in each equation represents the radial shear of the horizontal wind.

Finally, the horizontal energy equation is

$$\begin{aligned}\frac{\partial\mathscr{T}}{\partial t}+(\gamma-1)\mathscr{T}\left(\frac{1}{r}\frac{\partial u_\theta}{\partial\theta}+\frac{1}{r\cos\theta}\frac{\partial u_\phi}{\partial\phi}-\frac{u_\theta\tan\theta}{r}\right)\\ +\frac{u_\theta}{r}\frac{\mathscr{T}}{\partial\theta}+\frac{u_\phi}{r\cos\theta}\frac{\partial\mathscr{T}}{\partial\phi}=0\end{aligned} \tag{2.14}$$

2.2.2 Ion Equations

In this subsection, the equations related to the ions are presented, which is a summary of the Sections 2.2 and 2.3 of *Ridley et al.* (2006) with some corrections and more discussions.

The ion momentum equation is:

$$\begin{aligned}\rho_i \frac{d\mathbf{v}}{dt} =& -\nabla(P_i + P_e) + \rho_i \mathbf{g} \\ &+ eN_e(\mathbf{E} + \mathbf{v} \times \mathbf{B_0}) - \rho_i \nu_{in}(\mathbf{v} - \mathbf{u})\end{aligned} \tag{2.15}$$

Here, ρ_{i} is the ion mass density, $\mathbf{v}$ is the ion bulk velocity, $\mathrm{P_i}$ and $\mathrm{P_e}$ are the ion and electron pressures, $\mathbf{g}$ is the gravitation accleration, e is the electron charge, $\mathrm{N_e}$ is the electron number density (is assumed to be equal to the total ion number density), $\mathbf{E}$ is the ionospheric electric field, $\mathbf{B_0}$ is the geomagnetic main field, ν_{in} is the ion-neutral collision frequency and $\mathbf{u}$ is the neutral bulk velocity (i.e., neutral wind speed). The Eq. 2.15 can be simplified by assuming its LHS term is negligible to other terms, i.e.,

$$\mathbf{v} = \frac{\mathbf{A}}{\rho_i \nu_{in}} + \frac{eN_e}{\rho_i \nu_{in}}(\mathbf{v} \times \mathbf{B_0}) \tag{2.16}$$

Where

$$\mathbf{A} = \rho_i \mathbf{g} + eN_e \mathbf{E} - \nabla(P_i + P_e) + \rho_i \nu_{in} \mathbf{u} \tag{2.17}$$

So that

$$\mathbf{v} = \frac{\mathbf{A} \cdot \mathbf{b}}{\rho_i \nu_{in}} + \frac{\rho_i \nu_{in} \mathbf{A}_\perp + eN_e \mathbf{A}_\perp \times \mathbf{B_0}}{\rho_i^2 \nu_{in}^2 + e^2 N_e^2 B_0^2} \tag{2.18}$$

where $\mathrm{B}_0 = |\mathbf{B_0}|$ is the magnitude of the geomagnetic main field, $\mathbf{b} = \mathbf{B_0}/\mathrm{B}_0$ is the unit vector of $\mathbf{B_0}$, and $\mathbf{A}_\perp$ is the component of $\mathbf{A}$ that is perpendicular to $\mathbf{B_0}$.

With the ion bulk velocity $\mathbf{v}$, the changes in the ion number density for species *j* can be calculated from the ion continuity equation,

$$\frac{\partial N_j}{\partial t} + \nabla \cdot (N_j \mathbf{v}) = \mathscr{S}_j \tag{2.19}$$

which is separated into horizontal

$$\frac{\partial N_j}{\partial t}+N_j\left(\frac{1}{r}\frac{\partial v_\theta}{\partial \theta}+\frac{1}{r\cos\theta}\frac{\partial v_\phi}{\partial \phi}-\frac{v_\theta \tan\theta}{r}\right) + \frac{v_\theta}{r}\frac{N_j}{\partial \theta}+\frac{v_\phi}{r\cos\theta}\frac{\partial N_j}{\partial \phi}=\mathscr{S}_j \tag{2.20}$$

and vertical

$$\frac{\partial \mathscr{N}_j}{\partial t}+\frac{\partial v_r}{\partial r}+2\frac{v_r}{r}+v_r\frac{\partial \mathscr{N}_j}{\partial r}=0 \tag{2.21}$$

directions in GITM. Here, r, θ and ϕ represent altitude, north latitude and east longitude, respectively; v_r, v_θ and v_ϕ are upward, northward and eastward ion velocities, respectively; N_j is the number density of the jth ion species, $\mathscr{N}_j = \ln(N_j)$ and $\mathscr{S}_j$ is the total of the sources and losses of the ions due to the chemistry. In GITM, only O^+ is advected since O^+ is the dominant ion in the low collision region of the ionosphere (*Schunk and Nagy*, 2000).

Similar to that described in *Wang et al.* (1999), the ion temperature is calculated by assuming that the energy gained by ions from the Joule heating and electron-ion interaction is balanced by the energy lost to neutrals through ion-neutral collisions. To calculate the ion neutral temperature, besides the neutral temperature and Joule heating that can be calculated through equations listed in Section 2.2.1, the electron temperature is also needed. The electron temperature T_e can be calculated through:

$$\frac{\partial T_e}{\partial t}=-\frac{2}{3}T_e\nabla\cdot\mathbf{v}_e-\mathbf{v}_e\cdot\nabla T_e+\frac{2}{3N_e k}(-\nabla\cdot\mathbf{q}_e+Q_e-L_e) \tag{2.22}$$

Where $\mathbf{v}_e$ is the $\mathbf{E}\times\mathbf{B}$ velocity, Q_e and L_e are the heating and cooling rates, respectively, and $\mathbf{q}_e$ is the heating flux. Details discussion of Q_e, L_e and $\mathbf{q}_e$ can be found in *Ridley et al.* (2006).

2.2.3 Chemistry scheme

The source terms in the neutral and ion continuity equations are calculated within GITM's chemistry scheme, which contains reactions between the ions and neutrals, ions

and electrons, and neutrals and neutrals. Essentially, GITM does not assume the local chemical equilibrium and investigate the chemical dynamics closely. The chemistry equations in *Rees* (1989) are all included in GITM and *Lin et al.* (2018) has recently updated the original GITM's chemistry scheme in order to improve the NO chemistry in GITM. Details can be referred to those papers and references therein. In this subsection, a brief introduction of chemical processes related to the ion production in GITM is presented.

The primary dayside ionization source is the solar EUV ionization, GITM includes solar irradiance models developed by *Hinteregger et al.* (1981) and *Tobiska* (1991), which are based on the daily averaged $F_{10.7}$ and the 81-day averaged $F_{10.7}$. The models have been modified to output the solar flux in 55 wavelengths that are then used in combination with the ionization cross section specified by *Torr et al.* (1979) to calculate the ionization rates.

Another import ionization source is the precipitating auroral electrons, especially on the night side. The ionization production rates due to the electron precipitation are derived from the formulation described by *Frahm et al.* (1997) and the partitioning of ionization rates among O^+, O_2^+ and N_2^+ described in *Rees* (1989).

2.2.4 New electrodynamo solver

The original electrodynamo solver in GITM generating the low- and mid-latitude electric fields is developed by *Vichare et al.* (2012), which cannot well reproduce the local time variations of the equatorial vertical ion drift as shown in measurements (e.g., *Scherliess and Fejer*, 1999), especially at solstices. Therefore, in order to further improve the low- and mid-latitude electrodynamics in GITM, a recently developed electrodynamo model, the National Center for Atmospheric Research (NCAR) 3D ionospheric electrodynamo model (*Maute and Richmond*, 2017), has been coupled into GITM. The new electrodynamo model is based on the electrodynamo solver in the NCAR-TIEGCM (*Richmond et al.*, 1992; *Richmond*, 1995), which was able to better reproduce the measured local time

variations of the equatorial vertical ion drift under different conditions (e.g., *Fesen et al.*, 2000).

The NCAR 3D ionospheric electrodynamo model solves for the global ionospheric electric fields, and can determine the global 3-dimensional ionospheric currents system and magnetic perturbations associated with the neutral wind dynamo, with gravity, pressure gradient forces and with FACs flowing between the two hemispheres or between ionosphere and magnetosphere in modified apex coordinates (*Richmond*, 1995) between 80 km and 1000 km. It uses fixed-height grids which are distributed on magnetic field lines specified by the International Geomagnetic Reference Field-12 (IGRF-12) model (*Thébault et al.*, 2015). The grids are evenly distributed in longitude while the vertical and latitudinal grid spacings are uneven: the vertical grid spacing increases with the altitude and the latitudinal spacing increases from the equator to midlatitudes and then decreases from midlatitudes to high latitudes, so that the strong height and latitudinal variations at low-latitude ionosphere can be resolved.

The NCAR 3D ionospheric electrodynamo model aims to solve the current continuity equation (Eq. 1.6). If the electric fields associated with the gravity and pressure gradient force are ignored, Eq. 1.6 becomes

$$\frac{1}{R^2\cos\lambda_m}\left[\frac{\partial}{\partial\phi_m}\left(\frac{\Sigma^T_{\phi\phi}}{\cos\lambda_m}\frac{\partial\Phi}{\partial\phi_m}+\Sigma^T_{\phi\lambda}\frac{\partial\Phi}{\partial|\lambda_m|}\right)+\frac{\partial}{\partial\lambda_m}\left(\Sigma^T_{\lambda\phi}\frac{\partial\Phi}{\partial\phi_m}+\Sigma^T_{\lambda\lambda}\cos\lambda_m\frac{\partial\Phi}{\partial|\lambda_m|}\right)\right] = \frac{1}{R\cos\lambda_m}\left[\frac{\partial K^{DT}_{m\phi}}{\partial\phi_m}+\frac{\partial(K^{DT}_{m\lambda}\cos\lambda_m)}{\partial|\lambda_m|}\right]+J_{Mr} \tag{2.23}$$

Here, ϕ_m, λ_m are the magnetic longitude and latitude in modified apex coordinates, respectively. R is the radius of the ionosphere base, and Φ is the electrostatic potential ($\mathbf{E}=-\nabla\Phi$). The Σ^T_{ij} (i, j $= \phi,\ \lambda$) terms are essentially related to the field-line integrated conductivities. The K^T_{ij} (i, j $= \phi,\ \lambda$) terms are associated with the field-line integrated neu-

tral wind dynamo. The superscript T denotes the sum of a quantity at conjugate locations in the two hemispheres. J_{Mr} represents the magnetospheric source of current, which is the sum of the upward radial currents (J_{mr}) at magnetic conjugate locations in northern and southern hemispheres. J_{Mr} is typically assumed to be zero at low and middle latitudes, while it can be specified by the FAC at high latitudes (*Marsal et al.*, 2012). More details about Eq. 2.23 can be found in *Richmond* (1995) and *Laundal and Richmond* (2017).

When coupling into GITM, the NCAR ionospheric electrodynamo model is typically initialized at the root processor and reads neutral winds, ionospheric conductivities and high-latitude electric potential from all processors. The global electric fields calculated in the NCAR ionospheric electrodynamo model are then broadcasted to all processors. Figure 2.2(c) summarizes the coupling scheme.

2.2.5 High-latitude electric field and electron precipitation

The high-latitude electric field and electron precipitation in GITM can be specified through different ways. For example, the electric field and electron precipitation in GITM are typically specified by *Weimer* (2005) and *Fuller-Rowell and Evans* (1987) empirical models, respectively. However, other models can also be easily coupled into GITM. For event studies, the electric field and electron precipitation patterns derived from the Assimilative Mapping of Ionospheric electrodynamics (AMIE) technique (*Richmond and Kamide*, 1988; *Richmond*, 1992) can be used. GITM is also part of the Space Weather Modeling Framework (SWMF, *Tóth et al.*, 2005), so that the high-latitude electric field and electron precipitation can also be specified by outputs of a global magnetohydrodynamic (MHD) model.

2.2.6 Comparisons with other GCMs

GCMs are widely used in studying the I-T system in the upper atmospheric research. In addition to GITM, there are several other well-developed GCMs, such as the NCAR thermosphere-ionosphere-electrodynamics general circulation model (TIEGCM, *Richmond et al.*, 1992; *Qian et al.*, 2014), NCAR thermosphere-ionosphere-mesosphere-electrodynamics general circulation model (TIMEGCM, *Roble and Ridley*, 1994), NCAR Whole Atmosphere Community Climate Model with thermosphere and ionosphere extension (WACCM-X) model (*Liu et al.*, 2018) and the coupled thermosphere-ionosphere-plasmasphere electrodynamics (CTIPe) model (*Millward et al.*, 2001). Each one has its own advantages as well as disadvantages and may be most suitable for specific scientific purposes. For example, all these models use pressure grids and make hydrostatic assumptions, but computationally they are less expensive and can be faster than GITM. In addition, TIMEGCM and WACCM-X account in atmosphere from 30 km and the sea level, respectively, so they have more self-consistent coupling between lower and upper atmospheres. Moreover, CTIPe includes the plasmasphere, so that the mass flow between hemispheres and the upper boundary condition of the ion flow maybe better specified than other GCMs.

2.3 Figures and tables

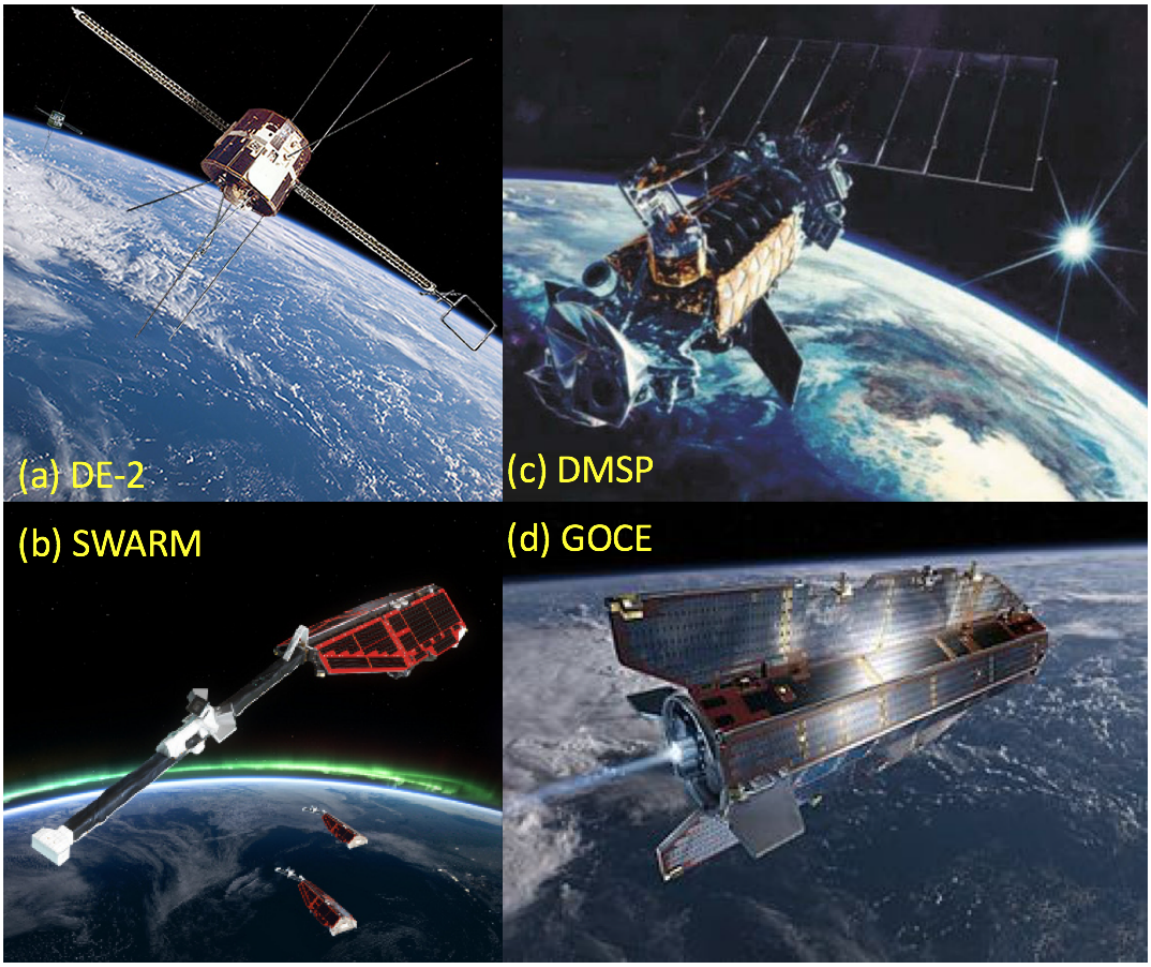

Figure 2.1: Artist's renditions of the (a) DE-2 (b) SWARM (c) DMSP (d) GOCE satellites orbiting the Earth (Credit: Wikipedia).

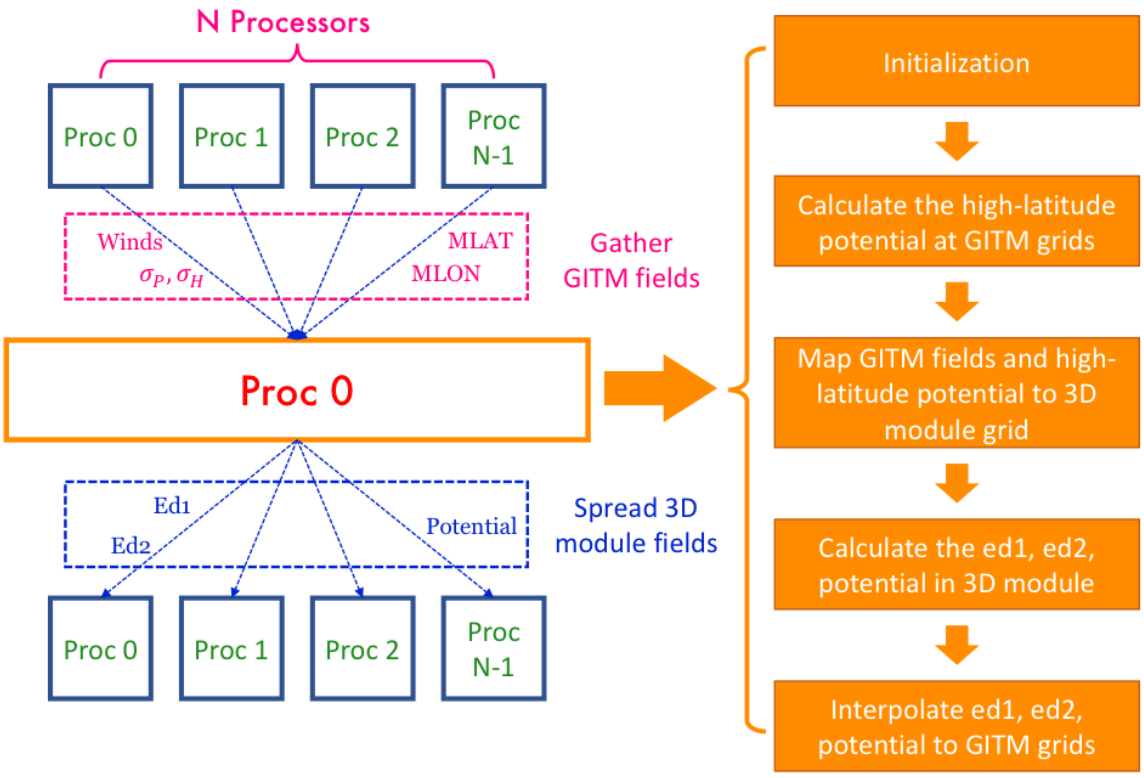

Figure 2.2: Coupling between the GITM and NCAR 3D ionospheric electrodynamo model.

CHAPTER 3

Impacts of the vertical neutral dynamics on the thermosphere at low and middle latitudes

As discussed in Section 1.2.1, although previous modeling studies have pointed out the significance of the vertical dynamics in the formation of the equatorial thermosphere anomaly (ETA), the vertical dynamics in their models are not directly calculated from the vertical momentum equation (Eq. 2.6) due to the imbedded hydrostatic assumption. Hence, the impacts of the vertical dynamics on the ETA formation may not well captured in their models. This chapter aims to advancing the understanding on the role of the vertical dynamics plays in the formation of ETA using the GITM, in which the vertical momentum equation is directly solved. In addition to the ETA formation, other non-hydrostatic phenomena are also investigated in this chapter. In the remaining part of this chapter, a brief overview of the simulations carried out in this chapter is provided at first. Results are then presented along with discussion. Lastly, the primary findings in this chapter are summarized.

3.1 Simulation setups

Two GITM simulations have been carried out and compared. The first simulation represents the background case where only the electric fields associated with high latitude ionospheric convection pattern are imposed into GITM, and no electric field from the elec-

trodynamo model is included (hereafter, Run 1). The second simulation represents the case in which the low and mid-latitude electric fields from the electrodynamo model are included (hereafter, Run 2). Both GITM simulations were conducted under high solar activity ($F_{10.7}$=200 sfu) and quiet geomagnetic condition (Bz=-1 nT, HP=1 GW). The spatial resolution is 2.5° by 5° by 1/3 scale height in latitude, longitude and altitude. The temporal resolution is 2 seconds. Meanwhile, the time interval is from 1200 UT to 1300 UT on 09/22/2002, and a 24-hour pre-run has been conducted prior to the period of interest. For Run 2, the low and mid-latitude electric fields were turned on at 1200 UT on 09/22/2002.

3.2 Results and Discussion

3.2.1 Formation of the EIA and ETA in GITM

Figures 3.1(a) and 3.1(b) show the altitude-latitude distributions of the electron and neutral mass densities in Run 2 at the longitude of 17.5°E and at 1300 UT, 09/22/2002 (LT=14:10). The geomagnetic equator is located at 10°N at this longitude. Apparently, the EIA and ETA features appeared after introducing the electric field at low and middle latitudes in GITM. The latitudinal variations of the electron and neutral mass densities at the altitude of 400 km along this longitude are displayed in Figure 3.1(c), as indicated by the black and blue lines, respectively (solid lines represent results from Run 2 and dashed lines represent results from Run 1). The crests of the electron density in Run 2 were located at around 6°S and 24°N, which were 16° and 14° away from the geomagnetic equator, respectively. The ETA crests in Run 2 were roughly located at 16°S and 29°N, which were 26° and 19° a way from the geomagnetic equator, respectively. Clearly, the ETA crests were more poleward than the EIA crests, which is consistent with the previous CHAMP observations (e.g., *Liu et al.*, 2005, 2007; *Lei et al.*, 2010). Moreover, the average of the crest-to-trough ratio for the neutral mass density was $\sim$1.09 at this longitude, which is com-

parable to the climatological result ($\sim$1.05 around equinoxes) from CHAMP observations (e.g., *Liu et al.*, 2007).The blue dashed line in Figure 1c represents the neutral mass density in Run 1. Obviously, as compared with Run 1, the neutral mass density in Run 2 showed a clear reduction near the geomagnetic equator, which reached $\sim 1 \times 10^{-12}$ kg/m3 at longitude of 17.5°E. However, the neutral mass density in Run 2 did not show distinct changes near the ETA crests.

In order to address the main contributors to the density variations near the geomagnetic equator, the term analysis has been applied to the continuity equation of the neutral mass density. The continuity equation can be expressed as:

$$\frac{\partial \rho}{\partial t} = -\mathbf{u} \cdot \nabla \rho - \rho(\nabla \cdot \mathbf{u}) + \mathscr{S} \tag{3.1}$$

Here, ρ is the neutral mass density, $\mathbf{u}$ is the neutral wind vector and $\mathscr{S}$ stands for the chemical source term. The $-\mathbf{u} \cdot \nabla \rho$ represents the dynamic term and the $-\rho(\nabla \cdot \mathbf{u})$ is the divergence term. The dynamic term is related to the wind velocities and the gradients of the neutral mass density in zonal, meridional and vertical directions. Similarly, the divergence term is determined by the neutral mass density and the divergence of neutral wind, which is the sum of the zonal wind gradient in the zonal direction, the meridional wind gradient in the meridional direction and the vertical wind gradient in the vertical direction. Hence, each term was splitted into three terms with one for each direction in our analysis.

Figure 3.2 shows the temporal variations of those 6 terms in Run 2 near the geomagnetic equator (17.5°E, 12°N and 400 km) from 12 to 13 UT (1310-1410 LT) on 09/22/2002. Apparently, the vertical dynamic term (green dashed line) and the meridional divergence term (red solid line) significantly contributed to the neutral mass density variations near the magnetic equator in Run 2 throughout the simulation. Specifically, the daytime upward vertical wind tends to increase the local neutral mass density through the vertical dynamic

term due to the large vertical gradient of the neutral mass density. In contrast, the divergence in the meridional wind tends to transport the neutral mass density away from the geomagnetic equator. Although the vertical divergence term (blue solid line) also showed important contribution and mostly results in the reduction of the neutral mass density in the first 10 minutes, it became trivial after the first 15 minutes. Therefore, the divergence of the meridional wind was the most important contributor to the reduction of the neutral mass density near the geomagnetic equator and might contribute to the formation of the ETA trough. This is the first time that the impact of the vertical dynamics on the neutral mass density of the thermosphere at low and middle latitude is shown, where the vertical dynamics is calculated from the vertical momentum equation.

A possible cause for the divergence of the meridional wind near the geomagnetic equator is the field-aligned ion-drag force (close to the meridional direction near the geomagnetic equator) as mentioned in previous studies (e.g., *Maruyama et al.*, 2003; *Lei et al.*, 2012a; *Hsu et al.*, 2014). GITM includes the field-aligned ion-drag force, and its meridional component has a large contribution to the total meridional ion-drag in GITM near the geomagnetic equator. Figure 3.3 exhibits the differences between Run 2 and Run 1 in the meridional ion-drag force and in the meridional wind along the longitude of 17.5°E. As shown in Figures 3.3(a)-3.3(d), the meridional ion-drag force was more poleward with respect to the geomagnetic equator in Run 2 as compared with Run 1, and the change of the meridional ion-drag force was more confined to the EIA region after 1230 UT, 09/22/2002. The poleward meridional ion-drag force led to the divergence in the meridional wind as shown in Figures 3.3(e)-3.3(h), which is consistent with the findings of previous studies (e.g., *Maruyama et al.*, 2003; *Lei et al.*, 2012a; *Hsu et al.*, 2014).

The dominant forces in the meridional direction include both the ion-drag and pressure gradient forces. Therefore, the evolution of the meridional pressure gradient force along the longitude of 17.5°E has been examined as well. Figure 3.4 depicts the differ-

ence of the meridional pressure gradient force between Run 2 and Run 1. The change of the meridional pressure gradient force was indistinct during the first 10 minutes when the ETA has not yet developed. The change became clearer near the geomagnetic equator when the ETA started to form and was opposite to the change of the meridional ion-drag force. The difference in the meridional pressure gradient force became larger as the ETA trough became more profound. It can slightly exceed the meridional ion drag force after approximately 1230 UT, 09/22/2002, resulting in the deceleration of the meridional wind difference shown in Figure 3.4(h). Consequently, the divergence of the meridional wind near the magnetic equator decreased as shown in Figure 3.2 .

3.2.2 Evolutions of the vertical forces

In this section, the changes in the vertical forces after including the electric fields have been examined. Since the vertical ion-drag and pressure gradient forces are the dominant forces and change most significantly with the vertical dynamics as compared with other forces in Eq. 2.6, therefore, the changes of vertical ion-drag and pressure gradient forces are primarily investigated in this subsection.

Figure 3.5 shows the changes of the vertical ion-drag and pressure gradient forces at four different times at the longitude of 17.5°E. As shown in Figure 3.5(a), the upward ion drift associated with the electric fields at low and middle latitudes resulted in the upward enhancement of the ion-drag force on the neutrals at 1205 UT, 09/22/2002. Figures 3.5(b) shows a more remarkable enhancement in the upward vertical ion-drag force near the geomagnetic equator as compared with 5 minutes earlier, and the maximum change of the upward ion-drag force was greater than 0.1 m/s^2. Later on, the changes of the vertical ion-drag force became more confined to the geomagnetic equator with a reduced magnitude as compared with that at 1210 UT, 09/22/2002. The vertical pressure gradient force exhibited a reduction at 1205 UT, 09/22/2002 as shown in Figure 3.5(e). The difference can

reach 0.2 m/s^2 at the altitude $\sim$300 km, suggesting that the change in the vertical pressure gradient force was roughly 2% of the local gravity force. The change in the vertical pressure gradient force reflected the non-hydrostatic effect, since the pressure gradient force is exactly equal to the local gravity force everywhere and all the time under the hydrostatic assumption. Interestingly, as compared with Run 1, the upward pressure gradient force showed an enhancement at 400-500 km altitude and at 1210 UT, 09/22/2002, whereas the upward pressure gradient force underwent reductions at other altitudinal ranges in Run 2. It might reflect wave features and will be addressed in the next paragraph. Figures 3.5(g) and 3.5(h) show that there was a persistent reduction of the upward pressure gradient force near the magnetic equator. The magnitudes of the reductions in the upward vertical pressure gradient force (Figures 3.5(g) and 3.5(h)) were almost the same as the enhancements of the upward ion-drag forces (3.5(c) and 3.5(d)), suggesting that the forces in the vertical direction roughly reached quasi-equilibrium after 1230 UT, 09/22/2002. Overall, the vertical ion-drag force due to the vertical ion drift can change the vertical dynamics and the changing dynamics can feedback to the vertical ion-drag and pressure gradient forces acting on the thermosphere as shown in Figure 3.5.

Since the predominant changes of the vertical ion-drag and pressure gradient forces occurred near the geomagnetic equator, the temporal variations of the vertical ion-drag and pressure gradient forces near the geomagnetic equator are studied during the period we have focused on, and the results are shown in Figure 3.6. The top panel of Figure 3.6 shows the temporal variations of the vertical ion-drag and pressure gradient forces in Run 1. The vertical ion-drag force (Figure 3.6(a)) was close to zero since the electric fields at low and middle latitudes are excluded. Meanwhile, the vertical pressure gradient force (Figure 3.6(b)) was upward and almost constant at the altitude of 400 km. The middle panel of Figure 3.6 shows the temporal variations of the vertical ion-drag and pressure gradient

forces in Run 2. Clearly, Figure 3.6(c) shows that the vertical ion-drag force was upward due to the upward ion drift after including the low and mid-latitude electric fields. The maximum vertical ion-drag force was ~ 0.1 m/s^2 at 400 km around 8 minutes after adding in the electric field. As shown in Figure 3.6(d), the vertical pressure gradient force exhibited a perturbation at 400 km around 8 minutes after including the electric field and became almost constant afterwards. The differences of the vertical ion-drag and pressure gradient forces between Run 2 and Run 1 are exhibited in the bottom panel of Figure 3.6. As shown in Figure 3.6(e), the vertical ion-drag force generally showed an upward enhancement with the magnitude greater than 0.05 m/s^2 above 400 km, and the evolution of the vertical ion-drag force difference roughly followed the evolution of the vertical ion-drag force in Run 2 (3.6(c)) since the vertical ion-drag force in Run 1 was almost zero. It is also noticeable that there was an apparent enhancement of the vertical ion-drag force propagating upward up to the 12th minute below 600 km after adding in the electric fields at low and middle latitudes. The enhancement of the vertical ion-drag force reached 0.11 m/s^2 at 400 km 8 minutes after start time. After that enhancement, the changes of the vertical ion-drag force returned to the values comparable with or even smaller than the values at the beginning. Figure 3.6(f) depicts the temporal variation of the difference in the vertical pressure gradient force between Runs 1 and 2. Clearly, the change of the vertical pressure gradient force was not zero in general, indicating that the thermosphere was away from the hydrostatic equilibrium throughout the simulation. Meanwhile, the feature standing out is the apparent perturbations at the beginning of the simulation. The perturbation can reach -0.3 m/s^2 at 400 km, indicating that the vertical pressure gradient force was $\sim$4% away from the local gravity. It is worth noting that the propagations of the disturbances in the vertical ion-drag and pressure gradient forces were most likely acoustic waves. First, it took $\sim$3 minutes for the phase to propagate from 400 km to 600 km, the phase speed was ~ 1100 m/s , which is close to the acoustic speed at these altitudes. Secondly, the change of the vertical pressure

gradient force at 400 km reached the minimum of -0.3 m/s^2 7 minutes after the start time and the maximum of 0.05 m/s^2 at 9 minutes after the start time, so the half period (T/2) was 2 minutes. The frequency ($\omega = \frac{2\pi}{\mathrm{T}}$) was around 0.03 rad/s, and the Brunt-Väisälä frequency (N) is $\sim$0.0075 rad/s above 200 km. Hence, $\omega \approx 4\mathrm{N}$, which falls into the range for the acoustic wave (Typically, the frequency of the acoustic wave in the thermosphere is greater than 2N).

It is also worth noting that the perturbation in the vertical pressure gradient force near the geomagnetic equator started with a negative phase, which was opposite to the results in *Deng et al.* (2008, 2011) where the consequences of abrupt enhancements in Joule heating at high latitudes have been simulated. In those studies, the vertical buoyancy ($-\frac{1}{\rho}\frac{\partial \mathrm{p}}{\partial \mathrm{r}} + \mathbf{g}$) underwent a substantial enhancement at first, which was directly caused by the significant enhancement in the upward pressure gradient force, and the initial enhancement of the upward pressure gradient force was a result of the substantial enhancement of Joule heating. However, in our case, the Joule heating was remarkably weaker at low and middle latitudes than that at high latitudes shown in *Deng et al.* (2008, 2011), so the Joule heating at low and middle latitudes did not significantly contribute to the changing vertical pressure gradient force. Rather, the initial decrease in the upward pressure gradient force might be related to the upward vertical wind caused by the upward ion-drag force, which extended the thermosphere to high altitudes and decreased the vertical gradient of the neutral density. It should be pointed out that the acoustic wave feature shown in Figure 3.6(f) was related to the sudden introduction of the electric fields at low and middle latitudes at 1200 UT, which might not appear in the typical quiet and steady case. Nevertheless, it suggests that, when the equatorial vertical ion drift experiences a sudden and substantial enhancement (e.g., during the storm time), larger vertical ion-drag forces as well as larger perturbations in the vertical pressure gradient force could be expected than those shown in Figures 3.5 and 3.6.

3.3 Summary

In this chapter, specifications of the electric fields at low and middle latitudes are improved by coupling the NCAR ionospheric electrodynamo model into GITM, offering an opportunity to investigate the impact of the vertical dynamics on thermosphere at low and middle latitudes. The main results are summarized as follows:

The equatorial ionization anomaly (EIA) and the equatorial thermosphere anomaly (ETA) were well reproduced. The characteristics of the EIA and ETA were generally consistent with the findings in previous studies. The daytime upward wind near the geomagnetic equator led to the enhancement of the neutral mass density at 400 km altitude, while the divergence in the meridional wind associated with the meridional ion-drag force transported the neutral mass density away from the geomagnetic equator, which may contribute to the formation of the ETA trough.

The changes of the vertical forces acting on the neutrals resulted in the change of the vertical dynamics of the thermosphere, which feedbacked to the vertical ion-drag and pressure gradient forces. The vertical ion-drag and pressure gradient forces showed predominant changes near the geomagnetic equator throughout the simulation. More specifically, the daytime vertical ion-drag force was generally upward near the geomagnetic equator and the daytime upward pressure gradient force near the geomagnetic equator was reduced at most times after adding in the electric fields at low and middle latitudes. The sudden introduction of the electric fields at low and middle latitudes induced acoustic waves in the vertical pressure gradient force during the first 12 minutes in the simulation.

3.4 Figures and tables

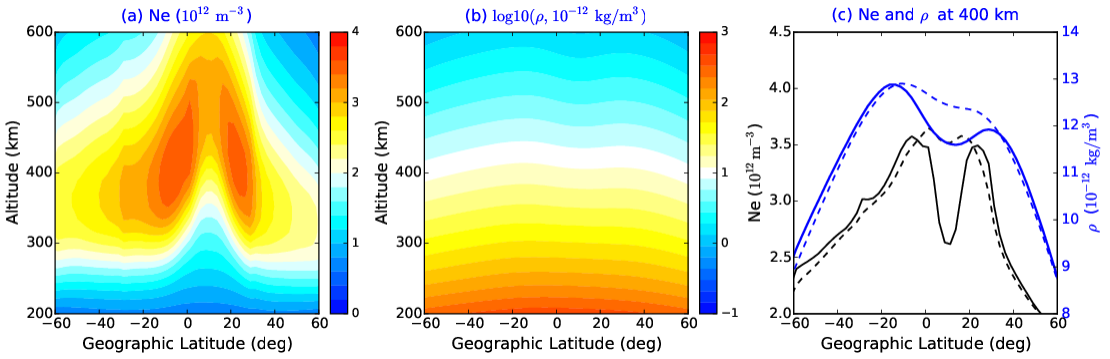

Figure 3.1: (a) The electron density and (b) the neutral density as a function of altitude and geographic latitude at the longitude of 17.5°E and 1300 UT, 09/22/2002 in Run 2. (c) The latitudinal distributions of the electron densities (black lines) and the neutral mass densities (blue lines) at the altitude of 400 km. The solid lines and dashed lines stand for the results from Run 2 and Run 1, respectively. The geomagnetic equator is located at around 10°N at this longitude.

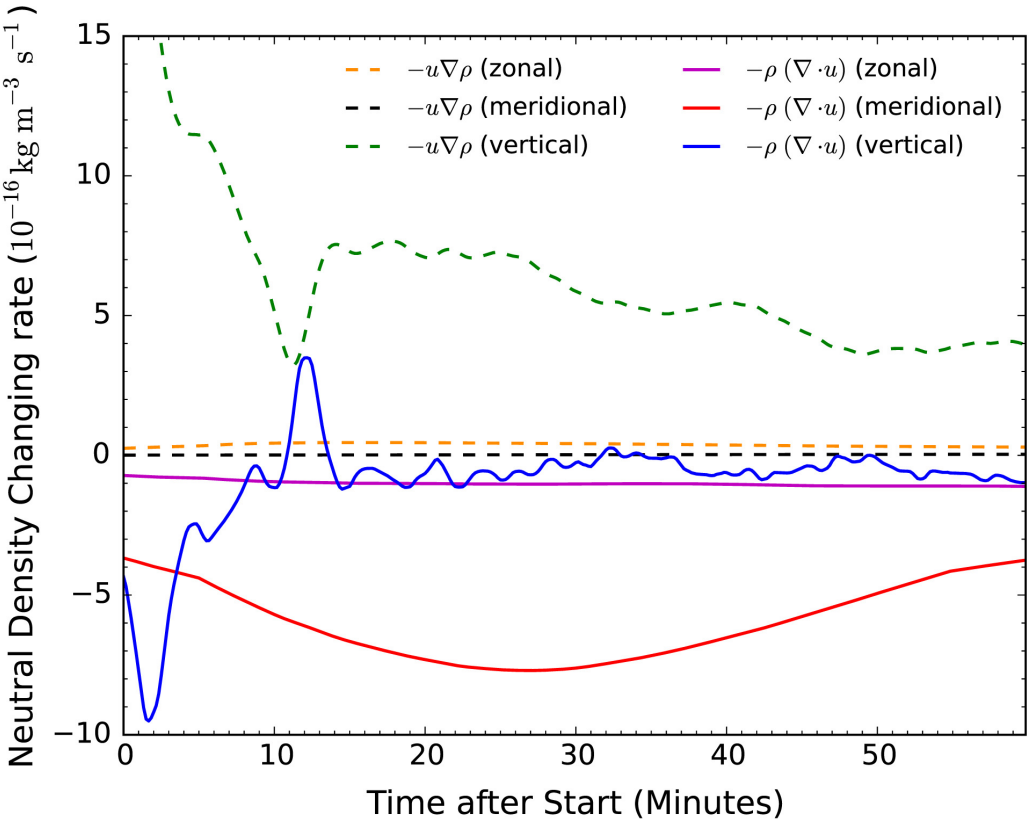

Figure 3.2: Temporal variations of the dynamic terms (dashed lines) and divergence terms (solid lines) in the Eq. 3.1 at 17.5°E, 12°N and 400 km.

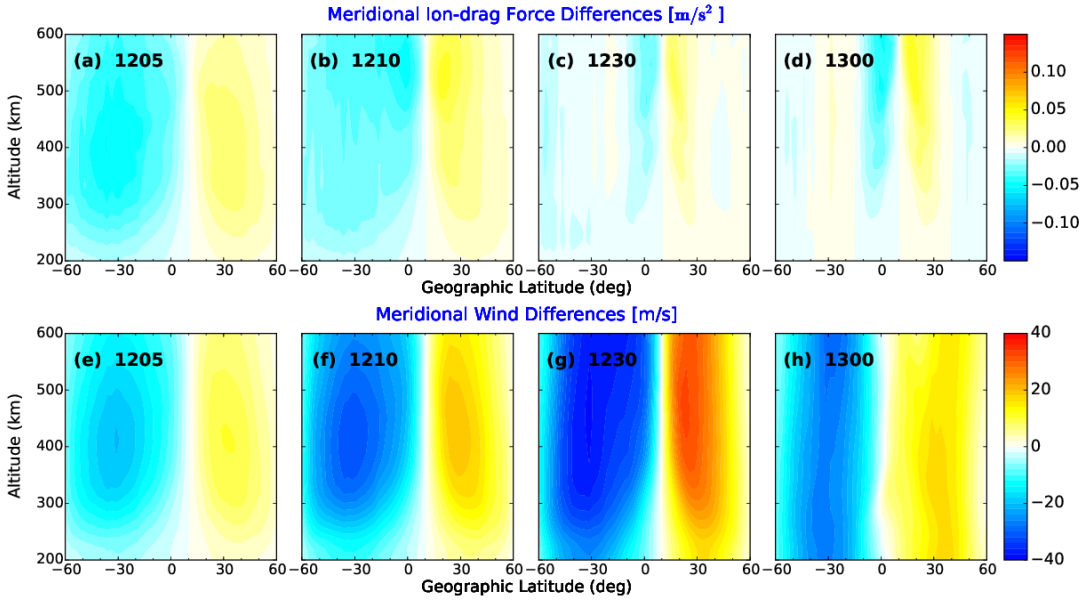

Figure 3.3: The differences of (a-d) the meridional ion-drag force and (e-h) the meridional wind between Run 2 and Run 1 along the longitude of 17.5°E at four different times. All plots are presented as a function of altitude and geographic latitude. The positive value represents northward direction. Note the geomagnetic equator is located at around 10°N at this longitude.

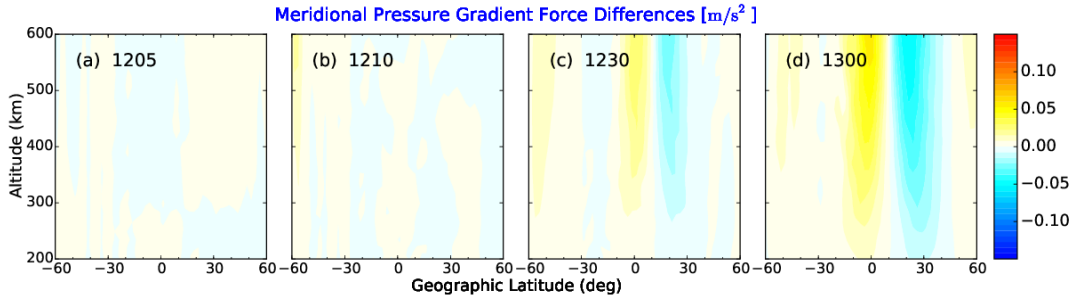

Figure 3.4: The differences of the meridional pressure gradient force between Run 2 and Run 1 along the longitude of 17.5° E at four different moments. All plots are presented as a function of altitude and geographic latitude. The positive value represents northward direction. Note the geomagnetic equator is located at around 10°N at this longitude.

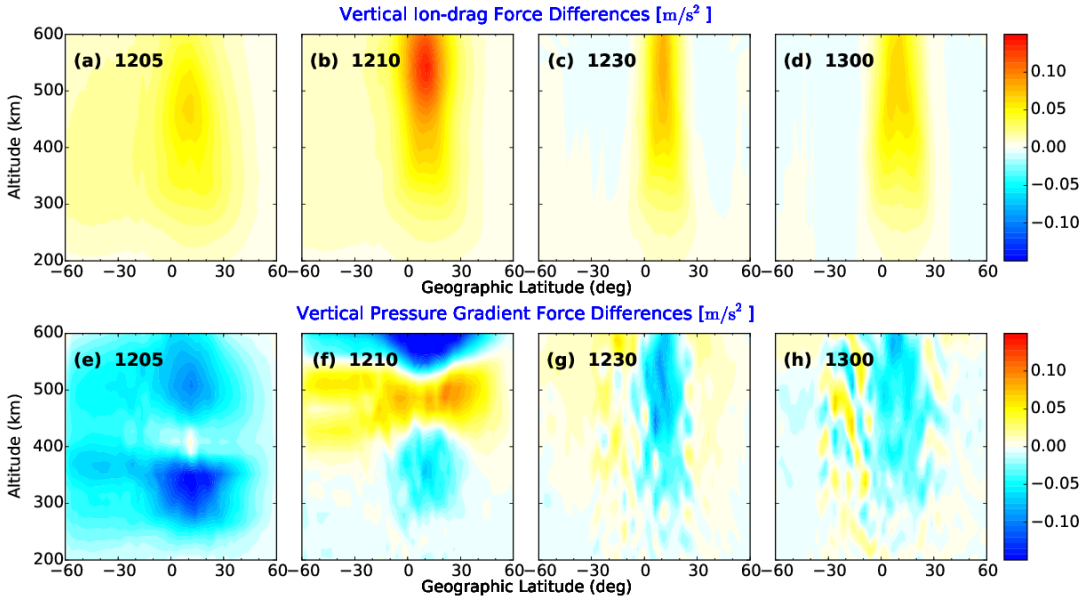

Figure 3.5: The differences of (a-d) the vertical ion-drag force and (e-h) the vertical pressure gradient force between Run 2 and Run 1 along the longitude of 17.5°E at four different times. All plots are presented as a function of altitude and geographic latitude. The enhancement in the upward direction is shown by positive value. Note the geomagnetic equator is located at around 10°N at this longitude.

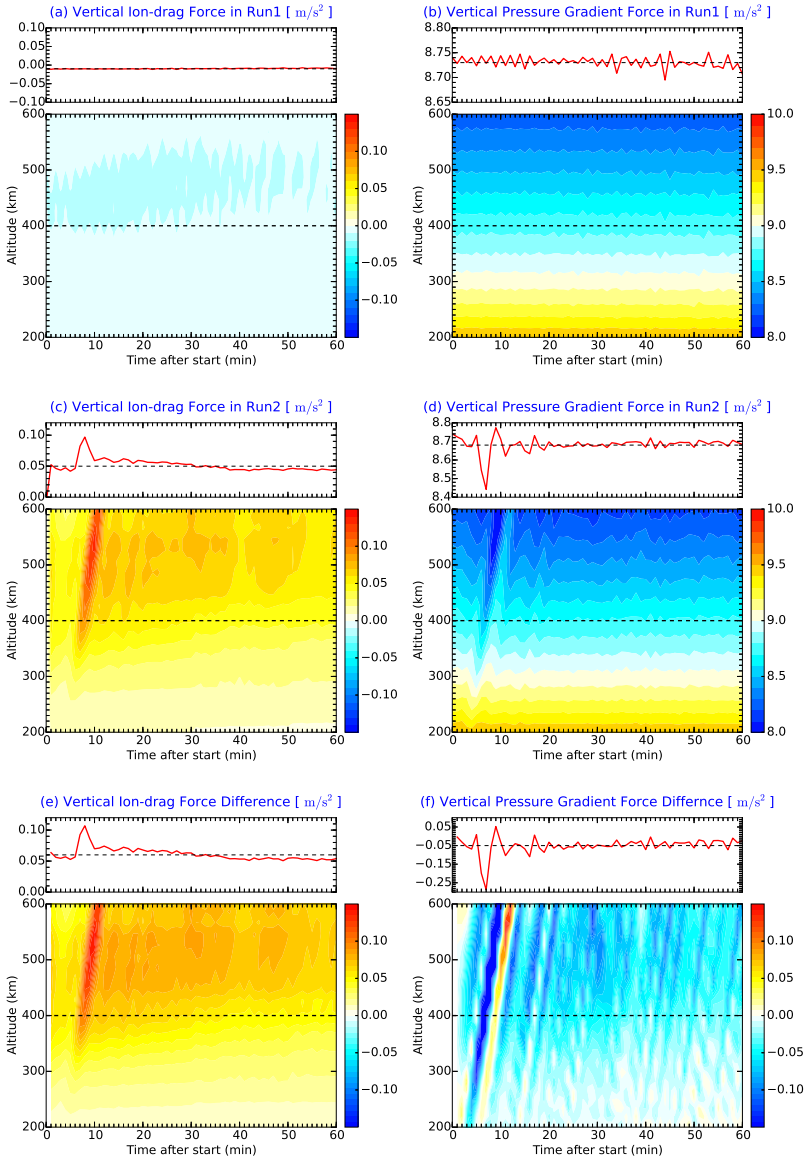

Figure 3.6: (Top) (a) Vertical ion-drag force and (b) vertical pressure gradient force in Run 1; (Middle) (c) Vertical ion-drag force and (b) vertical pressure gradient force in Run 2; (Bottom) Differences of (e) vertical ion-drag force and (f) vertical pressure gradient force between Run 2 and Run1. For each subplot, the bottom box represents the evolution of the corresponding parameter as a function of altitude and time, and the top box shows the temporal variation of the parameter at 400 km as indicated by the black dashed line in the bottom box. The position is at 17.5°E, 12°N and the positive direction is upward.

CHAPTER 4

Small-scale and mesoscale structures in high-latitude electrodynamical forcings and their impacts on Joule heating

As discussed in Section 1.2.3, high-latitude electrodynamical forcings (i.e., electric field, electron precipitation and FACs) have highly variable small-scale and mesoscale structures. Statistically, they can be treated as variabilities that deviates from the large-scale pattern as will be shown later. To date, our knowledge of small-scale and mesoscale variabilities in in high-latitude electrodynamical forcings is still insufficient, so that their impacts on the I-T system are not well evaluated in GCMs. Therefore, the goal of this chapter is to further the understanding on small scale and mesoscale variabilities in high-latitude electrodynamical forcings and their impacts on Joule heating through a combination of data analysis and numerical simulations. More specifically, two studies have been carried out: Section 4.1 seeks to establish a statistical understanding on the small-scale and mesoscale electric field and electron precipitation variabilities. Besides, the impacts of small-scale and mesoscale electric field and electron precipitation variabilities on Joule heating will be investigated; Section 4.2 intends to establish a comprehensive understanding on the relationship between electric fields and FACs on different scales in order to provide insights for the impacts of small-scale and mesoscale FACs on Joule heating. Each of the following sections are organized as follows: first a brief introduction is provided to outline the objectives of each section; The data used in each section and their process are introduced

subsequently; The next part presents the results along with the discussion. Finally, a summary of the primary findings in each section is presented.

4.1 Small-scale and mesoscale variabilities in the electric field and electron precipitation and their impacts on Joule heating

4.1.1 Introduction

Although distributions of small-scale and mesoscale electric field variabilities has been studied recently, the statistical distributions of small-scale and mesoscale electron precipitation are still lacking (Section 1.2.3). Further, the correlation between the small-scale and mesoscale electric field and electron precipitation variabilities at different locations remains unexplored. Therefore, the first objective of this section is to investigate the distribution of the small-scale and mesoscale electron precipitation variabilities and to quantify their correlations with the small-scale and mesoscale electric field variabilities by using the Dynamic Explorer 2 (DE-2) satellite (Section 2.1.1) measurements. Besides, the second objective is to assess to what extent the Joule heating can be affected by the small-scale and mesoscale variabilities in the electric field and the electron precipitation by using GITM.

4.1.2 DE-2 Data

DE-2 measured the along-track and the cross-track ion drifts, which were taken by the Retarding Potential Analyzer (RPA, *Hanson et al.*, 1981) and the Ion Drift Meter (IDM, *Heelis et al.*, 1981), respectively. The bulk ion drift vector ($\mathbf{V}$) is the combination of those two components, and the electric field can be calculated according to $\mathbf{E} = -\mathbf{V} \times \mathbf{B_0}$. Here B_0 is the geomagnetic main field from the International Geomagnetic Reference Field

(IGRF) model. The electric field is decomposed in modified apex coordinates (*Richmond*, 1995) according to the following formula:

$$\mathbf{E} = E_{d1} \cdot \mathbf{d_1} + E_{d2} \cdot \mathbf{d_2} \tag{4.1}$$

Here E_{d1} and E_{d2} represent the magnetic eastward and northward components of electric field, respectively, which are constant along the same geomagnetic field line, while $\mathbf{d_1}$ and $\mathbf{d_2}$ are the base vectors at magnetic eastward and northward directions, respectively, at the satellite height. Then the mapped electric field at 110 km can be obtained according to Eq. 4.1 by using $\mathbf{d_1}$ and $\mathbf{d_2}$ along same geomagnetic field line and at the altitude of 110 km, and its magnitude ($|\mathbf{E}|$) can be computed. The electric field intensity mentioned in the remaining part refers to the intensity of electric field at 110 km. More details involving modified apex coordinates and the decomposition procedure can be found in *Richmond* (1995).

The electron precipitation measurements on DE-2 were taken by the Low-Altitude Plasma Instrument (LAPI, *Winningham et al.*, 1981). LAPI provides the differential electron energy flux on different energy channels for both the electron and the ion ranging from 5 eV to 32 keV. The total electron energy flux (Φ_E) is determined by integrating the differential electron energy flux over different energy channels and multiplying by the factor of π if the downward differential electron energy flux is assumed to be isotropic. For a steady-state isotropic flux without field-aligned electric field, the particle power per unit area is constant along the geomagnetic field. In this study, we specifically focus on the total energy flux of the electron precipitation.

In addition to the DE-2 data, interplanetary magnetic field (IMF) data are used in order to investigate the distributions of the high-latitude electric field and electron precipitation and their correlations under specific IMF conditions. Two parameters are used to

categorize the IMF condition: 1) IMF transverse component magnitude B_t, which represents the strength of the IMF projection onto the Geocentric-Solar-Magnetospheric (GSM) Y-Z plane, i.e., $B_t = \sqrt{{B_y}^2 + {B_z}^2}$; 2) IMF clock angle ($\theta$), which stands for the angle between GSM north and the IMF projection onto the GSM Y-Z plane and is given by $\theta = \text{atan2}(B_y, B_z)$. The IMF data used here are the hourly averaged data based on the Interplanetary Monitoring Platform 8 (IMP-8) and International Sun-Earth Explorer 3 (ISEE-3) satellite measurements.

4.1.3 Results and Discussion

4.1.3.1 Electric field and electron precipitation on different scales

In order to extract the small-scale spatial variabilities from the electric field as well as the electron precipitation observations, a 500-km moving window is applied on the data along each pole-pass track. It is worth noting that the satellite measurement involves both spatial and temporal variations. However, if it is assumed that structures the satellite encounters are stationary for a short period (1-2 min), the time series data from the satellite can be converted to spatial data by using the speed of the satellite (*Chen and Heelis*, 2018). Since DE-2 travels 500 km in 63s, we believe that most of the variabilities extracted by the 500-km moving window are spatial variability below 500 km.

One example using the moving window is shown in Figure 4.1. For the left column, the black lines indicate the derived quantities (E_{d1}, E_{d2}, electric field intensity and electron energy flux, top to bottom) from the electric field and electron precipitation measurements. The red line in each plot indicates the smoothed result for the corresponding quantity after applying the 500-km moving window, which represents the large-scale structure of that quantity. The differences between the red and the black lines in each plot are referred to as the small-scale and mesoscale variabilities (will be called small-scale variabilities in this

section for simplicity) of the corresponding quantity, which are shown in the right column. It is worth noting that the small-scale variabilities represent variabilities at the scale size smaller than 500 km. Different choices of the moving window size may lead to slightly different results. However, due to the limitation of the available data, it is noted that a roughly 500-km by 500-km bin size helps to maintain enough data points in most bins and to ensure the statistical significance. Hence, the 500-km sliding window is utilized in this study.

The quantities shown in Figure 4.1 are then binned as a function of magnetic local time (MLT) and magnetic latitude (MLAT). The bin size is chosen to be 5° in MLAT and variable size in MLT (0.64 h at 62.5° MLAT and 2.25 h at 82.5° MLAT, i.e., ∼500 km along MLT) to keep a roughly constant area at different latitudes. For this study, we focus on the case where the IMF B_t is between 4 to 10 nT and the IMF clock angle is between 135° and 225°, when both the electric field and electron precipitation are fairly strong.The data from both hemispheres and all seasons are combined in order to have a reasonable data coverage.

Figure 4.2 displays the binning results for the electric field intensity ($|\mathbf{E}|$) and the electron energy flux (Φ_E). The averages of the large-scale electric field intensity and electron energy flux are calculated in each bin and their distributions are shown in the first column of Figure 4.2. Clearly, the patterns shown in the first column are similar to the patterns from empirical models (e.g., *Weimer*, 2005; *Fuller-Rowell and Evans*, 1987; *Newell et al.*, 2009). The second column exhibits the distributions of the standard deviation of the large-scale electric field intensity and electron energy flux in each bin. The standard deviation of large-scale quantity primarily reflects variations in the solar wind condition. In addition, seasonal variations and hemispherical asymmetry may also contribute to the standard deviations. Clearly, the standard deviations of large-scale electric field intensity and electron energy flux are not negligible, yet they are generally smaller than the mean

fields except for the electron energy flux in the evening sector. It is noted that the standard deviations of the large-scale quantities would be reduced if there were sufficient data for subdividing the case into more specific conditions with respect to the IMF, season and hemisphere, since the variability represented by these conditions adds to the large-scale standard deviations shown in the second column. The third and fourth columns show the averages and the standard deviations of small-scale electric field intensity and the electron energy flux variabilities, respectively. Unlike what is shown on large scale, the averages of the small-scale variabilities are close to zero since the subtraction of the moving average tends to leave residuals with means near zero. On the other hand, the standard deviation of the small-scale electric field intensity variabilities are generally 10-15 mV/m at 60°-75° MLAT, which are comparable to the standard deviation of the large-scale electric field intensity. As for the electron precipitation, there is a distinct peak in the standard deviation of the small-scale electron energy flux variabilities in the evening, which may account for the intense aurora structures at scale sizes of tens to a few hundreds of kilometers that cannot be resolved by a 500-km sliding window.

The linear correlations between the large-scale electric field intensity and electron energy flux and between small-scale variabilities of electric field intensity and electron energy flux are calculated in each bin, and distributions of the coefficient distributions are presented in Figures 4.3(a) and 4.3(b), respectively. Here, only the correlation coefficients in the bins where the number of trajectories passing through that bin is greater than four and the number of data points is larger than 200 are kept, otherwise they are set to be zero (grey shaded areas, which indicate the data are not sufficient). It is clear that the pattern shown in Figure 4.3(a) is more complicated than that shown in Figure 4.3(b). More specifically, for the large-scale electric field intensity and electron precipitation, Figure 4.3(a) indicates that a positive correlation occurs mostly on the dawn side, whereas an anti-correlation occurs mostly in the early evening sector as well as around noon and midnight. In contrast, the

electric field intensity variability tends to be anti-correlated with the electron energy flux variability in general on small scales.

The FACs are closed by the ionospheric currents which are related to the electric field and the conductance in the ionosphere, and the conductance is strongly influenced by the electron precipitation at night. The correlation between the electric field intensity and the electron energy flux shown in Figure 4.3 therefore may be helpful to answer the question whether the magnetosphere tends to act as a current generator or a voltage generator in magnetosphere-ionosphere system on different scales, especially in the aurora region. Evidently, Figure 4.3(b) shows a consistent anti-correlation between the electric field intensity and electron energy flux variabilities in the aurora region on small scales, indicating that the magnetosphere tends to behave as a current generator at those scales in the aurora region, which is consistent with previous findings (e.g., *Lysak*, 1985; *Vickrey et al.*, 1986). On large scale, it is clear that the electric field intensity tends to be positively correlated with the electron energy flux on the morning side. This may result from variability of the low-latitude boundary of the auroral oval, with increases in both precipitation and the electric field at a given location near the boundary as the boundary moves equatorward. However, the electric field intensity appears to be anti-correlated with the electron energy flux in the evening, which is different from the theoretical prediction in *Lysak* (1985). It has been known that the type of the magnetospheric generator depends on the solar wind conditions. Recently, *Weimer et al.* (2017) found that the magnetosphere probably acts as a current source on large scale when the interplanetary electric field is large. Since the interplanetary electric field intensity has not been taken into account in the binning process, it is likely that some observations were taken when the interplanetary electric field was fairly large. Therefore, the data trend may have been strongly influenced by those observations. Larger datasets for the ionospheric electric field and the electron precipitation as well as better specification of the solar wind conditions may be helpful to extend the analysis.

In general, the DE-2 data provides similar large-scale average patterns of the electric field and the electron precipitation as the empirical models. However, the large-scale patterns overlook the considerable variabilities. Furthermore, the electric field intensity variability tends to be anti-correlated with the electron energy flux variability at small-scales. The remaining question is to what degree the small-scale variabilities in the electric field and the electron precipitation can contribute to the Joule heating. In the following subsection, we will address this question by implementing the distributions of electric field and electron precipitation and their correlations from statistical analysis of DE-2 data in GITM.

4.1.3.2 Impacts of the small-scale variabilities on Joule heating

To highlight the importance of the small-scale electric field and electron precipitation variabilities on Joule heating, three GITM runs have been carried out in this study. Specifically, Run 1 is a reference run, where only the averages as well as their variabilities of electric field and electron precipitation on large scale are included. Run 2 is based on Run 1 but also includes the small-scale electric field variabilities. Run 3 has same specifications as Run 2 except that the small-scale electron precipitation variations are further included. Table 4.1 serves as a summary of simulations we have conducted and detailed descriptions of each run will be discussed in following paragraphs. The spatial resolution for all simulations is 5° in longitude by 5° latitude and $\frac{1}{3}$ scale height in the altitude. The temporal resolution is 2 s. All simulations are conducted under high solar activity ($F_{10.7} = 150$ sfu) and at the September equinox. In addition, a 24-hour pre-run (00:00:00, 09/22/2002 $\sim$ 00:00:00, 09/23/2002) has been carried out, so that the neutral dynamics in GITM reached a steady state when simulations are conducted.

In Run 1, the large-scale average electric field (both E_{d1} and E_{d2} components) and electron precipitation patterns from DE-2 data were included in GITM. On top of that,

the large-scale electric field and electron precipitation variabilities were also included. To include the large-scale electric field variability, a similar methodology as used in *Deng et al.* (2009) was adopted. At each time step, superimposed on the average electric field, the variable electric field, which is constructed by the standard deviations of large-scale E_{d1} and E_{d2} components, was introduced at each grid point and its sign was flipped every 2 minutes. This procedure effectively assumes that the variable electric field changes rapidly enough that the wind cannot respond to it, and that the two are uncorrelated, although this may not be true in reality. For example, contributions to the electric-field variability due to seasonal changes may have long-lasting components that could affect the wind and produce a correlation. We neglected such effects. Meanwhile, in order to include the large-scale electron precipitation variability according to its correlation with the large-scale electric field variability, the best-fit line, which was used to calculate the linear correlation between the large-scale electric field intensity and electron energy flux shown in Figure 4.3(a), has been implemented in GITM. Our approach was to calculate the modification in the electric field intensity due to the inclusion of the large-scale electric field variability at each grid point first, then by using the best-fit line, the corresponding change in the electron energy flux can be obtained. The modified electron energy flux induces the change in the conductivity. Both modified electric field and conductivity have been used to calculate Joule heating. It was effectively assumed that the variability of the electron precipitation is not correlated with the variability of the wind when calculating Joule heating, although this assumption might not be valid under certain circumstances (e.g., *Zou et al.*, 2018). Figure 4.4(a) shows the 4-min average of height-integrated Joule heating from Run 1.

On the basis of Run 1, the small-scale electric field variabilities were further included in Run 2 to assess its impact on the Joule heating. Similar to the way to include the large-scale electric field variability, the standard deviations of variabilities of small-scale E_{d1} and E_{d2} components in each bin were used to construct the small-scale variable electric field

introduced into GITM, with the flip cadence of 1 minute. Here, the different choice of flip cadence for the small-scale variable electric field from that for the large-scale variable electric field is based on the assumption that electric field variabilities are not correlated across different scale sizes. Run 2 used the same electron precipitation as Run 1. Figure 4.4(b) shows the 4-min average of the Joule heating from Run 2. It is seen that there was a $\sim$27% enhancement in the hemispheric integrated Joule heating after including the small-scale electric field variabilities as compared with the Joule heating in Run 1 (Figure 4.4(a)). Combining the results shown in Figures 4.4(a) and 4.4(b) together, it is clear that the small-scale electric field variabilities play a significant role in accurately specifying the Joule heating (e.g., *Codrescu et al.*, 1995).

To assess the potential impact on Joule heating associated with the small-scale electron precipitation variations, the small-scale electron precipitation variabilities has been introduced into Run 3 on the basis of Run 2, and the approach is similar to that of including the large-scale electron precipitation variability. For each grid point and at each time step, the change of the electric field magnitude due to the inclusion of the small-scale electric field variabilities was calculated. Then by utilizing the best-fit lines, which are used to obtain the linear correlation coefficient distribution in Figure 4.3(b), the modification of the electron energy flux at each grid point was obtained. Thus, the corresponding change in conductivity can be calculated in GITM. The modified electric field and conductivity were utilized to calculate Joule heating. It was assumed that the variabilities of the electric field at different scales are uncorrelated, and that the variabilities of the electron precipitation at different scales are uncorrelated, so that the correlations between the electric field and electron precipitation variabilities can be treated separately for the large-scale component and small-scale components. The possible importance of non-linear correlations between the electric field and electron precipitation were also neglected, which probably deserves to be addressed in the future work. The 4-min averaged height-integrated Joule heating is

presented in Figure 4.4(c). Comparing with Run 2 (Figure 4.4(b)), the total Joule heating in the whole hemisphere underwent approximately 10 GW (5%) reduction in Run 3. Moreover, the distribution of Joule heating percentage change of Run 3 relative to Run 2, as shown in Figure 4.4(d), evidently shows that the local reduction of Joule heating can reach up to $\sim$17.5% on the dusk side, indicating that the anti-correlation between the small-scale electric field and electron precipitation variabilities cannot be neglected, especially locally, for the calculation of Joule heating.

4.1.4 Summary

In this study, the averages and variabilities of the electric field and electron precipitation at different spatial scale sizes have been investigated for the case of dominant southward IMF B_z. In addition, the impacts on Joule heating associated with the small-scale electric field and electron precipitation variabilities have been assessed in GITM. It is the first time that the correlation between the electric field and the electron precipitation variabilities at small-scales has been quantified. Furthermore, the impact on Joule heating associated with the correlation between the small-scale electric field and electron precipitation variabilities has been quantitatively evaluated in GCM unprecedentedly. The primary findings are summarized as follows:

(1) The variabilities of electric field and electron precipitation are not negligible as compared with the large-scale average electric field and electron precipitation.

(2) The electric field variability tends to be anti-correlated with the electron energy flux variability on small scale, indicating that the magnetosphere is likely to behave as a current generator on small scales.

(3) Although Joule heating can be significantly elevated by the small-scale electric field variability ($\sim$27% globally), the corresponding change in the electron precipitation tends to depress such enhancement ($\sim$-5% globally) due to the anti-correlation be-

tween the small-scale electric field and electron precipitation variabilities. The localized reduction can reach $\sim$17.5% on the dusk side, suggesting that the impact of the anti-correlation between the small-scale electric field and electron precipitation variabilities on Joule heating is not negligible there.

4.2 Impacts of multiscale field-aligned currents (FACs) on the ionosphere thermosphere system

4.2.1 Introduction

To explore the impacts of strong small-scale and mesoscale FACs to the I-T system, it is important to understand the difference and relationship between FACs and ionospheric electric fields on different scales. The FAC data from the Swarm satellites (Section 2.1.2) and the electric field data from the DE-2 satellite (Section 2.1.1) have been utilized to provide more insights for this question. Furthermore, the statistical results of the FACs on different scales have been utilized to specify the high-latitude electrodynamics in GITM in order to study impacts of multiscale FACs on Joule heating.

4.2.2 Swarm FAC Data

Since the DE-2 electric field data and their process has been introduced in Section 4.1.2, only the Swarm FAC data are introduced in this subsection. Each Swarm satellite is equipped with a vector fluxgate magnetometer (VFM), which measures the vector magnetic field with high precision and cadence. The time resolution of the magnetic field measurement can reach up to 50 Hz and the precision can be better than 0.1 nT. The horizontal magnetic perturbation, which is related to the field-aligned current density, is obtained by subtracting the background magnetic field from the measured magnetic field. The vertical current density is calculated through Ampere's law, under the assumptions of an infinite

current sheet perpendicular to the flight direction and stationarity (*Gjerloev et al.*, 2011; *Lühr et al.*, 2015), and the FAC density is calculated by dividing the vertical current density by the sine of the magnetic inclination. Two Level 2 FAC data products are provided: 1) single- and 2) dual-satellite estimates. The single-satellite FAC resolves FACs at the scale size larger than 7.5 km, while the dual-satellite FAC primarily represents the FAC at the scale size above 150 km. More details can be found in *Ritter et al.* (2013). In this chapter, to investigate the FACs from small scale to large scale, single-satellite FAC data spanning 2015-2016 from Swarm A and C satellites in the Northern hemisphere are analyzed.

4.2.3 Results and Discussion

In this study, following *Forsyth et al.* (2017), the FAC and electric field (both E_{d1} and E_{d2} components) on large scale are obtained by applying a Hanning filter with the window width of 67 s ($\sim$500 km) to the Swarm FAC data and DE-2 electric field data, respectively. A window of this width largely removes wavelengths shorter than this width. A Hanning filter with the window width of 13 s ($\sim$100 km) is then applied on the residuals, which are obtained through subtracting the large-scale FAC/electric field from the observations, to extract the mesoscale FAC/electric field. Finally, the small-scale quantities are obtained by subtracting the large-scale and mesoscale components from the observations.

In addition, it is worth to note that the single-satellite FAC estimation is subject to the assumption that FACs are stationary as the satellite is crossing the current sheet and during successive satellite measurements. However, such an assumption could break down under certain circumstances, particularly when the spatial scale size decreases (e.g., *McGranaghan et al.*, 2017; *Forsyth et al.*, 2017; *Gjerloev et al.*, 2011; *Lühr et al.*, 2015). Therefore, it is necessary to exclude the single-satellite FAC data that violate the stationary assumption to increase the data fidelity. The robust technique used in *McGranaghan et al.* (2017), first developed by *Forsyth et al.* (2017), is adopted to remove unreliable

single-satellite FAC data. This technique identifies the unreliable FAC data according to the correlation and the gradient of the least square fit between Swarm A and C FAC measurements. The filtering thresholds used in *McGranaghan et al.* (2017)) are adopted in this study, i.e., 0.5 for the correlation and 0.5-1.5 for the least square fit. Detailed descriptions of this technique can be found in Section 3 of *Forsyth et al.* (2017) and Section 3.2 of *McGranaghan et al.* (2017).

4.2.3.1 FAC on different scales

Cleaned data on each scale are then mapped to 110 km altitude and binned according to the geomagnetic local time and geomagnetic latitude. The data from all seasons and all IMF conditions are used. The bin size is 1° in magnetic latitude (MLAT) by 500 km in magnetic local time (MLT) (i.e., 0.4 MLT at 50° MLAT and 3.11 MLT at 85° MLAT). The average and standard deviation in each bin are calculated and their distributions are exhibited in Figure 4.5. The large-scale average is dominant in general while average contributions from other scales are trivial. However, the variabilities, represented by the standard deviations, are not negligible on small- and meso-scales. In general, the small- and meso-scale FAC variabilities are greater than 0.5 $\mu A/m^2$, which is two or three times the large-scale FAC variability. Moreover, the FAC variability increases as scale size decreases. It is noticeable that the peak of small-scale (8-100 km) FAC variability is located around noon and can reach 1-1.5 $\mu A/m^2$, which is consistent with previous studies (e.g., *Hasunuma et al.*, 2008).

It should be recognized that the average FAC and its variability (standard deviation) depend on how the geophysical conditions for the average are specified. In this study, we combined data for all seasons and IMF conditions together. Because of this, part of the variability is due to changing seasons and IMF conditions. If we had separated the data into different seasons and/or IMF conditions the averages would depend on the geophysical

state, and the variability would tend to be smaller, also dependent on the geophysical state. For example, if we were to separate the data into two sets for negative and positive IMF B_y, letting J_- and J_+ be their respective mean FAC densities and δJ_- and δJ_+ their respective standard deviations, then averaging the two distributions together would give a mean FAC density of $(J_- + J_+)/2$ and a variance of $(\delta J_-^2 + \delta J_+^2)/2 + [(J_- - J_+)/2]^2$, which is the average of the variances of the two data sets plus an enhancement owing to the difference between the averages J_- and J_+.

4.2.3.2 Ionospheric electric field on different scales

Figure 4.6 displays the distributions of the magnitude of the average vector electric field and electric field variability on different scales. In each bin, the average vector electric field ($\overline{\mathbf{E}}$) is calculated through Eq. 4.1 by using the averages of E_{d1} and E_{d2} components in each bin (i.e., $\overline{\mathbf{E}} = \overline{E}_{d1} \cdot \mathbf{d_1} + \overline{E}_{d2} \cdot \mathbf{d_2}$). The electric field variability δE is the square root of the sum of squares of the standard deviations of E_{d1} and E_{d2} components in each bin (i.e., $\delta E = \sqrt{\delta E_{d1}^2 + \delta E_{d2}^2}$). As shown in Figure 4.6, as with the FAC, the large-scale average electric field is more important than the average electric field on other scales. The distribution of the average electric field on large scale is similar to that given by empirical models (e.g., *Weimer*, 2005). However, the magnitude of the electric field variability appears to decrease with descending scale size, which is opposite to the behavior of the FAC variability shown in Figure 4.5.

The comparison between Figures 4.5 and 4.6 implies that the FAC and ionospheric electric field tend to have different amplitude spectra, which is supported by Figure 4.7. Figure 4.7 compares the spectra of FAC and the magnetic perturbation (dB_y) in the east-west direction along one specific pole-pass track. dB_y is known to have a similar spectrum as the electric field in the north-south direction (E_x) (e.g., *Sugiura et al.*, 1982; *Sugiura*, 1984; *Weimer et al.*, 1985; *Kozelov et al.*, 2008). As revealed by Figure 4.7, the spectrum

of the FAC is roughly constant with scale size while the spectrum of the electric field magnitude decreases with the decreasing scale size.

The question then arises as to why the strong FAC variability cannot be transmitted to the strong ionospheric electric field variability on small scale and mesoscale. A possible explanation for this question may come as follows. At high latitudes and under a static condition, the FAC is equal to the divergence of the horizontal ionospheric currents, i.e., $\mathbf{J}_{\parallel} = -\nabla_{\perp} \cdot (\Sigma \cdot \mathbf{E}_{\perp})$, where $\mathbf{J}_{\parallel}$ is the FAC density, Σ is the conductance tensor and $\mathbf{E}_{\perp}$ is the ionospheric electric field perpendicular to the geomagnetic field line. If we consider four assumptions: 1) geomagnetic field lines are vertical; 2) the Hall conductance is ignored; 3) the horizontal gradient of the Pedersen conductance is ignored; and 4) the electric field lies in the x direction, then the FAC would be proportional to the spatial derivative of the electric field, i.e., $J_{\parallel} \propto \frac{dE_x}{dx}$. By applying dimensional analysis, we can simplify the relationship to $|J_{\parallel}| \propto \frac{|E_x|}{L}$, where L represents the scale size. Thus, the magnitude of the electric field is proportional to the magnitude of the FAC multiplied by the scale size L. In other words, the influence of the FAC on the ionospheric electric field is weighted by the scale size, which indicates that the magnitude of the electric field decreases as the scale size L decreases if the magnitude of the FAC remains constant. Therefore, strong FACs on small- and meso-scales do not necessarily correspond to strong electric fields on those scales. Collectively, the FACs and ionospheric electric fields on different scales are analyzed in the previous two subsections. It is found that although the FAC tends to be stronger on smaller scales, the ionospheric electric field tends to be weaker on smaller scales, which should be considered when including multiscale FACs into GCMs. One approach to include multiscale FACs will be described next.

4.2.3.3 Impacts of FAC variabilities on the I-T system

In this part, the impacts of FAC variabilities on the I-T system will be investigated in GITM, and the large-scale and mesoscale FAC variabilities are the primary focuses. To highlight the contributions of the large-scale and mesoscale FAC variabilities to Joule heating, three sets of simulations are carried out (summarized in Table 4.2). Run 1 is a reference run, where only the large-scale average FAC (Figure 4.5(a)) is included. In Run 2, in addition to the large-scale average FAC, the large-scale FAC variability (Figure 4.5(d)) is included in a manner described below. Run 3 is similar to Run 2, but includes only the mesoscale FAC variability (Figure 4.5(d)). The spatial resolution of GITM for all simulations is 5° in longitude by 1° in latitude and 1/3 scale height in altitude. The temporal resolution is 2 s. All simulations were conducted under moderate solar activity ($F_{10.7} = 100$ sfu) at the September equinox. In addition, the electron precipitation in this study was specified by the *Fuller-Rowell and Evans* (1987) model with the hemispheric power (HP) of 10 GW. Moreover, a 24-hour pre-run (00:00:00, 09/22/2002 - 00:00:00, 09/23/2002) has been conducted, so that the neutral dynamics in GITM reached a quasi-steady state when the simulations driven by the FACs were conducted. Regarding the NCAR electrodynamo model, the number of grid points in the MLT and MLAT directions are 100 and 381, respectively, which correspond to a 0.24 h grid size in the MLT direction and a $\sim$0.6°-0.8° grid size in the MLAT direction between 60°-80° MLAT, respectively.

In this study, J_{Mr} in Eq. 2.23 was set to zero at $|\text{MLAT}| < 50$ and was calculated from the FAC density from the statistical Swarm results in Section 4.2.3.1 at $|\text{MLAT}| \geq 50$. In addition, following the methodology used in *Marsal et al.* (2012), at each hemisphere, J_{mr} was set to zero where the integrated conductance along the field line is smaller than 2 S, which helped avoid unrealistic potential values in the region where the ionospheric conductance is low. Further, the correction technique applied in *Marsal et al.* (2012) was adopted

to balance globally integrated upward and downward currents. The correction applied at each grid point was proportional to the Pedersen conductance and the absolute value of J_{mr}.

Figure 4.8 shows the electric field intensity and Joule heating outputs from Run1 in the Northern Hemisphere. Three distinct peaks emerged, with the largest peak occurring on the dusk side (Figure 4.8(a)), which is similar to our statistical DE-2 results (Figure 4.6(a)). This indicates that the statistical average FAC and electric field were mutually compatible with respect to the potential solver (Eq. 2.23) using GITM conductances and winds, giving us confidence that FAC variabilities can also be reliably introduced into GITM.

Figure 4.9 serves as a schematic diagram to illustrate our approach to include the FAC variability into GITM. For each grid point of the NCAR ionospheric electrodynamo model, the magnitude of the variable J_{mr}, ΔJ_{mr}, was determined by using the variable FAC density from the Swarm data analysis on the corresponding scale. But the sign of ΔJ_{mr} was alternated every few adjacent grid points in both MLAT and MLT directions. The sign of ΔJ_{mr} was also flipped every 1 minute. The way we determined the spatial separation of the altering sign was quite empirical: according to what we have found in Section 4.2.3.2, the magnitude of the ionospheric electric field is proportional to the magnitude of the FAC multiplied by a characteristic distance, L, which is proportional to the spatial separation of the upward and downward currents. Therefore, strong electric field variability can be generated on large scales due to the large spatial separations of the upward and downward variable FACs, even if the magnitude of the FAC variability on large scales is relatively weak. On the other hand, moderate spatial separations are needed for the inclusion of the mesoscale FAC variability. To find the most ideal separations, an iterative process has been employed: we started with an initial spatial separation, compared the simulated electric field variability caused by the FAC variability to the observed values (Figures 4.6(d) and 4.6(e)) and obtained agreement by adjusting the FAC spatial separations through changing

the number of neighboring points with the same sign of the variable FAC. The ideal spatial separations are 16 and 8 grid points in MLT and MLAT directions for the large-scale FAC variability and are 4 and 3 grid points in MLT and MLAT directions for the mesoscale FAC variability. Figure 4.10 shows the distributions after the empirical tuning process.

As shown in Figure 4.10, the electric field variability derived from the FAC variability in our approach can generally reproduce the predominant features in those derived from the observations. For example, when the large-scale FAC variability has been included into GITM, the electric field variability exhibited a peak intensity near noon (Figure 4.10(a)). Meanwhile, when the mesoscale FAC variability was included, the electric field variability displayed two peaks in its intensity, one on the dayside and one on the nightside. The dayside peak appeared to be $\sim$3 mV/m (25%) larger than the nightside one. Although our approach worked well in a general sense, there were some discrepancies between the electric field variability derived from the DE-2 observations and from the FAC-driven simulations. For example, it is clear that the electric field variability derived from the FAC-driven simulations near the magnetic pole was smaller than that derived from the DE-2 observations. This is because the statistical FAC variability shown in Figure 4.5 was not included in the simulations over the polar cap due to the low conductance (smaller than 2 S) in the model. Therefore, a small electric field variability computed from the FAC-driven simulations in that region is expected.

Figure 4.11 displays the changes of the height-integrated Joule heating in Run 2 and Run 3 with respect to Run 1 in the Northern Hemisphere. Figure 4.11(a) clearly shows that the height-integrated Joule heating was enhanced by $4 \sim 5$ mW$/$m^2 near noon when the large-scale FAC variability was included into GITM, which means that the height-integrated Joule heating near the noon was approximately increased by a factor of 5. In addition, the hemispheric-integrated Joule heating increased by $\sim$160% after including the large-scale FAC variability. As for the change associated with the mesoscale FAC

variability, Figure 4.11(b) shows that the maximum enhancement of the height-integrated Joule heating was ~ 1 mW/m^2 near noon, and the hemispheric-integrated Joule heating increased by $\sim$36% associated with the mesoscale FAC variability, suggesting that the contribution of the mesoscale FAC variability to Joule heating was not negligible.

Although the results here may imply that the contribution from the large-scale FAC variability to Joule heating is predominant and more important than that from the mesoscale FAC variability, it should be remembered that the large-scale FAC variability would tend to be smaller if we had defined the averages and standard deviations based on data sets separated into different solar wind conditions and seasons, instead of based on data for all geophysical conditions combined. Therefore, the contribution from the large-scale FAC variability can be better captured and represented in the model simulations once the dependence of the FAC on solar wind condition and season is better specified. In a test where we separated the data into negative and positive IMF B_y conditions (not shown), we found that the locations of dayside maximum large-scale variability shifted in MLT, but that the relative importance of the large-scale variability overall was not much less than that shown in Figure 4.11. Unlike the large-scale variability, the magnitude of the meso-scale variability would not necessarily be reduced by the well-specified solar wind conditions and season owing to its random nature, although the mesoscale variability would likely be found to depend on the geophysical conditions and season. In other words, the magnitude of the mesoscale variability relative to the large-scale variability may change once the conditions are better specified for real event simulations.

The small-scale FAC variability has not been included into GITM in this study, since it is found that small-scale electric field variability is much smaller as compared with large-scale and mesoscale electric field variabilities (Figure 4.6). Therefore, the contributions of the small-scale FAC/electric field to Joule heating are assumed to be trivial. This assumption is supported by previous studies: For example, *Park et al.* (2017) showed that the

small-scale Poynting flux at noon is generally smaller than 0.2 $\mathrm{mW/m^2}$ on average, which is much smaller than the average Joule heating enhancement related to large-scale and mesoscale FAC/electric field variabilities at noon (> 1 $\mathrm{mW/m^2}$, Figure 4.11).

To recapitulate, the large-scale and mesoscale FAC variabilities were included into GITM to examine their impacts on Joule heating. The way how the FAC variability was included is by tuning the separation between the upward and downward variable FACs to get good agreement of the electric field variability between the FAC-driven simulations and the DE-2 observations. Our approach here may indicate another way to include electric field variability into GCMs. Although the spatial separation between the upward and downward variable FACs adopted in this study can lead to good agreement between the simulated electric field variability and our static electric field variability, it is worth noting that such spatial separation may vary with the solar wind condition and season. Therefore, the empirical relationship of the spatial separation with respect to the solar wind condition and season may help extend the application of our approach. In addition, Swarm dual-satellite FAC estimations (e.g., *Ritter et al.*, 2013) which depend on fewer assumptions and therefore more reliable can also benefit the effort of building an empirical relationship. However, building an empirical relationship is beyond the scope of the current study and deserves future study with larger FAC and electric field datasets.

4.2.4 Summary

In this section, we utilized the Swarm single-satellite FAC data and DE-2 electric field data to investigate the FAC and ionospheric electric field and their relationships at different scale sizes. Moreover, the large-scale and mesoscale FAC variabilities were included into GITM to study their impacts on the I-T system. The main findings are summarized as follows:

(1) For both FAC and ionospheric electric field, the large scales dominate the average. However, the variabilities of the two parameters show opposite dependence on scale: the FAC variability increases with decreasing scale size, while the electric field variability decreases with decreasing scale size, indicating that the strong FACs on small scale and mesoscale do not necessarily correspond to strong ionospheric electric field on those scales.

(2) The large-scale and mesoscale FAC variabilities were included into GITM and the corresponding impacts on Joule heating were investigated. It was found that the large-scale FAC variability may significantly increase the Joule heating, especially when the large-scale FAC variability includes that associated with variable solar-wind and seasonal conditions, and that the contribution from the mesoscale FAC variability was not negligible.

4.3 Figures and tables

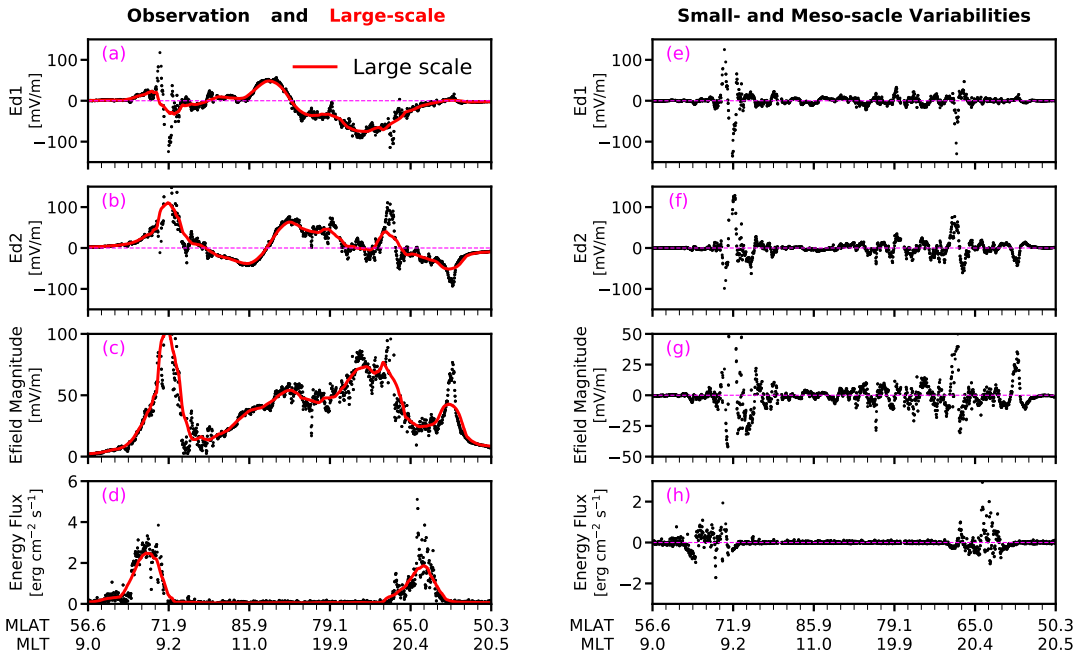

Figure 4.1: (Left): Observations (Black) and large-scale structures (Red, which are averages in a 500-km moving window) of (a) magnetic eastward (E_{d1}) and (b) equatorward (E_{d2}) components of the electric field, (c) the electric field intensity and (d) the electron energy flux along one track on Day 303, 1982; (Right) Small-scale variabilities (which are residuals after subtracting the average from the observation) of corresponding parameters shown in the left column. The UT is in the format of HHMMSS.

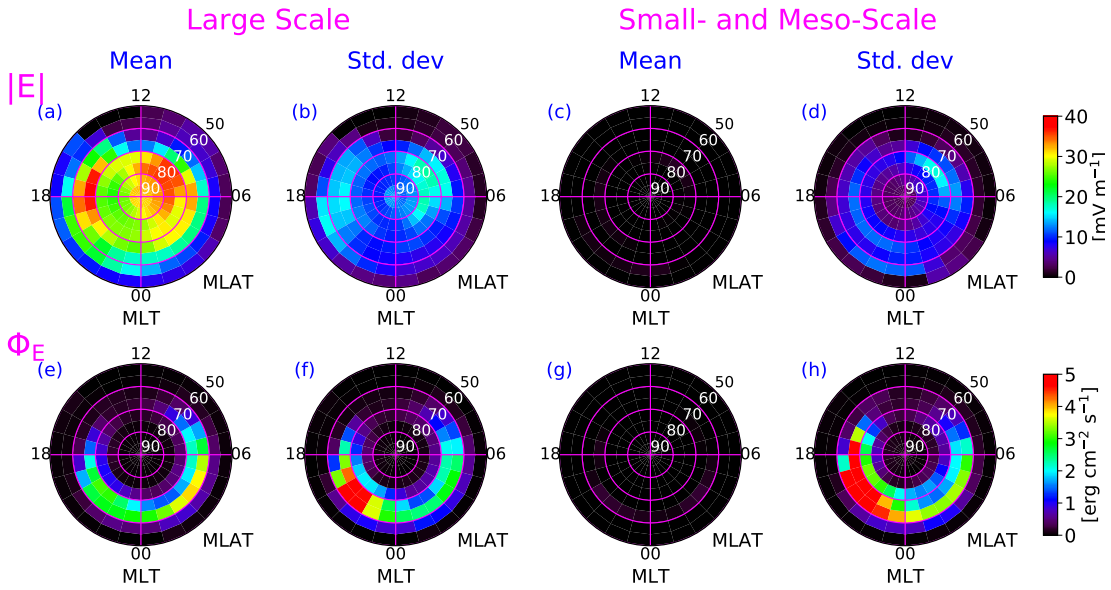

Figure 4.2: (Top) The distributions of the mean and standard deviations of the (a-b) large-scale electric field intensity and (c-d) small-scale variabilities of electric field intensity; (Bottom) The distributions of the mean and standard deviations of the (e-f) large-scale electron energy flux and (g-h) small-scale variabilities of electron energy flux under the condition when IMF clock angle is between 135° and 225°, and IMF B_t ranges from 4-10 nT. All plots are presented as a function of MLAT and MLT.

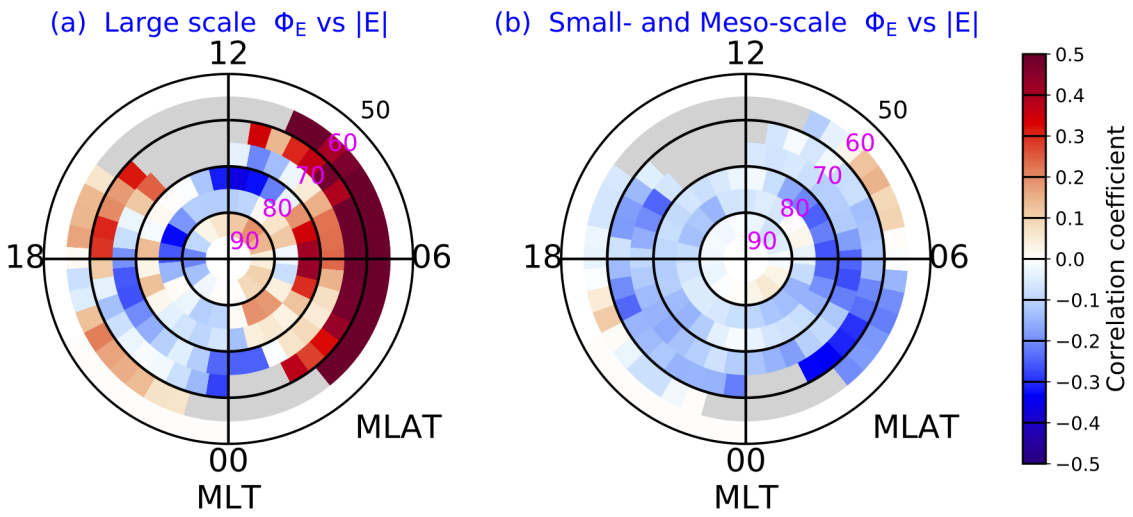

Figure 4.3: The distributions of the linear correlation coefficient (a) between the large-scale electric field intensity and electron energy flux and (b) between small-scale variabilities of electric field intensity and electron energy flux when IMF clock angle is between 135° and 225°, and IMF B_t ranges from 4-10 nT. All plots are presented as a function of MLAT and MLT. The grey shaded areas represent bins without sufficient data.

Run	Average Fields	Large-scale Variability		Small-scale Variability	
		Electric Field	Particle Precipitation	Electric Field	Particle Precipitation
1	✓	✓	✓	—	—
2	✓	✓	✓	✓	—
3	✓	✓	✓	✓	✓

Table 4.1: Summary of small-scale electric field and electron precipitation simulations: The check mark indicates the corresponding quantity is included in GITM, while the dashed line indicates that the corresponding quantity is not included in GITM. Detailed descriptions can be found in text.

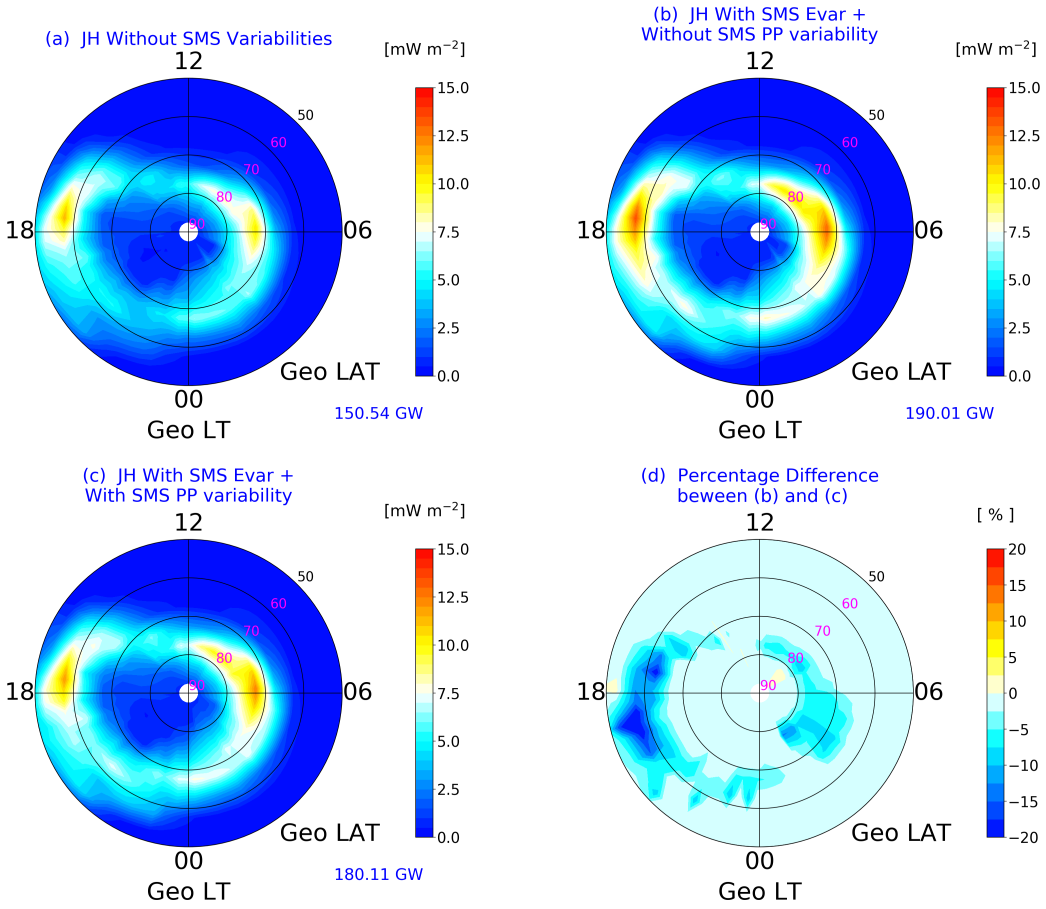

Figure 4.4: (a) Height-integrated Joule heating for the case without small-scale (SMS) variabilities (Run 1); (b) Height-integrated Joule heating for the case including the small-scale electric field variability (Run 2); (c) Height-integrated Joule heating for the case including the small-scale variabilities in both electric field and electron precipitation and the correlation between them has been considered (Run 3), and plots a-c represent the 4-min average of Joule heating outputs between 00:08:00 and 00:12:00, 09/23/2002; (d) Percentage difference between Run 2 and Run 3. The hemispheric-integrated Joule heating is labeled at the bottom right of plots a-c. All plots are presented in geographic coordinates.

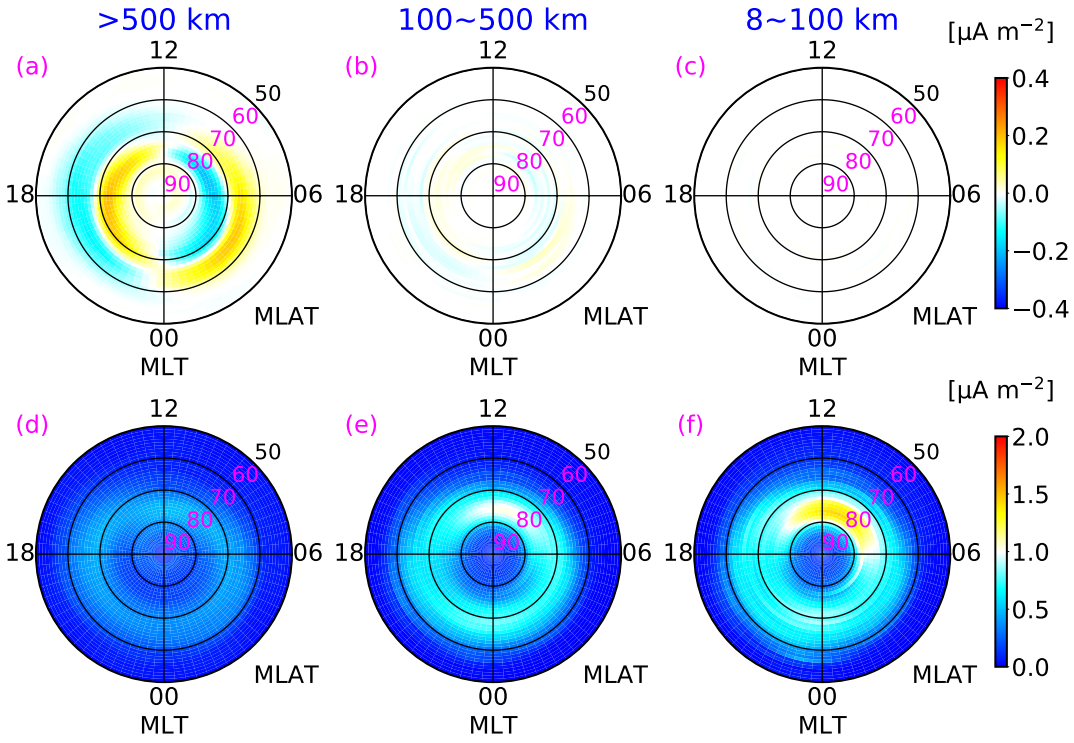

Figure 4.5: Distributions of the (top) average and (bottom) standard deviation of the FAC in each bin on (Left) large scale, (Middle) mesoscale and (Right) small scale. The ranges of the colorbar are -0.4 to 0.4 μA/m^2 for the top row and 0 to 2.0 μA/m^2 for the bottom row, respectively. All plots are presented as a function of magnetic local time and geomagnetic latitude

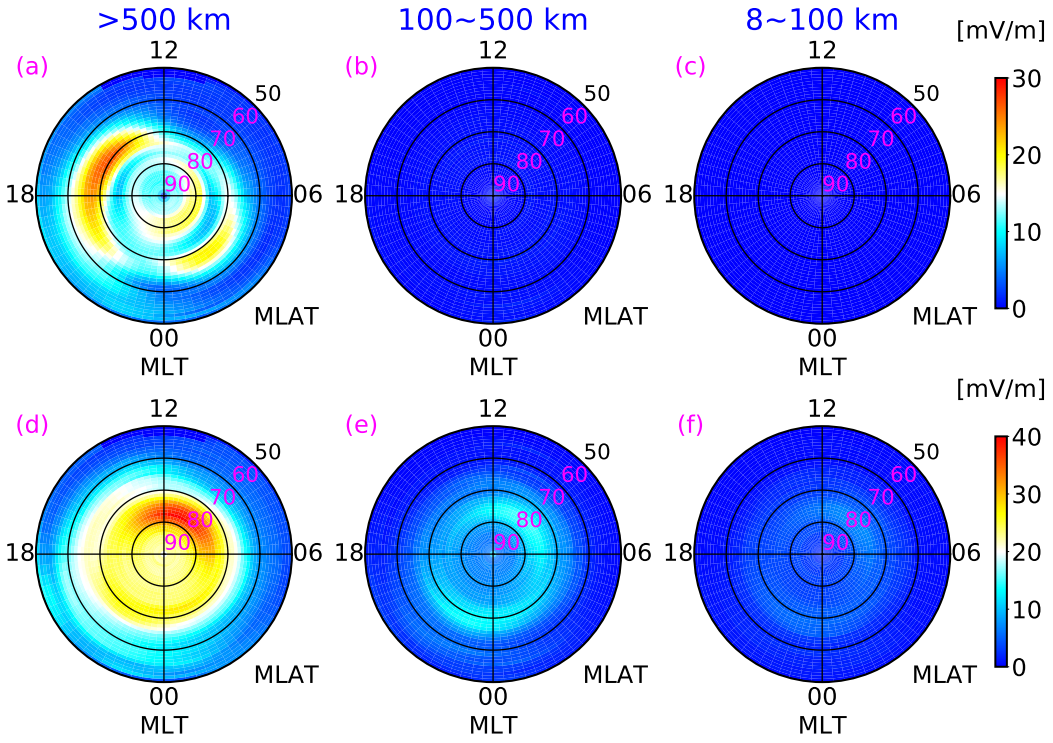

Figure 4.6: Distributions of the magnitude of the (Top) average electric field and (Bottom) electric field variability in each bin on (Left) large scale, (Middle) mesoscale and (Right) small scale. The ranges of the colorbar are 0 to 30 mV/m for the top row and 0 to 40 mV/m for the bottom row, respectively. All plots are presented as a function of magnetic local time and geomagnetic latitude.

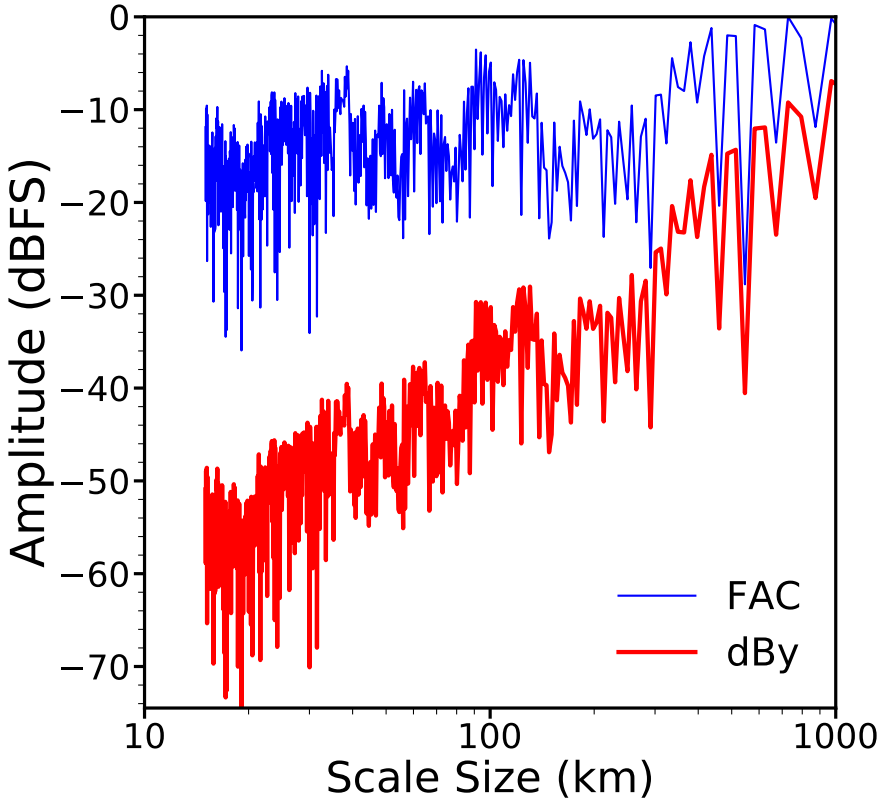

Figure 4.7: The spectra of the FAC (blue) and magnetic perturbation in the east-west direction, dB_y, (red) along one specific Swarm C Northern-hemisphere pole-pass track (UT: 08:02:09 - 08:21:33, 03/17/2015)

Run	Large-scale average FAC	Large-scale FAC variability	Mesoscale FAC variability
1	✓	—	—
2	✓	✓	—
3	✓	—	✓

Table 4.2: Summary of FAC simulations: The check mark indicates the corresponding quantity is included in GITM, while the dashed line indicates that the corresponding quantity is not included in GITM. Detailed descriptions can be found in text.

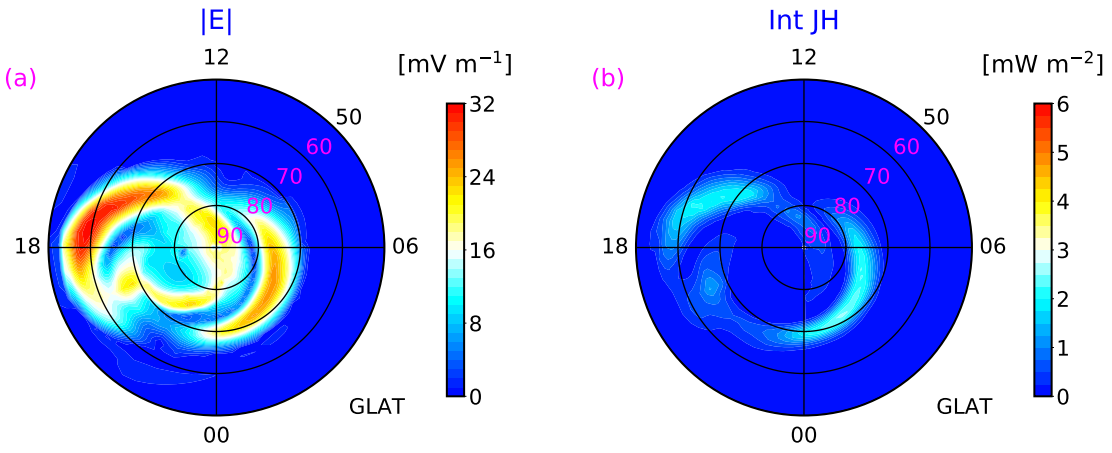

Figure 4.8: (a) Electric field intensity and (b) height-integrated Joule heating from Run 1. All plots are presented in geographic coordinates.

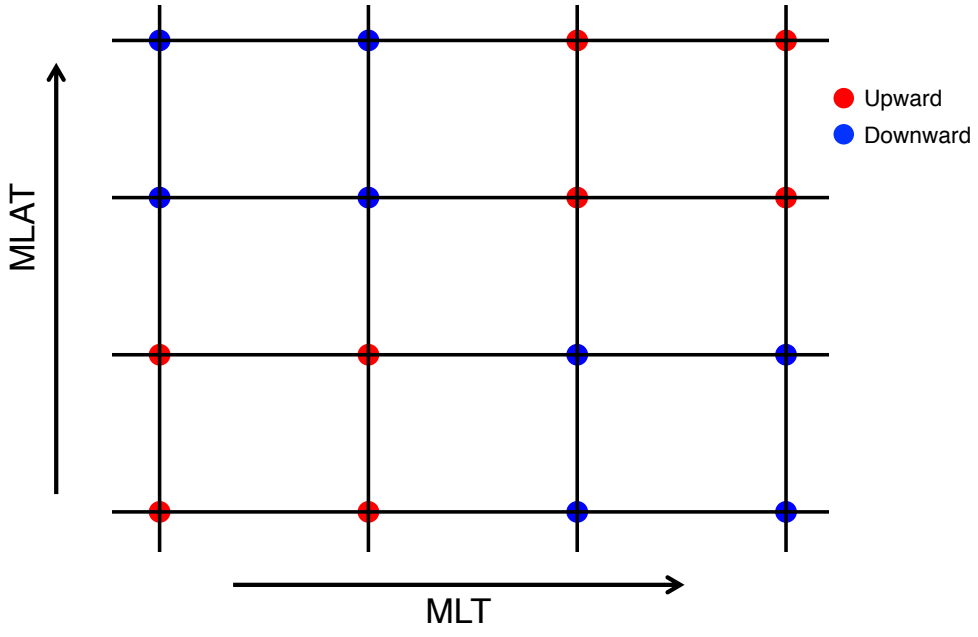

Figure 4.9: Schematic diagram to illustrate the way to include the FAC variability into GITM.

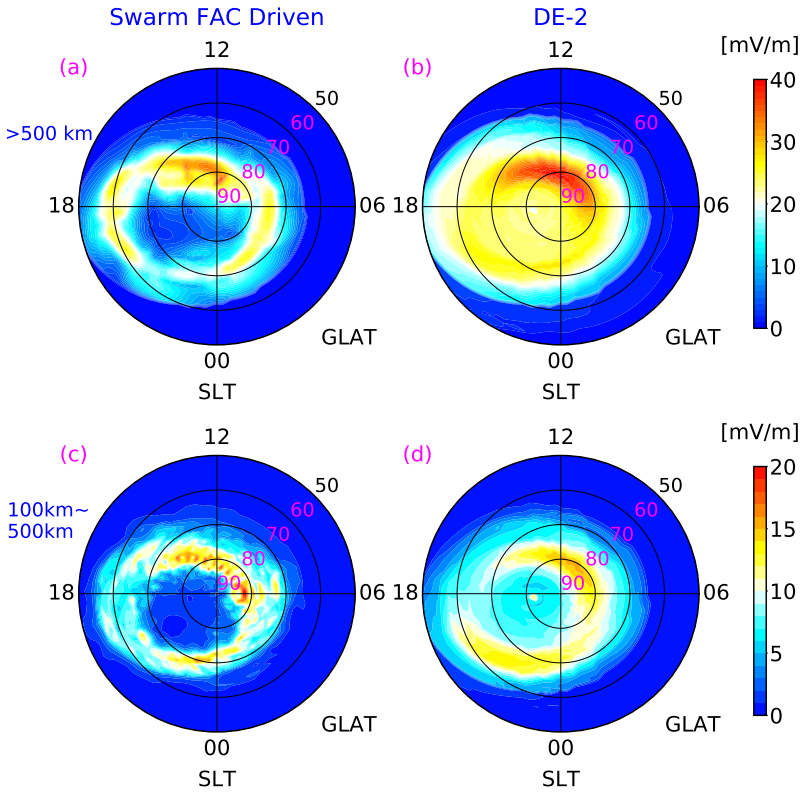

Figure 4.10: Electric field variability (Left) derived from GITM after including the FAC variability and (Right) derived from DE-2 observations on (Top) large scale and (Bottom) mesoscale. All plots are presented in geographic coordinates.

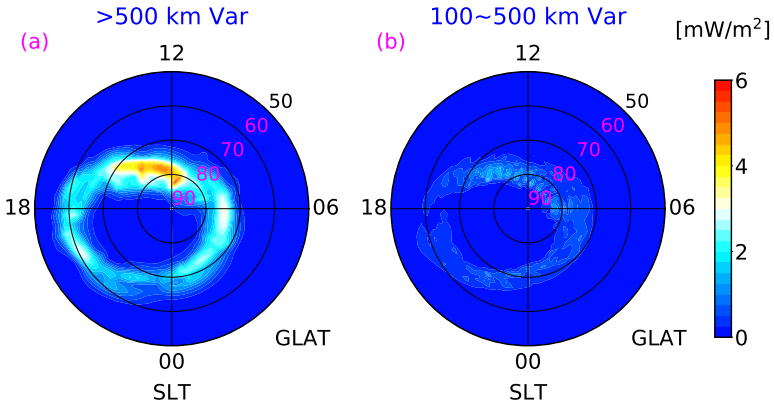

Figure 4.11: Joule heating enhancement after including the (a) large-scale FAC variability and (b) mesoscale FAC variability. All plots are presented in geographic coordinates.

CHAPTER 5

Improvements in high-latitude electrodynamical forcing specifications

In this chapter, improvements in the specification of high-latitude electrodynamical forcings that we have made are introduced. First, a new empirical model, ASHLEY, that can improve specifications of high-latitude electron precipitation and electric field has been developed: The electron precipitation component of ASHLEY, ASHLEY-A, can improve soft electron precipitation specifications in GCMs; In addition, the electric field components, ASHLEY-E and ASHLEY-Evar, can provide consistent large-scale mean electric field and electric field variability. In addition, we have also explored potential improvements in the binning method that can further improve high-latitude electrodynamical forcing specifications apart from including more physics. The remaining part of this chapter is organized as follows: Section 5.1 provides a detailed introduction of the auroral electron precipitation model (ASHLEY-A) component of the ASHLEY model; Section 5.2 investigates impacts of soft electron precipitations on the neutral mass density and satellite drag estimations during a moderate storm; Section 5.3 introduces another two components of the ASHLEY model: electric potential model (ASHLEY-E) and electric field variability model (ASHLEY-Evar); Section 5.4 demonstrates the impacts of binning methods on high-latitude electron precipitation and electric potential patterns; All figures and tables are present in Section 5.5.

5.1 New auroral electron precipitation model: ASHLEY-A

5.1.1 Introduction

In this section, the electron precipitation component of ASHLEY, ASHLEY-A, is present. The first part is the introduction of the data used in this section. Then the methodology of the ASHLEY-A development is present. Next, the general behavior of ASHLEY-A together with the outputs of ASHLEY-A are exhibited. The final part provides a summary of this this section.

5.1.2 Data

The in-situ auroral electron precipitation measurements from DMSP F16-F18 satellites during 2010-2015 are used in this study. All three satellites flew in circular Sun-synchronous orbits at an altitude of $\sim$840 km with an inclination of $\sim$98.8°. The measurements were taken by the onboard Special Sensor for Precipitating Particles, version 5 (SSJ/5), which measures incident electrons and ions from 30 eV and 30 keV every second using 19 logarithmically-spaced energy channels (*Hardy et al.*, 2008; *Redmon et al.*, 2017). The field of view of the SSJ/5 is a 4° by 90° fan ranging from the zenith to the horizon and the 90° field of view is divided into six 15° zones. In this study, we will focus on the electron precipitation and particularly the differential energy fluxes in 19 energy channels. The differential energy flux data are obtained from the dataset created by *Redmon et al.* (2017) and details about the derivation can be found in that paper.

In addition to the DMSP data, the IMF B_y and B_z components as well as solar wind speed (V_{sw}) and plasma density (N_{sw}) are also used. Similar to Section 4.1.2, the IMF transverse component magnitude (B_t) and IMF clock angle (θ_c) are calculated using the IMF B_y and B_z data. The IMF and solar wind data used in this study are 5-min averaged data obtained from Space Physics Data Facility OMNIWeb interface. The averaged B_t, θ_c,

V_{sw} and N_{sw} from 30 minutes prior to the start of the polar passing to 10 minutes prior to the end of the polar passing are calculated and are used to represent the mean IMF and solar wind conditions corresponding to that polar crossing. If the IMF/solar wind data are missing or exhibit large variations, the corresponding polar crossing will not be excluded. Overall, there are $> 10^5$ polar crossings with good data quality used in this study, and the number of trajectories from the Northern Hemisphere (NH) and Southern Hemisphere (SH) are roughly comparable (NH: 53,348; SH: 52,670).

5.1.3 Methodology of the ASHLEY-A development

5.1.3.1 Categorization

Each trajectory is categorized according to two parameters: ε_t and θ_c, where

$$\varepsilon_t = V_{sw}^{\frac{4}{3}} B_t^{\frac{2}{3}} N_{sw}^{\frac{1}{6}} \tag{5.1}$$

ε_t (in the unit of $(\mathrm{km})^{\frac{4}{3}}(\mathrm{s})^{-\frac{4}{3}}(\mathrm{nT})^{\frac{2}{3}}(\mathrm{cm})^{-\frac{1}{2}}$) is essentially the combination of B_t and V_{sw} in the Newell coupling function (*Newell et al.*, 2007) multiplied by $N_{sw}^{\frac{1}{6}}$. As discussed in *Newell et al.* (2007), the term $N_{sw}^{\frac{1}{6}}$ was supposed to be in their coupling function and was omitted on purpose to achieve better correlations with more parameters tested in their study. However, it was found that including the term $N_{sw}^{\frac{1}{6}}$ can slightly improve the correlation with the auroral power (*Newell et al.*, 2007). In addition, it was also found that soft electron precipitations can be affected by N_{sw} (e.g., *Newell and Meng*, 1994). Since the soft electron precipitation is one primary focus of the ASHLEY-A, thus the term $N_{sw}^{\frac{1}{6}}$ is kept.

A mirror correction (i.e., $\theta_c' = 360° - \theta_c$) has been applied for SH trajectories in order to account in the different impacts of the IMF B_y component on high-latitude electrodynamic forcings in different hemispheres. Since the magnetic local time (MLT) coverages of DMSP F15-F18 satellites in NH and SH are limited, trajectories from both hemispheres are combined together in order to achieve the best MLT coverage. Meanwhile, trajecto-

ries from all seasons are combined together in this study to best maintain the number of categories and the data amount in each category in order to achieve statistical meaningful results in this study. In the future, the seasonal dependence will be added in the models if more data become available.

For trajectories with good electron precipitation data, all trajectories of which ε_t is smaller than 3000 (roughly corresponds to the IMF $B_t < 1$ nT case under normal solar wind conditions) are categorized as one category regardless of θ_c. Other trajectories with $3000 < \varepsilon_t < 30000$ are sorted into 8 ε_t bins and 8 θ_c bins (i.e., $8 \times 8 + 1 = 65$ categories in total). The 360° span of θ_c is evenly divided into 8 bins with each centered at a multiple of 45°. An upper boundary of 30000 is set for ε_t to exclude a small amount of trajectories (<1%) under very extreme IMF and solar wind conditions. Table 5.1 summarizes the boundaries and medians for different ε_t bins.

5.1.3.2 Binning and fitting

For each category, the differential energy flux data in each energy channel (19 energy channels in total) are binned according to their MLTs and magnetic latitudes (MLATs). The sizes of the MLT and MLAT bins are 1 hour and 1°, respectively. Then the average of the differential energy flux in each bin (if has more than 100 data) is calculated. The subsequent steps are to fill the data gaps at noon and midnight by applying a linear interpolation according to values in the adjacent bins and to smooth the distribution in MLT and MLAT directions.

With the smoothed averaged pattern of the differential energy flux in each energy channel, the next steps are to capture the MLT and IMF clock angle dependences of the

differential energy flux in each latitudinal bin: First, the differential energy flux (J_E) at each latitudinal bin is fitted to a sixth-order Fourier series, having the form:

$$J_E = \sum_{n=0}^{6} \left(A_n \cos\left(\frac{MLT}{12} n\pi\right) + B_n \sin\left(\frac{MLT}{12} n\pi\right)\right). \tag{5.2}$$

The maximum order of 6 is determined after trial-and-error tests, where it has been found that a higher-order Fourier series would not improve the fitting results yet will introduce unrealistic small-scale structures. After the MLT fitting, the Fourier coefficients A_n and B_n (n=0-6) in Eq. 5.2 are fitted to a fourth-order Fourier series constructed by the IMF clock angle to capture IMF clock angle variations, i.e.,

$$A_n(or\ B_n) = \sum_{n=0}^{4} \left(C_m \cos(m\omega) + B_n \sin(m\omega)\right), \tag{5.3}$$

where $\omega = \frac{\theta_c}{180^\circ}\pi$. In order to implement a fourth-order fitting, the Fourier coefficients A_n and B_n Eq. 5.2 are interpolate at the multiples of $\frac{\pi}{8}$ (original A_n and B_n are at the multiples of $\frac{\pi}{4}$).

5.1.3.3 Extrapolation

Since the range of ε_t used in this study is limited, extrapolations are needed to obtain electron precipitation patterns at large ε_ts. The extrapolations are done by tracking the hemispheric-integrated differential energy flux evolutions in different channels. Figure 5.1 shows the hemispheric-integrated differential energy fluxes in 19 energy channels and in the 8 ε_t bins with $\varepsilon_t \geq 3000$ when $202.5^\circ < \theta_c < 247.5^\circ$. The x-axis locations of the dots shown in each plot correspond to median ε_ts listed in Table 5.1. As shown in Figure 5.1, the hemispheric-integrated differential energy fluxes in the highest 11 energy channels (central energy >500 eV) approximately linearly increase with ε_t, while the hemispheric-integrated differential energy fluxes tend to increase quadratically with ε_t in the lowest 8

energy channels. Similar trends can also be found in other θ_c bins although the rates might be different.

The trends shown in Figure 5.1 are used to extrapolate the hemispheric-integrated differential energy in each energy channel when ε_t is larger than 22770. For the highest 11 energy channels, the hemispheric-integrated differential energy flux is assumed to be a linear function of ε_t in each channel, i.e., $y = k\varepsilon_t + b$, where k and b are obtained according to the best-fit lines shown in Figure 1 and are functions of θ_c. For the lowest 8 energy channels, the hemispheric integrated differential energy flux in each channel for a given ε_t (ε_{in}) can be calculated by the increase rate of the hemispheric integrated differential energy flux in the largest two ε_t bins (k_8) and the hemispheric integrated differential energy flux in the largest ε_t bin (y_8) at the given θ_c, i.e., $y = y_8 + k_8(\varepsilon_{in} - 22770)$. Although such method may underestimate <500 eV electron precipitations for a very large ε_t than a quadratic extrapolation, this method can at least provide a lower limit for <500 eV electron precipitations at a large ε_t since the data coverage at a large ε_t is sparse.

5.1.3.4 Expansion of the auroral oval

Since the auroral oval expands equatorward with the increasing geomagnetic activity (e.g., *Feldstein and Starkov*, 1967), so the expansion of the auroral oval is also taken into account. Figure 5.2 shows the co-MLATs (r_1) of the poleward auroral boundaries (PABs) identified using the technique developed by *Kilcommons et al.* (2017) on dawn (4-8 MLT) and dusk (16-20 MLT) sides as a function of ε_t when $157.5° < \theta_c < 202.5°$. Clearly, the PAB becomes more equatorward as ε_t increases. To obtain the location of the PAB at a large ε_t, it is assumed that r_1 is a linear function of β, i.e., $r_1 = \alpha_1\beta + \alpha_2$, where

$$\beta = \frac{\varepsilon_t}{\sqrt{1 + \left(\frac{\varepsilon_t}{\varepsilon_{inf}}\right)^2}}. \tag{5.4}$$

The reason why r_1 is assumed to have such formate is to take the saturation of the polar cap area for intense solar wind and IMF conditions (e.g., *Ridley and Kihn*, 2004; *Merkin and Goodrich*, 2007) in account, and those studies suggested that the radius of the polar cap approximately saturates at around co-MLAT=21°. However, the PAB is found to be $\sim$ 1°-2° equatorward of the convection reversal boundary (CRB) on dawn and dusk sides when the IMF B_z is southward (Section 5.4), and the CRB is a good indicator of the polar cap boundary on dawn and dusk sides when the IMF B_z is southward (*Sotirelis et al.*, 2005). Therefore, ε_{inf} is set to 20000 so that r_1 saturates at co-MLAT=23° (red thick line in Figure 5.2), which is 2° equatorward of the predicted saturation radius of the polar cap boundary. The same procedure is repeated for other IMF clock angle bins using same $\varepsilon_{inf} = 20000$.

With the predicted r_1, the expansion rate (er_1) of the PAB can be calculated, which can be expressed as: $er_1 = \dfrac{r_{11}}{r_{10}} - 1$. Here, r_{11} and r_{10} are the co-MLATs of the PAB at ε_{in} and $\varepsilon_t = 22770$ ($\varepsilon_{in} \geq 22770$), respectively. A careful check of er_1 at several large ε_ts suggests that er_1 at a given θ_c (θ_{in}) is roughly equal to er_1 at $\theta_c = 180°$ multiplied by a factor of $\sin^2(\omega/2)$, where $\omega = \dfrac{\theta_{in}}{180°}\pi$. Therefore, er_1 is used to capture the expansion of the auroral oval, which is expressed as: $er_1(\theta_{in},\ \varepsilon_{in}) = er_1(180°,\ \varepsilon_{in})\sin^2(\omega/2)$.

5.1.3.5 Reconstruct the differential energy flux pattern at given inputs

To reconstruct the different energy fluxes in 19 energy channels for angy given ε_{in} and θ_{in}, the procedure described below is adopted: The first step is to determine which of the following three cases applies: 1) $\varepsilon_{in} < 2579$; 2) $2579 \leq \varepsilon_{in} < 22770$; 3) $\varepsilon_{in} \geq 22770$. If it is the first case, then coefficients corresponding to the Cat-0 pattern are used to reconstruct the Cat-0 pattern; If it is the second case, then the two closet median values of ε_t listed in Table 5.1 are determined, namely ε_i and ε_{i+1} ($0 \leq i \leq 7$). Then, coefficients corresponding to the Cat-i and Cat-(i+1) patterns are used to generate the Cat-i and Cat-(i+1)

patterns at θ_{in}. The two patterns are combined according to their corresponding weights, w_i and w_{i+1}, where $w_i = \frac{\varepsilon_{i+1} - \varepsilon_{in}}{\varepsilon_{i+1} - \varepsilon_i}$ and $w_{i+1} = 1 - w_i$. Otherwise, coefficients corresponding to the Cat-8 pattern are used to reconstruct the Cat-8 pattern at θ_{in}. Meanwhile, the expansion rate is calculated and the Cat-8 pattern is expanded according to the expansion rate. Furthermore, the differential energy flux at each energy channel is extrapolated to obtain the predicted hemispheric-integrated differential energy flux at ε_{in} according to the procedures described in Section 5.1.3.3.

5.1.4 Comparisons between measured and modeled data

To examine the general reliability of the empirical models developed in this study, the modeled results along all polar crossings used in the model development are calculated under their corresponding IMF and solar wind conditions. The modeled and measured data in each $\varepsilon_t - \theta_c$ category are binned according to their MLATs and MLTs, and binning results of modeled and measured data are compared. The sizes of the MLT and MLAT bins are 1 hour and 1°, respectively. Figure 5.3 compares distributions of integrated energy flux of >500 eV and <500 eV electrons under low and high solar wind and IMF conditions. Clearly, the binning results of modeled data are similar to the binning results of measurements. Moreover, Figure 5.4 compares the differential energy fluxes in 19 energy channels in all MLAT-MLT bins and from all categories. In general, the binning results of the modeled data are comparable with those of the measured data since all the grey dots shown in Figure 5.4 are concentrated around the y = x lines (blue-dashed lines) and the best-fit lines (red-thick lines) according to the grey dots are not significantly deviated from the y = x lines. Therefore, the ASHLEY-A is well-behaved in capturing large-scale electron precipitation patterns in different energy channels.

5.1.5 Results: Model outputs

Figure 5.5 shows the ASHLEY-A outputs of the directional differential energy fluxes in 19 energy channels when the IMF is purely southward (the IMF $B_z = -8$ nT, $V_{SW} = 450$ km/s and $N_{SW} = 5$ cm^{-3}). It is clear that >500 eV electrons are mainly distributed on the night side while <500 eV electrons are more likely to precipitate on the day side and are located at higher MLATs than >500 eV electrons, which is consistent with results shown in *Hardy et al.* (1985). Meanwhile, a salient peak can be found near the magnetic noon and between 70° - 75° MLAT in channels with their central energies around 100 eV. The peak location indicates the location of the dayside cusp since the precipitating electrons in the cusp typically have the average energy around 100 eV (*Newell and Meng*, 1988).

Figure 5.6 compares differential energy fluxes in three energy channels when IMF is purely northward, eastward, westward and southward (the IMF $B_t = 8$nT, $V_{SW} = 450$ km/s and $N_{SW} = 5$ cm^{-3}). For >1 keV electrons, the precipitation is most intense and equatorward for the southward IMF case and weakest and most poleward for the northward IMF case. Meanwhile, there is no significant difference in the differential energy flux when the direction of the IMF B_y direction is flipped. However, for electrons with the energy around 100 eV, although the location of the dayside peak is most equatorward when the IMF is southward, the peak magnitude is the weakest in comparison with other IMF clock angle cases. Instead, the dayside peak has the largest magnitude and MLT extension when the IMF is purely northward. Moreover, the location of the dayside peak found in soft electrons appears to depend on the IMF B_y polarity. The peak location tends to shift to the dawn side as the IMF B_y becomes more negative, indicating that the cusp tends to shift to the dawn side as the IMF B_y becomes more negative This is consistent with previous studies (e.g., *Candidi et al.*, 1983; *Newell et al.*, 1989). It has been found that the cusp is more likely to

be located in the post-noon when the IMF B_y is positive than the case when the IMF B_y is negative, , which is similar to what is shown in the right column of Figure 5.6.

Figure 5.7(a) serves as an example to illustrate how the modeled energy spectrum is deviated from a Maxwellian spectrum determined from the total energy flux and average energy. The total energy flux and average energy at different locations can be calculated from the spectrum by using Eq. 2 in *Robinson et al.* (1987), and the lower and upper boundaries of the integral in both numerator and denominator of that equation are 500 eV and 30 keV, respectively. The IMF and solar wind conditions are: $B_y = 0$, $B_z = -8$ nT, $V_{SW} = 450$ km/s, $N_{SW} = 5$ cm^{-3}, and the location is on the dawn side (MLT = 4.5 h, MLAT = 64.5°). For the spectrum shown in Figure 5.7, $Q_0 = 4.87$ mW/m^2 and $\overline{E}$ = 5.08 keV. In general, the Maxwellian spectrum overestimates the keV electrons and underestimates both <1 keV and >10 keV electrons. Specifically, the Maxwellian spectrum remarkably underestimates <1 keV electron precipitations and the difference can be approximately 2 orders in the magnitude at ∼100 eV, so that the contribution of soft electron precipitations to the I-T system can be significantly underrated if a Maxwellian energy spectrum is assumed.

5.1.6 Discussion

5.1.6.1 Similarities and differences with previous empirical models

Hardy et al. (1985) established distributions of the average spectrum in 7 Kp bins (Kp range: 0-6) based on 2.5 years of DMSP SSJ3 measurements. Although quantitative comparisons between statistical results from two different solar cycles and two different versions of SSJ may not be meaningful, our results are qualitatively consistent with *Hardy et al.* (1985). However, the Kp index is a low-resolution geomagnetic index, which may not be suitable to capture the dynamic changes of the auroral precipitation when the IMF

and solar wind conditions are quite dynamic. Moreover, the IMF and solar wind conditions can be considerably different even the Kp index is the comparable, which may not well capture the electron precipitation under a specific condition. For example, a $+B_y$ case probably gives a very similar Kp as a $-B_y$ case as long as the magnitude of By and solar wind conditions are similar (*Newell et al.*, 2008). However, as shown in Figure 5.6, the differences in the soft electron precipitation is significant although differences in the keV electrons are trivial. Therefore, the soft electron precipitation specifications precipitation may not well specified in the statistical patterns built by *Hardy et al.* (1985). In addition, ASHLEY-A can provide distributions of the average energy spectrum under intense IMF and solar wind conditions based on reasonable extrapolations and expansions, therefore the ASHLEY-A can be useful in studying the storm-time I-T system when coupling into GCMs.

The Ovation Prime (OP) models developed by *Newell et al.* (2009) and *Newell et al.* (2014) show some improvements in the energy spectrum specification of the electron precipitation. The major characteristic of the OP models is that they provides the total energy flux, total number flux and probability of three types of electron precipitation with different energy spectra: diffuse, mono-energetic and broadbands. However, there could be a large uncertainty in the identification of the precipitation type (*Wing et al.*, 2019). For example, as pointed out by *Wing et al.* (2019), it is highly possible that an energy spectrum matches none of the above three types and is labeled as the diffuse type (Maxwellian spectrum) for simplicity and convenience, so that the Maxwellian-type may still dominate in the OP models. Moreover, the Newell coupling function does not distinguish the IMF B_y polarity either. Furthermore, all parameters in the OP models are assumed to be a linear function of the Newell coupling function, but as implied by Figure 5.1, a linear function may underestimate the evolution of $<$500 eV electrons. Therefore, the contribution of the soft electron precipitation may still not be accurately estimated in the OP models.

5.1.6.2 The low-energy tail

The strong low-energy tail shown in Figure 5.7 is frequently seen in observations (e.g., *Evans*, 1974; *Evans and Moore*, 1979; *Hardy et al.*, 1985; *Fung and Hoffman*, 1988; *Wing et al.*, 2019) and its sources are considerably complex since the electron precipitation is not a simple one-way transport of electrons from the magnetosphere to the ionosphere. For example, if a field-aligned potential drop is present, the upgoing electrons without sufficient kinetic energy to overcome such potential drop will be reflected downward and subsequently are observed as downward precipitation flux (e.g., *Evans*, 1974; *Evans and Moore*, 1979; *Richards*, 2013). In addition, it is also possible the upgoing superthermal electrons from the conjugate hemisphere can also contribute to the low-energy tail (e.g., *Khazanov et al.*, 2014). The measured downward precipitation flux can contribute to the ionization of the thermosphere at F-region altitudes increasing the F-region conductivities although may not significantly change the height-integrated conductivities. The impacts of soft electron precipitations on the I-T system will be more comprehensively investigated in the future by coupling the ASHLEY-A to a GCM.

Meier et al. (1989) have developed an empirical formula (hereafter, M89 formula) to account for the low-energy tail which was later used in *Strickland et al.* (1993). The blue dashed line in Figure 5.7(b) indicate the spectrum constructed by the M89 formula using $Q_0 = 4.87$ mW/m^2 and $\overline{E} = 5.08$ keV (hereafter, M89-I spectrum). Although the low-energy tail has been significantly improved in contrast to a simply Maxwellian spectrum, the magnitude of the low-energy tail is underestimated by 50% in general. However, the M89 formula is based on the total energy and average energy from *Hardy et al.* (1985), which are calculated by using the whole energy spectrum, while the total energy and average energy from the ASHLEY-A are calculated by use the >500 eV portion of the energy spectrum. Hence, if the whole energy spectrum shown in Figure 5.7(a), $Q_0^{'} = 5.01$ mW/m^2

and $\overline{E}^{'} = 2.92$ keV.and the corresponding spectrum calculated from the M89 formula is indicated by the green dashed line in Figure 5.7(b) (hereafter, M89-II spectrum). It is clear that the calculated low-energy tail by using $Q_0^{'}$ and $\overline{E}^{'}$ is more comparable with the averaged spectrum from the ASHLEY-A than that using Q_0 and $\overline{E}$. However, the discrepancies of 1-10 keV electrons the M89-II spectrum and the ASHLEY-A energy spectrum are larger than those between the M89-I spectrum and the ASHLEY-A energy spectrum, which are a general case in the auroral oval although may vary quantitively at different locations (not shown). Therefore, the ionospheric conductances may be significantly overestimated when the M89-II spectrum is utilized to drive a GCM. The calculation of the ionospheric conductances when using the Maxwellian spectrum determined by the total energy flux and average energy of the whole energy spectrum may be inaccurate, which has been previously pointed out by *Robinson et al.* (1987). Therefore, it might be necessary to propose a new empirical formula for the incident electron energy spectrum in order to obtain the I-T response at both E-region and F-region altitudes correctly.

5.1.6.3 Future improvements

With more available data, the seasonal effects can be accounted in the ASHLEY-A. In addition, instead of combining IMF magnitude, solar wind speed and number density into one parameter, the electron precipitation can be studied in more specific conditions, which may further the specification of soft electron precipitations. Furthermore, a boundary-oriented binning technique can be utilized instead of the static-binning method utilized in this section, which may help resolving the smoothing issue caused by the traditional static-binning method (see Section 5.4) .

5.1.7 Summary

In this section, based on 6 years of the DMSP electron precipitation measurements, a new empirical electron precipitation model (ASHLEY-A) is developed. The ASHLEY-A can directly provide the averaged directional differential energy flux in 19 DMSP energy channels under different IMF and solar wind conditions without making any assumptions about the energy spectrum. Hence, soft electron precipitation specifications can be remarkably improved. The ASHLEY-A outputs indicate that the distributions of $>$500 eV and $<$500 eV electrons can be significantly different, where $>$500 eV electrons mainly precipitate on the night side whereas $<$500 electrons mainly precipitate on the day side. Moreover, the distributions of the differential energy flux displays a salient peak near the local noon in channels with their central energy around 100 eV, which indicates the location of the dayside cusp. Furthermore, the impact of the IMF B_y polarity on the electron precipitation is also taken into account in the ASHLEY-A, which is most predominant for soft electron precipitations.

5.2 Impacts of soft electron precipitations on the neutral density and satellite drag during the 28-29 May 2010 geomagnetic storm

5.2.1 Introduction

While several simulation studies have been carried out to evaluate the influence of soft electrons on the F-region neutral density and have found that soft electron precipitation can effectively increase the F-region neutral density (e.g., *Deng et al.*, 2013; *Zhang et al.*, 2012, 2015b; *Brinkman et al.*, 2016), most of those studies either were idealized studies or only introduced soft electron precipitation in limited regions (e.g., the cusp region). Therefore, and it still remains unclear the overall impacts of soft electron precipitation

on the whole I-T system during geomagnetic storms owing to inadequate knowledge of the global distribution of soft electron precipitation. The ASHLEY-A developed in the previous section can provide better global specifications of soft electron precipitations, making it a suitable tool to address this question. In this section, the ASHLEY-A model was coupled with the GITM and the simulation results were compared with those from the default GITM run as well as measurements from the GOCE satellite during the May 28-29, 2010 geomagnetic storm in order to evaluate how the neutral density and therefore satellite drag estimations during a geomagnetic storm can be improved by improving global soft electron precipitation specifications in GCMs. Moreover, since empirical thermospheric density models play an important role in satellite operations and debris monitoring (e.g., *Emmert*, 2015), neutral density variations from a public accessible empirical thermospheric density model developed by *Bowman et al.* (2008, hereafter JB2008) were also compared with measurements and GITM simulations to examine its performance in estimating neutral mass density and satellite drag during the same event. In the remaining part of this section, a brief introduction of the JB2008 model is provided followed by a short summary of the geophysical condition of the May 28-29, 2010 geomagnetic storm. The results and discussion are presented subsequently. The final part summarizes the primary findings of this section.

5.2.2 JB2008 model

The JB2008 model was developed based on multiple data sources including direct density measurements and model outputs from previous empirical models (*Bowman et al.*, 2008). In comparison with its earlier versions, new solar indices are used to drive the model. In addition, the JB2008 model can better describe the semi-annual variation of the neutral density. Furthermore, the JB2008 model replaces the older Ap index (3-h resolution) with the Dst index (1-h resolution) to improve its geomagnetic activity driver. It has been shown

that those improvements can significantly reduce errors in the neutral density estimation (*Bowman et al.*, 2008).

5.2.3 Geophysical Conditions During the May 28-29, 2010 Geomagnetic Storm

Variations of the interplanetary magnetic field (IMF), solar wind and SYM-H index during this event are shown in Figures 5.8(a)-5.8(d). Prior to the arrival of the corona mass ejection (CME) at ∼03:15 UT on 05/28/2010, the IMF B_y and B_z components and the solar wind were relatively steady. After the arrival of the CME, the IMF B_y and B_z components had strong oscillations and the solar wind speed and dynamic pressure increased significantly. At around ∼21:00 UT on 05/28/2010, a magnetic cloud arrived at bow shock as indicated by the decreased solar wind speed and dynamic pressure. During the passage of the magnetic cloud, the IMF turned southward gradually and the period with a consistent southward IMF B_z lasted for ∼23 hours. The SYM-H index reached its minimum (-74 nT) at ∼13:00UT on 05/29/2010, indicating the May 28-29, 2010 event was a moderate geomagnetic storm (*Gonzalez et al.*, 1994).

5.2.4 Results and Discussion

Figure 5.8(e) compares the ASHLEY-A hemispheric power (HP) with NOAA HP during the May 28-29, 2010 event, where the ASHLEY-A HP was calculated by by integrating the total energy flux above 45° MLAT. Details about calculations of the total energy flux and average energy are described in Section 5.1. It is clear that the ASHLEY-A HP and NOAA HP showed similar trends during this event while the ASHLEY-A HP was ∼40% smaller than the NOAA HP on average during 7-17 UT on 05/29/2010, which is likely due to the fact that the NOAA HP is calculated from both the empirical model and observations whereas the ASHLEY-A HP is a direct model output. Therefore, in order to be keep the total energy flux into GITM comparable in different simulations as will be described later,

the outputted differential energy fluxes in 19 energy channels from the ASHLEY-A model are scaled by the ratio between the NOAA HP and the original ASHLEY-A HP every time step when the electron precipitation in GITM is specified by the ASHLEY-A model.

Figure 5.9(a) shows the evolution of the neutral mass density measured by the GOCE satellite during the May 28-29, 2010 event. The 10-s data are shown as the grey line and the black dotted line denotes the variation of the orbital averaged (90-min averaged) neutral mass density. The peak orbital average neutral mass density during the passage of the CME (03:15 UT, 05/28/2010 - 20:30 UT, 05/29/2010) was $\sim 2.83 \times 10^{-11}$ kg/m^3, which was $\sim$102% higher than the pre-CME baseline ($\sim 1.4 \times 10^{-11}$ kg/m^3).

The simulation results along the GOCE orbit during the May 28-29, 2010 event are shown in Figures 5.9(b) and 5.9(c), following the same format as Figure 5.9(a). Figure 5.9(b) displays results from the default run where the electron precipitation in GITM is specified by the *Fuller-Rowell and Evans* (1987) model (hereafter Run 1), and Figure 5.9(c) shows results from the run when the electron precipitation in GITM is specified by the ASHLEY-A model (hereafter Run 2). The spatial resolution for both simulations was 5° in longitude by 1° in latitude and 1/3 of the scale height in altitude, and both Run 1 and Run 2 were conducted after a 24-h pre-run. The electric potential in GITM is specified by the *Weimer* (2005) model. Figure 5.9(d) further compares orbital averaged neutral mass densities from the observations and GITM simulations during the May 28-29, 2010 event. Although the orbital averaged neutral mass density in both Runs 1 and 2 underwent a large enhancement during the passage of the CME, the enhancement with respect to the pre-CME baseline was better estimated in Run 2 than Run 1. The results from Run 1 were consistently underestimated ($\sim$10-15%) as compared with the GOCE observations during the CME passage while the results from Run 2 were more comparable with the observation than those from Run 1 (Figure 5.9(d)).

It is clear that the different electron precipitation specifications were responsible for the different neutral mass density evolutions between Runs 1 and 2. However, differences in the electron precipitation between Runs 1 and 2 involved not only differences in the soft electron but also differences in distributions of the total energy flux and average energy. Figures 5.10(a) and 5.10(b) show the total energy fluxes from Runs 1 and 2 at 12:00 UT on 05/29/2010, and there were noticeable differences in the distribution of the total energy flux despite modest differences in the hemispheric integrated energy flux. Figure 5.10(c) further compares the energy spectra of the electron precipitation at a location on the dawn side (local time: 06:10; geographic latitude: 54.5° N) between Run 1 (Blue) and Run 2 (Red). In addition to significant differences in the low-energy portion, differences in the total energy flux (Q_0) and average energy ($\overline{E}$) are were nontrivial (Run 1: $Q_0 = 7.6$ mW/m^2, $\overline{E} = 3.5$ keV; Run 2: $Q_0 = 9.12$ mW/m^2, $\overline{E} = 4.27$ keV). The question then arises as to whether differences in distributions of the total energy flux and average energy played an important role in causing large differences in the evolution of the neutral mass density between Runs 1 and 2. To address this question, an additional run (Run 3) has been carried out, where, instead of using the outputted spectra from the ASHLEY-A model to drive GITM like that in Run 2, the Maxwellian spectra determined by the total energy flux and average energy from the ASHLEY-A model were used to drive GITM. For example, the orange dots in Figure 5.10(c) indicate the Maxwellian spectrum constructed by using the total energy flux and average energy from Run 2 at the same location (Details about the total energy flux and average energy can be found in Section 5.1). It is worth noting that horizontal distributions of the total energy flux, average energy and HP inputs in Run 2 and Run 3 were essentially the same and the only difference between Run 2 and Run 3 was the incident electron energy spectrum specification (Non-Maxwellian vs Maxwellian). The evolution of the orbital averaged neutral mass density along the GOCE orbit from Run 3 is shown in Figure 5.9(d) as the orange triangle line, which is almost the same as that from

Run 1, indicating differences in distributions of the total energy flux and average energy between the *Fuller-Rowell and Evans* (1987) and ASHLEY-A models were not the major causes for the distinctly different neutral mass density variations between Run 1 and Run 2. Rather, it is the vastly stronger soft electron precipitation as shown in Figure 5.10(c) that primarily led to significantly higher neutral mass density in Run 2. The stronger soft electron precipitation produced greater ionizations in the F-region, which increased the F-region conductivity. Hence, more Joule heating was deposited in the F-region and the neutral mass density was enhanced in the F-region (e.g., *Deng et al.*, 2011, 2013; *Zhang et al.*, 2012, 2015b).

Apart from GITM simulations, the results from the JB2008 model have also been compared with observations, which are shown in Figure 5.11(a). Note here the JB2008 outputs were scaled by a factor of 0.8 to ensure the pre-CME baseline was comparable with that from the observation. It is clear that the orbital averaged neutral mass density from the JB2008 model underwent two obvious bumps (up to 30%) on May 28, 2010, which were not shown in the observation. On May 29, 2010, the orbital averaged neutral mass density from the JB2008 model continuously increased before reaching its maximum ($\sim 2.5 \times 10^{-11}$ kg/m^3) at $\sim$15:00 UT then decreased afterwards. When compared with observations, the peak magnitude of the orbital averaged neutral mass density from the JB2008 model was $\sim$12% smaller and the peaking time was $\sim$4 h earlier, indicating that the JB2008 model did not well capture the density variation during the May 28-29, 2010 geomagnetic storm.

Finally, the estimations of the satellite drag effect from different simulations during the May 28-29, 2010 event are compared in Figure 5.11(b). Similar to previous studies (e.g., *Anderson et al.*, 2009; *Chen et al.*, 2012; *Oliveira and Zesta*, 2019), a parameter proportional to the time integral of the neutral mass density was used to evaluate the cumulative effect of the satellite drag. Figure 5.11(b) compares the track-integrated neutral mass

densities calculated from observations, Run 1, Run 2 and the JB2008 model after 00:00 UT on May 28, 2010, where the track-integrated neutral mass density is the time integral of the neutral mass density multiplied by the satellite velocity ($\sim$7.5 km/s). The track-integrated neutral mass density from Run 2 (red) was most consistent with that from observations (black) than those from Run 1 (blue) and the JB2008 model (purple). As compared to the track-integrated neutral mass density from GOCE observations, those from Run 1 and JB2008 generally represented an underestimation and overestimation, respectively. The difference between the track-integrated neutral mass densities calculated from Run 1 and Run 2 (or observations) was $\sim$15% at 20:30 UT on 05/29/2010. Clearly, the improvements in the satellite drag estimations associated with improved soft electron precipitation specifications were not negligible.

5.2.5 Summary

In this study, a novel empirical electron precipitation model, which relaxes assumptions on the electron energy spectrum and is able to better specify the global soft electron precipitation distributions than most existing electron precipitation models, has been coupled into GITM. Impacts of soft electron precipitations on the neutral mass density and satellite drag have been evaluated during the May 28-29, 2010 geomagnetic storm by comparing different GITM simulation results and observations. It was found that estimations of the storm-time neutral mass density and satellite drag were remarkably improved when the soft electron precipitation was better specified in GITM. The results unprecedentedly reveal the importance of the knowledge of the global soft electron precipitation distribution to the improvement of the F-region neutral density estimation in GCMs. Furthermore, the neutral density from an empirical thermosphere model (JB2008 model) were also examined in this study, and it was found the JB2008 model did not well capture the neutral mass density and satellite drag variations during this event.

5.3 New empirical models for high-latitude electric field and its variability

5.3.1 Introduction

In this section, another two components of the ASHLEY model, ASHLEY-E and ASHLEY-Evar, will be introduced. Those two models are based on the DMSP bulk ion drift measurements. In this section, the data and their process are introduced at first. Then the methodology is present. Next, model outputs are exhibited. The final part summarizes this section and provides some discussions.

5.3.2 Data

The Special Sensor for Ions, Electrons and Scintillation (SSIES) onboard the DMSP satellites measures the full bulk ion drift vector ($\mathbf{V}$) in the spacecraft coordinate system (i.e., $\mathbf{V} = V_x\hat{\mathbf{x}} + V_y\hat{\mathbf{y}} + V_z\hat{\mathbf{z}}$, where $\hat{\mathbf{x}}$ is along the the satellite trajectory, $\hat{\mathbf{z}}$ is outward of the center of the Earth and $\hat{\mathbf{y}}$ completes righthanded system; V_x, V_y and V_z are components in directions corresponding to their subscripts, respectively). In this study, ion drift measurements from DMSP F15-F18 satellites during 2010-2018 are used. DMSP F16-F18 carry the most latest version of the SSIES (version 3) which has the temporal resolution of 1 second, whereas DMSP F15 carries the previous version of the SSIES (version 2) which has the temporal resolution of 4 seconds. Despite using different versions of the SSIES, it is found that there are no significant deviations in the statistical electric potential and electric field results in regions where all satellite flew by (not shown here). In addition, since the DMSP F15 data improve the data coverage at noon and midnight, DMSP F15 bulk ion drift measurements are included in the dataset.

After removing the spacecraft velocity with respect to the Earth and the velocity associated with the upper atmosphere's corotation with the Earth, the residual ion drift vector has been used for the derivation of the electric potential and electric field. Because

the SSIES is sensitive to the density and concentration of the O^+ in the ionosphere, the measurements are generally in poor quality when the ionospheric O^+ density is low or other ion species (such as H^+) are dominant. In this study, only measurements with a relatively high background O^+ concentration (>90%) and density ($> 4 \times 10^3 \mathrm{cm}^{-3}$) are utilized. Meanwhile, only data with the best quality flag (flag = 1) are used. If a trajectory has many unavailable data (i.e., large data gap) or clear baseline issue, the trajectory will be excluded in the final dataset. Overall, more than half of trajectories in the original dataset are discarded, and the remaining dataset has more trajectories from the Northern Hemisphere (NH: 51126; SH: 29602) and excludes a large amount of trajectories in the local winter.

To calculate the electric field and electric potential, linear baseline corrections of V_x, V_y and V_z components are applied to ensure they are zero at both ends of each polar crossing (i.e., |MLAT|=45° in this study). Since the V_x component is generally noisier than another two components, so it could be difficult to determine its baseline sometimes. Therefore, in order to obtain a reliable V_x baseline, the standard deviations of V_x data measured in the first minute and last minute of each polar crossing are calculated. If both standard deviation is smaller than 100 m/s, the V_x data along that track are used, otherwise the V_x data are discarded and the electric field vector along that track is not calculated. In addition, only the large-scale V_x data (smoothed by a 70-s sliding window) are utilized to avoid introducing unreliable small-scale and mesoscale structures in the V_x data. If all components of the ion drift vector after the baseline correction ($\mathbf{V}'$) are available, the electric field vector ($\mathbf{E}$) can be calculated through $\mathbf{E} = -\mathbf{V}' \times \mathbf{B_0}$. Here $\mathbf{B_0}$ is background geomagnetic main field vector at the satellite location from the International Geomagnetic Reference Field-12 (IGRF-12) model (*Thébault et al.*, 2015). Similar to Section 4.1, the electric field vector is then decomposed into the magnetic eastward (E_{d1}) and equatorward (E_{d2}) components as defined in the modified APEX coordinate system (*Richmond*, 1995).

More details related to the modified APEX coordinates and the decomposition procedure can be found in *Richmond* (1995) and *Laundal and Richmond* (2017).

The electric potential can be calculated from the along-track electric field ($\mathbf{E_x}$, $\mathbf{E_x}$ = $E_x\hat{\mathbf{x}}$), which can be approximated through $\mathbf{E_x} = -\mathbf{V'_y} \times \mathbf{B_{0z}}$, where $\mathbf{V'_y}$ is the horizontal cross-track ion drift vector after applying the baseline correction and $\mathbf{B_{0z}}$ is the vertical component of the geomagnetic main field $\mathbf{B_0}$. The contribution of the vertical ion drift to E_x is generally small and therefore be neglected in our calculation. The along-track electric field is then integrated over the satellite pass to determine the electric potential along that pass. However, to obtain a reliable electric potential, the electric field and electric potential must both be zero at the ends of the satellite pass. The aforementioned baseline correction ensures the electric field being zero at the ends but does not necessarily lead to zero potentials at the ends. Thus, a correction proportional to $|E_x|$ is applied to E_x, i.e., $E'_x = E_x + c|E_x|$, to ensure that the integration of E'_x along the trajectory i.e., ($|\text{MLAT}| > 45°$) is zero. The correction factor c can be calculated as:

$$c = -\frac{\int_s^f E_x dx}{\int_s^f |E_x| dx}. \tag{5.5}$$

Here, s and f denote the start and final points of the pass and dx is the distance between two consecutive measurements. The tracks of which $|c| > 0.2$ are excluded in order to effectively remove the passes during which the IMF conditions have a significant temporal change.

In addition to the DMSP data, the IMF B_y and B_z components as well as solar wind speed (V_{sw}) and plasma density (N_{sw}) are also used. The IMF and solar wind process are similar to those described in Section 5.1.2.

5.3.3 Methodology - ASHLEY-E

5.3.3.1 Categorization

Similar to the method we have used in Section 5.1.3.1, all polar crossings with good electric field/potential data are categorized according to their ε_t and θ_c (Note θ_cs for SH polar crossings are mirror corrected). Again, trajectories from both hemispheres and all seasons are combined in order to obtain best data coverage. All polar crossings of which $\varepsilon_t < 3000$ are categorized as one category regardless of θ_c and other crossings with $3000 < \varepsilon_t < 24000$ are sorted into 6 ε_t bins and 8 θ_c bins, i.e. $6 \times 8 + 1 = 49$ categories in total. The boundaries as well as medians for different ε_t bins are summarized in Table 5.2. Fewer ε_t bins and smaller upper boundary of ε_t than those set in the analysis of electron precipitation data (Section 5.1.3.1) are primarily due to the smaller amount of trajectories with good electric field/potential data especially in the SH.

5.3.3.2 Spherical harmonic and IMF clock angle fittings

Since the ionospheric net charge density is equal to zero, the electrostatic potential (Φ) satisfies the relationship: $\nabla^2\Phi = 0$. Therefore, Φ can be expanded by the spherical harmonics in a spherical coordinate system (*Jackson*, 2007). Following *Weimer* (1995), if only working with the real part of the spherical harmonics, Φ can be expressed as:

$$\Phi(\theta,\ \Phi) = \sum_{l=0}^{12} A_{l0} P_l^0(\cos\theta) + \sum_{l=1}^{12} \sum_{m=1}^{min(l,\ 4)} (A_{lm}\cos m\phi + B_{lm}\sin m\phi) P_l^m(\cos\theta). \qquad (5.6)$$

Here, P_l^m is the associated Legendre function, θ is the polar angle converted from the MLAT ($\theta = \dfrac{\frac{\pi}{2} - \lambda_m}{\frac{\pi}{2} - \lambda_0}$, where λ_m is the MLAT in radians and λ_0 is the MLAT of the lower boundary in radians which is set to $\dfrac{\pi}{4}$ in this study) and ϕ is the azimuthal angle converted from the MLT ($\phi = \dfrac{\text{MLT}}{12}\pi$). Since the ASHLEY-E aims to representing the large-scale

patterns of the high-latitude electric potential and electric fields, so it is reasonable to terminate the expansion at certain points since higher order expansions will introduce unrealistic small-scale and mesoscale structures. We found that terminating the expansion at $l = 12$ and $m = 4$ appear to be reasonable by trial and error tests.

In this study, similar to *Maute and Richmond* (2006), the electric field component (E_{d1} and E_{d2}) data are also used in addition to the electric potential data, so that the electric potential and electric field patterns are consistent. By using the Eqs. 4.8 and 4.9 in *Richmond* (1995) and Eq. 5.6, the expansions of E_{d1} and E_{d2} can be expressed as:

$$E_{d1}(\theta,\, \Phi) = \sum_{l=1}^{12} \sum_{m=1}^{min(l,\, 4)} \frac{m}{R\cos\lambda_m}(A_{lm}\sin m\phi - B_{lm}\cos m\phi)P_l^m(\cos\theta) \tag{5.7}$$

and

$$\begin{aligned} E_{d2}(\theta,\, \Phi) = & \frac{4\sin\theta}{R\sin I_m}\sum_{l=0}^{12} A_{l0}\left.\frac{\partial P_l^0(x)}{\partial x}\right|_{x=\cos\theta} + \frac{4\sin\theta}{R\sin I_m}\sum_{l=1}^{12}\sum_{m=1}^{min(l,\, 4)} \\ & (A_{lm}\cos m\phi + B_{lm}\sin m\phi)\left.\frac{\partial P_l^m(x)}{\partial x}\right|_{x=\cos\theta}, \end{aligned} \tag{5.8}$$

respectively. The coefficients in Eqs. 5.7 and 5.8 are the same as those used in Eq. 5.6. R in Eq. 5.8 is set to 6482 km and $\sin I_m$ in Eq. 5.8 are calculated by using Eq. 3.7 in *Richmond* (1995). By using all available good P_l^m, E_{d1} and E_{d2} data and their locations, the best-fit coefficients A_{lm} and B_{lm} in each category are obtained. Then A_{lm} and B_{lm} in each category with $\varepsilon_t > 3000$ are fitted to a fourth-order Fourier series constructed by θ_c to capture their IMF clock angle variations, and the procedure is similar to that described in Section 5.1.3.2.

5.3.3.3 Extrapolation

The extrapolation of the ASHLEY-E is based on the extrapolation of the cross-polar-cap potential (CPCP), which will be illustrated in this paragraph. The dots in Figure 5.12(a)

represent the CPCPs from the six ε_t bins with $\varepsilon_t \geq 3000$ and $157.5° < \theta_c < 202.5°$, and their x-axis locations correspond to the median values of ε_t listed in Table 5.2. As expected, the CPCP increases with ε_t However, it was found that the CPCP might be saturated at a certain point under intense solar wind and IMF conditions (e.g., *Shepherd*, 2007, and references therein). Therefore, to account in the saturation of the CPCP at large ε_ts, the CPCP (Φ_{PC}) is assumed to be linear with β defined in Eq. 5.4, i.e., $\Phi_{PC} = c_1\beta + c_2$, where $\varepsilon_{inf} = 40000$ is used to calculate β so that Φ_{PC} can saturate at a level of $\sim$190 kV (red thick line in Figure 5.12(a)) which is comparable to the level reported in *Hairston et al.* (2005). The procedure is repeated for other IMF clock angles by using the same ε_{inf}. It is found that the saturated Φ_{PC} for IMF B_y large and dominant cases from the ASHLEY-E is comparable to those reported in *Mitchell et al.* (2010) and the saturated reversal convection potential (the potential across the reversal cells) from the ASHLEY-E is also comparable to that reported in *Wilder et al.* (2008). Therefore, our method and the choice of ε_{inf} can well capture the electric potential saturation in general. Since c_1 and c_2 are also a function of the IMF clock angle, so their variations are captured by the Fourier fitting and c_1 and c_2 at any θ_c can be obtained thereby.

5.3.3.4 Expansion of the electric potential pattern

The electric potential pattern also expands as the solar wind and IMF conditions become more intense (e.g., *Weimer*, 2005), and a procedure aimed at capturing the expansion of the electric potential pattern is described in the subsequent paragraph.

Figure 5.12(b) shows the co-MLATs (r_2) of the electric potential maxima and minima detected on dawn (4-8 MLT) and dusk (16-20 MLT) sides when $157.5° < \theta_c < 202.5°$. The locations of the potential maxima and minima are likely to be the convection reversal boundaries (CRBs) especially when the IMF B_z is southward, and CRBs are good indicators of the polar cap boundary when the IMF B_z is southward (e.g., *Sotirelis et al.*, 2005).

Similar to the procedure described in Section 5.1.3.4, r_2 is assumed to be linear with β defined in Eq. 5.4, where ε_{inf} is chosen to be 24000 in the calculation of β so that r_2 can saturate at co-MLAT$\sim$21° that has been reported in previous studies (e.g., *Ridley and Kihn*, 2004; *Merkin and Goodrich*, 2007) as indicated by the red thick line in Figure 5.12(b). Next, the expansion rate, er_2, is calculated from $er_2 = \frac{r_{21}}{r_{20}} - 1$. Here, r_{21} and r_{20} are the co-MLATs of the CRBs at input ε_t (ε_{in}) and $\varepsilon_t = 18357$ ($\varepsilon_{in} > 18357$), respectively. Moreover, similar to Section 5.1.3.4, it is assumed that $er_2(\theta_{in},\ \varepsilon_{in}) = er_2(180°,\ \varepsilon_{in})\sin^2(\omega/2)$, where $\omega = \frac{\theta_{in}}{180°}\pi$.

5.3.3.5 Reconstruct the electric potential pattern for given inputs

To reconstruct the electric potential for given ε_{in} and θ_{in}, the first step is to determine which of the following three cases applies: 1) $\varepsilon_{in} < 2583$; 2) $2583 \leq \varepsilon_{in} < 18357$; 3) $\varepsilon_{in} \geq 18357$. If it is the first case, then coefficients corresponding to the Cat-0 pattern are used to reconstruct the Cat-0 pattern; If it is the second case, then the two closet median values of ε_t listed in Table 5.2 are determined, namely ε_i and ε_{i+1} ($0 \leq i \leq 5$). Then, coefficients corresponding to the Cat-i and Cat-(i+1) patterns are used to generate the Cat-i and Cat-(i+1) patterns at θ_{in}. The two patterns are combined according to their corresponding weights, w_i and w_{i+1}, where w_i and w_{i+1} ($w_i = \frac{\beta_{in} - \beta_i}{\beta_{i+1} - \beta_i}$ and $w_{i+1} = 1 - w_i$. Here, β_i, β_{i+1} and β_{in} are calculated from ε_i, ε_{i+1} and ε_{in} using Eq. 5.4 and $\varepsilon_{inf} = 40000$. Otherwise, coefficients corresponding to the Cat-6 pattern are used to reconstruct the Cat-6 pattern at θ_{in}. Meanwhile, the expansion rate is calculated and the Cat-6 pattern is expanded according to the expansion rate described in Section 5.3.3.4. Furthermore, the electric potential is extrapolated to obtain the predicted CPCP at ε_{in} according to the procedures described in Section 5.3.3.3.

5.3.4 Methodology - ASHLEY-Evar

5.3.4.1 Data preparation

The development of the ASHLEY-Evar is based on the ASHLEY-E described in Section 5.3.3. Since the electric field variability in this study represents structures not well captured by the large-scale mean electric field model, therefore for each track with the electric field data available, the modeled E_{d1} and E_{d2} from the ASHLEY-E under the corresponding solar wind and IMF conditions are subtracted from the original E_{d1} and E_{d2} data, i.e., $E'_{di} = E_{di} - E^{m}_{di}$ (i = 1, 2). Here E_{di} and E^{m}_{di} represent the measured and modeled electric field components, respectively. Then the E'_{di} data are categorized in the same way as described in Section 5.3.3.1.

5.3.4.2 Binning and fitting

E'_{di} $(i = 1,2)$ data are according to their MLTs and MLATs in each category, and the sizes of the MLT and MLAT bins are 1 hour and 2°, respectively. Larger MLAT bin size than that used in Section 5.1.3.2 is chosen due to smaller amount of electric field data. The standard deviations of E'_{d1} and E'_{d2} (σ_1 and σ_2) are calculated in each bin (if has $>$100 data points) subsequently and are used to quantify the magnitudes of E_{d1} and E_{d2} variabilities.

With data gaps near noon and midnight filled and patterns smoothed in MLT and MLAT directions, the MLT and IMF clock angle dependences of σ_1 and σ_2 at each latitudinal bin are captured by the Fourier fitting. The procedure and the fitting orders are same as those described in Section 5.1.3.2.

5.3.4.3 Extrapolation and expansion

For the ASHLEY-Evar, the extrapolations of σ_1 and σ_2 are based on the extrapolation of the CPCP described in Section 5.3.3.3 and expansions of their patterns are same as that

described in Section 5.3.3.4. Since the electric fields variability is supposed to be consistent with the background electric field model, so that same procedures for the extrapolation and expansion implemented in the ASHLEY-E model are adopted here.

5.3.4.4 Reconstruct σ_1 and σ_2 patterns for given inputs

To reconstruct σ_1 and σ_2 patterns for any given ε_{in} and θ_{in}, the first step is to determine which of the following three cases applies: 1) $\varepsilon_{\text{in}} < 2583$; 2) $2583 \leq \varepsilon_{\text{in}} < 18357$; 3) $\varepsilon_{\text{in}} \geq 18357$. If it is the first case, then coefficients corresponding to the Cat-0 pattern are used to reconstruct the Cat-0 pattern; If it is the second case, then the two closet median values of ε_t listed in Table 5.2 are determined, namely ε_{i} and $\varepsilon_{\text{i}+1}$ ($0 \leq \text{i} \leq 5$). Then, coefficients corresponding to the Cat-i and Cat-(i+1) patterns are used to generate the Cat-i and Cat-(i+1) patterns at θ_{in}. The two patterns are combined according to their corresponding weights determined in Section 5.3.3.5. Otherwise, coefficients corresponding to the Cat-6 pattern are used to reconstruct the Cat-6 pattern at θ_{in}. Meanwhile, the expansion rate is calculated and the Cat-6 pattern is expanded according to the expansion rate described in Section 5.3.3.4. Furthermore, the same expansion rate and extrapolation factor used in Section 5.3.3.5 are used to obtain σ_1 and σ_2 patterns at ε_{in} and θ_{in}.

5.3.5 Comparisons between measured and modeled data

To examine the general reliability of the empirical models developed in this section, the modeled results along all polar crossings used in the model development are calculated under their corresponding IMF and solar wind conditions. The modeled and measured data in each $\varepsilon_t - \theta_c$ category are binned according to their MLATs and MLTs, and binning results of modeled and measured data are compared. The sizes of the MLT and MLAT bins are 1 hour and 2°, respectively. Figure 5.13 shows the comparisons of binning results of measured and modeled electric potential, E_{d1} and E_{d2} data and Figure 5.14 shows the com-

parisons of E_{d1} and E_{d2} variabilities under low and high IMF and solar wind conditions. Overall, the modeled results are comparable to the measured results for those two specific cases. Figure 5.15 further compares binning results of modeled and measured electric potential, mean electric field and electric field variability in each MLAT-MLT bin from all 49 $\varepsilon_t - \theta_c$ categories studied in this section. The x and y axes in Figures 5.15(a)-5.15(c) represented averages of the measured and modeled parameters in each bin, respectively. The x axis in Figures 5.15(d) and 5.15(e) represents the standard deviation of the measured parameter in each MLAT-MLT bin while the y axis in Figures 5.15(d) and 5.15(e) represents the root mean square of modeled variabilities in each MLAT-MLT bin. Overall, the binning results of the modeled data are comparable with those of the measured data since all the grey dots shown in Figure 5.15 are concentrated around the y = x lines (blue-dashed lines) and the best-fit lines (red-thick lines) according to the grey dots are not significantly deviated from the y = x lines, indicating that the ASHLEY-E can well capture the large-scale electric potentials as well as their gradients (i.e., mean electric fields) and the ASHLEY-Evar can well capture the electric field variability.

5.3.6 Results: Model outputs

Figure 5.16 shows the electric potential outputs from the ASHLEY-E for 8 different IMF clock angles with a constant IMF magnitude of 8 nT. In addition, the solar wind speed is 450 km/s and the solar wind number density is 4 cm^{-3}. In general, the electric potential displays a two-cell pattern except for the northward IMF B_z case, where a multiple-cell pattern appears. In addition, the negative cell on the dusk side and the positive cell on the dusk side are shaped into round (crescent) and crescent (round) cells when the IMF B_y is positive (negative), and the round cell typically has a large absolute extremum than the crescent cell. Moreover, the CPCP varies with the IMF clock angle (Figure 5.18(a)), which maximizes and minimizes when the IMF B_z is southward and northward, respectively. Overall,

the outputs from the ASHLEY-E are consistent with from previous empirical models (e.g., *Heppner and Maynard*, 1987; *Papitashvili and Rich*, 2002; *Weimer*, 2005; *Cousins and Shepherd*, 2010).

Figure 5.17 compares the magnitudes of the mean electric field (E_1, $E_1 = \sqrt{\overline{E}_{d1}^2 + \overline{E}_{d2}^2}$) and electric field variability (E_2, $E_2 = \sqrt{\sigma_1^2 + \sigma_2^2}$) at different IMF clock angles ($B_t = 8$nT, $V_{SW} = 450$ km/s, $N_{SW} = 4$ cm^{-3}). $\overline{E}_{d1}$ and $\overline{E}_{d2}$ are calculated from the electric potential outputs from the ASHLEY-E by using Eqs. 4.8 and 4.9 in *Richmond* (1995), and σ_1 and σ_2 are outputs from the ASHLEY-Evar. The magnitude of the mean electric field typically displays a three-peak structure and a more complex pattern appears when the IMF B_z is purely northward. As for the magnitude of the electric field variability, it tends to peak on the dawn and dusk sides when the IMF is purely southward and the peak on the dawn side has a higher magnitude, while it tend to have a single peak on the day side when the IMF is purely northward. In addition, the distribution of the electric field variability magnitude depend on the IMF B_y polarity: the electric field variability magnitude tends to peak on the morning side when the IMF B_y is positive with a relatively wide MLT span, whereas it tends to peak near the noon the IMF B_y is negative with a weaker magnitude and a narrower MLT span (except for the southward IMF B_z case, where the MLT span of the peak is also large). Figure 5.18(b) exhibits the IMF clock angle dependences of the polar averaged E_1 and E_2. In general, both the polar averaged E_1 and E_2 maximize when the IMF is purely southward and the polar averaged E_2 is generally comparable with (much larger than) the polar averaged E_1 when the IMF is southward (northward), indicating the Joule heating can be significantly underestimated when electric field variability is not taken into account especially when the IMF has a northward component. Overall, the results shown in Figures 5.17 and 5.18(b) are consistent with results shown in *Matsuo et al.* (2003).

5.3.7 Discussion and summary

In this section, empirical models that are able to consistently specify high-latitude large-scale mean electric field and electric field variability are present. The model outputs are generally consistent with previous statistical results. Furthermore, with the inclusion of the ASHLEY-Evar, the high-latitude Joule heating can be better estimated especially during the northward IMF case.

Several large-scale mean electric field models have been established based on different measurements, but most models do not provide a consistent electric field variability model, leading underestimations of Joule heating in GCMs. *Maute and Richmond* (2006) have developed consistent empirical mean electric field and electric field variability model s based on the DE-2 bulk ion drift measurements. The DE-2 model has the seasonal variation since their measurements were taken during solar maximum ($F_{10.7}$>150 sfu). However, the solar wind dependence is not taken into account in the DE-2 model due to the limited amount of data. In addition, the expansion of the CRB under intense solar wind and IMF conditions is taken into account in our model, which is not well specified in their models.

More importantly, most electric field models are developed separately from the electron precipitation model. For example, the default high-latitude drivers used in GITM, *Weimer* (2005) and *Fuller-Rowell and Evans* (1987) models, are developed from two different datasets and using quite different methodologies. Thus, the self-consistency between those two models may be lacking. *Sheng et al.* (2019) found the CRB from the *Weimer* (2005) model can have a very large offset with respect to the PAB from the *Fuller-Rowell and Evans* (1987) model under intense IMF and solar wind conditions, which is not consistent with the findings from previous studies (e.g., *Sotirelis et al.*, 2005). The offset between the CRB and PAB results in significant underestimation of Joule heating. However, all components in the ASHLEY model utilize datasets from same satellites and the time cov-

erage between the electric field and electron precipitation datasets are similar. Moreover, the consistency between the CRB and PAB is better taken into account. Hence, the consistency between the electron precipitation model and electric field model should be better than most existing empirical models, which is one primary advantage of the ASHLEY model.

With more available data, the electric fields and their variabilities can be studied under more specific conditions. Besides, a boundary-oriented binning technique can be utilized instead of the static-binning method (see Section 5.4). Furthermore, it might be necessary to model the correlation between electric field and electron variabilities on different scales, which can help improve the localized Joule heating estimation (Section 4.1).

5.4 Impacts of binning methods on high-latitude electrodynamic forcing: static vs boundary-oriented binning methods

5.4.1 Introduction

To test the sensitivity of the high-latitude electrodynamic forcing patterns to the binning method, the DMSP electron precipitation (total energy flux and average energy) and electric potential data from 2010-2014 are binned in both static and boundary-oriented binning approaches for the purpose of illustration. First, the quantitative comparisons between patterns obtained from both binning methods are provided. For the boundary-oriented binning approach, the particle precipitation data are organized according to the poleward and equatorward auroral boundaries to avoid mixtures of data inside and outside of the aurora zone. Meanwhile, the electric potential data are organized according to the CRB to avoid mixtures of the ionospheric convection poleward and equatorward of the CRB. Moreover, both static and boundary-oriented patterns are implemented in the GITM to evaluate the impacts on Joule heating.

5.4.2 Comparisons of results obtained from different binning methods: Electron precipitation

5.4.2.1 Auroral boundary identification

Figure 5.19(a) represents the electron energy spectrogram along a DMSP F16 polar pass in the Southern Hemisphere. Overplotted red lines indicate the auroral boundaries identified along this track by using the technique developed by *Kilcommons et al.* (2017) for the DMSP electron precipitation data, which is an improved version of the technique developed by *Redmon et al.* (2010). The first step of this technique is to identify all aurora region candidates on both dawn and dusk sides that correspond to regions where the integrated energy flux for electron above 1kV is continuously above an empirical threshold (10^9 eV/cm^2/s/sr). Then a figure of merit (FOM) is used to rate the likelihood of a pair of the candidate regions (one on the dawn side and the other on the dusk side) being main auroral ovals, and the pair of regions with a highest FOM are defined as the main auroral ovals. However, if the highest FOM is smaller than 3, the track is excluded. The poleward and equatorward boundaries of the main auroral oval can be determined accordingly. More details about how the FOM is calculated and how the main auroral ovals are selected can be found in *Kilcommons et al.* (2017). We have collected about 3100 tracks with auroral boundaries identified under the IMF conditions considered in this Chapter.

The top panel of Figure 5.20 shows distributions of the auroral boundaries that were identified in the dataset as a function of MLAT and MLT. Different colors correspond to different satellites. To achieve a better data coverage, boundaries from both hemispheres and all seasons are combined. It is clear that the most poleward auroral boundaries (PABs) are located within $70^\circ - 80^\circ$ |MLAT| and most equatorward auroral boundaries (EABs) are mainly located within $60^\circ - 70^\circ$ |MLAT|. The bottom panel of Figure 5.20 displays distributions of the median MLAT of the corresponding boundary in each 0.5-hour MLT

bin. Only medians in bins where the number of boundaries is greater than 30 are calculated, as indicated by the red dots. For bins without sufficient data, the median locations are obtained through an elliptical fitting based on the red dots, as indicated by blue plus signs. The median PAB is close to a circle, of which the center has a small offset ($\sim 1^\circ$) from the geomagnetic pole, while the median EAB tends to be more elliptical. Overall, the general characteristics of the auroral boundaries are consistent with previous studies under moderately disturbed geomagnetic conditions (e.g., *Feldstein and Starkov*, 1967; *Sotirelis and Newell*, 2000).

5.4.2.2 Boundary-oriented binning approach

In this study, similar approaches used in *Redmon et al.* (2010) and *Kilcommons et al.* (2017) have been adopted to organize the particle precipitation data according to auroral boundaries. First, the high-latitude region is divided into three zones: 1) poleward of the auroral zone (PZ): $|\mathrm{MLAT}^{\mathrm{m}}_{\mathrm{PAB}}| \leq |\mathrm{MLAT}^{\mathrm{m}}| \leq 90^\circ$; 2) auroral zone (AZ): $|\mathrm{MLAT}^{\mathrm{m}}_{\mathrm{EAB}}| \leq |\mathrm{MLAT}^{\mathrm{m}}| < |\mathrm{MLAT}^{\mathrm{m}}_{\mathrm{PAB}}|$; 3) equatorward of the auroral zone (EZ): $45^\circ \leq |\mathrm{MLAT}^{\mathrm{m}}| < |\mathrm{MLAT}^{\mathrm{m}}_{\mathrm{PAB}}|$. Here, $\mathrm{MLAT}^{\mathrm{m}}$ represents the MLAT of a measurement, and the MLATs of the identified PAB and EAB on the side of the track where the measurement is taken are denoted by $\mathrm{MLAT}^{\mathrm{m}}_{\mathrm{PAB}}$ and $\mathrm{MLAT}^{\mathrm{m}}_{\mathrm{EAB}}$, respectively. Second, we calculated the fractional distances of the measurements (L) in corresponding regions, which can be expressed as follows:

$$\mathrm{L} = \begin{cases} \dfrac{|\mathrm{MLAT}^{\mathrm{m}}| - |\mathrm{MLAT}^{\mathrm{m}}_{\mathrm{PAB}}|}{90^\circ - |\mathrm{MLAT}^{\mathrm{m}}_{\mathrm{PAB}}|} & \text{if in PZ} \\ \dfrac{|\mathrm{MLAT}^{\mathrm{m}}| - |\mathrm{MLAT}^{\mathrm{m}}_{\mathrm{EAB}}|}{|\mathrm{MLAT}^{\mathrm{m}}_{\mathrm{PAB}}| - |\mathrm{MLAT}^{\mathrm{m}}_{\mathrm{EAB}}|} & \text{if in AZ} \\ \dfrac{|\mathrm{MLAT}^{\mathrm{m}}| - 45^\circ}{|\mathrm{MLAT}^{\mathrm{m}}_{\mathrm{EAB}}| - 45^\circ} & \text{if in EZ} \end{cases}$$

The data are mapped latitudinally according to the statistical locations of the equatorward and poleward boundaries of the region where the data is located and the fractional distance relative to those boundaries. The modified magnetic latitude after mapping ($MLAT^n$) in different regions can be expressed as follows:

$$MLAT^n = \begin{cases} MLAT^s_{PAB} + L_{PZ} \times (90^\circ - MLAT^s_{PAB}) & \text{if in PZ} \\ MLAT^s_{EAB} + L_{AZ} \times (MLAT^s_{PAB} - MLAT^s_{EAB}) & \text{if in AZ} \\ 45^\circ + L_{EZ} \times (MLAT^s_{EAB} - 45^\circ) & \text{if in EZ} \end{cases}$$

$MLAT^s_{PAB}$ and $MLAT^s_{EAB}$ represent median MLATs of the PAB and EAB in the corresponding MLT bin. Then the mapped data are binned according to its MLT and modified MLAT.

5.4.2.3 Static vs Boundary-oriented binning results

Figure 5.21 summarizes the averages of the total electron energy flux and average electron energy in each bin as a function of MLT and MLAT obtained through different binning approaches. The bin size is 1 hour in MLT by 1° in MLAT, and grey-shaded areas indicate bins without sufficient data point (<400). Figures 5.21(a) and 5.21(b) depict the static total electron energy flux and average electron energy patterns. The total energy flux shows a horseshoe shape that is roughly symmetric about the 1-13 MLT meridian and is generally 2-3 erg cm^{-2} s^{-1} on the night side. Meanwhile, the maximum of the average energy is located on the morning side. The general behaviors are similar to those shown in previous studies under moderately disturbed conditions (e.g., *Hardy et al.*, 1987; *Fuller-Rowell and Evans*, 1987; *Zhang and Paxton*, 2008; *Newell et al.*, 2009). Figures 5.21(c) and 5.21(d) exhibit the total energy flux and average energy patterns obtained from the boundary-oriented approach. The average energy pattern (Figure 5.21(d)) seems to

be similar to the static pattern (Figure 5.21(b)), where the maximum is still located on the morning side but its magnitude increases by 10-20%. However, the peak total energy fluxes are more intense in the 14-24 MLT sector than the 2-12 MLT sector as shown in Figure 5.21(c), which is not captured by the static pattern (Figure 5.21(a)). Our results are consistent with the boundary-oriented patterns shown in *Sotirelis and Newell* (2000) under moderately disturbed conditions, although a more sophisticated boundary was utilized in their study. In addition, the total energy fluxes in the statistical auroral zone (regions enclosed by red dashed lines) tend to be higher in the boundary-oriented pattern (Figure 5.21(c)) than those in the static pattern (Figure 5.21(a)). The enhancements are more substantial in the 14-24 MLT sector than those in 2-12 MLT sector. More specifically, the enhancements of the peak magnitude in the 14-24 MLT sector can exceed 50% of the peak magnitude in the static binning results, while the enhancements of the peak magnitude in 2-12 MLT are smaller than 25% of the peak magnitude in the static binning results in general.

Figure 5.22 provides detailed comparisons of the latitudinal profiles of different parameters from different binning results at 5-6 and 17-18 MLT sectors. The difference in responses of the total energy flux to the binning methods on dawn and dusk sides identified in Figure 5.21 can also be seen in Figures 5.22(a) and 5.22(c). Clearly, the changes in the latitudinal profiles on the dawn side (Figure 5.22(a)) are not as dramatic as those on the dusk side (Figure 5.22(c)). On the dusk side, the full width at half maximum (FWHM) of the latitudinal profile obtained from the boundary-oriented binning approach is $\sim$50% smaller than that from the static binning approach, while the peak magnitude undergoes a $\sim$80% elevation. Similar differences can also be seen in the latitudinal profiles along other meridians (not shown here), indicating that the boundary-oriented binning method can lead to a particle precipitation pattern with significantly sharper transitions near the auroral boundaries on the dusk side. On the dusk side, the relatively intense and dynamic mono-energetic

electron precipitation frequently occurs (e.g., *Newell et al.*, 2009). The significant increase of the peak total energy flux on the dusk side from the boundary-oriented binning method suggests that the boundary-oriented binning method may better represent the contribution of the mono-energetic electron precipitations than the static binning method. Meanwhile, the fact that substorms occur more frequently on the dusk side, and that the static binning method cannot well capture these rapid expansions/contractions might also contribute to the larger differences between the static and boundary-oriented patterns on the dusk side.

5.4.3 Comparisons of results obtained from different binning methods: Electric potential

5.4.3.1 CRB identification

Figure 5.19(b) shows the smoothed and corrected horizontal cross-track ion drift (V_y) measurements along the same trajectory as shown in Figure 5.19(a), which is utilized to identify CRBs. The technique used in this study is similar to that used in *Chen et al.* (2015), which aims to search locations of the reversal points of V_y, as indicated by blue lines in Figure 5.19(b). The CRBs identified through the method developed by *Chen et al.* (2015) are statistically found to be in good agreement with the OCBs identified through a recently developed method based on the Active Magnetosphere and Planetary Electrodynamics Response Experiment (AMPERE) magnetic perturbation observations (*Burrell et al.*, 2020). Although the example shown in Figure 5.19(b) is quite straightforward, it is worth noting that the configuration of the convection pattern and its relationship with the configuration of satellite trajectory can bring in more complexities for CRB identification (*Chen et al.*, 2015). For instance, it is possible that more than two CRBs are encountered along a trajectory owing to the appearance of a multi-cell convection pattern. It is also possible that no CRB can be identified along a track since the convection pattern is relatively small and the satellite does not cross it. In this study, all tracks with two CRBs identified

are included and all tracks with no CRB identified are excluded. For other cases, if a single zero-potential point can be found between the potential maximum and minimum (also should be extrema) and if a single CRB can be identified on one side of the zero-potential point, the corresponding part of the track is kept, otherwise the whole track is discarded. We have collected approximately 2000 tracks with CRB identified under moderately strong and dominant southward IMF conditions. In this study, it is not required that the CRBs and auroral boundaries are identified simultaneously along the same trajectory, otherwise the number of available trajectories would be substantially reduced and would not have a good coverage near noon and midnight.

5.4.3.2 Boundary-oriented binning approach

In this and following paragraphs, we illustrate how to organize the electric potential data from a geomagnetic coordinate to CRB-oriented coordinate referenced to a reference CRB (obtained as described in the next subsection) and to a reference zero-potential line. Figure 5.23(a) shows the locations of zero-potential points of all the individual passes and the reference zero-potential line fitted to these points. As in *Hairston and Heelis* (1990), the reference zero-potential line is defined as a parabola with the equation $\beta = c_1\alpha^2 + c_2$. The α axis is defined as a straight line fitted to the collection of zero-potential points and the β axis is orthogonal to this, passing through the pole. The constants c_1 and c_2 are found by least-squares fitting to the points. Each individual pass is then adjusted such that its zero-potential point lies on the zero-potential line and its maximum or minimum potential lies on the dawn-side or dusk-side reference CRB, respectively, in order to avoid mixing data from the positive and negative potential cells.

With reference to Figure 5.23(b), the adjustments are carried out as follows. First, each track included in our dataset is displaced by the minimum distance that brings its zero-potential point (point A) to lie on the zero-potential parabola, with the displaced track

(black dotted line) remaining parallel to the original. Next, we draw a line (green dashed) from the extremum potential of the displaced track (point B) to the vertex of the parabola (magenta star), which lies near the center of the convection pattern. We then displace the track again and contract or elongate it such that its potential extremum (point D) lies on the intersection of the green line with the statistical CRB (blue ellipse) and its zero-potential point (point C) is shifted along the reference zero-potential parabola, with the displaced track (red dotted line) remaining parallel to the original. The potential data on the mapped track are subsequently binned with respect to the modified MLAT and MLT.

5.4.3.3 Static vs Boundary-oriented binning results

Figure 5.24 shows the electric potential pattern obtained from the static binning method, which exhibits a clear two-cell pattern and is consistent with those obtained by previous studies (e.g., *Thomas and Shepherd*, 2018, and references therein). The red dashed ellipse in Figure 5.24(a) denotes the best-fit ellipse of locations of the maximum electric potential magnitude at different MLTs, which is used as the reference CRB for the boundary-oriented binning method as shown in Figure 5.23(b). The electric potential pattern obtained from the boundary-oriented binning method is shown in Figure 5.24(b), which does not exhibit significant changes in the overall pattern. However, in comparison with the static pattern, the cross-polar-cap potential (CPCP) increases from 65.07 kV to 72.47 kV ($\sim$11%). Moreover, as revealed by the latitudinal profiles of the electric potential on the dawn and dusk sides (Figures 5.24(c) and 5.24(d)), the boundary-oriented binning approach also tends to increase the magnitude of the electric potential gradient (i.e., the electric field) near the CRB. Therefore, it implies that the boundary-oriented pattern may be better able than the static pattern to capture the sharp transitions of the cross-track ion drift near the CRB that are typically shown in the observations (e.g., Figure 11c in *Weimer*, 2005).

From the boundary-oriented binning pattern, the unbiased CRB can be determined by finding the MLAT of the maximum electric potential magnitude at each MLT, as indicated by the green triangles in Figure 5.24(b). Figure 5.25 provides a comparison between the locations of the average PAB and the unbiased CRB on the dawn (2-10 MLT) and dusk sides (14-22 MLT). Clearly, the separation between CRB and PAB is generally small, suggesting a good alignment between the PAB and CRB. More specifically, the separations are relatively smaller on the dawn side ($<2°$) in comparison with those on the dusk side ($<3°$) as shown in Figure 5.25(b). Previous studies based on ground-based SuperDARN radar and DMSP particle precipitation measurements (e.g., *Newell et al.*, 2004; *Sotirelis et al.*, 2005) indicate that there is a good alignment between OCB and CRB. Given the good alignment between OCB and PAB (*Newell et al.*, 1996), our results are qualitatively consistent with previous results, although quantitative discrepancies could exist owing to the differences in the CRB and auroral boundary identification techniques used in our study and previous studies. For example, the auroral region identified in this study is dependent on a threshold total energy flux level for electrons above 1 keV and may not well capture the low-latitude boundary layer, of which the poleward edge is usually found to be collocated with the OCB (*Drake et al.*, 2009). Thus while, the auroral boundary locations are useful to determine the impacts on the ionosphere and thermosphere, the location of particle sources in the magnetosphere may not be well identified with the auroral boundary identification technique used in this study.

5.4.4 Impacts on Joule heating by using patterns from different binning methods

In the previous two sections, we have applied both static and boundary-oriented binning approaches to bin the particle precipitation and electric potential data. As compared with the static binning results, the boundary-oriented binning approach results in stronger changes in the particle precipitation on the dusk side, whereas the changes on the dawn side

are relatively modest. Meanwhile, the cross-polar-cap potential as well as the magnitude of the electric potential gradient (i.e., electric field) near the CRB increase on both dawn and dusk sides. As expected, changes in the localized Joule heating would occur if a GCM is driven by results from different binning methods. However, it is still unclear to what degree the Joule heating peak values would change on dawn and dusk sides. Moreover, it still remains unknown whether the hemispheric-integrated Joule heating would undergo a significant change when a GCM is driven by results from different binning methods. Quantitative investigations are provided in this section to shed light on those questions

Two simulations were carried out: Run 1 is a reference run, where the high-latitude forcing of GITM is specified by the static binning results (Figures 5.21(a), 5.21(b) and 5.24(a)); In Run 2, the high-latitude forcing of GITM is specified by the boundary-oriented binning results (Figures 5.21(c), 5.21(d) and 5.24(b)). The data gaps (grey-shaded areas) at noon and midnight are filled by applying a linear interpolation based on values in adjacent bins. The patterns are then smoothed in MLT and MLAT directions. The spatial resolution for all simulations is 5° in longitude by 1° in latitude and 1/3 scale height in altitude. The temporal resolution is 2 s. All simulations are conducted under moderate solar activity ($F_{10.7} = 120$ sfu) and at the September equinox. In addition, a 24-hour pre-run (00 UT on 09/22/2002 - 00 UT on 09/23/2002) has been carried out, so that the neutral dynamics in GITM reached a quasi-steady state when the simulations were conducted.

Figures 5.26(a) and 5.26(b) summarize outputs of the height-integrated Joule heating from both runs at 10 minutes after the pre-run (i.e., 00:10:00 UT on 09/23/2002). As compared with the case when GITM is driven by static patterns (5.26(a)), the GITM simulation driven by the boundary-oriented patterns (5.26(b)) showed larger height-integrated Joule heating peaks on both dawn and dusk sides, although they tend to be located at higher latitudes (Figures 5.26(c) and 5.26(d)). The peak values of Joule heating in Run 2 increased by 112% and 94% as compared with Run 1 on dawn and dusk sides, respectively. However,

even though the regions with intense height-integrated Joule heating are located at higher latitudes in Run 2, the hemispheric-integrated Joule heating still increased from 29.29 GW to 34.76 GW (18%), which is not negligible.

5.4.5 Summary

In this study, electron precipitation and electric potential data from the DMSP satellites are analyzed under conditions when IMF is moderately strong and dominantly southward. First, statistical MLATs of auroral boundaries and CRB as a function of MLT have been investigated. Second, the particle precipitation and electric potential data are binned through static and boundary-oriented methods and the results are compared quantitatively. Finally, both static and boundary-oriented binning results are utilized to drive GITM in order to assess the impacts of the electrodynamic forcing patterns obtained from different binning methods on Joule heating. The primary findings are as follows:

(1) The CRB is well aligned with the poleward auroral boundary ($<3^\circ$ separations in general).

(2) In comparison with the static binning results, the boundary-oriented binning method significantly changes the morphology of the electron precipitation which is more predominant on the dusk side. In addition, the boundary-oriented binning method increases the cross-polar-cap potential by 11% and the magnitude of the electric potential gradient (electric field) near the CRB.

(3) As compared with the case in which GITM is driven by static patterns, GITM simulation driven by the boundary-oriented patterns shows an 18% increase of the hemispheric-integrated Joule heating, even though the regions with intense height-integrated Joule heating are more poleward.

5.5 Figures and tables

I	0	1	2	3	4	5	6	7	8
Left boundary	0	3000	5000	7000	9000	11000	13000	16000	20000
Right boundary	3000	5000	7000	9000	11000	13000	16000	20000	30000
Median (ε_I)	2579	4283	6073	7956	9939	11942	14254	17590	22770

Table 5.1: Summary of the left/right boundary and median of each ε_t bin used in binning the electron precipitation data.

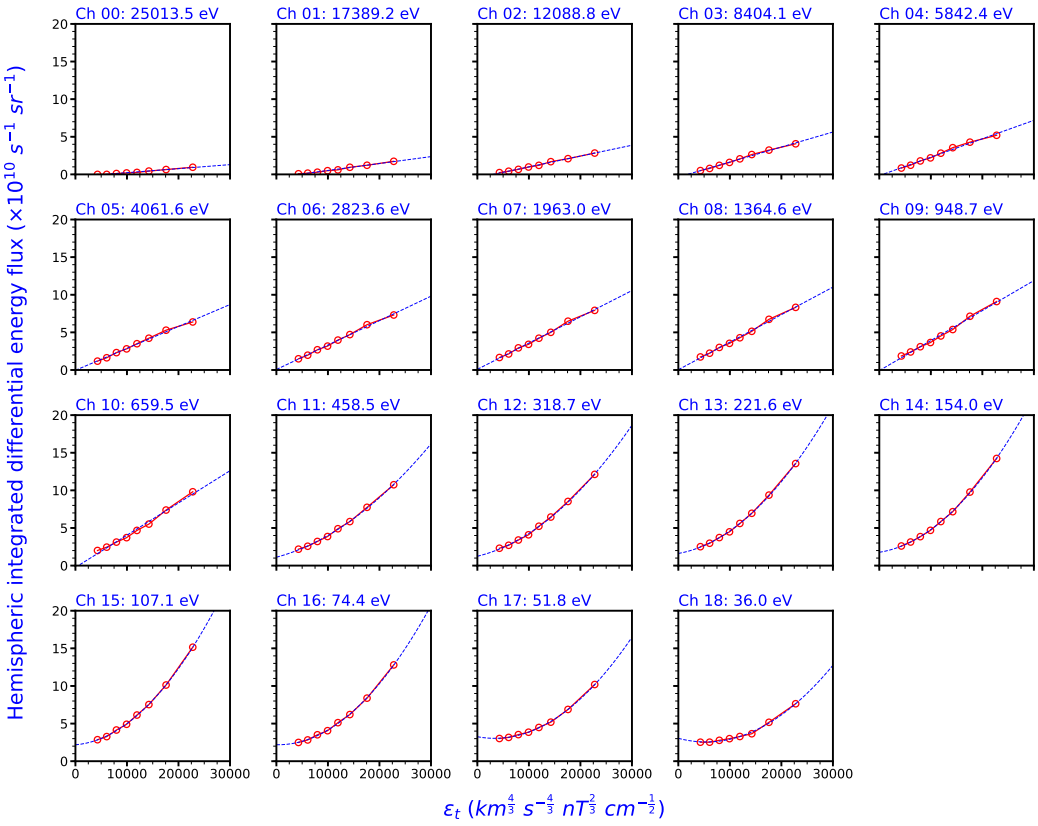

Figure 5.1: Evolutions of the hemispheric integrated differential energy flux with ε_t in 19 energy channels under IMF southward and dominant conditions (iCa=5). The x locations of 8 dots in each plot correspond to ε_Is listed in Table 5.1 (I=1,8). The blue dashed lines represent the best-fit lines (parabolas) according to the red dots in the first 11 (last 8) plots.

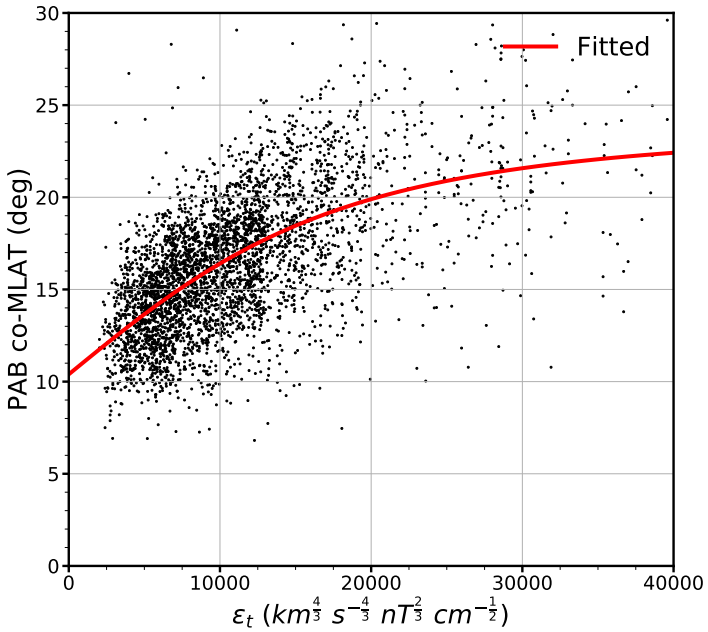

Figure 5.2: Co-MLATs of the poleward auroral boundaries (PABs) as a function of their corresponding ε_ts under southward and dominant IMF conditions (iCa=4). The red thick line represents the best-fit curve according to black dots.

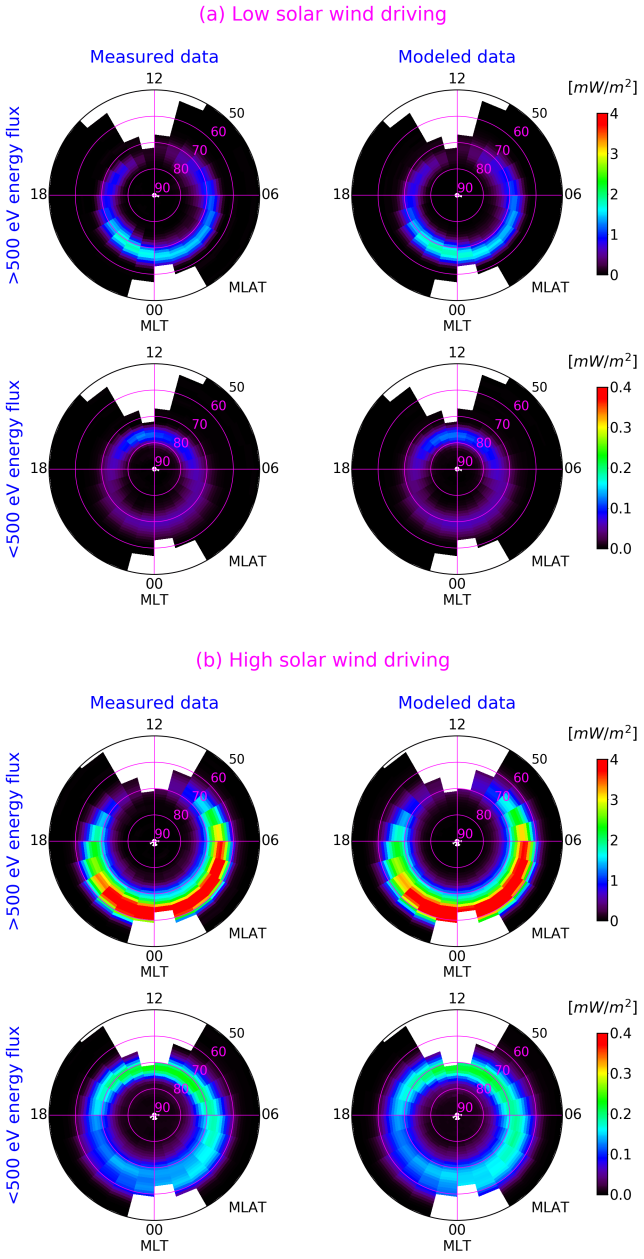

Figure 5.3: Comparisons of binning results of measured and modeled data under (a) low and (b) high solar wind driving conditions. The top and bottom row of each subplot correspond to the integrated energy fluxes of >500 eV and <500 eV electrons, respectively.

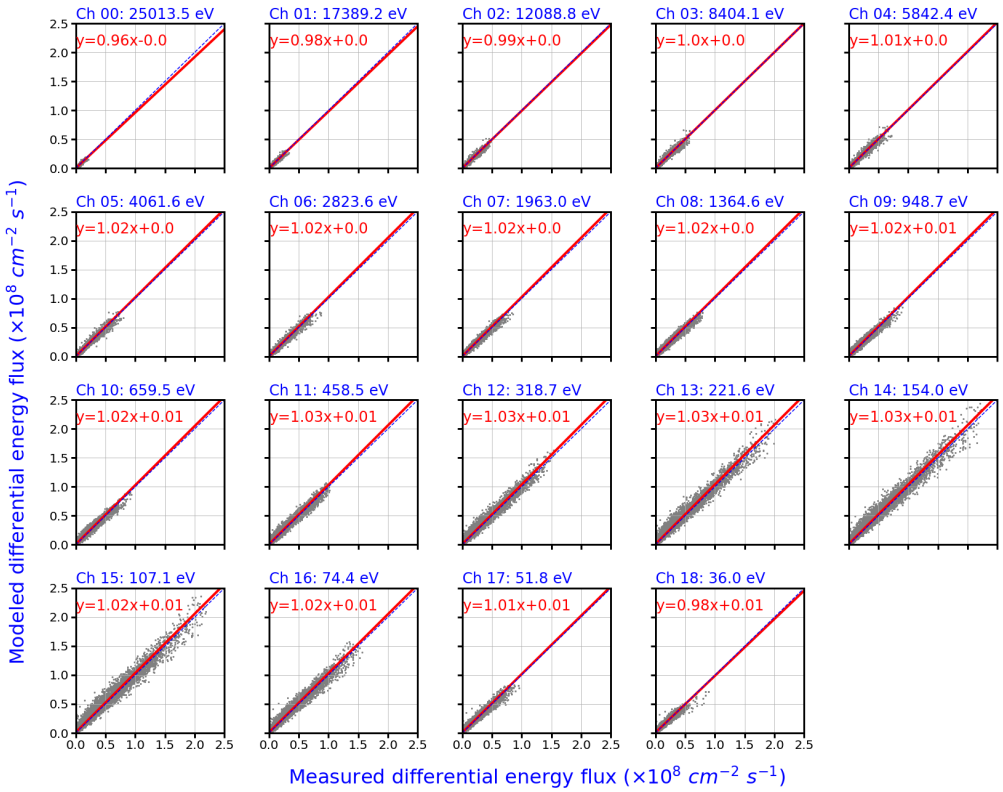

Figure 5.4: Comparisons of binning results of measured and modeled differential energy fluxes in 19 energy channels in all IMF and solar wind categories illustrated in Section 5.1.3.1. The blue dashed line in each subplot denotes the y = x line, and the red thick line represents the best-fit line according to the grey dots.

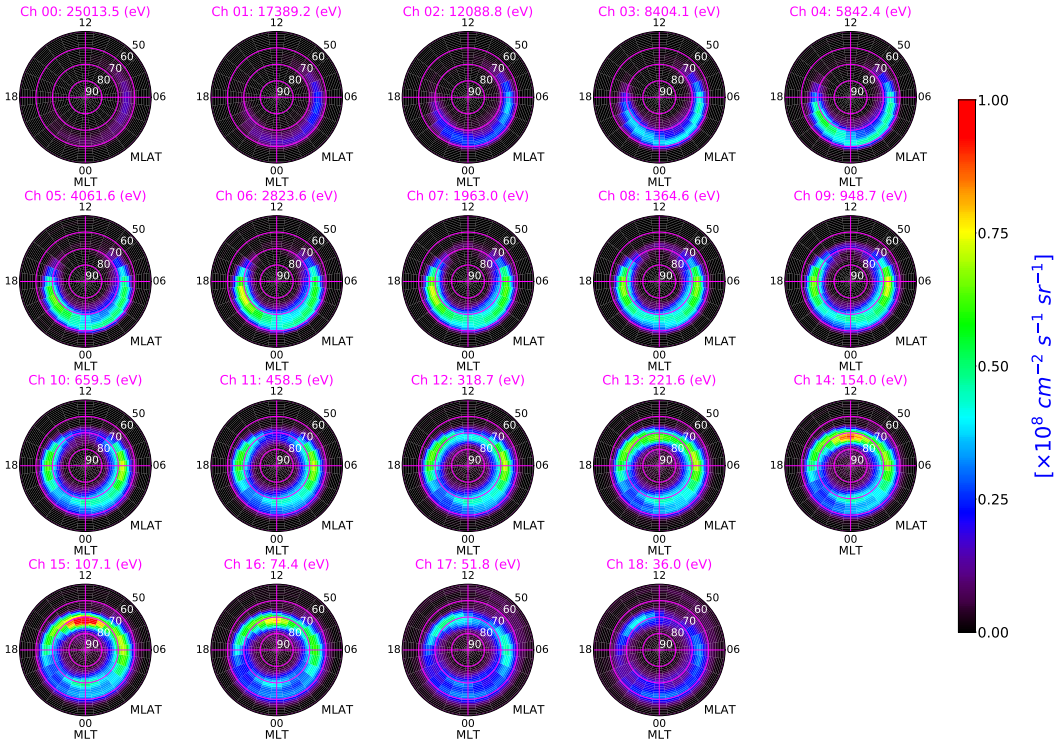

Figure 5.5: Distributions of the differential energy fluxes in 19 energy channels as a function of MLT and MLAT when the IMF $B_y = 0$, IMF $B_z = -8$nT, V_{SW} = 450 km/s and $N_{SW} = 5$ cm^{-3}. All plots are presented in geomagnetic coordinates.

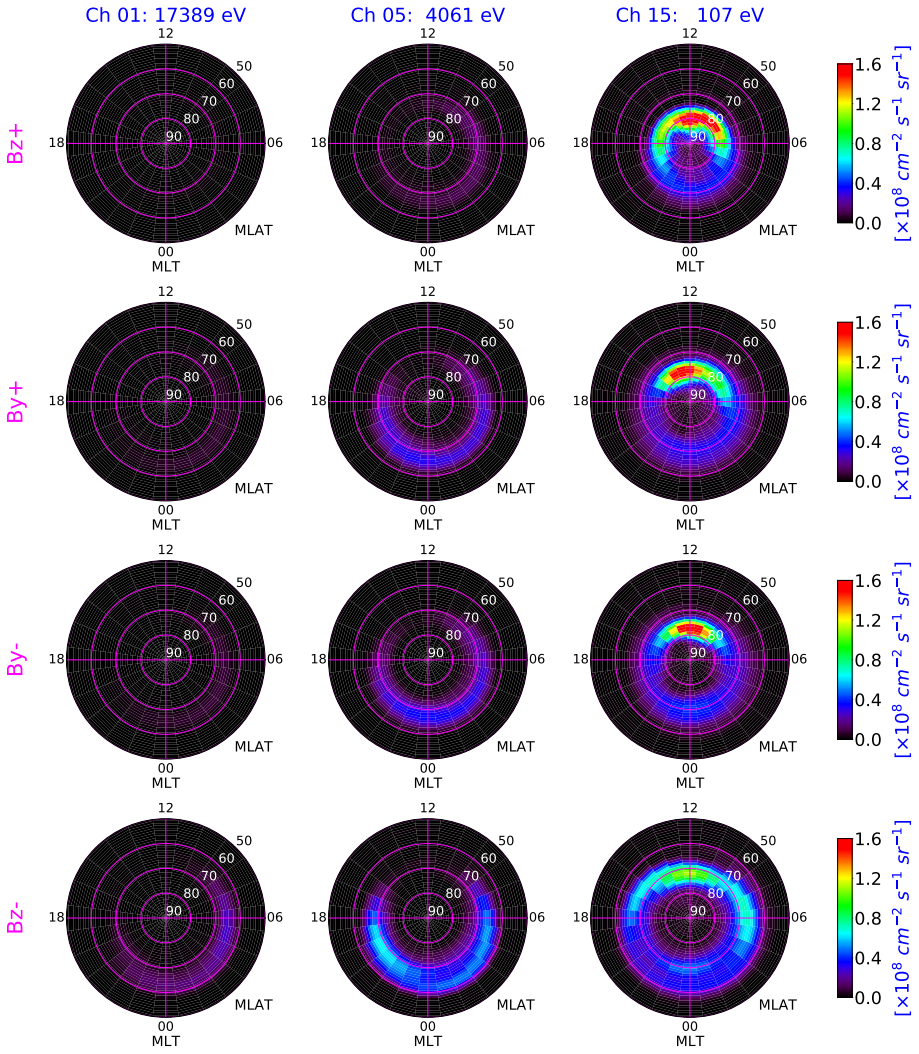

Figure 5.6: Distributions of the differential energy flux in 3 energy channels as a function of MLAT and MLT when (from top to bottom) the IMF clock angle is northward, eastward, westward and southward. For these four cases, the IMF $B_t = 8$nT, $V_{SW} = 450$ km/s and $N_{SW} = 5$ cm^{-3}. All plots are presented in geomagnetic coordinates.

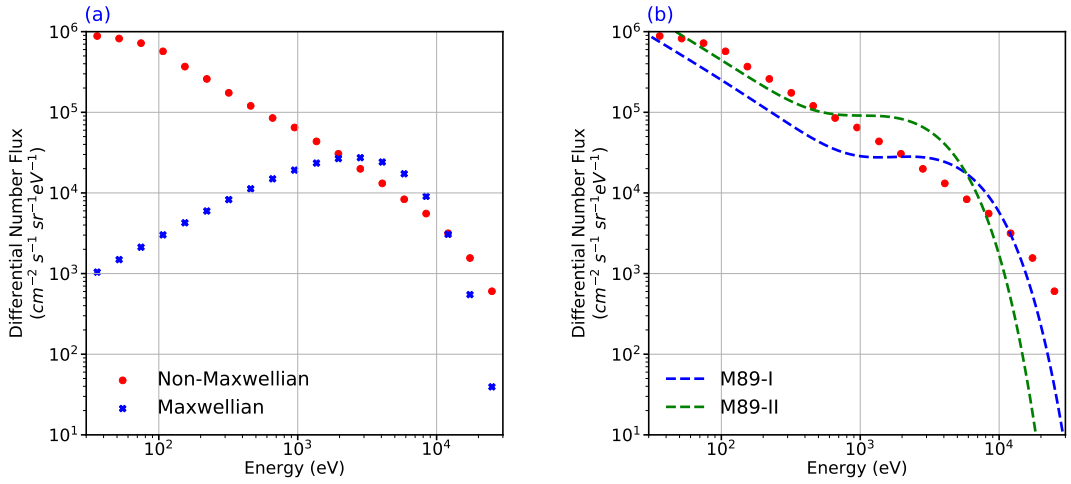

Figure 5.7: (a) Comparisons of the directional differential number fluxes between the modeled spectrum (Red dots) and a Maxwellian spectrum (Blue crosses) derived from the total energy flux and average energy of the modeled spectrum. (b) Comparisons of the directional differential number fluxes between the modeled spectrum (Red dots) and two spectra calculated by using the Meier 1989 formula (blue and black dashed lines). The geomagnetic location is MLT=4.5 h and MLAT=64.5°. The IMF and solar wind conditions are: IMF $B_y = 0$, IMF $B_z = -8$nT, $V_{SW} = 450$ km/s and $N_{SW} = 5$ cm^{-3}.

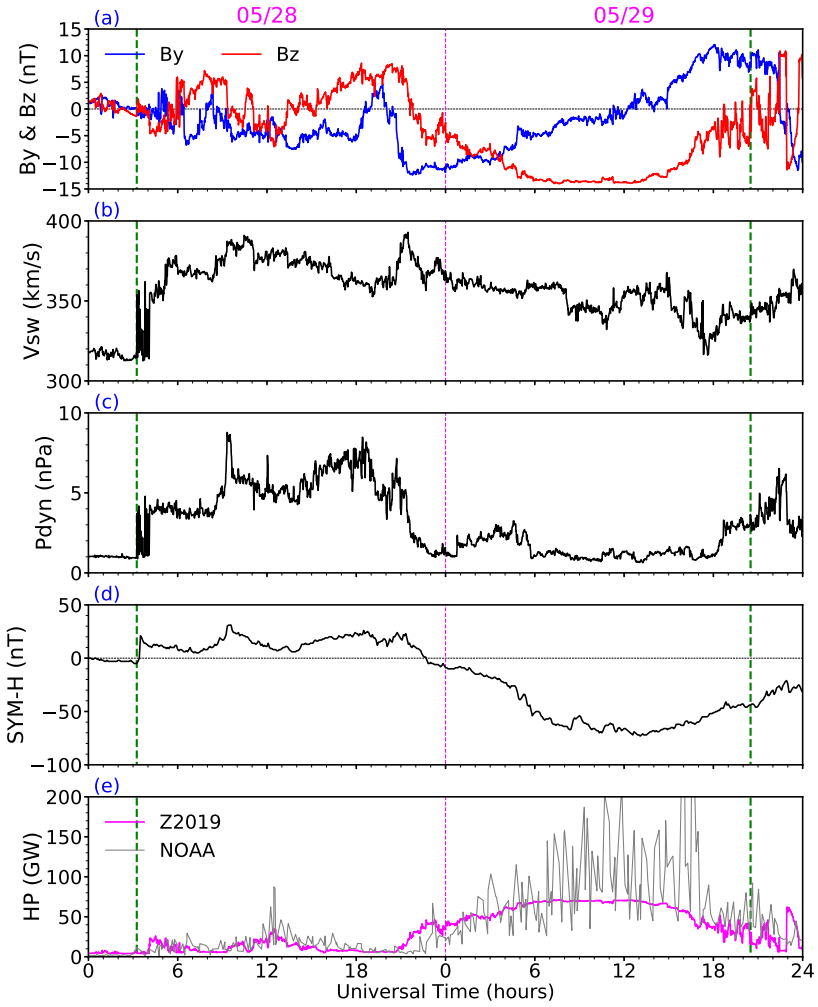

Figure 5.8: Variations of the (a) Interplanetary magnetic field (IMF) y (Blue) and z (Red) components in geocentric solar magnetospheric (GSM) coordinates (b) Solar wind bulk flow speed (c) Solar wind dynamic pressure (d) SYM-H index and (e) Hemispheric power (HP) during the May 28-29, 2010 event. In Plot (e), the grey line denotes the HP provided by the National Ocean and Atmospheric Administration and the magenta line indicates the HP provided by the ASHLEY-A model. The green lines indicates the start and end of the passage of the CME.

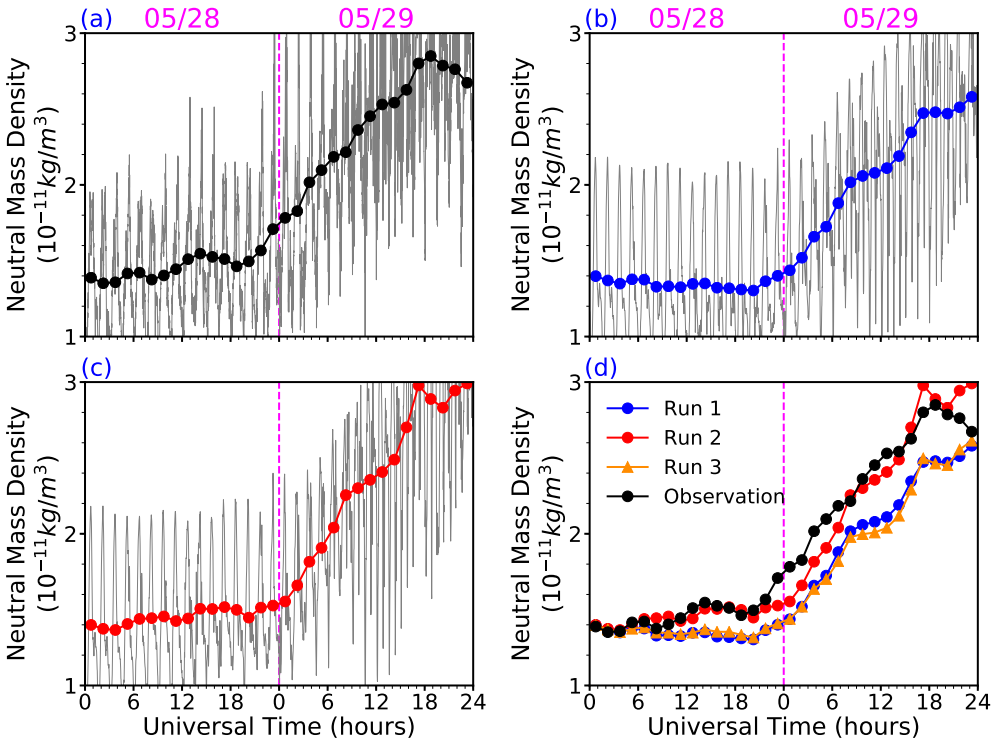

Figure 5.9: Neutral mass densities along the GOCE satellite from (a) the observation (b) Run 1 and (c) Run 2. The 10-s data/simulation outputs are denoted by the grey lines and the orbital averaged values are denoted by dotted lines in Plots (a)-(c). (d) Comparisons of the orbital averaged neutral mass densities from (black) the observation (blue) Run 1 (red) Run 2 and (orange) Run 3. See text for details.

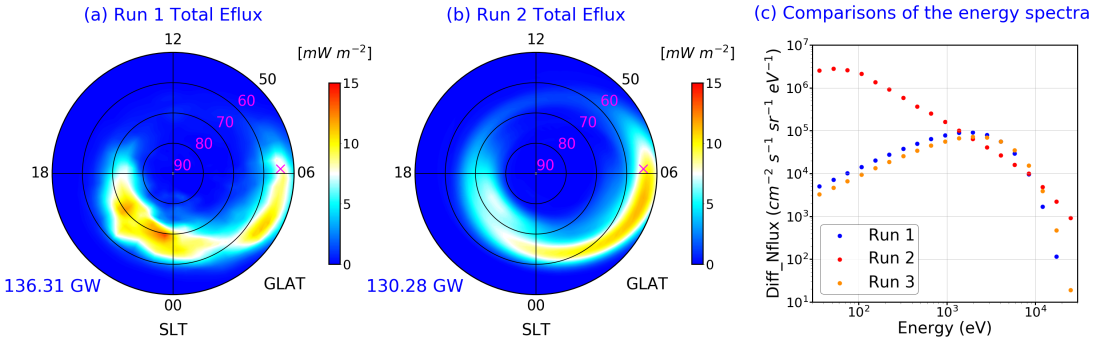

Figure 5.10: Total energy fluxes from (a) Run 1 and (b) Run 2 at 12:00 UT, 05/29/2010 in geographic coordinates, and their hemispheric integrated energy fluxes are shown on the bottom left of each plot. (c) Comparisons of the electron precipitation energy spectra at the location marked by the cross sign in Plots (a) and (b) (Local time: 06:10; Geographic latitude: 54.5° N) from three GITM simulations.

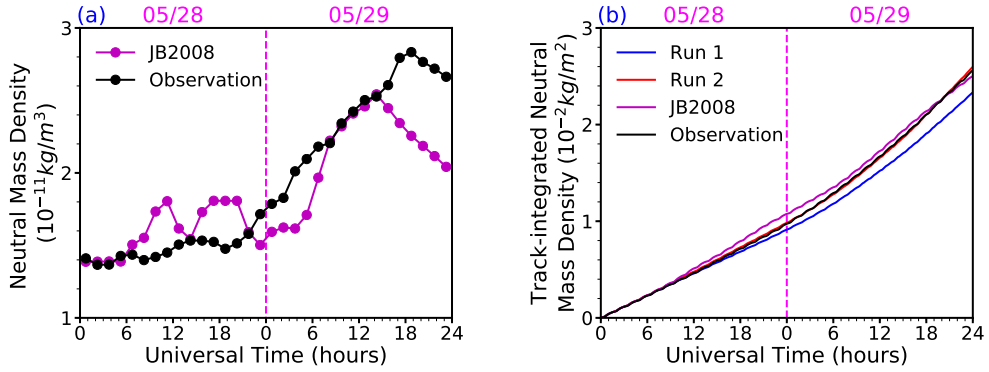

Figure 5.11: (a) Comparisons of the orbital averaged neutral mass densities along the GOCE satellite trajectory from (purple) the JB2008 model and (black) the observation during May 28-29, 2010; (b) Comparisons of the track-integrated neutral mass densities calculated by using results from (blue) Run 1, (red) Run 2, the (purple) JB2008 model and (black) the observation after May 28, 2010.

I	0	1	2	3	4	5	6
Left boundary	0	3000	5500	7500	9500	12000	16000
Right boundary	3000	5500	7500	9500	12000	16000	24000
Median (ε_I)	2583	4615	6539	8465	10614	13524	18357

Table 5.2: Summary of the left/right boundary and median of each ε_t bin used in binning the electric potential/field data.

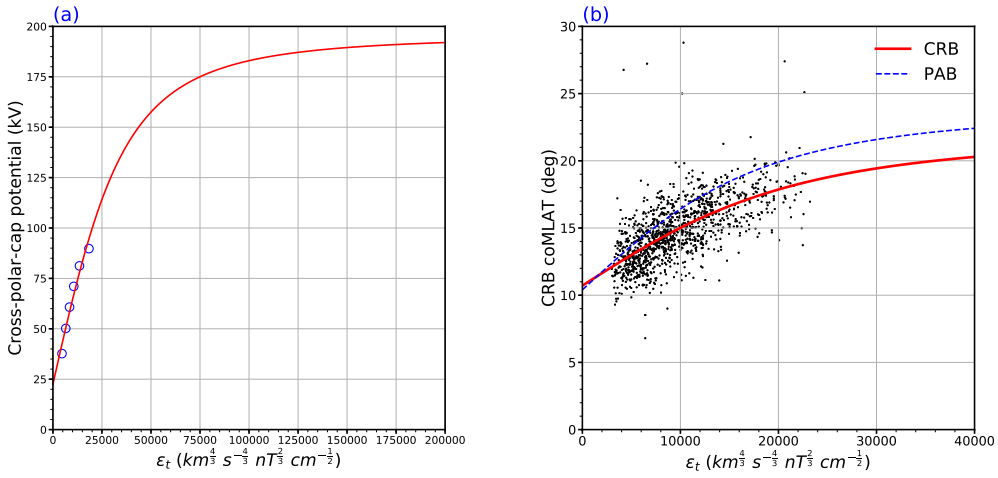

Figure 5.12: (a) Evolution of the cross-polar-cap potential (CPCP) as a function of median ε_ts listed in Table 5.2 and the red thick line represent the best-fit curve according to the blue dots; (b) Co-MLATs of the convection reversal boundary (CRB, black dots) as a function of their corresponding ε_ts under southward and dominant IMF conditions (iCa=4) and the red thick line represent the best-fit curve according to black dots. The blue dashed line is the same best-fit curve for the PAB shown in Figure 5.2.

(a) Low IMF and solar wind conditions

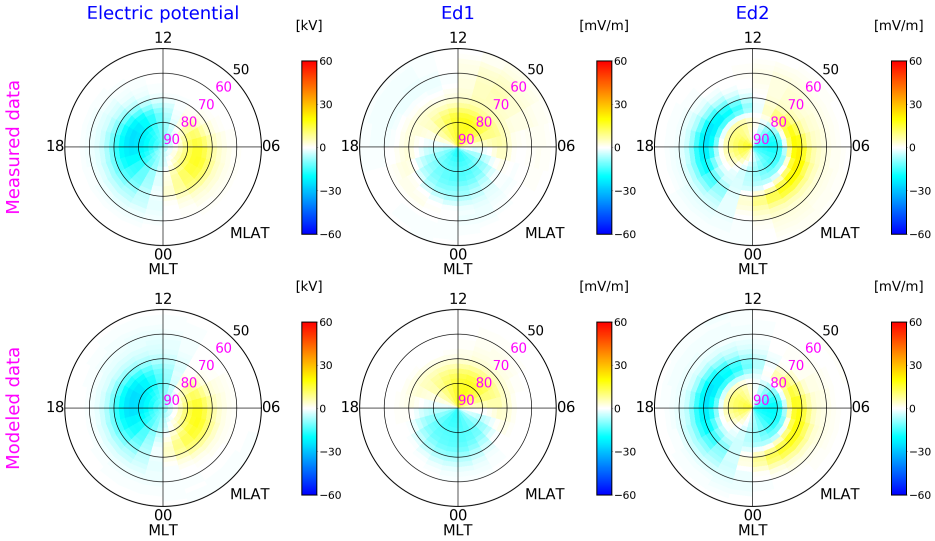

(b) High IMF and solar wind conditions

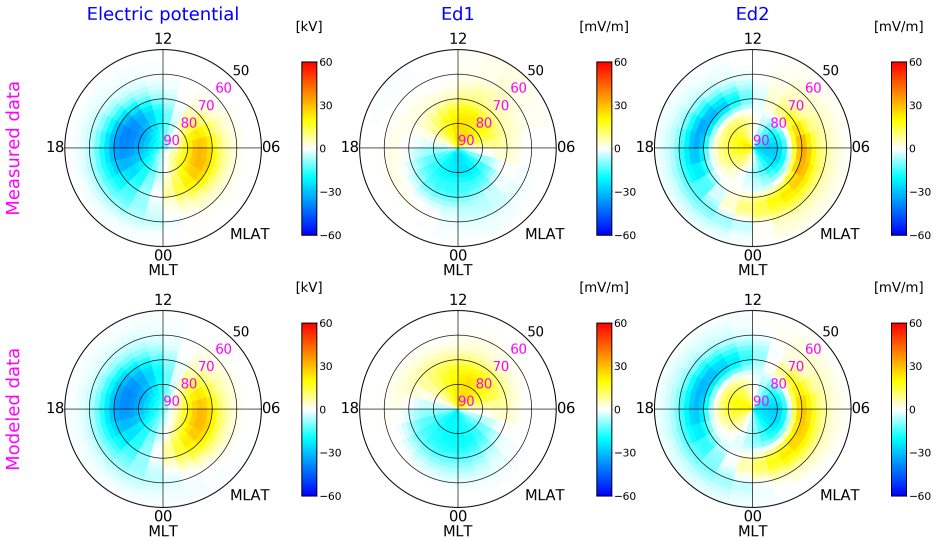

Figure 5.13: Comparisons of the distributions of binning results of measured and modeled electric potential, E_{d1} and E_{d2} data under (a) Low and (b) High IMF and solar wind conditions. All plots are represented in geomagnetic coordinates

(a) Low IMF and solar wind conditions

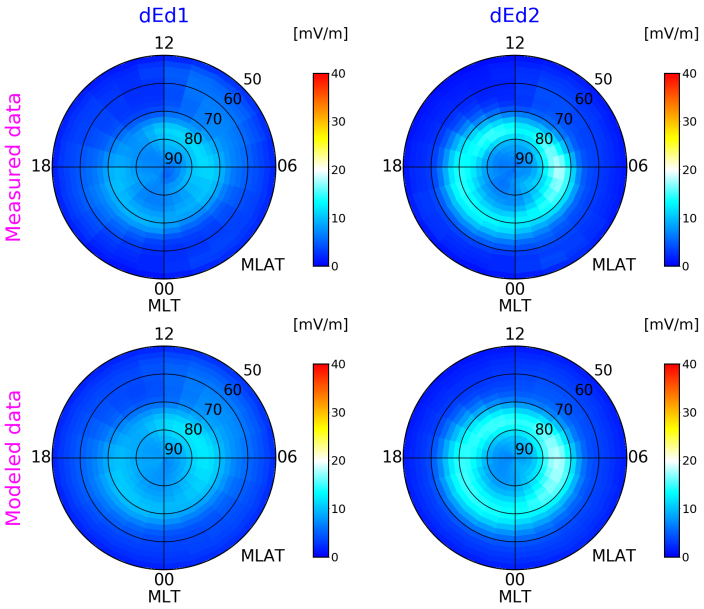

(b) High IMF and solar wind conditions

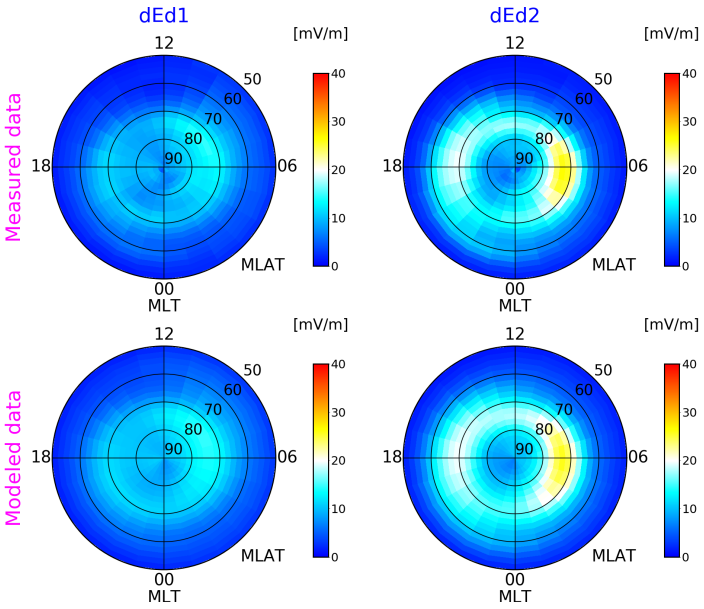

Figure 5.14: Comparisons of the distributions of binning results of measured and modeled E_{d1} and E_{d2} variabilities under (a) Low and (b) High IMF and solar wind conditions. All plots are represented in geomagnetic coordinates.

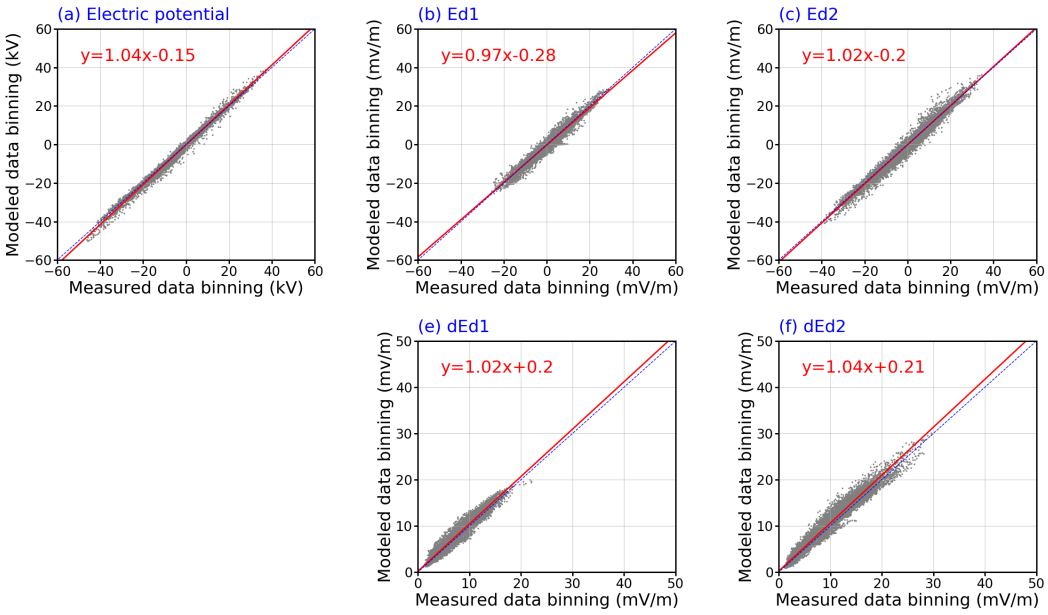

Figure 5.15: Comparisons of binning results of measured and modeled a) electric potential (b) E_{d1} (c) E_{d2} (d) E_{d1} variability and (e) E_{d2} variability in all categories in all IMF and solar wind categories illustrated in Section 5.3.3.1. The blue dashed line in each subplot denotes the y = x line, and the red thick line represents the best-fit line according to the grey dots. The equation corresponding to the best-fit line is given in each plot.

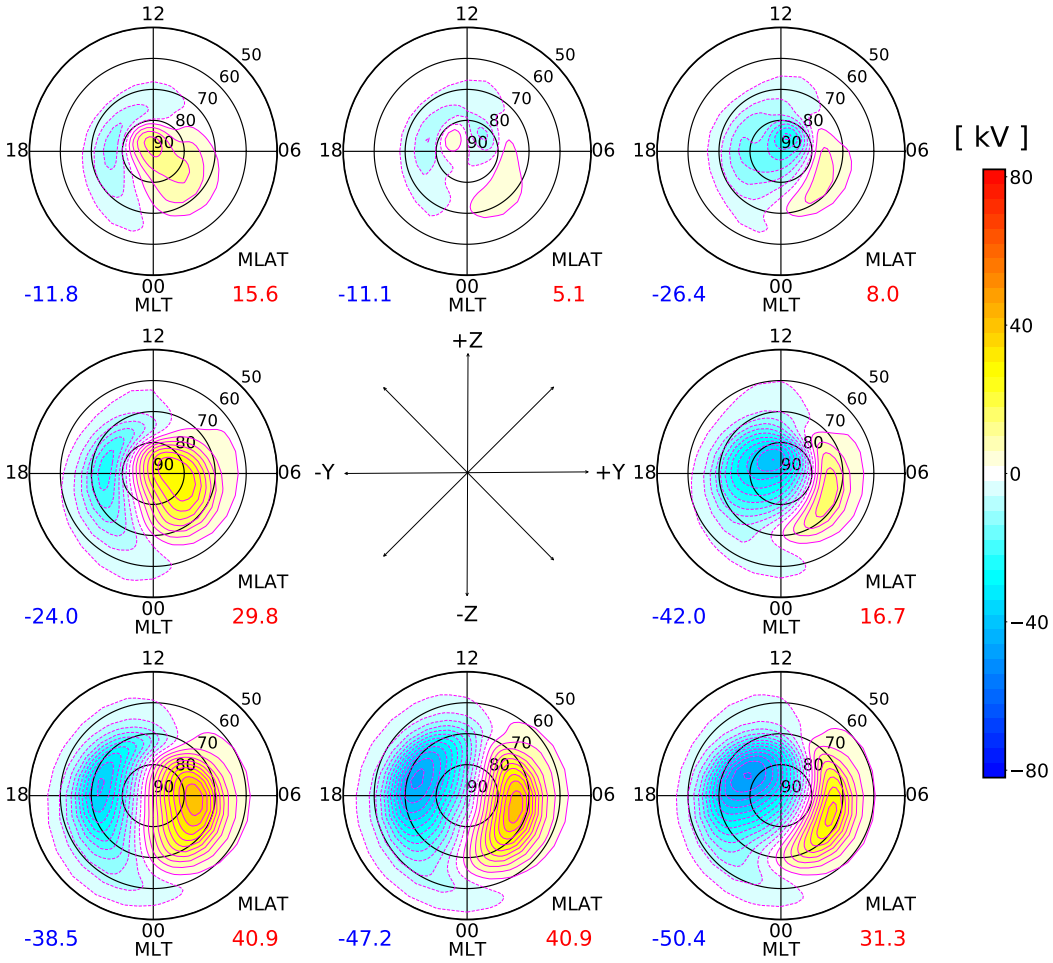

Figure 5.16: High-latitude electric potential as a function of MLAT and MLT for eight different IMF clock angles. The IMF $B_t = 8$nT, $V_{SW} = 450$ km/s and $N_{SW} = 4$ cm^{-3}. The maximum and minimum potential values are indicated on the bottom left and right side of each plot, respectively, and the contour interval is 4 kV. All plots are represented in geomagnetic coordinates.

(a) Magnitude of the mean electric field

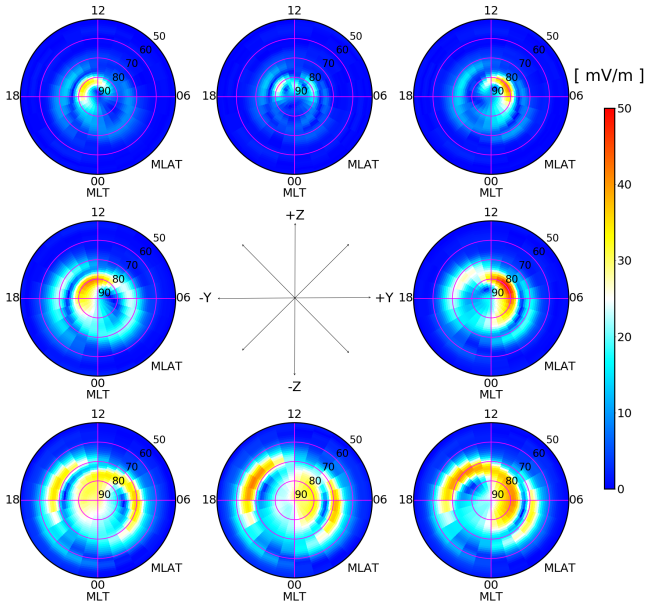

(b) Magnitude of the electric field variability

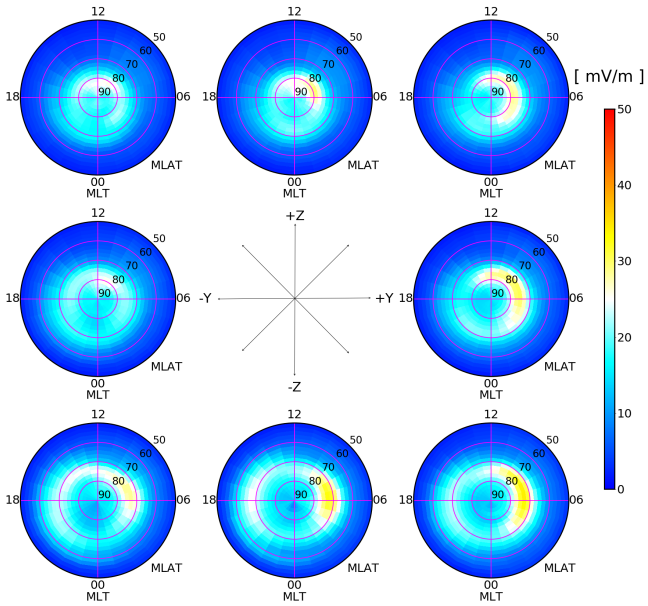

Figure 5.17: High-latitude (a) mean electric field and (b) electric field variability magnitudes as a function of MLAT and MLT for eight different IMF clock angles. The IMF $B_t = 8$nT, $V_{SW} = 450$ km/s and $N_{SW} = 4$ cm^{-3}. All plots are represented in geomagnetic coordinates.

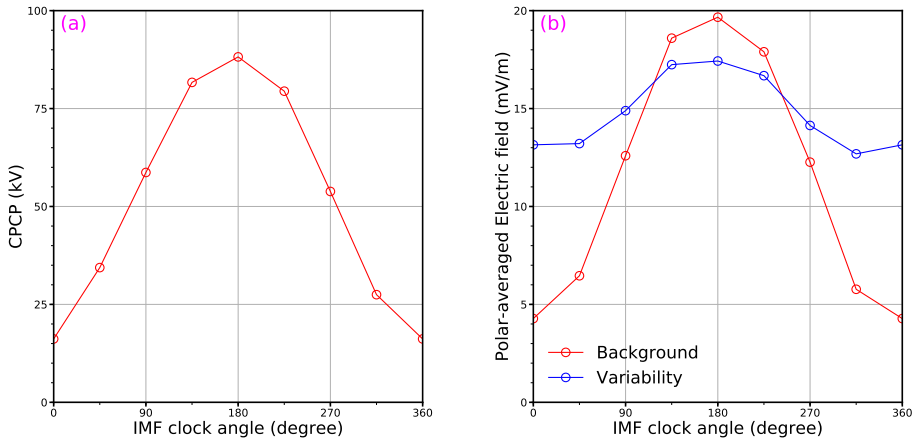

Figure 5.18: The IMF clock angle variations of (a) cross-polar-cap potential as well as (b) polar averages of mean electric field (blue) and electric field variability (red) magnitudes when the IMF $B_t = 8$nT, $V_{SW} = 450$ km/s and $N_{SW} = 4$ cm^{-3}.

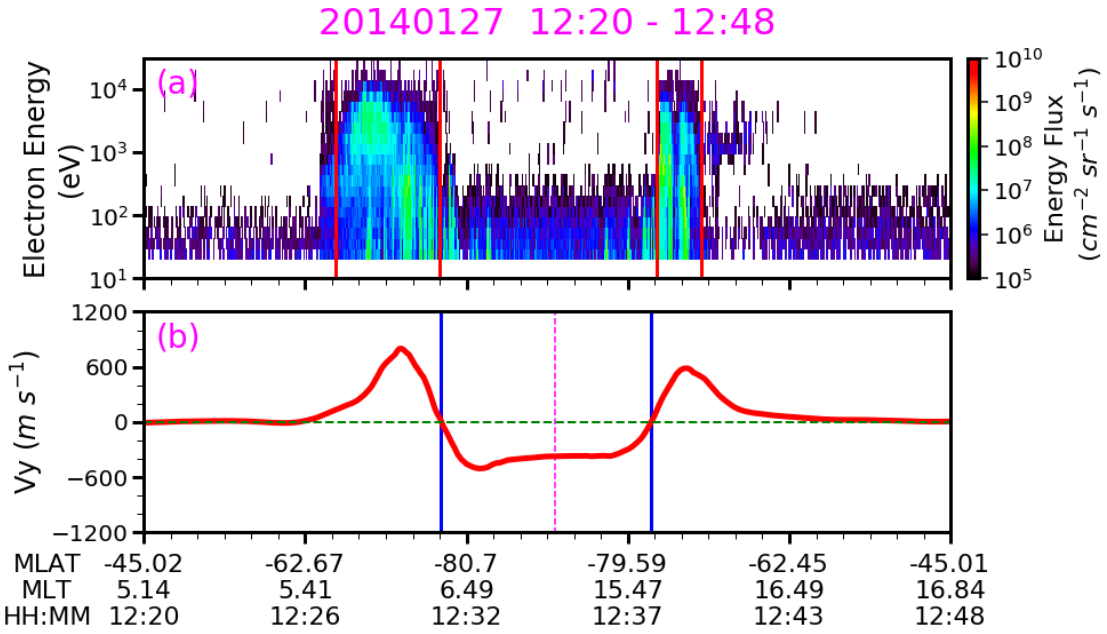

Figure 5.19: (a) The electron energy spectrogram from a DMSP F16 polar trajectory in the Southern Hemisphere; (b) The horizontal cross-track ion drift (V_y) measurements smoothed by a 500-km moving average window along the same trajectory. Vertical red lines in Plot (a) and vertical blue lines in Plot (b) denote the auroral boundaries and convection reversal boundaries (CRBs) along this trajectory, respectively. Vertical magenta dashed line in Plot (b) denotes the zero-potential point of this trajectory

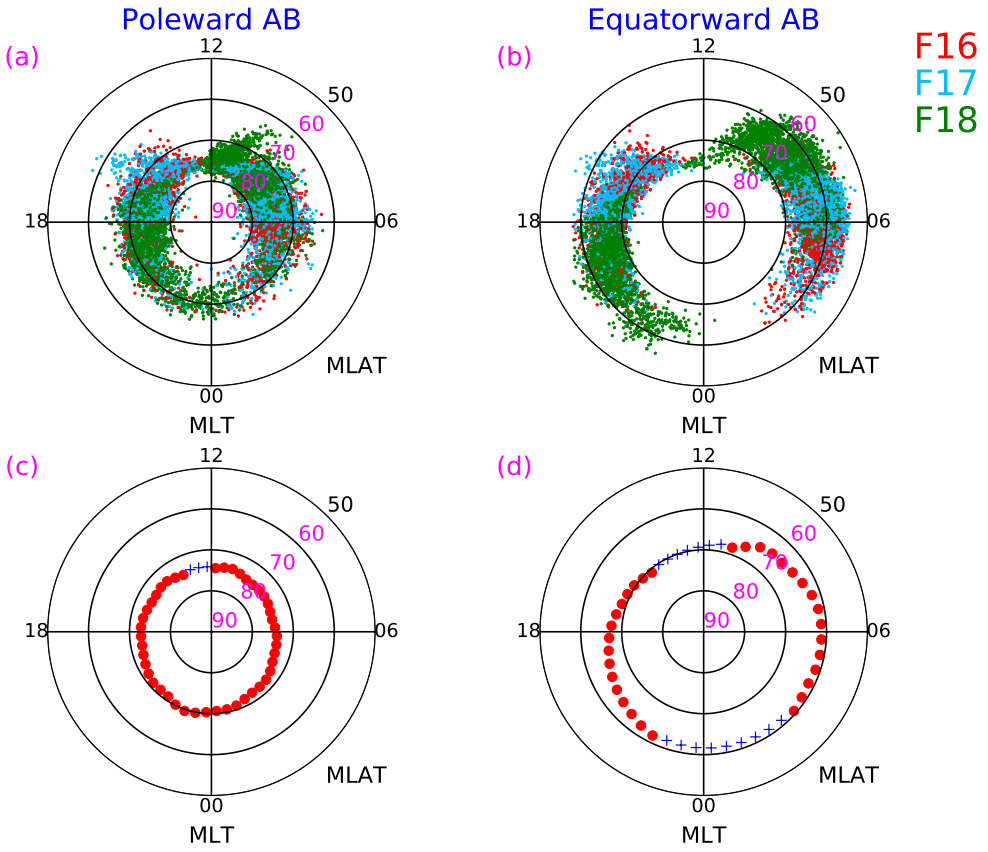

Figure 5.20: Scatters of (a) poleward auroral boundary and (b) equatorward auroral boundary identified under moderately strong and dominant southward interplanetary magnetic field (IMF) conditions as a function of magnetic local time (MLT) and magnetic latitude (MLAT). Different colors denote different satellites (Red: F16; Blue: F17; Green: F18); (Bottom) Distributions of the median MLAT of (c) poleward auroral boundary and (d) equatorward auroral boundary. Red dots indicate bins with sufficient boundaries whereas blue plus signs suggest bins without enough boundaries and represent fitted MLATs.

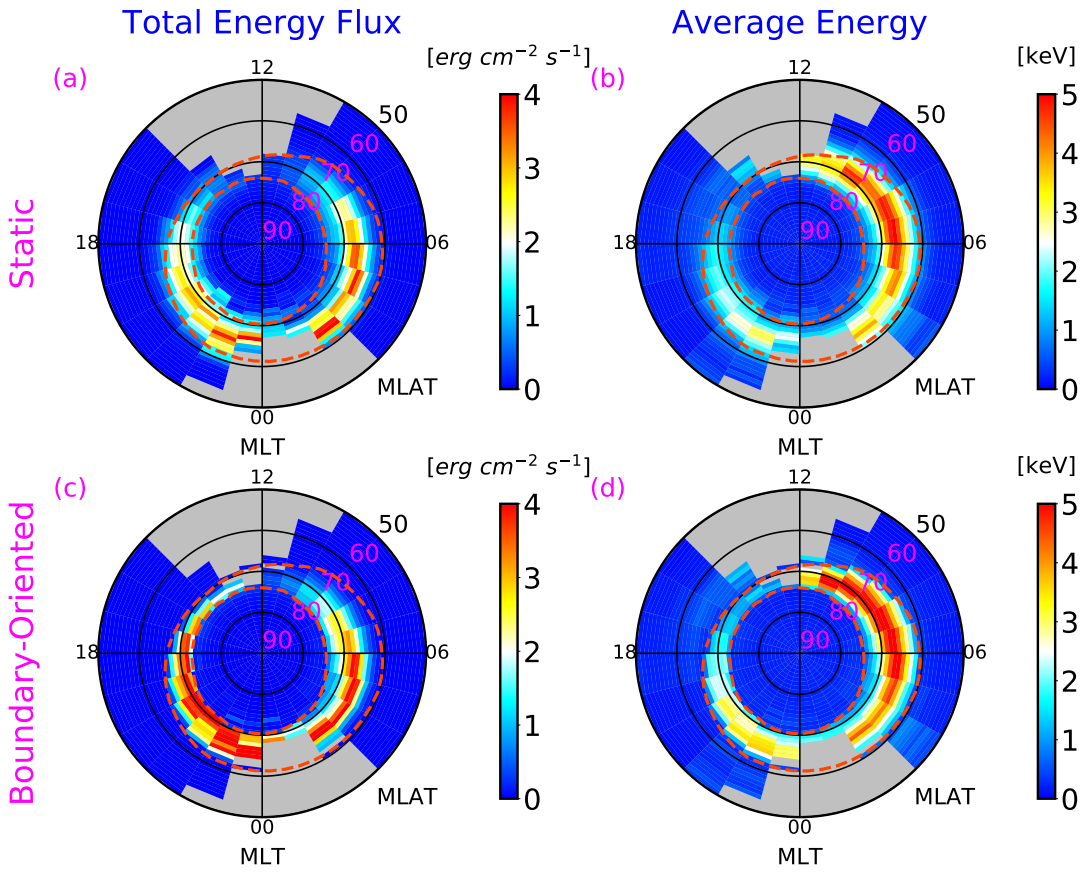

Figure 5.21: (Top) Static and (Bottom) Boundary-oriented binning results for (Left) total electron energy flux and (Right) average electron energy. Red dashed lines stand for statistical locations of the auroral boundaries. Grey shaded areas indicate regions without enough data. All plots are presented in geomagnetic coordinates.

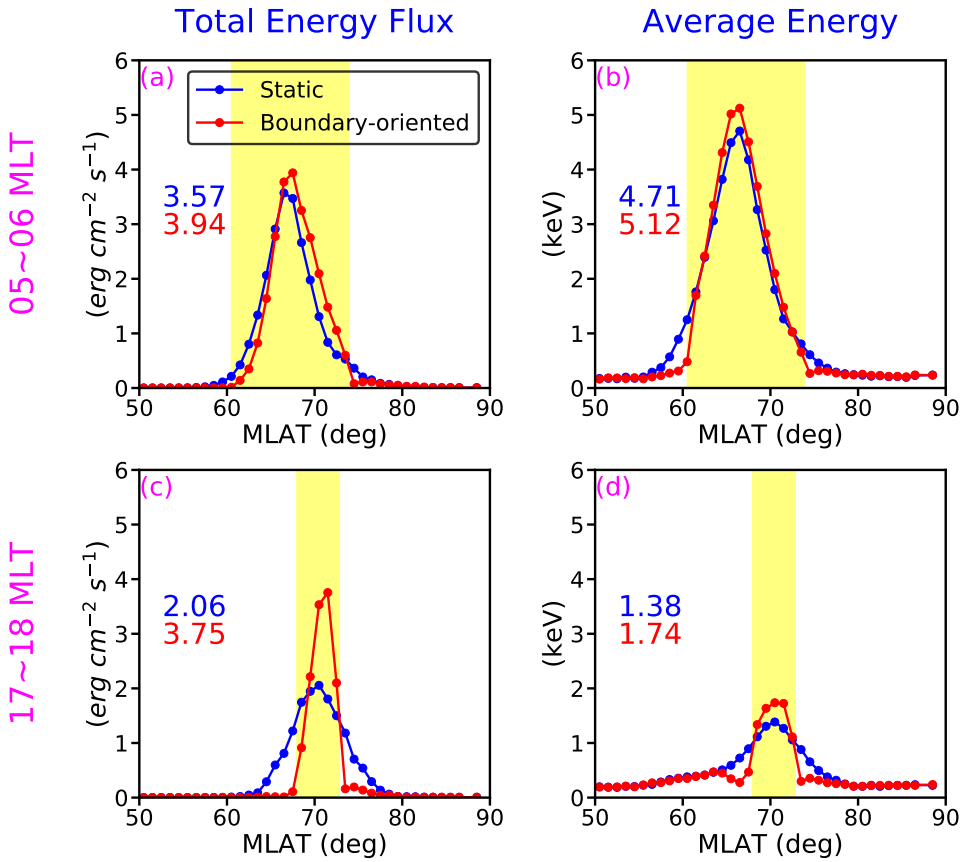

Figure 5.22: Comparisons of latitudinal profiles of (Left) total electron energy flux and (Right) average electron energy obtained through different binning methods in (Top) 5-6 MLT and (Bottom) 17-18 MLT sectors. Blue and red lines denote static and boundary-oriented binning results, respectively. Yellow-shaded areas correspond to the auroral zone. The numbers in each plot represent the values of the maximum magnitude of the static (blue) and boundary-oriented (red) profiles.

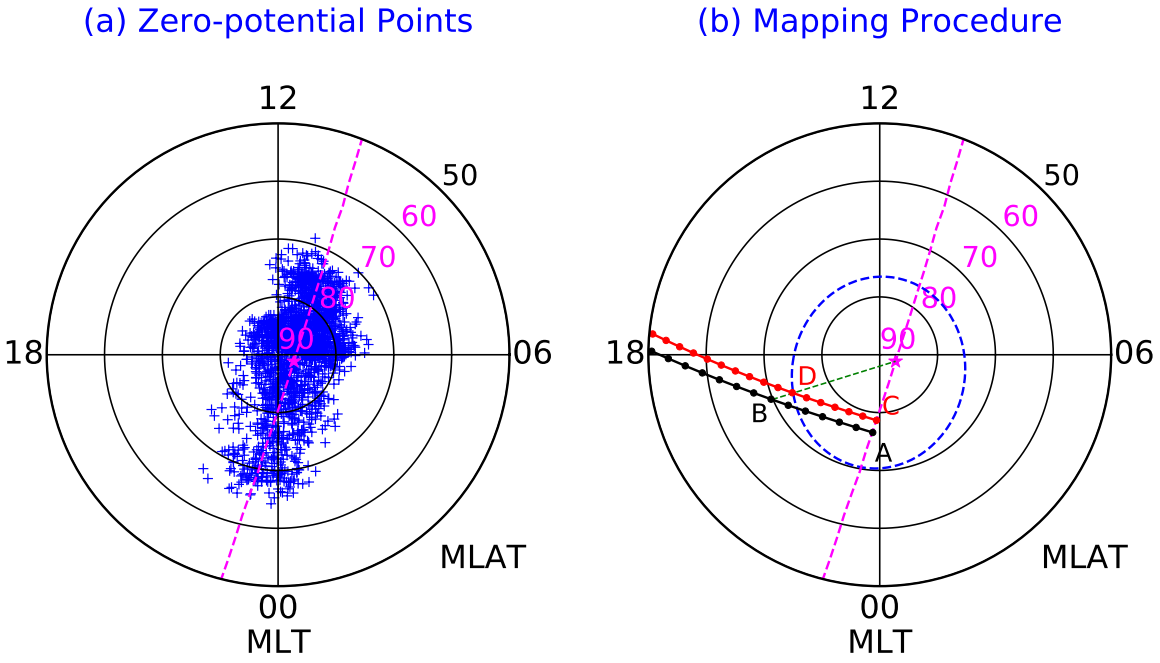

Figure 5.23: (a) Distributions of the zero-potential points identified under moderately strong and dominant southward interplanetary magnetic field (IMF) conditions as a function of magnetic local time (MLT) and magnetic latitude (MLAT). Magenta dashed line indicates the best-fit parabola of the zero-potential points and the magenta star denotes the vertex of the parabola. (b) An example to illustrate how to organize electric potential data according to the CRB. Blue dashed line indicates the location of the reference CRB. The black dotted line indicates the trajectory after the minimum displacement that makes its zero-potential potential point lie on the parabola. The red dotted line indicates the mapped trajectory, involving a further displacement as well as a contraction or elongation to make the CRB for that pass lie on the reference CRB. See text for more details.

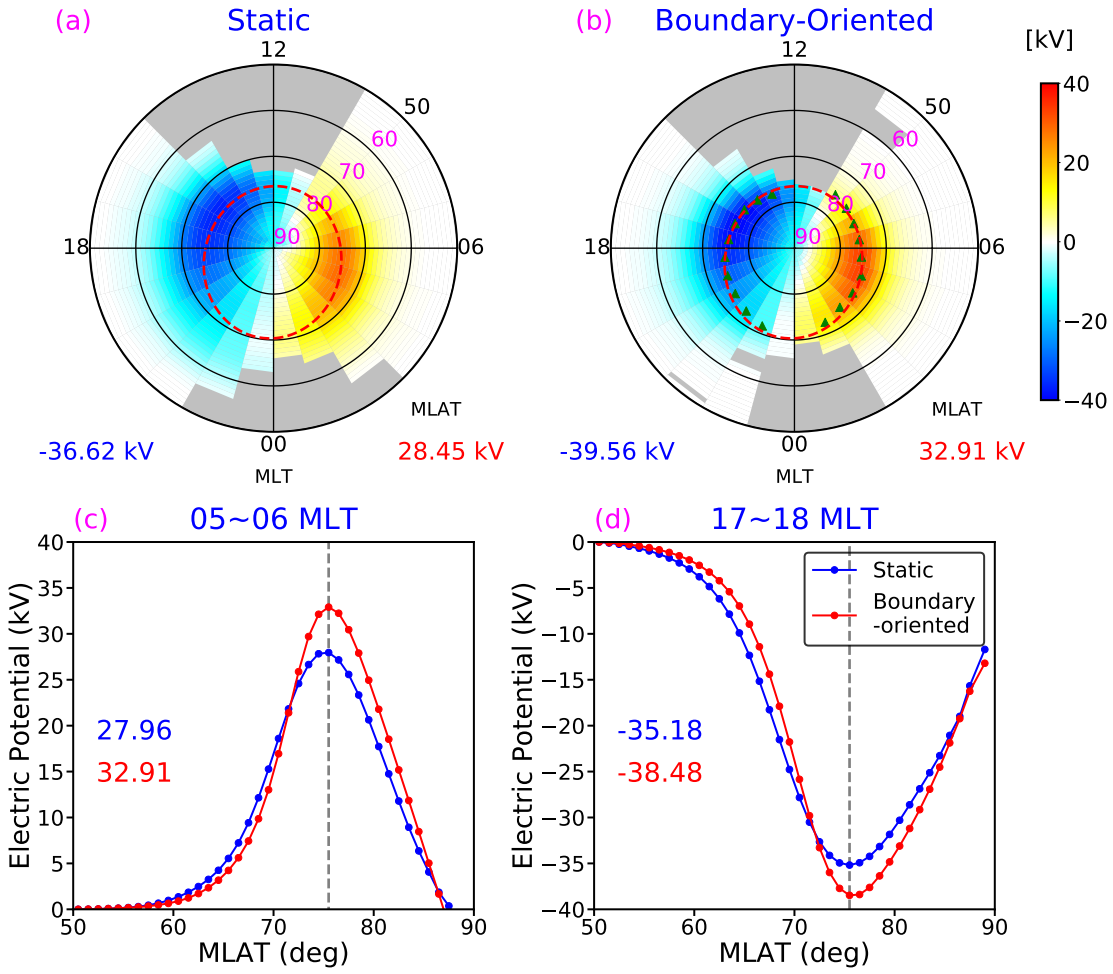

Figure 5.24: (Top) Electric potential pattern derived from the (a) static and (b) boundary-oriented binning methods, respectively. The potential maximum and minimum for each pattern are labeled at the bottom right and left sides of plots (a) and (b), respectively. Red dashed line in Plots (a) and (b) denotes the location of the reference CRB. Green triangles in Figure 6b denotes the unbiased CRB. Grey shaded areas indicate regions without enough data. Both plots are presented in geomagnetic coordinates; (Bottom) Comparisons of latitudinal profiles of electric potential obtained through different binning methods in (c) 5-6 MLT and (d) 17-18 MLT sectors. The grey dashed lines correspond to the convection reversal boundary. The numbers in both plots represent the values of the maximum magnitude of the static (blue) and boundary-oriented (red) profiles.

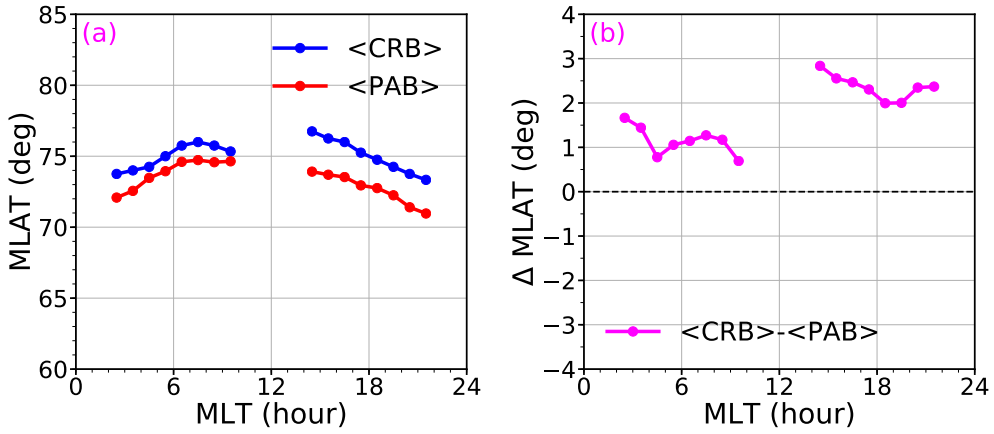

Figure 5.25: (a) Distributions of the magnetic latitudes (MLATs) of the unbiased CRB and average PAB as a function of magnetic local time (MLT) (b) MLAT offsets between the locations of the unbiased CRB and average PAB as a function of MLT.

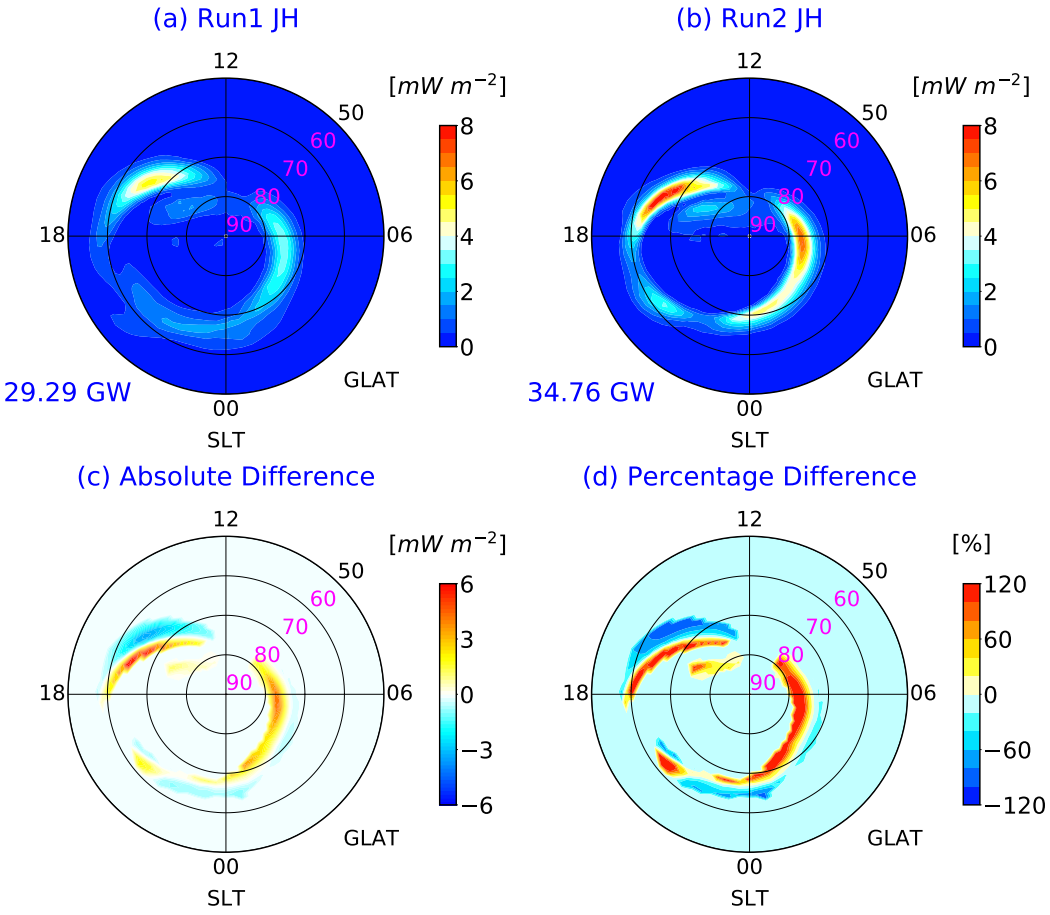

Figure 5.26: (a) Distribution of the height-integrated Joule heating from Run 1; (b) Distribution of the height-integrated Joule heating from Run 2. The hemispherical-integrated Joule heating are denoted at the left bottom of each plots. (c) Absolute difference of the height-integrated Joule heating between Run 2 and Run 1 (Run 2 − Run 1); (d) Percentage difference of the height-integrated Joule heating between Run 2 and Run 1 ((Run 2 − Run 1)/Run 1 × 100%).All plots are presented in geographic coordinates.

CHAPTER 6

Summary and Future work

6.1 Summary

This dissertation aims to advance the knowledge of multiscale ionospheric electrodynamics. On the one hand, this dissertation focused on the low- and mid-latitude electrodynamics which is related to the internal wind dynamo process. In particular, we have investigated impacts of the vertical neutral dynamics on the thermosphere in a non-hydrostatic model, GITM for the first time. It is found that:

(1) The equatorial ionization anomaly (EIA) and the equatorial thermosphere anomaly (ETA) are well reproduced after including the electric fields at low and middle latitudes. The characteristics of the EIA and ETA are generally consistent with the findings in previous studies. The daytime upward wind near the geomagnetic equator leads to the enhancement of the neutral mass density at 400 km altitude, while the divergence in the meridional wind associated with the meridional ion-drag force transports the neutral mass density away from the geomagnetic equator, which may contribute to the formation of the ETA trough.

(2) The changes of the vertical forces acting on the neutrals result in changes in the vertical dynamics of the thermosphere, which feedback to the vertical ion-drag and pressure gradient forces. The vertical ion-drag and pressure gradient forces show predominant changes near the geomagnetic equator throughout the simulation. More specifically,

the daytime vertical ion-drag force is generally enhanced near the geomagnetic equator and the daytime upward pressure gradient force near the geomagnetic equator is reduced at most times after adding in the electric fields at low and middle latitudes. The sudden introduction of the electric fields at low and middle latitudes induces acoustic waves in the vertical pressure gradient force.

On the other hand, this dissertation has also focused on the high-latitude electrodynamics which is mainly controlled by the solar wind-magnetosphere-ionosphere coupling. This begins with advancing the statistical knowledge of the small-scale and mesoscale structures in high-latitude electrodynamic forcings as well as their impacts on Joule heating, which is still lacking to date. First, this dissertation has studied small-scale and mesoscale electric fields and electron precipitations, it is found that:

(1) The electric field and electron precipitation are not negligible on mesoscale and small scale and can be treated as variabilities with respect to the large-scale pattern statistically. More importantly, the electric field tends to be anti-correlated with the electron energy on small scale and mesoscale, indicating that the magnetosphere is likely to behave as a current generator on small scale and mesoscale.

(2) Although Joule heating can be significantly elevated by the small-scale and mesoscale electric field variability, the corresponding change in the particle precipitation tends to depress such enhancement due to the anti-correlation between the small-scale and mesoscale electric field and particle precipitation variabilities. Moreover, the localized reduction is significant on the dusk side, suggesting that the impact of the anti-correlation between the small-scale and mesoscale electric field and particle precipitation variabilities on Joule heating is not negligible there.

Second, this dissertation also studies the relationship between FAC and electric field on small scale and mesoscale, where it is found that strong FACs on small scale and

mesoscale do not necessarily correspond to strong ionospheric electric fields on those scales. However, the impacts on Joule heating associated with mesoscale FACs cannot be simply ignored.

As for the high-latitude electrodynamics, this dissertation also focuses on improving specifications of high-latitude electrodynamical forcings in GCMs, which is a challenging topic in the community. In particular, a new empirical model, ASHLEY, have been developed, which can improve soft electron precipitation and electric field variability specifications and can further improve estimations of both the altitudinal distribution and the total input of Joule heating in GCMs. More specifically:

(1) Based on 6 years of the DMSP electron precipitation measurements, a new empirical electron precipitation model (ASHLEY-A) is developed. The auroral electron precipitation component, ASHLEY-A, can directly provide the averaged differential energy flux in 19 DMSP energy channels under different IMF and solar wind conditions without making any assumptions about the energy spectrum. Hence, soft electron precipitation specifications can be remarkably improved, which can further improve the altitudinal distribution of Joule heating in GCMs.

(2) Based on DMSP bulk ion drift measurements, empirical models that are able to consistently describe high-latitude large-scale mean electric field (ASHLEY-E) and electric field variability (ASHLEY-Evar) have been developed. With the inclusion of the ASHLEY-Evar, the total Joule heating input can be better estimated in GCMs especially during northward IMF cases.

Moreover, by coupling the ASHLEY-A with GITM, the impacts on the storm-time neutral density and satellite drag estimations in GCMs when the high-latitude soft electron precipitations are better specified have also been investigated in this dissertation through the data-model comparison. It is found that estimations of the storm-time neutral mass density

and satellite drag have been remarkably improved when the soft electron precipitation is better specified.

Finally, this dissertation also explores potential improvements in the binning method that may be able to improve the high-latitude forcing specifications in empirical models. A novel boundary-oriented binning method has been applied in establishing statistical electron precipitation and electric potential patterns and the results are quantitatively compared with those established by using traditional static binning method. In addition, both static and boundary-oriented patterns are implemented in the GITM to assess the impacts on Joule heating. It is found that the boundary-oriented binning method is able to effectively address the smoothing issue caused by the traditional static binning method, which can further improve the Joule heating estimation in GCMs.

6.2 Future work

While the above have enhanced the present understanding of multiscale ionospheric electrodynamics, there still remains many open questions. A few of them are listed below that may be able to be addressed by the continuation of this dissertation:

6.2.1 Neutral wind response to small-scale and mesoscale electrodynamical forcings

In Section 4.1, the small-scale and mesoscale electric field and electron precipitation are included in GITM as fast-varying variabilities and are assumed to be uncorrelated with the neutral wind. However, the small-scale and mesoscale electric field and electron precipitation structures can persist for a long time ($>$30 min) in reality, which may cause significant disturbances in the neutral winds. For example, *Zou et al.* (2018) found that the F-region neutral wind disturbances maximized on $<$20 min after the ion flows when quasi-steady mesoscale auroral structures appears during substorms, and the time delay is

much smaller than that determined in previous studies which is on the order of hours (e.g., *Heelis et al.*, 2002). The high-latitude F-region neutral winds are primarily influenced by the pressure gradient and ion-drag forces (e.g., *Killeen and Roble*, 1984), however it is still unclear the relative significance of the pressure gradient and ion drag forces in the rapid response of the neutral winds. To address this question, the high-resolution SuperDARN convection patterns (*Bristow*, 2019) and together with auroral patterns obtained by all-sky imagers (*Mende et al.*, 2008) will be used to improve high-latitude drivers of an updated version of GITM in which the localized refinement technique is implemented (GITM-R, *Deng et al.*, 2019). The term analysis will be conducted to determine the relative contributions of the pressure gradient and ion drag forces to the fast response of the neutral winds.

6.2.2 Driving GCMs with asymmetric FACs

The large-scale FAC distributions at both NH and SH can be provided by the AMPERE based on measurements from the Iridium Constellation in a quite high temporal cadence. The standard temporal resolution of AMPERE is 10 min and *Shi et al.* (2020) has developed an methodology that is able to improve the temporal resolution to 2 min recently. Such high temporal resolution can substantially resolve large-scale FAC variabilities so that the performance of GCMs can be significantly improved (Section 4.2). In addition, the relatively good spatial coverage of the Iridium Constellation is another advantage of using AMPERE data to drive GCMs. Hence, with proper electron precipitation distributions, the FAC-driving GCM simulations may be able to better represent the I-T response to a geomagnetic storm.

Nevertheless, like the NCAR 3D electrodynamo solver used in GITM (Section 2.2.4), the electrodynamo solver used in GCMs intrinsically assumes that the NH and SH have symmetric FAC distributions at high latitudes (to reduce computational challenges), which

may be invalid under certain circumstances. For example, the FACs are typically larger in the summer hemisphere than the winter hemisphere (e.g., *Coxon et al.*, 2016). Meanwhile, the distributions of NH and SH FACs can be substantially different during geomagnetic storms (e.g., *Anderson et al.*, 2018). Therefore, it is necessary to improve the ionospheric electrodynamo solver used in GCMs so that it can deal with the asymmetric FAC cases.

Once the electrodynamo solver is updated and validated, the 2-min AMPERE FAC distributions derived by *Shi et al.* (2020) will be used to drive GITM together with appropriate electron precipitation inputs for the March 17-18, 2013 geomagnetic storm. The I-T response to the high-resolution inputs will be examined in detail. Moreover, results will be compared between the simulations driven by FAC patterns with different temporal resolutions to investigate the role that large-scale FAC variability play during this event. Further, different storms will be investigated.

6.2.3 Generation mechanism of the poleward propagating large-scale traveling ionospheric disturbances

During the geomagnetic storms, equatorward LSTADs and LSTIDs can be generated although their relationship is still unknown (*Heelis and Maute*, 2020). In addition, *Lu et al.* (2016) also found that the poleward propagating LSTADs (PP-LSTADs) can be generated during geomagnetic storms, which may contribute to the neutral mass density maxima found in the polar cap (*Huang et al.*, 2017). Recently, *Zhang et al.* (2019) found that the LSTIDs may also be able to propagate poleward in the polar cap on the day side. However, the generation mechanism of the dayside poleward propagating LSTIDs (PP-LSTIDs) is still unknown. There might be two candidate mechanisms that are responsible for the generation of the PP-LSTIDs: 1) PP-LSTADs: *Knipp et al.* (2011) found that extreme Poynting flux depositions frequently occurred in the dayside cusp region, the heating may be able to excite PP-LSTADs that can further generate PP-LSTIDs via the ion-neutral coupling; 2)

Dayside soft electron precipitations: the ionization associated with the dayside soft electron precipitations may be able to produce low-density patches (*Walker et al.*, 1999), and oscillations in the dayside soft electron precipitations due to transient magnetospheric processes may be able to produce a series of low-density polar cap patches (*Nishimura et al.*, 2014). Those patches subsequently propagate anti-sunward along with the large-scale ionospheric convection and may be detected as the PP-LSTID. The controlled GITM simulations may shed lights on the generation mechanism.

6.2.4 Relative contributions of the electric field variability and soft electron precipitation to the storm-time neutral mass density

In Section 5.2, while impacts of soft electron precipitations on the storm-time neutral mass density has been investigated, the relative contributions of the soft electron precipitation and electric field variability to the storm-time neutral mass density are still unknown. The relative significance may vary at different storm phases or in different storms, thus it might be necessary to establish a comprehensive understanding on their relative significances. More insights can be provided after coupling all components of the ASHLY model into GITM and conducting several data-model comparisons.

6.2.5 Application of the machine learning technique in the empirical model development

The empirical models established in Chapter 5 are developed through traditional fitting procedures. However, since machine learning is a rising discipline, it is promising to apply some machine learning algorithms to the abundant electric field and electron precipitation data and establish new empirical models. The behavior of new empirical models can be further compared with the models established in Chapter 5.

APPENDIX A

Usage of previously published materials

Figure 1.2 originally appeared as Figure 4 of *Heelis* (2004) and is reprinted from Journal of Atmospheric and Solar-Terrestrial Physics, 66(10), R.A. Heelis, Electrodynamics in the low and middle latitude ionosphere, 825-838, 2004, with permission from Elsevier.

Figure 1.3 originally appeared as Figure 1 of *Fejer* (2011) and is reprinted by permission from the Springer Nature: Springer, Space Science Review, Low Latitude Ionospheric Electrodynamics, Bela G. Fejer, 2011.

Figure 1.5 originally appeared as Figure 1 of *Lyons* (1992) and is reprinted from Reviews of Geophysics, 30(2), L. R. Lyons, Formation of auroral arcs via magnetosphere-ionosphere coupling, 1992, with permission from John Wiley and Sons.

Figure 1.6 originally appeared as Figure 1 of *Le et al.* (2010) and is reprinted from Journal of Geophysical Research: Space Physics, 115(A7), G. Le, J. A. Slavin and, R. J. Strangeway, Space Technology 5 observations of the imbalance of regions 1 and 2 field-aligned currents and its implication to the cross-polar cap Pedersen currents, 2010, with permission from John Wiley and Sons.

Chapter 3 is modified from *Zhu et al.* (2017). Section 4.1 is modified from *Zhu et al.* (2018) and Section 4.2 is modified from *Zhu et al.* (2019). Section 5.4 is modified from *Zhu et al.* (2020). Part of the introduction from those four papers are used in Section 1.2.

I would also like to acknowledge the John Wiley and Sons for the reuse of the amended version of my own articles for this dissertation.

REFERENCES

Anderson, B. J., C. N. Olson, H. Korth, R. J. Barnes, C. L. Waters, and S. K. Vines (2018), Temporal and Spatial Development of Global Birkeland Currents, *Journal of Geophysical Research (Space Physics)*, *123*(6), 4785–4808, doi:10.1029/2018JA025254.

Anderson, R. L., G. H. Born, and J. M. Forbes (2009), Sensitivity of Orbit Predictions to Density Variability, *Journal of Spacecraft and Rockets*, *46*(6), 1214–1230, doi: 10.2514/1.42138.

Appleton, E. V. (1946), Two Anomalies in the Ionosphere, *Nature*, *157*(3995), 691, doi: 10.1038/157691a0.

Baker, J. B., C. R. Clauer, A. J. Ridley, V. O. Papitashvili, M. J. Brittnacher, and P. T. Newell (2000), The nightside poleward boundary of the auroral oval as seen by DMSP and the Ultraviolet Imager, *J. Geophys. Res.*, *105*(A9), 21,267–21,280, doi: 10.1029/1999JA000363.

Baker, J. B. H., Y. Zhang, R. A. Greenwald, L. J. Paxton, and D. Morrison (2004), Height-integrated Joule and auroral particle heating in the night side high latitude thermosphere, *Geophys. Res. Lett.*, *31*(9), L09807, doi:10.1029/2004GL019535.

Billett, D. D., A. Grocott, J. A. Wild, M. T. Walach, and M. J. Kosch (2018), Diurnal Variations in Global Joule Heating Morphology and Magnitude Due To Neutral

Winds, *Journal of Geophysical Research (Space Physics)*, *123*(3), 2398–2411, doi: 10.1002/2017JA025141.

Blanc, M., and A. D. Richmond (1980), The ionospheric disturbance dynamo, *J. Geophys. Res.*, *85*(A4), 1669–1686, doi:10.1029/JA085iA04p01669.

Bowman, B., W. K. Tobiska, F. Marcos, C. Huang, C. Lin, and W. Burke (2008), A new empirical thermospheric density model jb2008 using new solar and geomagnetic indices, in *AIAA/AAS Astrodynamics specialist conference and exhibit*, p. 6438.

Brinkman, D. G., R. L. Walterscheid, J. H. Clemmons, and J. H. Hecht (2016), High-resolution modeling of the cusp density anomaly: Response to particle and Joule heating under typical conditions, *Journal of Geophysical Research (Space Physics)*, *121*(3), 2645–2661, doi:10.1002/2015JA021658.

Bristow, W. A. (2019), Application of RADAR Imaging Analysis to SuperDARN Observations, *Radio Science*, *54*(7), 692–703, doi:10.1029/2019RS006851.

Bristow, W. A., and J. Spaleta (2013), An investigation of the characteristics of the convection reversal boundary under southward interplanetary magnetic field, *Journal of Geophysical Research (Space Physics)*, *118*(10), 6338–6351, doi:10.1002/jgra.50526.

Burch, J. L., P. H. Reiff, J. D. Menietti, R. A. Heelis, W. B. Hanson, S. D. Shawhan, E. G. Shelley, M. Sugiura, D. R. Weimer, and J. D. Winningham (1985), IMF B_y-dependent plasma flow and Birkeland currents in the dayside magnetosphere 1. Dynamics Explorer observations, *J. Geophys. Res.*, *90*(A2), 1577–1594, doi:10.1029/JA090iA02p01577.

Burrell, A. G., G. Chisham, S. E. Milan, L. Kilcommons, Y.-J. Chen, E. G. Thomas, and B. Anderson (2020), Ampere polar cap boundaries, *Annales Geophysicae*, *38*(2), 481–490, doi:10.5194/angeo-38-481-2020.

Candidi, M., H. W. Kroehl, and C. I. Meng (1983), Intensity distribution of dayside polar soft electron precipitation and the IMF, *Planetary and Space Science*, *31*(5), 489–498, doi:10.1016/0032-0633(83)90040-5.

Carter, J. A., S. E. Milan, J. C. Coxon, M. T. Walach, and B. J. Anderson (2016), Average field-aligned current configuration parameterized by solar wind conditions, *Journal of Geophysical Research (Space Physics)*, *121*(2), 1294–1307, doi: 10.1002/2015JA021567.

Chen, G.-M., J. Xu, W. Wang, J. Lei, and A. G. Burns (2012), A comparison of the effects of CIR- and CME-induced geomagnetic activity on thermospheric densities and spacecraft orbits: Case studies, *Journal of Geophysical Research (Space Physics)*, *117*(A8), A08315, doi:10.1029/2012JA017782.

Chen, Y.-J., and R. A. Heelis (2018), Mesoscale Plasma Convection Perturbations in the High-Latitude Ionosphere, *Journal of Geophysical Research (Space Physics)*, *123*(9), 7609–7620, doi:10.1029/2018JA025716.

Chen, Y. J., R. A. Heelis, and J. A. Cumnock (2015), Response of the ionospheric convection reversal boundary at high latitudes to changes in the interplanetary magnetic field, *Journal of Geophysical Research (Space Physics)*, *120*(6), 5022–5034, doi: 10.1002/2015JA021024.

Chisham, G. (2017), A new methodology for the development of high-latitude ionospheric climatologies and empirical models, *Journal of Geophysical Research (Space Physics)*, *122*(1), 932–947, doi:10.1002/2016JA023235.

Clayton, R., K. Lynch, M. Zettergren, M. Burleigh, M. Conde, G. Grubbs, D. Hampton, D. Hysell, M. Lessard, R. Michell, A. Reimer, T. M. Roberts, M. Samara, and R. Varney

(2019), Two-Dimensional Maps of In Situ Ionospheric Plasma Flow Data Near Auroral Arcs Using Auroral Imagery, *Journal of Geophysical Research (Space Physics)*, *124*(4), 3036–3056, doi:10.1029/2018JA026440.

Codrescu, M. V., T. J. Fuller-Rowell, and J. C. Foster (1995), On the importance of E-field variability for Joule heating in the high-latitude thermosphere, *Geophys. Res. Lett.*, *22*(17), 2393–2396, doi:10.1029/95GL01909.

Codrescu, M. V., T. J. Fuller-Rowell, J. C. Foster, J. M. Holt, and S. J. Cariglia (2000), Electric field variability associated with the Millstone Hill electric field model, *J. Geophys. Res.*, *105*(A3), 5265–5274, doi:10.1029/1999JA900463.

Codrescu, M. V., T. J. Fuller-Rowell, V. Munteanu, C. F. Minter, and G. H. Millward (2008), Validation of the Coupled Thermosphere Ionosphere Plasmasphere Electrodynamics model: CTIPE-Mass Spectrometer Incoherent Scatter temperature comparison, *Space Weather*, *6*(9), 09005, doi:10.1029/2007SW000364.

Cole, K. D. (1962), Joule Heating of the Upper Atmosphere, *Australian Journal of Physics*, *15*, 223, doi:10.1071/PH620223.

Cosgrove, R., M. McCready, R. Tsunoda, and A. Stromme (2011), The bias on the joule heating estimate: Small-scale variability versus resolved-scale model uncertainty and the correlation of electric field and conductance, *Journal of Geophysical Research: Space Physics*, *116*(A9), doi:10.1029/2011JA016665.

Cosgrove, R. B., and J. P. Thayer (2006), Parametric dependence of electric field variability in the sondrestrom database: A linear relation with kp, *Journal of Geophysical Research: Space Physics*, *111*(A10), doi:10.1029/2006JA011658.

Cousins, E. D. P., and S. G. Shepherd (2010), A dynamical model of high-latitude convection derived from SuperDARN plasma drift measurements, *Journal of Geophysical Research (Space Physics)*, *115*(A12), A12329, doi:10.1029/2010JA016017.

Cousins, E. D. P., and S. G. Shepherd (2012a), Statistical characteristics of small-scale spatial and temporal electric field variability in the high-latitude ionosphere, *Journal of Geophysical Research (Space Physics)*, *117*(A3), A03317, doi:10.1029/2011JA017383.

Cousins, E. D. P., and S. G. Shepherd (2012b), Statistical maps of small-scale electric field variability in the high-latitude ionosphere, *Journal of Geophysical Research (Space Physics)*, *117*(A12), A12304, doi:10.1029/2012JA017929.

Coxon, J. C., S. E. Milan, L. B. N. Clausen, B. J. Anderson, and H. Korth (2014), The magnitudes of the regions 1 and 2 Birkeland currents observed by AMPERE and their role in solar wind-magnetosphere-ionosphere coupling, *Journal of Geophysical Research (Space Physics)*, *119*(12), 9804–9815, doi:10.1002/2014JA020138.

Coxon, J. C., S. E. Milan, J. A. Carter, L. B. N. Clausen, B. J. Anderson, and H. Korth (2016), Seasonal and diurnal variations in AMPERE observations of the Birkeland currents compared to modeled results, *Journal of Geophysical Research (Space Physics)*, *121*(5), 4027–4040, doi:10.1002/2015JA022050.

de la Beaujardiere, O., D. Alcayde, J. Fontanari, and C. Leger (1991), Seasonal dependence of high-latitude electric fields, *J. Geophys. Res.*, *96*(A4), 5723–5735, doi:10.1029/90JA01987.

Deng, Y., and A. J. Ridley (2006), Dependence of neutral winds on convection E-field, solar EUV, and auroral particle precipitation at high latitudes, *Journal of Geophysical Research (Space Physics)*, *111*(A9), A09306, doi:10.1029/2005JA011368.

Deng, Y., A. D. Richmond, A. J. Ridley, and H.-L. Liu (2008), Assessment of the non-hydrostatic effect on the upper atmosphere using a general circulation model (GCM), *Geophys. Res. Lett.*, *35*(1), L01104, doi:10.1029/2007GL032182.

Deng, Y., A. Maute, A. D. Richmond, and R. G. Roble (2009), Impact of electric field variability on Joule heating and thermospheric temperature and density, *Geophys. Res. Lett.*, *36*(8), L08105, doi:10.1029/2008GL036916.

Deng, Y., T. J. Fuller-Rowell, R. A. Akmaev, and A. J. Ridley (2011), Impact of the altitudinal Joule heating distribution on the thermosphere, *Journal of Geophysical Research (Space Physics)*, *116*(A5), A05313, doi:10.1029/2010JA016019.

Deng, Y., T. J. Fuller-Rowell, A. J. Ridley, D. Knipp, and R. E. Lopez (2013), Theoretical study: Influence of different energy sources on the cusp neutral density enhancement, *Journal of Geophysical Research (Space Physics)*, *118*(5), 2340–2349, doi:10.1002/jgra.50197.

Deng, Y., Q. Zhu, C. Y. T. Lin, C. Sheng, Y. Zhao, and J. Tyska (2019), Influence of mesoscale forcing on the ionosphere-thermosphere system: GITM simulations, in *AGU Fall Meeting Abstracts*, vol. 2019, pp. SA51A–03.

Ding, G.-X., F. He, X.-X. Zhang, and B. Chen (2017), A new auroral boundary determination algorithm based on observations from TIMED/GUVI and DMSP/SSUSI, *Journal of Geophysical Research (Space Physics)*, *122*(2), 2162–2173, doi:10.1002/2016JA023295.

Doornbos, E., S. Bruinsma, B. Fritsche, P. Visser, J. Van Den IJssel, J. T. Encarnacao, and M. Kern (2013), Air Density And Wind Retrieval Using GOCE Data, in *ESA Living Planet Symposium*, *ESA Special Publication*, vol. 722, p. 7.

Drake, K. A., R. A. Heelis, M. R. Hairston, and P. C. Anderson (2009), Electrostatic potential drop across the ionospheric signature of the low-latitude boundary layer, *Journal of Geophysical Research (Space Physics)*, *114*(A4), A04215, doi:10.1029/2008JA013608.

Dungey, J. W. (1961), Interplanetary magnetic field and the auroral zones, *Phys. Rev. Lett.*, *6*, 47–48, doi:10.1103/PhysRevLett.6.47.

Emmert, J. T. (2015), Thermospheric mass density: A review, *Advances in Space Research*, *56*(5), 773–824, doi:10.1016/j.asr.2015.05.038.

Evans, D. S. (1974), Precipitating electron fluxes formed by a magnetic field aligned potential difference, *J. Geophys. Res.*, *79*(19), 2853, doi:10.1029/JA079i019p02853.

Evans, D. S., and T. E. Moore (1979), Precipitating electrons associated with the diffuse aurora: evidence for electrons of atmospheric origin in the plasma sheet, *J. Geophys. Res.*, *84*(A11), 6451–6457, doi:10.1029/JA084iA11p06451.

Evans, D. S., N. C. Maynard, J. Troim, T. Jacobsen, and A. Egeland (1977), Auroral vector electric field and particle comparisons, 2, Electrodynamics of an arc, *J. Geophys. Res.*, *82*(16), 2235, doi:10.1029/JA082i016p02235.

Fedrizzi, M., T. J. Fuller-Rowell, and M. V. Codrescu (2012), Global Joule heating index derived from thermospheric density physics-based modeling and observations, *Space Weather*, *10*(3), 03001, doi:10.1029/2011SW000724.

Fejer, B. G. (2011), Low Latitude Ionospheric Electrodynamics, *Space Sci. Rev.*, *158*(1), 145–166, doi:10.1007/s11214-010-9690-7.

Fejer, B. G., and L. Scherliess (1997), Empirical models of storm time equatorial zonal electric fields, *J. Geophys. Res.*, *102*(A11), 24,047–24,056, doi:10.1029/97JA02164.

Fejer, B. G., E. R. de Paula, S. A. González, and R. F. Woodman (1991), Average vertical and zonal F region plasma drifts over Jicamarca, *J. Geophys. Res.*, *96*(A8), 13,901–13,906, doi:10.1029/91JA01171.

Feldstein, Y. I., and G. V. Starkov (1967), Dynamics of auroral belt and polar geomagnetic disturbances, *Planetary and Space Science*, *15*(2), 209–229, doi:10.1016/0032-0633(67)90190-0.

Fesen, C. G., G. Crowley, R. G. Roble, A. D. Richmond, and B. G. Fejer (2000), Simulation of the pre-reversal enhancement in the low latitude vertical ion drifts, *Geophys. Res. Lett.*, *27*(13), 1851–1854, doi:10.1029/2000GL000061.

Forbes, J. M., S. E. Palo, and X. Zhang (2000), Variability of the ionosphere, *Journal of Atmospheric and Solar-Terrestrial Physics*, *62*(8), 685–693, doi:10.1016/S1364-6826(00)00029-8.

Forsyth, C., I. J. Rae, I. R. Mann, and I. P. Pakhotin (2017), Identifying intervals of temporally invariant field-aligned currents from Swarm: Assessing the validity of single-spacecraft methods, *Journal of Geophysical Research (Space Physics)*, *122*, 3411–3419, doi:10.1002/2016JA023708.

Foster, J. C., J. M. Holt, R. G. Musgrove, and D. S. Evans (1986), Ionospheric convection associated with discrete levels of particle precipitation, *Geophys. Res. Lett.*, *13*(7), 656–659, doi:10.1029/GL013i007p00656.

Frahm, R. A., J. D. Winningham, J. R. Sharber, R. Link, G. Crowley, E. E. Gaines, D. L. Chenette, B. J. Anderson, and T. A. Potemra (1997), The diffuse aurora: A significant source of ionization in the middle atmosphere, *J. Geophys. Res.*, *102*(D23), 28,203–28,214, doi:10.1029/97JD02430.

Fuller-Rowell, T. J., and D. S. Evans (1987), Height-integrated Pedersen and Hall conductivity patterns inferred from the TIROS-NOAA satellite data, *J. Geophys. Res.*, *92*(A7), 7606–7618, doi:10.1029/JA092iA07p07606.

Fuller-Rowell, T. J., M. V. Codrescu, R. G. Roble, and A. D. Richmond (1997a), How does the thermosphere and ionosphere react to a geomagnetic storm?, *Washington DC American Geophysical Union Geophysical Monograph Series*, *98*, 203–225, doi:10.1029/GM098p0203.

Fuller-Rowell, T. J., M. V. Codrescu, B. G. Fejer, W. Borer, F. Marcos, and D. N. Anderson (1997b), Dynamics of the low-latitude thermosphere: quiet and disturbed conditions, *Journal of Atmospheric and Solar-Terrestrial Physics*, *59*, 1533–1540, doi:10.1016/S1364-6826(96)00154-X.

Fung, S. F., and R. A. Hoffman (1988), On the spectrum of the secondary auroral electrons, *J. Geophys. Res.*, *93*(A4), 2715–2724, doi:10.1029/JA093iA04p02715.

Gjerloev, J. W., S. Ohtani, T. Iijima, B. Anderson, J. Slavin, and G. Le (2011), Characteristics of the terrestrial field-aligned current system, *Annales Geophysicae*, *29*, 1713–1729, doi:10.5194/angeo-29-1713-2011.

Golovchanskaya, I. V., Y. P. Maltsev, and A. A. Ostapenko (2002), High-latitude irregularities of the magnetospheric electric field and their relation to solar wind and geomagnetic conditions, *Journal of Geophysical Research (Space Physics)*, *107*(A1), 1001, doi:10.1029/2001JA900097.

Gonzalez, W. D., J. A. Joselyn, Y. Kamide, H. W. Kroehl, G. Rostoker, B. T. Tsurutani, and V. M. Vasyliunas (1994), What is a geomagnetic storm?, *Journal of Geophysical Research: Space Physics*, *99*(A4), 5771–5792, doi:10.1029/93JA02867.

Haaland, S. E., G. Paschmann, M. Förster, J. M. Quinn, R. B. Torbert, C. E. McIlwain, H. Vaith, P. A. Puhl-Quinn, and C. A. Kletzing (2007), High-latitude plasma convection from Cluster EDI measurements: method and IMF-dependence, *Annales Geophysicae*, *25*(1), 239–253, doi:10.5194/angeo-25-239-2007.

Hairston, M. R., and R. A. Heelis (1990), Model of the high-latitude ionospheric convection pattern during southward interplanetary magnetic field using DE 2 data, *J. Geophys. Res.*, *95*(A3), 2333–2343, doi:10.1029/JA095iA03p02333.

Hairston, M. R., K. A. Drake, and R. Skoug (2005), Saturation of the ionospheric polar cap potential during the October-November 2003 superstorms, *Journal of Geophysical Research (Space Physics)*, *110*(A9), A09S26, doi:10.1029/2004JA010864.

Hanson, W. B., and R. J. Moffett (1966), Ionization transport effects in the equatorial F region, *J. Geophys. Res.*, *71*(23), 5559–5572, doi:10.1029/JZ071i023p05559.

Hanson, W. B., R. A. Heelis, R. A. Power, C. R. Lippincott, D. R. Zuccaro, B. J. Holt, L. H. Harmon, and S. Sanatani (1981), The Retarding Potential Analyzer for Dynamics Explorer-B, *Space Science Instrumentation*, *5*, 503–510.

Hardy, D. A., M. S. Gussenhoven, and E. Holeman (1985), A statistical model of auroral electron precipitation, *J. Geophys. Res.*, *90*(A5), 4229–4248, doi:10.1029/JA090iA05p04229.

Hardy, D. A., M. S. Gussenhoven, R. Raistrick, and W. J. McNeil (1987), Statistical and functional representations of the pattern of auroral energy flux, number flux, and conductivity, *J. Geophys. Res.*, *92*(A11), 12,275–12,294, doi:10.1029/JA092iA11p12275.

Hardy, D. A., E. G. Holeman, W. J. Burke, L. C. Gentile, and K. H. Bounar (2008), Probability distributions of electron precipitation at high magnetic latitudes, *Journal of Geophysical Research (Space Physics)*, *113*(A6), A06305, doi:10.1029/2007JA012746.

Hasunuma, T., T. Nagatsuma, R. Kataoka, Y. Takahashi, H. Fukunishi, A. Matsuoka, and A. Kumamoto (2008), Statistical study of polar distribution of mesoscale field-aligned currents, *Journal of Geophysical Research (Space Physics)*, *113*, A12214, doi: 10.1029/2008JA013358.

He, M., J. Vogt, H. Lühr, E. Sorbalo, A. Blagau, G. Le, and G. Lu (2012), A high-resolution model of field-aligned currents through empirical orthogonal functions analysis (MFACE), *Geophys. Res. Lett.*, *39*(18), L18105, doi:10.1029/2012GL053168.

Hedin, A. E., and H. G. Mayr (1973), Magnetic control of the near equatorial neutral thermosphere, *J. Geophys. Res.*, *78*(10), 1688, doi:10.1029/JA078i010p01688.

Heelis, R. A. (2004), Electrodynamics in the low and middle latitude ionosphere: a tutorial, *Journal of Atmospheric and Solar-Terrestrial Physics*, *66*(10), 825–838, doi: 10.1016/j.jastp.2004.01.034.

Heelis, R. A., and A. Maute (2020), Challenges to understanding the earth's ionosphere and thermosphere, *Journal of Geophysical Research: Space Physics*, p. e2019JA027497.

Heelis, R. A., W. B. Hanson, C. R. Lippincott, D. R. Zuccaro, L. H. Harmon, B. J. Holt, J. E. Doherty, and R. A. Power (1981), The Ion Drift Meter for Dynamics Explorer-B., *Space Science Instrumentation*, *5*, 511–521.

Heelis, R. A., D. McEwen, and W. Guo (2002), Ion and neutral motions observed in the winter polar upper atmosphere, *Journal of Geophysical Research (Space Physics)*, *107*(A12), 1476, doi:10.1029/2002JA009359.

Heppner, J. P., and N. C. Maynard (1987), Empirical high-latitude electric field models, *J. Geophys. Res.*, *92*(A5), 4467–4490, doi:10.1029/JA092iA05p04467.

Hinteregger, H. E., K. Fukui, and B. R. Gilson (1981), Observational, reference and model data on solar EUV, from measurements on AE-E, *Geophys. Res. Lett.*, *8*(11), 1147–1150, doi:10.1029/GL008i011p01147.

Holt, J. M., R. H. Wand, J. V. Evans, and W. L. Oliver (1987), Empirical models for the plasma convection at high latitudes from Millstone Hill observations, *J. Geophys. Res.*, *92*(A1), 203–212, doi:10.1029/JA092iA01p00203.

Holzworth, R. H., and C. I. Meng (1975), Mathematical representation of the auroral oval, *Geophys. Res. Lett.*, *2*(9), 377–380, doi:10.1029/GL002i009p00377.

Hsu, V. W., J. P. Thayer, J. Lei, and W. Wang (2014), Formation of the equatorial thermosphere anomaly trough: Local time and solar cycle variations, *Journal of Geophysical Research (Space Physics)*, *119*(12), 10,456–10,473, doi:10.1002/2014JA020416.

Huang, C. Y., Y. Huang, Y. J. Su, T. Huang, and E. K. Sutton (2017), High-Latitude Neutral Mass Density Maxima, *Journal of Geophysical Research (Space Physics)*, *122*(10), 10,694–10,711, doi:10.1002/2017JA024334.

Huang, Y., A. D. Richmond, Y. Deng, and R. Roble (2012), Height distribution of Joule heating and its influence on the thermosphere, *Journal of Geophysical Research (Space Physics)*, *117*(A8), A08334, doi:10.1029/2012JA017885.

Hurd, L. D., and M. F. Larsen (2016), Small-scale fluctuations in barium drifts at high latitudes and associated Joule heating effects, *Journal of Geophysical Research (Space Physics)*, *121*(1), 779–789, doi:10.1002/2015JA021868.

Iijima, T., and T. A. Potemra (1976a), The amplitude distribution of field-aligned currents at northern high latitudes observed by Triad, *J. Geophys. Res.*, *81*(13), 2165, doi: 10.1029/JA081i013p02165.

Iijima, T., and T. A. Potemra (1976b), Field-aligned currents in the dayside cusp observed by triad, *J. Geophys. Res.*, *81*(A34), 5971–5979, doi:10.1029/JA081i034p05971.

Iijima, T., and T. A. Potemra (1978), Large-scale characteristics of field-aligned currents associated with substorms, *J. Geophys. Res.*, *83*(A2), 599–615, doi: 10.1029/JA083iA02p00599.

Jackson, J. D. (2007), *Classical electrodynamics*, John Wiley & Sons.

Johnson, E. S., and R. A. Heelis (2005), Characteristics of ion velocity structure at high latitudes during steady southward interplanetary magnetic field conditions, *Journal of Geophysical Research (Space Physics)*, *110*(A12), A12301, doi:10.1029/2005JA011130.

Juusola, L., K. Kauristie, O. Amm, and P. Ritter (2009), Statistical dependence of auroral ionospheric currents on solar wind and geomagnetic parameters from 5 years of CHAMP satellite data, *Annales Geophysicae*, *27*(3), 1005–1017, doi:10.5194/angeo-27-1005-2009.

Kelley, M. C. (2009), *The Earth's ionosphere: plasma physics and electrodynamics*, Academic press.

Khazanov, G. V., A. Glocer, and E. W. Himwich (2014), Magnetosphere-ionosphere energy interchange in the electron diffuse aurora, *Journal of Geophysical Research (Space Physics)*, *119*(1), 171–184, doi:10.1002/2013JA019325.

Kilcommons, L. M., R. J. Redmon, and D. J. Knipp (2017), A new DMSP magnetometer and auroral boundary data set and estimates of field-aligned currents in dynamic auroral

boundary coordinates, *Journal of Geophysical Research (Space Physics)*, *122*, 9068–9079, doi:10.1002/2016JA023342.

Killeen, T. L., and R. G. Roble (1984), An analysis of the high-latitude thermospheric wind pattern calculated by a Thermospheric general circulation model 1. Momentum forcing, *J. Geophys. Res.*, *89*(A9), 7509–7522, doi:10.1029/JA089iA09p07509.

Knipp, D., S. Eriksson, L. Kilcommons, G. Crowley, J. Lei, M. Hairston, and K. Drake (2011), Extreme Poynting flux in the dayside thermosphere: Examples and statistics, *Geophys. Res. Lett.*, *38*(16), L16102, doi:10.1029/2011GL048302.

Korth, H., Y. Zhang, B. J. Anderson, T. Sotirelis, and C. L. Waters (2014), Statistical relationship between large-scale upward field-aligned currents and electron precipitation, *Journal of Geophysical Research (Space Physics)*, *119*(8), 6715–6731, doi:10.1002/2014JA019961.

Koustov, A. V., and R. A. D. Fiori (2016), Seasonal and solar cycle variations in the ionospheric convection reversal boundary location inferred from monthly SuperDARN data sets, *Annales Geophysicae*, *34*(2), 227–239, doi:10.5194/angeo-34-227-2016.

Kozelov, B. V., I. V. Golovchanskaya, A. A. Ostapenko, and Y. V. Fedorenko (2008), Wavelet analysis of high-latitude electric and magnetic fluctuations observed by the Dynamic Explorer 2 satellite, *Journal of Geophysical Research (Space Physics)*, *113*(A3), A03308, doi:10.1029/2007JA012575.

Laundal, K. M., and A. D. Richmond (2017), Magnetic coordinate systems, *Space Science Reviews*, *206*(1-4), 27–59.

Le, G., J. A. Slavin, and R. J. Strangeway (2010), Space Technology 5 observations of the imbalance of regions 1 and 2 field-aligned currents and its implication to the cross-

polar cap Pedersen currents, *Journal of Geophysical Research (Space Physics)*, *115*(A7), A07202, doi:10.1029/2009JA014979.

Lei, J., J. P. Thayer, and J. M. Forbes (2010), Longitudinal and geomagnetic activity modulation of the equatorial thermosphere anomaly, *Journal of Geophysical Research (Space Physics)*, *115*(A8), A08311, doi:10.1029/2009JA015177.

Lei, J., J. P. Thayer, W. Wang, A. D. Richmond, R. Roble, X. Luan, X. Dou, X. Xue, and T. Li (2012a), Simulations of the equatorial thermosphere anomaly: Field-aligned ion drag effect, *Journal of Geophysical Research (Space Physics)*, *117*(A1), A01304, doi:10.1029/2011JA017114.

Lei, J., J. P. Thayer, W. Wang, X. Luan, X. Dou, and R. Roble (2012b), Simulations of the equatorial thermosphere anomaly: Physical mechanisms for crest formation, *Journal of Geophysical Research (Space Physics)*, *117*(A6), A06318, doi:10.1029/2012JA017613.

Lei, J., J. P. Thayer, W. Wang, J. Yue, and X. Dou (2014a), Nonmigrating tidal modulation of the equatorial thermosphere and ionosphere anomaly, *Journal of Geophysical Research (Space Physics)*, *119*(4), 3036–3043, doi:10.1002/2013JA019749.

Lei, J., W. Wang, J. P. Thayer, X. Luan, X. Dou, A. G. Burns, and S. C. Solomon (2014b), Simulations of the equatorial thermosphere anomaly: Geomagnetic activity modulation, *Journal of Geophysical Research (Space Physics)*, *119*(8), 6821–6832, doi:10.1002/2014JA020152.

Lei, J., W. Wang, A. G. Burns, X. Yue, X. Dou, X. Luan, S. C. Solomon, and Y. C. M. Liu (2014c), New aspects of the ionospheric response to the October 2003 superstorms from multiple-satellite observations, *Journal of Geophysical Research (Space Physics)*, *119*(3), 2298–2317, doi:10.1002/2013JA019575.

Lin, C. Y., Y. Deng, C. Sheng, and D. P. Drob (2017), A study of the nonlinear response of the upper atmosphere to episodic and stochastic acoustic-gravity wave forcing, *Journal of Geophysical Research (Space Physics)*, *122*(1), 1178–1198, doi: 10.1002/2016JA022930.

Lin, C. Y., Y. Deng, K. Venkataramani, J. Yonker, and S. M. Bailey (2018), Comparison of the Thermospheric Nitric Oxide Emission Observations and the GITM Simulations: Sensitivity to Solar and Geomagnetic Activities, *Journal of Geophysical Research (Space Physics)*, *123*(12), 10,239–10,253, doi:10.1029/2018JA025310.

Liu, H., H. Lühr, V. Henize, and W. KöHler (2005), Global distribution of the thermospheric total mass density derived from CHAMP, *Journal of Geophysical Research (Space Physics)*, *110*(A4), A04301, doi:10.1029/2004JA010741.

Liu, H., H. Lühr, and S. Watanabe (2007), Climatology of the equatorial thermospheric mass density anomaly, *Journal of Geophysical Research (Space Physics)*, *112*(A5), A05305, doi:10.1029/2006JA012199.

Liu, H.-L., C. G. Bardeen, B. T. Foster, P. Lauritzen, J. Liu, G. Lu, D. R. Marsh, A. Maute, J. M. McInerney, N. M. Pedatella, L. Qian, A. D. Richmond, R. G. Roble, S. C. Solomon, F. M. Vitt, and W. Wang (2018), Development and Validation of the Whole Atmosphere Community Climate Model With Thermosphere and Ionosphere Extension (WACCM-X 2.0), *Journal of Advances in Modeling Earth Systems*, *10*(2), 381–402, doi: 10.1002/2017MS001232.

Liu, R., H. Lühr, and S. Y. Ma (2010), Storm-time related mass density anomalies in the polar cap as observed by CHAMP, *Annales Geophysicae*, *28*(1), 165–180, doi: 10.5194/angeo-28-165-2010.

Lu, G., A. D. Richmond, B. A. Emery, and R. G. Roble (1995), Magnetosphere-ionosphere-thermosphere coupling: Effect of neutral winds on energy transfer and field-aligned current, *J. Geophys. Res.*, *100*(A10), 19,643–19,660, doi:10.1029/95JA00766.

Lu, G., L. P. Goncharenko, A. D. Richmond, R. G. Roble, and N. Aponte (2008), A day-side ionospheric positive storm phase driven by neutral winds, *Journal of Geophysical Research (Space Physics)*, *113*(A8), A08304, doi:10.1029/2007JA012895.

Lu, G., A. D. Richmond, H. Lühr, and L. Paxton (2016), High-latitude energy input and its impact on the thermosphere, *Journal of Geophysical Research (Space Physics)*, *121*(7), 7108–7124, doi:10.1002/2015JA022294.

Lühr, H., J. Warnecke, L. J. Zanetti, P. A. Lindqvist, and T. J. Hughes (1994), Fine structure of field-aligned current sheets deduced from spacecraft and ground-based observations: Initial FREJA results, *Geophys. Res. Lett.*, *21*(17), 1883–1886, doi:10.1029/94GL01278.

Lühr, H., M. Rother, W. Köhler, P. Ritter, and L. Grunwaldt (2004), Thermospheric upwelling in the cusp region: Evidence from CHAMP observations, *Geophys. Res. Lett.*, *31*(6), L06805, doi:10.1029/2003GL019314.

Lühr, H., J. Park, J. W. Gjerloev, J. Rauberg, I. Michaelis, J. M. G. Merayo, and P. Brauer (2015), Field-aligned currents' scale analysis performed with the Swarm constellation, *Geophys. Res. Lett.*, *42*, 1–8, doi:10.1002/2014GL062453.

Lyons, L. R. (1992), Formation of auroral arcs via magnetosphere-ionosphere coupling, *Reviews of Geophysics*, *30*(2), 93–112.

Lysak, R. L. (1985), Auroral electrodynamics with current and voltage generators, *J. Geophys. Res.*, *90*(A5), 4178–4190, doi:10.1029/JA090iA05p04178.

Mannucci, A. J., B. T. Tsurutani, B. A. Iijima, A. Komjathy, A. Saito, W. D. Gonzalez, F. L. Guarnieri, J. U. Kozyra, and R. Skoug (2005), Dayside global ionospheric response to the major interplanetary events of October 29-30, 2003 “Halloween Storms”, *Geophys. Res. Lett.*, *32*(12), L12S02, doi:10.1029/2004GL021467.

Marsal, S., A. D. Richmond, A. Maute, and B. J. Anderson (2012), Forcing the TIEGCM model with Birkeland currents from the Active Magnetosphere and Planetary Electrodynamics Response Experiment, *Journal of Geophysical Research (Space Physics)*, *117*(A6), A06308, doi:10.1029/2011JA017416.

Maruyama, N., S. Watanabe, and T. J. Fuller-Rowell (2003), Dynamic and energetic coupling in the equatorial ionosphere and thermosphere, *Journal of Geophysical Research (Space Physics)*, *108*(A11), 1396, doi:10.1029/2002JA009599.

Maruyama, N., A. D. Richmond, T. J. Fuller-Rowell, M. V. Codrescu, S. Sazykin, F. R. Toffoletto, R. W. Spiro, and G. H. Millward (2005), Interaction between direct penetration and disturbance dynamo electric fields in the storm-time equatorial ionosphere, *Geophys. Res. Lett.*, *32*(17), L17105, doi:10.1029/2005GL023763.

Matsuo, T., and A. D. Richmond (2008), Effects of high-latitude ionospheric electric field variability on global thermospheric Joule heating and mechanical energy transfer rate, *Journal of Geophysical Research (Space Physics)*, *113*(A7), A07309, doi: 10.1029/2007JA012993.

Matsuo, T., A. D. Richmond, and K. Hensel (2003), High-latitude ionospheric electric field variability and electric potential derived from DE-2 plasma drift measurements: Dependence on IMF and dipole tilt, *Journal of Geophysical Research (Space Physics)*, *108*(A1), 1005, doi:10.1029/2002JA009429.

Maute, A., and A. D. Richmond (2017), F-Region Dynamo Simulations at Low and Mid-Latitude, *Space Sci. Rev.*, *206*(1-4), 471–493, doi:10.1007/s11214-016-0262-3.

Maute, A. I., and A. D. Richmond (2006), A Set of Empirical Models of the High-Latitude Magnetosphere-Ionosphere Energy Transfer Based on Dynamic Explorer 2 Data, in *AGU Fall Meeting Abstracts*, vol. 2006, pp. SA13A–0259.

Mayr, H. G., A. E. Hedin, C. A. Reber, and G. R. Carignan (1974), Global characteristics in the diurnal variations of the thermospheric temperature and composition, *J. Geophys. Res.*, *79*(4), 619, doi:10.1029/JA079i004p00619.

McDiarmid, I. B., J. R. Burrows, and E. E. Budzinski (1975), Average characteristics of magnetospheric electrons (150 eV to 200 keV) at 1400 km, *J. Geophys. Res.*, *80*(1), 73, doi:10.1029/JA080i001p00073.

McGranaghan, R. M., A. J. Mannucci, and C. Forsyth (2017), A Comprehensive Analysis of Multiscale Field-Aligned Currents: Characteristics, Controlling Parameters, and Relationships, *Journal of Geophysical Research (Space Physics)*, *122*, 11, doi:10.1002/2017JA024742.

McIntosh, R. C., and P. C. Anderson (2014), Maps of precipitating electron spectra characterized by Maxwellian and kappa distributions, *Journal of Geophysical Research (Space Physics)*, *119*(12), 10,116–10,132, doi:10.1002/2014JA020080.

Meier, R. R., D. J. Strickland, J. H. Hecht, and A. B. Christensen (1989), Deducing composition and incident electron spectra from ground-based auroral optical measurements: A study of auroral red line processes, *J. Geophys. Res.*, *94*(A10), 13,541–13,552, doi:10.1029/JA094iA10p13541.

Mende, S. B., S. E. Harris, H. U. Frey, V. Angelopoulos, C. T. Russell, E. Donovan, B. Jackel, M. Greffen, and L. M. Peticolas (2008), The THEMIS Array of Ground-based Observatories for the Study of Auroral Substorms, *Space Sci. Rev.*, *141*(1-4), 357–387, doi:10.1007/s11214-008-9380-x.

Merkin, V. G., and C. C. Goodrich (2007), Does the polar cap area saturate?, *Geophys. Res. Lett.*, *34*(9), L09107, doi:10.1029/2007GL029357.

Milan, S. E., J. A. Carter, H. Korth, and B. J. Anderson (2015), Principal component analysis of Birkeland currents determined by the Active Magnetosphere and Planetary Electrodynamics Response Experiment, *Journal of Geophysical Research (Space Physics)*, *120*(12), 10,415–10,424, doi:10.1002/2015JA021680.

Millward, G. H., I. C. F. Müller-Wodarg, A. D. Aylward, T. J. Fuller-Rowell, A. D. Richmond, and R. J. Moffett (2001), An investigation into the influence of tidal forcing on F region equatorial vertical ion drift using a global ionosphere-thermosphere model with coupled electrodynamics, *J. Geophys. Res.*, *106*(A11), 24,733–24,744, doi:10.1029/2000JA000342.

Mitchell, E. J., R. E. Lopez, R. J. Bruntz, M. Wiltberger, J. G. Lyon, R. C. Allen, S. J. Cockrell, and P. L. Whittlesey (2010), Saturation of transpolar potential for large Y component interplanetary magnetic field, *Journal of Geophysical Research (Space Physics)*, *115*(A6), A06201, doi:10.1029/2009JA015119.

Mitchell, E. J., P. T. Newell, J. W. Gjerloev, and K. Liou (2013), OVATION-SM: A model of auroral precipitation based on SuperMAG generalized auroral electrojet and substorm onset times, *Journal of Geophysical Research (Space Physics)*, *118*(6), 3747–3759, doi:10.1002/jgra.50343.

Miyoshi, Y., H. Fujiwara, H. Jin, H. Shinagawa, H. Liu, and K. Terada (2011), Model study on the formation of the equatorial mass density anomaly in the thermosphere, *Journal of Geophysical Research (Space Physics)*, *116*(A5), A05322, doi:10.1029/2010JA016315.

Neubert, T., and F. Christiansen (2003), Small-scale, field-aligned currents at the top-side ionosphere, *Geophys. Res. Lett.*, *30*(19), 2010, doi:10.1029/2003GL017808.

Newell, P. T., and C.-I. Meng (1988), The cusp and the cleft/boundary layer: Low-altitude identification and statistical local time variation, *J. Geophys. Res.*, *93*(A12), 14,549–14,556, doi:10.1029/JA093iA12p14549.

Newell, P. T., and C.-I. Meng (1994), Ionospheric projections of magnetospheric regions under low and high solar wind pressure conditions, *J. Geophys. Res.*, *99*(A1), 273–286, doi:10.1029/93JA02273.

Newell, P. T., C.-I. Meng, D. G. Sibeck, and R. Lepping (1989), Some low-altitude cusp dependencies on the interplanetary magnetic field, *J. Geophys. Res.*, *94*(A7), 8921–8927, doi:10.1029/JA094iA07p08921.

Newell, P. T., Y. I. Feldstein, Y. I. Galperin, and C.-I. Meng (1996), Morphology of nightside precipitation, *J. Geophys. Res.*, *101*(A5), 10,737–10,748, doi:10.1029/95JA03516.

Newell, P. T., J. M. Ruohoniemi, and C. I. Meng (2004), Maps of precipitation by source region, binned by IMF, with inertial convection streamlines, *Journal of Geophysical Research (Space Physics)*, *109*(A10), A10206, doi:10.1029/2004JA010499.

Newell, P. T., T. Sotirelis, K. Liou, C. I. Meng, and F. J. Rich (2007), A nearly universal solar wind-magnetosphere coupling function inferred from 10 magnetospheric state variables, *Journal of Geophysical Research (Space Physics)*, *112*(A1), A01206, doi:10.1029/2006JA012015.

Newell, P. T., T. Sotirelis, K. Liou, and F. J. Rich (2008), Pairs of solar wind-magnetosphere coupling functions: Combining a merging term with a viscous term works best, *Journal of Geophysical Research (Space Physics)*, *113*(A4), A04218, doi: 10.1029/2007JA012825.

Newell, P. T., T. Sotirelis, and S. Wing (2009), Diffuse, monoenergetic, and broadband aurora: The global precipitation budget, *Journal of Geophysical Research (Space Physics)*, *114*(A9), A09207, doi:10.1029/2009JA014326.

Newell, P. T., K. Liou, Y. Zhang, T. Sotirelis, L. J. Paxton, and E. J. Mitchell (2014), OVATION Prime-2013: Extension of auroral precipitation model to higher disturbance levels, *Space Weather*, *12*(6), 368–379, doi:10.1002/2014SW001056.

Nishimura, Y., L. R. Lyons, Y. Zou, K. Oksavik, J. I. Moen, L. B. Clausen, E. F. Donovan, V. Angelopoulos, K. Shiokawa, J. M. Ruohoniemi, N. Nishitani, K. A. McWilliams, and M. Lester (2014), Day-night coupling by a localized flow channel visualized by polar cap patch propagation, *Geophys. Res. Lett.*, *41*(11), 3701–3709, doi: 10.1002/2014GL060301.

Ohtani, S., G. Ueno, and T. Higuchi (2005), Comparison of large-scale field-aligned currents under sunlit and dark ionospheric conditions, *Journal of Geophysical Research (Space Physics)*, *110*(A9), A09230, doi:10.1029/2005JA011057.

Oliveira, D. M., and E. Zesta (2019), Satellite orbital drag during magnetic storms, *Space Weather*, *17*(11), 1510–1533, doi:10.1029/2019SW002287.

Pant, T. K., and R. Sridharan (2001), Plausible explanation for the equatorial temperature and wind anomaly (ETWA) based on chemical and dynamical processes, *Journal of Atmospheric and Solar-Terrestrial Physics*, *63*(9), 885–891, doi:10.1016/S1364-6826(00)00196-6.

Papitashvili, V. O., and F. J. Rich (2002), High-latitude ionospheric convection models derived from Defense Meteorological Satellite Program ion drift observations and parameterized by the interplanetary magnetic field strength and direction, *Journal of Geophysical Research (Space Physics)*, *107*(A8), 1198, doi:10.1029/2001JA000264.

Park, J., H. Lühr, D. J. Knudsen, J. K. Burchill, and Y.-S. Kwak (2017), Alfvén waves in the auroral region, their Poynting flux, and reflection coefficient as estimated from Swarm observations, *Journal of Geophysical Research (Space Physics)*, *122*(2), 2345–2360, doi:10.1002/2016JA023527.

Qian, L., A. G. Burns, B. A. Emery, B. Foster, G. Lu, A. Maute, A. D. Richmond, R. G. Roble, S. C. Solomon, and W. Wang (2014), *The NCAR TIE-GCM*, chap. 7, pp. 73–83, American Geophysical Union (AGU), doi:10.1002/9781118704417.ch7.

Raghavarao, R., L. E. Wharton, N. W. Spencer, H. G. Mayr, and L. H. Brace (1991), An equatorial temperature and wind anomaly (ETWA), *Geophys. Res. Lett.*, *18*(7), 1193–1196, doi:10.1029/91GL01561.

Raghavarao, R., W. R. Hoegy, N. W. Spencer, and L. E. Wharton (1993), Neutral temperature anomaly in the equatorial thermosphere-A source of vertical winds, *Geophys. Res. Lett.*, *20*(11), 1023–1026, doi:10.1029/93GL01253.

Raghavarao, R., R. Suhasini, W. R. Hoegy, H. G. Mayr, and L. Wharton (1998), Local time variation of equatorial temperature and zonal wind anomaly (ETWA), *Journal of Atmospheric and Solar-Terrestrial Physics*, *60*(6), 631–642, doi:10.1016/S1364-6826(97)00130-2.

Redmon, R. J., W. K. Peterson, L. Andersson, E. A. Kihn, W. F. Denig, M. Hairston, and R. Coley (2010), Vertical thermal O^+ flows at 850 km in dynamic auroral boundary

coordinates, *Journal of Geophysical Research (Space Physics)*, *115*(A11), A00J08, doi: 10.1029/2010JA015589.

Redmon, R. J., W. F. Denig, L. M. Kilcommons, and D. J. Knipp (2017), New DMSP database of precipitating auroral electrons and ions, *Journal of Geophysical Research (Space Physics)*, *122*, 9056–9067, doi:10.1002/2016JA023339.

Rees, M. H. (1989), *Physics and chemistry of the upper atmosphere*, vol. 1, Cambridge University Press.

Reiff, P. H., and J. L. Burch (1985), IMF B_y-dependent plasma flow and Birkeland currents in the dayside magnetosphere: 2. A global model for northward and southward IMF, *J. Geophys. Res.*, *90*(A2), 1595–1610, doi:10.1029/JA090iA02p01595.

Rentz, S., and H. Lühr (2008), Climatology of the cusp-related thermospheric mass density anomaly, as derived from CHAMP observations, *Annales Geophysicae*, *26*(9), 2807–2823, doi:10.5194/angeo-26-2807-2008.

Rich, F. J., and M. Hairston (1994), Large-scale convection patterns observed by DMSP, *J. Geophys. Res.*, *99*(A3), 3827–3844, doi:10.1029/93JA03296.

Richards, P. G. (2013), Reevaluation of thermosphere heating by auroral electrons, *Advances in Space Research*, *51*(4), 610–619, doi:10.1016/j.asr.2011.09.004.

Richmond, A. (2016), Ionospheric electrodynamics, *Space weather fundamentals*, p. 35.

Richmond, A. D. (1992), Assimilative mapping of ionospheric electrodynamics, *Advances in Space Research*, *12*(6), 59–68, doi:10.1016/0273-1177(92)90040-5.

Richmond, A. D. (1995), Ionospheric Electrodynamics Using Magnetic Apex Coordinates., *Journal of Geomagnetism and Geoelectricity*, *47*(2), 191–212, doi:10.5636/jgg.47.191.

Richmond, A. D. (2020), *Joule heating in the thermosphere*, American Geophysical Union (AGU).

Richmond, A. D., and Y. Kamide (1988), Mapping electrodynamic features of the high-latitude ionosphere from localized observations: Technique, *J. Geophys. Res.*, *93*(A6), 5741–5759, doi:10.1029/JA093iA06p05741.

Richmond, A. D., E. C. Ridley, and R. G. Roble (1992), A thermosphere/ionosphere general circulation model with coupled electrodynamics, *Geophys. Res. Lett.*, *19*(6), 601–604, doi:10.1029/92GL00401.

Ridley, A. J., and E. A. Kihn (2004), Polar cap index comparisons with AMIE cross polar cap potential, electric field, and polar cap area, *Geophys. Res. Lett.*, *31*(7), L07801, doi:10.1029/2003GL019113.

Ridley, A. J., Y. Deng, and G. Tóth (2006), The global ionosphere thermosphere model, *Journal of Atmospheric and Solar-Terrestrial Physics*, *68*(8), 839–864, doi:10.1016/j.jastp.2006.01.008.

Rishbeth, H., and O. K. Garriott (1969), *Introduction to ionospheric physics*, vol. 14, Academic Press New York.

Ritter, P., H. Lühr, and J. Rauberg (2013), Determining field-aligned currents with the Swarm constellation mission, *Earth, Planets, and Space*, *65*(11), 1285–1294, doi:10.5047/eps.2013.09.006.

Robinson, R. M., R. R. Vondrak, K. Miller, T. Dabbs, and D. Hardy (1987), On calculating ionospheric conductances from the flux and energy of precipitating electrons, *J. Geophys. Res.*, *92*(A3), 2565–2570, doi:10.1029/JA092iA03p02565.

Roble, R. G. (1976), Solar EUV flux variation during a solar cycle as derived from ionospheric modeling considerations, *J. Geophys. Res.*, *81*(1), 265, doi: 10.1029/JA081i001p00265.

Roble, R. G., and E. C. Ridley (1994), A thermosphere-ionosphere-mesosphere-electrodynamics general circulation model (time-GCM): Equinox solar cycle minimum simulations (30-500 km), *Geophys. Res. Lett.*, *21*(6), 417–420, doi:10.1029/93GL03391.

Rodger, A. S., G. D. Wells, R. J. Moffett, and G. J. Bailey (2001), The variability of Joule heating, and its effects on the ionosphere and thermosphere, *Annales Geophysicae*, *19*(7), 773–781, doi:10.5194/angeo-19-773-2001.

Ruohoniemi, J. M., and R. A. Greenwald (1996), Statistical patterns of high-latitude convection obtained from Goose Bay HF radar observations, *J. Geophys. Res.*, *101*(A10), 21,743–21,764, doi:10.1029/96JA01584.

Ruohoniemi, J. M., and R. A. Greenwald (2005), Dependencies of high-latitude plasma convection: Consideration of interplanetary magnetic field, seasonal, and universal time factors in statistical patterns, *Journal of Geophysical Research (Space Physics)*, *110*(A9), A09204, doi:10.1029/2004JA010815.

Scherliess, L., and B. G. Fejer (1999), Radar and satellite global equatorial F region vertical drift model, *J. Geophys. Res.*, *104*(A4), 6829–6842, doi:10.1029/1999JA900025.

Schunk, R. W., and A. F. Nagy (2000), *Ionospheres: Physics, Plasma Physics, and Chemistry*, Cambridge Atmospheric and Space Science Series, Cambridge University Press, doi:10.1017/CBO9780511551772.

Sheng, C., Y. Deng, Y.-J. Chen, R. A. Heelis, and Y. Huang (2019), Effects of Alignment Between Particle Precipitation and Ion Convection Patterns on Joule Heat-

ing, *Journal of Geophysical Research (Space Physics)*, *124*(6), 4905–4915, doi: 10.1029/2018JA026446.

Shepherd, S. G. (2007), Polar cap potential saturation: Observations, theory, and modeling, *Journal of Atmospheric and Solar-Terrestrial Physics*, *69*(3), 234–248, doi: 10.1016/j.jastp.2006.07.022.

Shi, Y., D. J. Knipp, T. Matsuo, L. Kilcommons, and B. Anderson (2020), Event Studies of High-Latitude FACs With Inverse and Assimilative Analysis of AMPERE Magnetometer Data, *Journal of Geophysical Research (Space Physics)*, *125*(3), e27266, doi: 10.1029/2019JA027266.

Sotirelis, T., and P. T. Newell (2000), Boundary-oriented electron precipitation model, *J. Geophys. Res.*, *105*(A8), 18,655–18,673, doi:10.1029/1999JA000269.

Sotirelis, T., J. M. Ruohoniemi, R. J. Barnes, P. T. Newell, R. A. Greenwald, J. P. Skura, and C. I. Meng (2005), Comparison of SuperDARN radar boundaries with DMSP particle precipitation boundaries, *Journal of Geophysical Research (Space Physics)*, *110*(A6), A06302, doi:10.1029/2004JA010732.

Spiro, R. W., P. H. Reiff, and J. Maher, L. J. (1982), Precipitating electron energy flux and auroral zone conductances-an empirical model, *J. Geophys. Res.*, *87*(A10), 8215–8227, doi:10.1029/JA087iA10p08215.

Spiro, R. W., R. A. Wolf, and B. G. Fejer (1988), Penetrating of high-latitude-electric-field effects to low latitudes during SUNDIAL 1984, *Annales Geophysicae*, *6*, 39–49.

Strickland, D. J., J. Daniell, R. E., J. R. Jasperse, and B. Basu (1993), Transport-theoretic model for the electron-proton-hydrogen atom aurora 2. Model results, *J. Geophys. Res.*, *98*(A12), 21,533–21,548, doi:10.1029/93JA01645.

Sugiura, M. (1984), A fundamental magnetosphere-ionosphere coupling mode involving field-aligned currents as deduced from DE-2 observations, *Geophys. Res. Lett.*, *11*, 877–880, doi:10.1029/GL011i009p00877.

Sugiura, M., N. C. Maynard, W. H. Farthing, J. P. Heppner, B. G. Ledley, and J. Cahill, L. J. (1982), Initial results on the correlation between the magnetic and electric fields observed from the DE-2 satellite in the field-aligned current regions, *Geophys. Res. Lett.*, *9*(9), 985–988, doi:10.1029/GL009i009p00985.

Thayer, J. P., and J. Semeter (2004), The convergence of magnetospheric energy flux in the polar atmosphere, *Journal of Atmospheric and Solar-Terrestrial Physics*, *66*(10), 807–824, doi:10.1016/j.jastp.2004.01.035.

Thayer, J. P., and J. F. Vickrey (1992), On the contribution of the thermospheric neutral wind to high-latitude energetics, *Geophys. Res. Lett.*, *19*(3), 265–268, doi:10.1029/91GL02868.

Thayer, J. P., J. F. Vickrey, R. A. Heelis, and J. B. Gary (1995), Interpretation and modeling of the high-latitude electromagnetic energy flux, *J. Geophys. Res.*, *100*(A10), 19,715–19,728, doi:10.1029/95JA01159.

Thébault, E., C. C. Finlay, C. D. Beggan, P. Alken, J. Aubert, O. Barrois, F. Bertrand, T. Bondar, A. Boness, L. Brocco, E. Canet, A. Chambodut, A. Chulliat, P. Coïsson, F. Civet, A. Du, A. Fournier, I. Fratter, N. Gillet, B. Hamilton, M. Hamoudi, G. Hulot, T. Jager, M. Korte, W. Kuang, X. Lalanne, B. Langlais, J.-M. Léger, V. Lesur, F. J. Lowes, S. Macmillan, M. Mand ea, C. Manoj, S. Maus, N. Olsen, V. Petrov, V. Ridley, M. Rother, T. J. Sabaka, D. Saturnino, R. Schachtschneider, O. Sirol, A. Tangborn, A. Thomson, L. Tøffner-Clausen, P. Vigneron, I. Wardinski, and T. Zvereva (2015), Inter-

national Geomagnetic Reference Field: the 12th generation, *Earth, Planets, and Space*, *67*, 79, doi:10.1186/s40623-015-0228-9.

Thomas, E. G., and S. G. Shepherd (2018), Statistical Patterns of Ionospheric Convection Derived From Mid-latitude, High-Latitude, and Polar SuperDARN HF Radar Observations, *Journal of Geophysical Research (Space Physics)*, *123*(4), 3196–3216, doi:10.1002/2018JA025280.

Tobiska, W. K. (1991), Revised solar extreme ultraviolet flux model., *Journal of Atmospheric and Terrestrial Physics*, *53*, 1005–1018, doi:10.1016/0021-9169(91)90046-A.

Torr, D. G., M. R. Torr, H. C. Brinton, L. H. Brace, N. W. Spencer, A. E. Hedin, W. B. Hanson, J. H. Hoffman, A. O. Nier, J. C. G. Walker, and D. W. Rusch (1979), An experimental and theoretical study of the mean diurnal variation of O^+, NO^+, $O_2{}^+$, and $N_2{}^+$ ions in the mid-latitude F_1, layer of the ionosphere, *J. Geophys. Res.*, *84*(A7), 3360–3372, doi:10.1029/JA084iA07p03360.

Tóth, G., I. V. Sokolov, T. I. Gombosi, D. R. Chesney, C. R. Clauer, D. L. de Zeeuw, K. C. Hansen, K. J. Kane, W. B. Manchester, R. C. Oehmke, K. G. Powell, A. J. Ridley, I. I. Roussev, Q. F. Stout, O. Volberg, R. A. Wolf, S. Sazykin, A. Chan, B. Yu, and J. Kóta (2005), Space Weather Modeling Framework: A new tool for the space science community, *Journal of Geophysical Research (Space Physics)*, *110*(A12), A12226, doi:10.1029/2005JA011126.

Vichare, G., A. Ridley, and E. Yiğit (2012), Quiet-time low latitude ionospheric electrodynamics in the non-hydrostatic Global Ionosphere-Thermosphere Model, *Journal of Atmospheric and Solar-Terrestrial Physics*, *80*, 161–172, doi:10.1016/j.jastp.2012.01.009.

Vickrey, J. F., R. C. Livingston, N. B. Walker, T. A. Potemra, R. A. Heelis, M. C. Kelley, and F. J. Rich (1986), On the current-voltage relationship of the magneto-

spheric generator at intermediate spatial scales, *Geophys. Res. Lett.*, *13*(6), 495–498, doi:10.1029/GL013i006p00495.

Walker, I. K., J. Moen, L. Kersley, and D. A. Lorentzen (1999), On the possible role of cusp/cleft precipitation in the formation of polar-cap patches, *Annales Geophysicae*, *17*(10), 1298–1305, doi:10.1007/s00585-999-1298-4.

Wang, H., H. Lühr, and S. Y. Ma (2005), Solar zenith angle and merging electric field control of field-aligned currents: A statistical study of the Southern Hemisphere, *Journal of Geophysical Research (Space Physics)*, *110*(A3), A03306, doi:10.1029/2004JA010530.

Wang, W., T. L. Killeen, A. G. Burns, and R. G. Roble (1999), A high-resolution, three-dimensional, time dependent, nested grid model of the coupled thermosphere-ionosphere, *Journal of Atmospheric and Solar-Terrestrial Physics*, *61*(5), 385–397, doi:10.1016/S1364-6826(98)00079-0.

Weimer, D. R. (1995), Models of high-latitude electric potentials derived with a least error fit of spherical harmonic coefficients, *J. Geophys. Res.*, *100*(A10), 19,595–19,608, doi:10.1029/95JA01755.

Weimer, D. R. (2005), Improved ionospheric electrodynamic models and application to calculating Joule heating rates, *Journal of Geophysical Research (Space Physics)*, *110*(A5), A05306, doi:10.1029/2004JA010884.

Weimer, D. R., C. K. Goertz, D. A. Gurnett, N. C. Maynard, and J. L. Burch (1985), Auroral zone electric fields from DE 1 and 2 at magnetic conjunctions, *J. Geophys. Res.*, *90*(A8), 7479–7494, doi:10.1029/JA090iA08p07479.

Weimer, D. R., T. R. Edwards, and N. Olsen (2017), Linear response of field-aligned currents to the interplanetary electric field, *Journal of Geophysical Research (Space Physics)*, *122*(8), 8502–8515, doi:10.1002/2017JA024372.

Wharton, L. E., N. W. Spencer, and H. G. Mayr (1984), The Earth's thermospheric superrotation from Dynamics Explorer 2, *Geophys. Res. Lett.*, *11*(5), 531–533, doi:10.1029/GL011i005p00531.

Wilder, F. D., C. R. Clauer, and J. B. H. Baker (2008), Reverse convection potential saturation during northward IMF, *Geophys. Res. Lett.*, *35*(12), L12103, doi:10.1029/2008GL034040.

Wing, S., G. V. Khazanov, D. G. Sibeck, and E. Zesta (2019), Low Energy Precipitating Electrons in the Diffuse Aurorae, *Geophys. Res. Lett.*, *46*(7), 3582–3589, doi:10.1029/2019GL082383.

Winningham, J. D., J. L. Burch, N. Eaker, V. A. Blevins, and R. A. Hoffman (1981), The Low Altitude Plasma Instrument (LAPI)., *Space Science Instrumentation*, *5*, 465–475.

Zhang, B., W. Lotko, O. Brambles, M. Wiltberger, W. Wang, P. Schmitt, and J. Lyon (2012), Enhancement of thermospheric mass density by soft electron precipitation, *Geophys. Res. Lett.*, *39*(20), L20102, doi:10.1029/2012GL053519.

Zhang, B., W. Lotko, O. Brambles, M. Wiltberger, and J. Lyon (2015a), Electron precipitation models in global magnetosphere simulations, *Journal of Geophysical Research (Space Physics)*, *120*(2), 1035–1056, doi:10.1002/2014JA020615.

Zhang, B., R. H. Varney, W. Lotko, O. J. Brambles, W. Wang, J. Lei, M. Wiltberger, and J. G. Lyon (2015b), Pathways of F region thermospheric mass density enhancement via

soft electron precipitation, *Journal of Geophysical Research (Space Physics)*, *120*(7), 5824–5831, doi:10.1002/2015JA020999.

Zhang, S.-R., P. J. Erickson, A. J. Coster, W. Rideout, J. Vierinen, O. Jonah, and L. P. Goncharenko (2019), Subauroral and Polar Traveling Ionospheric Disturbances During the 7-9 September 2017 Storms, *Space Weather*, *17*(12), 1748–1764, doi: 10.1029/2019SW002325.

Zhang, Y., and L. J. Paxton (2008), An empirical Kp-dependent global auroral model based on TIMED/GUVI FUV data, *Journal of Atmospheric and Solar-Terrestrial Physics*, *70*(8-9), 1231–1242, doi:10.1016/j.jastp.2008.03.008.

Zhu, Q., Y. Deng, A. Maute, C. Sheng, and C. Y. Lin (2017), Impact of the vertical dynamics on the thermosphere at low and middle latitudes: GITM simulations, *Journal of Geophysical Research (Space Physics)*, *122*(6), 6882–6891, doi:10.1002/2017JA023939.

Zhu, Q., Y. Deng, A. Richmond, and A. Maute (2018), Small-Scale and Mesoscale Variabilities in the Electric Field and Particle Precipitation and Their Impacts on Joule Heating, *Journal of Geophysical Research (Space Physics)*, *123*(11), 9862–9872, doi: 10.1029/2018JA025771.

Zhu, Q., Y. Deng, A. Richmond, R. M. McGranaghan, and A. Maute (2019), Impacts of Multiscale FACs on the Ionosphere-Thermosphere System: GITM Simulation, *Journal of Geophysical Research (Space Physics)*, *124*(5), 3532–3542, doi: 10.1029/2018JA026082.

Zhu, Q., Y. Deng, A. Richmond, A. Maute, Y.-J. Chen, M. Hairston, L. Kilcommons, D. Knipp, R. Redmon, and E. Mitchell (2020), Impacts of Binning Methods on High-Latitude Electrodynamic Forcing: Static Versus Boundary-Oriented Bin-

ning Methods, *Journal of Geophysical Research (Space Physics)*, *125*(1), e27270, doi: 10.1029/2019JA027270.

Zou, Y., Y. Nishimura, L. Lyons, M. Conde, R. Varney, V. Angelopoulos, and S. Mende (2018), Mesoscale F Region Neutral Winds Associated With Quasi-steady and Transient Nightside Auroral Forms, *Journal of Geophysical Research (Space Physics)*, *123*(9), 7968–7984, doi:10.1029/2018JA025457.

BIOGRAPHICAL STATEMENT

Qingyu Zhu received a bachelor's degree in geophysics from the University of Science and Technology of China in 2015 and joined UT Arlington in 2015 as a graduate student under the supervision of Dr. Yue Deng. His main research interest is Earth's ionospheric electrodynamics at different latitudinal regions.

During his graduate career, he has received several scholarships from the Department of Physics. Besides, he was awarded by the Advanced Study Program (ASP) Graduate Visitor Program fellowship which allows him to collaborate with NCAR scientists. Moreover, he actively present in APS, CEDAR and AGU meetings and was awarded CEDAR poster prizes in 2018 and 2019. Furthermore, he was awarded the ASP postdoc fellowship in 2020. Qingyu was the first author of seven scientific papers, with five published, one under review and one in preparation. Qingyu was also co-authored in several other papers.